Interventions in Sphingosine-1-Phosphate Metabolism Modulate Hepatic and Adipose Lipid Homeostasis in the Development of Metabolic Disorders

Inaugural-Dissertation

zur Erlangung des Doktorgrades
der Mathematisch-Naturwissenschaftlichen Fakultät
der Heinrich-Heine-Universität Düsseldorf

vorgelegt von

Melissa Kim Nowak
aus Moers

Düsseldorf, Oktober 2025

aus dem Institut für Molekulare Medizin III
der Heinrich-Heine-Universität Düsseldorf

Gedruckt mit der Genehmigung der
Mathematisch-Naturwissenschaftlichen Fakultät der
Heinrich-Heine-Universität Düsseldorf

Berichterstatter:

1. Prof. Dr. med. Bodo Levkau
2. Prof. Dr. med. Tom Lüdde

Tag der mündlichen Prüfung: 26. Januar 2026

Table of Contents

Abstract

Driven by obesity and dysregulated lipid metabolism, metabolic syndrome (MetS) has emerged as a major global health challenge, intricately linked to type 2 diabetes (T2D), metabolic dysfunction-associated steatotic liver disease (MASLD), and cardiovascular disease. Although considerable progress has been made in understanding MetS, therapeutic options remain limited, highlighting the need for novel mechanistic insights and potential targets. In this context, sphingolipid metabolism has emerged as a pivotal regulator of metabolic processes, yet the underlying mechanisms remain only partially understood.

This study aimed to investigate how genetic and pharmacological interventions in sphingolipid metabolism influence lipid homeostasis in hepatic and adipose tissues, thereby modulating the onset and progression of metabolic disorders.

In a high-fat diet (HFD) mouse model, sphingosine-1-phosphate (S1P)-synthesizing enzymes (SphK) and the S1P-degrading enzyme S1P lyase were selectively targeted through genetic deletion and pharmacological inhibition. The metabolic status was comprehensively assessed by glucose and insulin tolerance tests, body weight monitoring, histological analysis of hepatic steatosis, and LC-MS/MS quantification of sphingolipid profiles. Complementary transcriptomic and molecular analyses included RNA sequencing and RT-qPCR targeting hepatic lipid metabolism genes, and protein-level confirmation by Western Blot.

Both genetic deletion and pharmacological inhibition of SphK2 conferred protection against obesity, hepatic steatosis, and impaired glucose homeostasis in mice. In both approaches, hepatic ceramide increased and plasma S1P levels were elevated. Similarly, pharmacological inhibition of S1P lyase attenuated weight gain, improved glucose homeostasis and reduced markers of hepatic injury, accompanied by higher hepatic ceramide and elevated plasma S1P levels under HFD conditions. Mechanistically, S1P activated atypical PKCζ in adipose tissue, promoting lipolysis via a MAPK/HSL-dependent pathway. In the liver, ceramide-induced PKCζ activation was observed, although the precise mechanism remains to be defined.

Together, these findings demonstrate that targeted manipulation of sphingolipid metabolism exerts protective and therapeutic effects against key features of MetS. Moreover, distinct sphingolipid signatures may serve as promising biomarkers for risk prediction, early diagnosis, and therapeutic targeting in metabolic disease.

Zusammenfassung

Das metabolische Syndrom gehört mit steigender Inzidenz zu den größten globalen Gesundheitsproblemen der heutigen Zeit und wird maßgeblich durch Obesitas sowie damit einhergehende Störungen des Fettstoffwechsels geprägt. Da es eng mit der Entstehung von Typ-2-Diabetes (T2D), metabolisch-assoziierten steatotischen Lebererkrankungen (MASLD) und kardiovaskulären Erkrankungen verknüpft ist, besteht eine zentrale Herausforderung in der Entwicklung wirksamer Präventions- und Therapiemöglichkeiten. Vor diesem Hintergrund wurde in der vorliegenden Arbeit der Sphingolipidmetabolismus untersucht, von dem gezeigt wurde, dass er wesentlich zur Krankheitsprogression beiträgt. Die zugrundeliegenden Mechanismen sind jedoch bislang nur unvollständig verstanden.

Ziel dieser Arbeit was es daher, zu untersuchen, wie Interventionen im Sphingolipidmetabolismus zur Regulation der Lipidhomöostase in Leber und Fettgewebe beitragen und dadurch die Entstehung und das Fortschreiten metabolischer Erkrankungen beeinflussen. Hierzu wurde im Mausmodell ergänzend zu einer 12- bzw. 16-wöchigen fettreichen Diät der Sphingolipidmetabolismus sowohl genetisch als auch pharmakologisch gezielt manipuliert. Dabei standen die Sphingosin-1-Phosphat (S1P) synthetisierenden Enzyme Sphingosinkinasen 1 und 2 (SphK) sowie das S1P-abbauende Enzym S1P-Lyase im Fokus.

Der metabolische Status wurde über Glukose- und Insulintoleranztests und die Gewichtsentwicklung bestimmt. Ergänzend wurden Organparameter wie Gewicht erfasst, Fetteinlagerungen in der Leber histologisch erfasst sowie Sphingolipidlevel, insbesondere S1P und Ceramid in Plasma, Leber und Fettgewebe, mittels LC-MS/MS quantifiziert. Zusätzlich erfolgten Genexpressionsanalysen mittels RNA-Sequenzierung und RT-qPCR mit Schwerpunkt auf zentralen Genen des hepatischen Lipidstoffwechsels.

Die Ergebnisse zeigen, dass ein Mangel an SphK2 auf genetischer Ebene vor Symptomen schützt, die mit dem metabolischen Syndrom einhergehen. Dieser protektive Effekt zeigte sich insbesondere bei Obesitas, Fettleber sowie Glukoseintoleranz und Insulinresistenz und konnte durch pharmakologische Hemmung der SphK2 bestätigt werden. Für beide Interventionen wurden erhöhte hepatische Ceramidspiegel sowie erhöhte S1P-Plasmaspiegel nachgewiesen. In ähnlicher Weise minderte die pharmakologische Hemmung der S1P-Lyase die Gewichtszunahme, verbesserte die Glu-

cosehomöostase und senkte Leberschädigungsmarker. Analog führte diese Intervention zu erhöhten hepatischen Ceramidspiegeln sowie erhöhten S1P Plasmaspiegeln unter fettreicher Diät. Mechanistisch konnte nachgewiesen werden, dass S1P im Fettgewebe die atypische PKCζ aktiviert und über einen MAPK/HSL-vermittelten Signalweg die Lipolyse fördert. In der Leber zeigte sich ein Ceramid-abhängiger Anstieg von PKCζ, dessen genauer Mechanismus jedoch noch weiterer Klärung bedarf.

Zusammenfassend konnte gezeigt werden, dass ein gezieltes Eingreifen in den Sphingolipidmetabolismus sowohl protektiv wirkt als auch bestehende Symptome metabolischer Erkrankungen therapeutisch verbessern kann. Im Hinblick auf zukünftige Therapien könnten krankheitsassoziierte Sphingolipidprofile zur Entwicklung von Risiko Scores beitragen. Dies würde sowohl eine schnellere und präzisere Diagnose ermöglichen als auch durch gezielte pharmakologische Eingriffe neue therapeutische Optionen eröffnen.

List of Figures

List of Tables

List of Abbreviations

α-SMA	Alpha Smooth Muscle Actin
ASM	Acid Sphingomyelinase
ABC	ATP-Binding Cassette Subfamily (ABCA1, Subfamily A Member 1; ABCC1, Subfamily C Member 1)
AC	Adenylate Cyclase
ACER	Alkaline Ceramidase
ACN	Acetonitrile
ACSL	Acyl-CoA Synthetase Long-Chain Family Member
AdipoR	Adiponectin Receptor
AI	Artificial Intelligence
AOC	Area Over the Curve
ApoM	Apolipoprotein M
ASAH	Acid Ceramidase
ASM	Acid Sphingomyelin Synthase
ATGL	Adipose Triglyceride Lipase
AUC	Area Under the Curve
BAT	Brown Adipose Tissue
C1P	Ceramide-1-Phosphate
Cer	Ceramide
CerS	Ceramide Synthase
CIDE	Cell Death-Inducing DNA Fragmentation Factor-Like Effector
CVD	Cardiovascular Disease
DAG	Diacylglycerol
DAMP	Damage-Associated Molecular Pattern
db/db	Leptin Receptor-Deficient Mouse
DEGS1	Dihydroceramide Desaturase 1
DGAT	Diacylglycerol O-Acyltransferase
DIO	Diet-Induced Obesity
DNL	De Novo Lipogenesis
ERK	Extracellular Signal-Regulated Kinase
FAO	Fatty Acid Oxidation
FFA	Free Fatty Acid
GPCR	G-Protein-Coupled Receptor
HCC	Hepatocellular Carcinoma

HDAC	Histone Deacetylase
HFD	High-Fat Diet
HFHCD	High-Fat High-Cholesterol Diet
HSC	Hepatic Stellate Cell
HSL	Hormone-Sensitive Lipase
IDF	International Diabetes Federation
ipGTT	Intraperitoneal Glucose Tolerance Test
ipITT	Intraperitoneal Insulin Tolerance Test
KDSR	3-Ketodihydrosphingosine Reductase
LC-MS/MS	Liquid Chromatography Tandem Mass Spectrometry
LCFA	Long-Chain Fatty Acids
MAPK	Mitogen-Activated Protein Kinase
MASH	Metabolic Dysfunction-Associated Steatohepatitis
MASLD	Metabolic Dysfunction-Associated Steatotic Liver Disease
MCP-1	Monocyte Chemoattractant Protein-1
MetS	Metabolic Syndrome
MFSD2B	Major Facilitator Superfamily Domain–Containing Protein 2B
MGL	Monoacylglycerol Lipase
NC	Normal Chow (Diet)
NEFA	Non-Esterified Fatty Acids
NSMase	Neutral Sphingomyelinase
ob/ob	Obese Leptin-Deficient Mouse
ORMDL	Orosomucoid-Like Protein
PBS	Phosphate-Buffered Saline
PC	Phosphatidylcholine
PCA	Principal Component Analysis
PKA	Protein Kinase A
PKC	Protein Kinase C
PKCζ	Atypical Protein Kinase Zeta
PLC	Phospholipase C
PLIN	Perilipin Family (PLIN1, PLIN2)
PLP	Pyridoxal Phosphate
PMA	Phorbol 12-Myristate 13-Acetate
PNPLA2	Patatin Like Phospholipase Domain-Containing Protein 2
PP1, PP2A	Protein Phosphatases
PPARα	Peroxisome Proliferator-Activated Receptor Alpha

PPARγ	Peroxisome Proliferator-Activated Receptor Gamma
RBC	Red Blood Cell
RNA-seq	RNA Sequencing
S1P	Sphingosine-1-Phosphate
S1PR	Sphingosine-1-Phosphate Receptor
SAT	Subcutaneous Adipose Tissue
SGPL1	Sphingosine-1-Phosphate Lyase 1
SM	Sphingomyelin
SMS	Sphingomyelin Synthase
Sph	Sphingosine
SphK	Sphingosine Kinase
SPNS2	Spinster Homolog 2
SPT	Serine Palmitoyl Transferase
STZ	Streptozotocin
T1D	Type-1 Diabetes
T2D	Type-2 Diabetes
TAG	Triacylglycerol
UCP1	Uncoupling Protein 1
VAT	Visceral Adipose Tissue
VLCFA	Very-Long-Chain Fatty Acids
WAT	White Adipose Tissue (gWAT, gonadal WAT; iWAT, inguinal WAT)
WT	Wild Type

1 Introduction

1.1 Obesity, Type 2 Diabetes, and MASLD: A Metabolic Triad

1.1.1 Metabolic Syndrome

In recent years, global burden of metabolic diseases has increased. Prevalence in interrelated metabolic diseases like obesity, hyperlipidemia, metabolic-associated steatotic liver disease (MASLD), type-2 diabetes mellitus (T2D), and hypertension has risen worldwide.[1] Since 1988, when American endocrinologist Gerald Reaven first proposed his theory, it has been widely accepted that metabolic diseases share common risk factors. Reaven's "Syndrome X" included insulin resistance, glucose intolerance, hyperinsulinemia, elevated very low-density lipoprotein (VLDL) triglycerides, reduced high-density lipoprotein (HDL) cholesterol, and hypertension.[2] The understanding of the relationships between pathophysiological mechanisms and risk factors has been a major part of the research and led to the more comprehensive term, metabolic syndrome (MetS).[3]

The International Diabetes Federation (IDF), National Cholesterol Education Program Adult Treatment Panel III (NCEP-ATP III), and the World Health Organization (WHO) have each proposed a slightly different set of criteria for the diagnosis of MetS.[4-6] However, pivotal risk factors include abdominal obesity and insulin resistance. According to the IDF, central obesity, defined by waist circumference with ethnicity-specific thresholds or a body mass index (BMI) ≥30 kg/m^2, is a mandatory requirement for diagnosing MetS. Additionally, at least two or more of the following criteria must be met: dyslipidemia (triglycerides ≥150 mg/dL and/or HDL-cholesterol <40 mg/dL in men and <50 mg/dL in women) or specific treatment for these lipid abnormalities, hypertension (systolic ≥130 mmHg and/or diastolic ≥85 mmHg) or treatment of previously diagnosed hypertension, and raised fasting plasma glucose (≥100 mg/dL) or a history of T2D.[4]

Major contributors to the development of MetS include genetic and epigenetic factors as well as a sedentary lifestyle and excessive caloric intake.[7] A high-calorie diet promotes visceral adiposity, which has been identified as a key trigger for the metabolic pathways leading to MetS. This in turn results in chronic inflammation, hormonal dysregulation, and insulin resistance.[8,9] Consequently, the presence of MetS significantly increases the risk of developing T2D and cardiovascular disease (CVD).[10] Notably, MetS plays a critical role in the onset of CVDs, which are the leading cause of

death in the WHO European Region. With hypertension as the leading risk factor, CVD accounted for 2 in 5 of all death in 2019.[11]

1.1.2 Driving Forces in the Development of Obesity

Obesity is a multifactorial disease marked by the accumulation of excessive or abnormal fat, which presents significant health risks. Previously regarded as a condition predominantly affecting high-income countries, obesity prevalence is now rising across all socioeconomic backgrounds and ethnicities, prompting the WHO to classify it as a global pandemic.[12] Recent data indicate that over one billion individuals worldwide are living with obesity, rendering it one of the most pressing global health and welfare challenges.[13] The WHO classifies adults aged 18 and older with a BMI of ≥ 30 kg/m^2 are classified as obese.[12] However, this definition can lead to both, over- and underdiagnosis, as BMI does not accurately differentiate between adipose mass and muscle mass in individuals with disparate muscle development.[14] To address this issue, a commission has been established recently to review the criteria for the definition and diagnosis of clinical obesity.[15]

As obesity is a primary risk factor for MetS, it is closely associated with conditions such as T2D, hypertension, dyslipidemia, hepatic steatosis, CVD, chronic kidney disease and certain forms of cancer.[16]

The etiology of obesity is complex and multifaceted, involving a combination of biological, psychological, environmental, and social factors.[17] Despite the identification of over 100 genes implicated in weight variation and obesity development, the fundamental mechanism driving obesity is the excessive accumulation of triglycerides in adipose tissue.[18] This accumulation is hypothesized to result from dysfunctional energy homeostasis, where energy intake consistently exceeds energy expenditure.[19]

1.1.3 Excessive Adipose Lipid Build-Up Causes Systemic Insulin Resistance

Adipose tissue functions not only as an energy storage organ but also as an endocrine and immunomodulatory organ. It is capable of regulating energy homeostasis in distant organs through the release of peptide and protein hormones, collectively referred to as adipokines.[20] In the human body, two major types of adipose tissues are prominent: white adipose tissue (WAT), which is the predominant type of fat in mammals, and brown adipose tissue (BAT).[21] Anatomically, WAT is categorized into two principal

types: subcutaneous adipose tissue (SAT), located beneath the skin, and visceral adipose tissue (VAT), which envelops abdominal organs. While visceral VAT obesity is considered detrimental, due to its high metabolic activity fueling FFAs into portal circulation flowing through the liver, SAT obesity is not.[22]

In mice, representative SAT depots include paired inguinal depots (iWAT) located in the limbs, while for VAT, gonadal WAT (gWAT), which is not present in humans, is a well-studied WAT depot associated with metabolic disorders.[21] Brown adipose tissue (BAT) plays a critical role in non-shivering thermogenesis through lipid oxidation, as brown adipocytes are rich in mitochondria and express high levels of uncoupling protein 1 (UCP1), which enables uncoupling of mitochondrial respiration from ATP-production.[23] While BAT primarily functions as an energy consumption organ, WAT is known for storing excessive energy in the form of fat, which is why studies on obesity attribute a key role to WAT in the development of obesity.[24]

The major source of lipid storage in WAT is white adipocytes, which comprise a single large lipid droplet occupying most of the cell volume, whereas the nucleus and other cell organelles are found in the periphery. Adipocytes derive from mesenchymal stem cells and play a central role in the regulation of systemic energy homeostasis by storing excess fat in the form of triglycerides, which can be mobilized during periods of caloric restriction through lipolysis.[25] Prolonged periods of excess caloric intake lead to an increase in size (hypertrophy) and number (hyperplasia) of mature adipocytes as they store increasing amounts of fat.[26] While hyperplasia correlates with obesity severity, hypertrophy is more likely to have diabetogenic properties as it has been shown to be a risk factor for developing T2D.[27,28]

The development of obesity under conditions of excess lipid supply is characterized by the overexpression of triacylglycerol (TAG) biosynthetic enzymes, including glycerophosphate acyltransferase (GPAT), in adipocytes. This drives TAG synthesis and is accompanied by an enhanced ability for lipid storage.[29] However, diacylglycerol O-acyltransferase (DGAT) enzymes are of particular significance in TAG synthesis as they account for nearly all TAG synthesis in the body.[30]

Adipocytes that accumulate excess fat enlarge and ultimately become dysfunctional as they encounter hypoxia-induced metabolic stress, thereby limiting their ability to store excess fat. This is considered a critical stage in the onset of obesity, as hypertrophic adipocytes, in association with hypoxia, have been demonstrated to secrete

pro-inflammatory cytokines, including TNF-α, IL-6, and IL-11, which contribute to adipose tissue inflammation.[9] This process is accompanied by dysregulation of the secretion of adipokines, such as adiponectin and leptin. Adiponectin, a hormone with anti-inflammatory and insulin-sensitizing effects, is found to be substantially decreased in individuals affected by obesity.[31,32] Concurrently, plasma levels of the adipokine leptin, which normally plays a key role in the regulation of glucose homeostasis and food intake, increase, ultimately resulting in hyperleptinemia, which leads to leptin resistance.[33] Indeed, mice lacking leptin (ob/ob) or the leptin receptor (db/db) exhibit weight gain, impaired glucose homeostasis, hyperinsulinemia, and insulin resistance.[34] Furthermore, an increase of monocyte chemoattractant protein-1 (MCP-1) levels correlates with obese adipose tissue, which facilitates macrophage infiltration and macrophage polarization to an M1 phenotype. The release of IL-1, IL-6, and TNF-α into adipose tissue further exacerbates inflammation and has been shown to play a role in the development of insulin resistance and hepatic steatosis.[31,32] Consequently, pro-inflammatory cytokines may regulate systemic inflammation in obesity.[35]

Due to the limited capacity of adipocytes to store TAGs, dysfunctional adipocytes exhibit increased lipolysis and decreased TAG syntheses.[36] Consequently, this leads to the release of non-esterified fatty acids (NEFAs) into the bloodstream, a condition referred to as hyperlipidemia, ultimately resulting in their accumulation in tissues such as the liver, heart, skeletal muscle, and pancreas.[37] Lipids such as diacylglycerols (DAGs), sphingomyelin (SM), sphingosine (Sph), and sphingosine-1-phosphate (S1P) are also prone to accumulate in non-adipose tissues.[38,39] This lipid “spillover” to non-adipose tissues may result in lipotoxic organ damage and systemic insulin resistance, characterized by reduced insulin responsiveness.[37] This, in turn, results in impaired glucose uptake and elevated blood glucose levels. Notably, lipotoxicity, rather than obesity per se, has been demonstrated to be a crucial factor in the pathogenesis of glucose intolerance. This is supported by the observation that mice overexpressing DGAT1 in adipose tissue develop severe obesity without exhibiting peripheral insulin resistance or glucose intolerance.[40]

1.1.4 Pathogenesis of Insulin Resistance and Type-2-Diabetes

Diabetes mellitus is an escalating global health issue, with type 2 diabetes accounting for the majority of cases. Type 1 diabetes (T1D), the autoimmune form of the disease,

constitutes approximately 5–10% of cases, and T2D accounts for 90–95% of diagnoses worldwide. In 2024, around 589 million adults between the ages 20 and 79 were living with diabetes, with projections suggesting this figure could climb to 853 million by 2050, as reported by the IDF.[41]

Therefore, T2D is a prevalent metabolic disorder and one of the most frequently occurring diseases globally and is characterized by two primary features: diminished insulin secretion from pancreatic β-cells and a weakened insulin response in typically insulin-sensitive tissues, resulting in hyperglycaemia.[42]

Although overt obesity is commonly linked to insulin resistance (see Section 1.1.2), the occurrence of insulin resistance does not necessarily lead to T2D.[43] This is attributed to the compensatory capacity of β-cells during the prediabetic phase. Initially, this compensation involves an increase in beta cell volume, as observed in both obese and non-diabetic individuals, as well as in diet-induced or genetically modified rodent models.[44-47] In addition, in the prediabetic stage, β-cells may adapt by boosting insulin production and secretion, resulting in hyperinsulinemia.[48]

Nonetheless, inadequate compensation by β-cells eventually leads to diminished glucose uptake, culminating in hyperglycemia. Prolonged hyperglycemia coupled with hyperlipidemia result in beta cell toxicity and failure.[49] Beta-cell failure may lead to progressive beta cell loss, driven by multiple, not mutually exclusive mechanisms such as a reduction in beta cell mass, functional impairment, and loss of beta cell identity, all of which remain incompletely understood.[50]

Insulin resistance, β-cell loss, and impaired insulin biosynthesis or secretion ultimately lead to dysfunctional insulin action. Under normal physiological conditions, insulin, in conjunction with its complementary hormone glucagon, precisely regulates glucose homeostasis. This regulation maintains blood glucose concentrations within the range of 3.3 and 3.5 mM, thereby ensuring normal physiological functions.[51] Glucagon is secreted by alpha cells under low glucose concentrations, initiating glycogenolysis and gluconeogenesis, leading to an increase in glucose levels.[52] In the postprandial state, characterized by elevated blood glucose levels, insulin is secreted by the β-cells. Insulin promotes glucose uptake by facilitating the relocation of glucose transporter 4 (GLUT4) to the plasma membrane in muscle and adipose tissues. In the liver, insulin enhances glycogenesis and suppresses gluconeogenesis, leading to a reduction in the blood glucose levels.[53] Moreover, insulin plays a role in lipid metabolism by promoting

the uptake of free fatty acids (FFAs) from the plasma into the liver and adipose tissue, which subsequently stimulates triglyceride synthesis and lipid storage.[53]
In the context of T2D, the precise regulatory function of insulin, particularly in glucose homeostasis, is compromised. This results in persistent hyperglycemia and diminished insulin levels in the bloodstream, rendering insulin therapy essential for patients with T2D in the advanced stages of the disease. While insulin therapy becomes essential in advanced stages of T2D, early disease management often relies on lifestyle interventions and non-insulin pharmacological treatments to address the disease's multifactorial nature.[54]

1.1.5 Metabolic Dysfunction-Associated Steatotic Liver Disease

The increasing prevalence of obesity and T2D is globally accompanied by a concomitant rise in the worldwide incidence of fatty liver disease, characterized by excessive ectopic lipid accumulation in hepatic tissue, which is increasingly recognized as the hepatic manifestation of metabolic syndrome.[55,56] In 2023, a new terminology for fatty liver diseases has been adopted by multinational liver society leaders at the “European Association for the Study of the Liver” (EASL) congress where steatotic liver disease (SLD) was chosen as a general and overarching term for fatty liver diseases to encompass different causes of steatosis.[57] The disease previously known as “Nonalcoholic Fatty Liver Disease” has been renamed to “Metabolic Dysfunction-associated Steatotic Liver Disease” which excludes increased daily alcohol consumption (≥ 20/30g per week for female/male patients) and is defined as the presence of excess lipid buildup (≥5% of hepatocytes with intracellular fat accumulation) in the liver identified by imaging or biopsy in conjunction with at least one of the following cardiometabolic risk factors (CMRFs): (pre)diabetes, obesity, hypertension, high plasma triglycerides or low plasma HDL-cholesterol.[57]
The etiology of MASLD is highly heterogenous, with three main pathomechanisms that drive its progression: MASLD with a dominant hepatic genetic component; MASLD with a stronger metabolic component related to hepatic de novo lipogenesis (DNL); and MASLD with a dominant metabolic component associated with adipose tissue dysfunction.[58] Genetic predisposition, as influenced by genetic variants, primarily impacts genes that regulate lipid metabolism, such as patatin-like phospholipase domain 3 (*PNPLA3*), which hydrolyzes triglycerides from lipid droplets.[59] Genetic variants

demonstrate an increased prevalence of hepatic steatosis, fibrosis, and lobular inflammation, but not with whole-body and adipose tissue insulin resistance.[59,60] A more pronounced metabolic component associated with hepatic DNL, characterized by elevated glucose or fructose intake and diabetes-associated hyperinsulinemia and hyperglycemia, is accompanied by hepatic and whole-body insulin resistance.[61] Furthermore, patients diagnosed with MASLD exhibiting a dominant metabolic component related to adipose tissue dysfunction experience an increased delivery of fatty acids to the liver due to dysregulated adipocyte lipolysis resulting from adipose tissue insulin resistance.[62] Notably, both metabolic pathomechanisms demonstrate an elevated risk of CVD, which is attributed to higher cause-specific mortality in individuals with MASLD.[63] Given that the etiological factors of MASLD are interconnected and may manifest concurrently, they encompass diverse mechanisms that collectively contribute to disease progression and clinical significance.

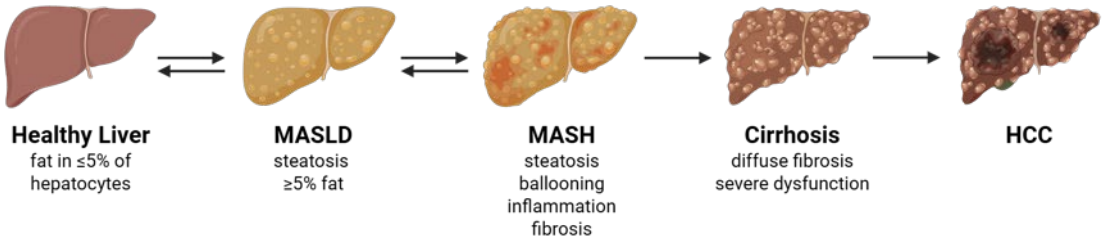

Figure 1. Schematic representation of liver disease progression from healthy tissue to hepatocellular carcinoma. Healthy liver tissue may develop metabolic-associated steatotic liver disease (MASLD) in the presence of excessive lipid accumulation. This can progress to metabolic-associated steatohepatitis (MASH), characterized by steatosis, ballooning, inflammation, and fibrosis. In advanced stages, irreversible cirrhosis and ultimately hepatocellular carcinoma (HCC) may develop. The illustration is based on and adapted from multiple published sources (see main text). Created with BioRender.com. Published under BioRender Publication License.

Individuals with MASLD exhibit simple steatosis, which is characterized by an abnormal lipid accumulation in ≥ 5% of hepatocytes. Early MASLD is usually asymptomatic and results from disturbances in hepatic fatty acid metabolism, which regulates the fatty acid uptake and transport, DNL, fatty acid oxidation (FAO), and lipoprotein secretion.[64] As hepatocytes are exposed to prolonged elevations of intracellular lipids, they experience mitochondrial dysfunction and oxidative stress, increasing the susceptibility for lipid peroxidation, which leads to plasma membrane damage.[65] This, in turn, triggers the activation of Kupffer cells that release pro-inflammatory cytokines such as TNF-α, IL-1β and IL-6, which then attract immune cells, exacerbating the inflammatory response further causing damage to the hepatocytes.[66] In response to this chronic

injury, hepatic stellate cells (HSC) are activated and undergo transdifferentiation from their quiescent state to a myofibroblast-like phenotype, which enables the production of extracellular matrix (ECM) proteins such as collagen thereby promoting the development of fibrosis and ultimately driving the progression to metabolic-associated steatohepatitis (MASH).[67] Histologically, MASH can be distinguished from MASLD in H&E-stained liver sections by the presence of hepatocyte ballooning, which refers to cytoplasmic swelling and loss of normal cell shape caused by hepatocyte injury.[68] It is estimated that within 8-13 years, 12-40% of MASLD cases will progress to the potentially reversible condition MASH, with a further 12-15% of these cases, if left untreated, advancing to cirrhosis, which is characterized by irreversibility.[69] Figure 1 (page 7) depicts the progressive stages from steatosis to advanced liver disease.

Liver cirrhosis can be classified as compensated or decompensated. In the compensated cirrhosis stage, the liver maintains its normal functions. However, individuals with decompensated liver cirrhosis experience severe symptoms due to the liver's inability to perform its vital functions.[70] Persistent fibrosis ultimately increases the risk of developing hepatocellular carcinoma (HCC), with up to 7% of patients with compensated cirrhosis progressing to HCC.[69,71] Accordingly, understanding the mechanisms that drive the transition from a healthy liver to MASLD and eventually to HCC is crucial for developing targeted therapies that prevent disease progression.

In this context, growing efforts focus on programmed cell death pathways to elucidate the mechanisms underlying stage transitions. Beyond apoptosis, regulated and immunogenic forms of cell death, such as pyroptosis, ferroptosis, and necroptosis are examined as contributors to liver disease progression.[72-74] Necroptosis, mediated by RIPK3 and MLKL, has been implicated in MASLD, as its lytic nature promotes inflammation and the release of damage-associated molecular patterns (DAMPs), thereby contributing to the inflammatory characteristic of MASH.[75] In this regard, sublethal necroptosis in hepatocytes can induce DAMP release, subsequently promoting fibrosis and hepatocarcinogenesis.[76] Accordingly, DAMPs are understood to actively contribute to hepatic inflammation and disease progression.[77]

1.2 Dysregulated Lipolysis in Metabolic Disease

Lipolysis plays a pivotal role in metabolic diseases, as its dysregulation may contribute to their onset and progression. In healthy individuals, adipose tissue lipolysis facilitates energy mobilization by breaking down TAGs into FFAs and glycerol, thereby contributing to the systemic energy supply. Additionally, in BAT, lipolytic products such as FFAs fuel thermogenesis, which occurs in mitochondria rich in UCP1.[23]

During periods of energy deprivation or cold exposure, lipolysis is activated through the release of catecholamines, such as norepinephrine and epinephrine, which stimulate β-adrenergic receptors.[78] Synthetic β-adrenergic agonists like isoprenaline (isoproterenol) may also stimulate lipolysis.[79] Upon activation of G protein-coupled β-adrenoreceptors (GPCRs), the $G\alpha_s$ subunit of the associated G_s protein becomes activated, ultimately leading to the stimulation of adenylyl cyclase (AC). This in turn, increases intracellular cAMP levels, leading to cAMP-dependent activation of protein kinase A (PKA).[80] PKA then phosphorylates target proteins such as hormone-sensitive lipase (HSL) and perilipin 1 (Plin1). While HSL-phosphorylation triggers its translocation to the surface of lipid droplets, Plin1, a lipid droplet coating protein, stabilizes lipid droplets by protecting them from lipases.[81] Its phosphorylation induces a conformational change that renders the lipid droplets more accessible to lipases, ultimately leading to the sequential hydrolysis of TAG to DAG, catalyzed by the rate-limiting step of the hydrolysis from TAGs.[82] This process is initiated and catalyzed by adipose triglyceride lipase (ATGL), which is encoded by the gene known as patatin-like phospholipase domain-containing protein 2 (PNPLA2) gene. Subsequent degradation by HSL and monoacylglycerol lipase (MGL) ultimately yields glycerol and FFAs, which are released into the bloodstream.[79] While FFAs may be either re-esterified to TAGs or serve as substrate for energy production in heart, muscle, and liver, glycerol is eventually taken up by the liver, where it feeds gluconeogenesis by conversion to dihydroxyacetone phosphate.[83]

During periods of caloric excess, insulin exerts negative regulatory effects on lipolysis through the PI3K/Akt-mediated activation of phosphodiesterase 3B (PDE3B), which subsequently degrades cAMP, a second-messenger essential for PKA activation.[84] In the context of T2D, this critical regulatory function of insulin is compromised due to the development of insulin resistance in peripheral tissues, often resulting from lipotoxic damage. Notably, mice deficient in MGL demonstrated improved glucose tolerance and

insulin sensitivity despite a weight gain comparable to controls.[85] Furthermore, mice with an adipocyte-specific knockout of ATGL exhibited reduced adipocyte lipolysis, which was associated with enhanced systemic glucose and insulin tolerance, as well as a significant reduction in diet-induced steatosis.[86]

Additionally, lipid droplet-associated proteins, such as perilipins and cell death-inducing DNA fragmentation factor-like effectors (CIDE), including CIDEA in brown adipose tissue and the liver, CIDEB in the liver, and CIDEC/FSP27 predominantly in white adipose tissues, may function as negative regulators of lipolysis. This is achieved by promoting the fusion of lipid droplets, thereby altering the surface-to-volume ratio and ultimately limiting lipase accessibility, leading to cellular lipid accumulation.[87] Interestingly, expression of both Cidea and Cidec is upregulated under conditions of obesity or high-fat diets. Supporting this, overexpressing Cidea in mouse liver resulted in hepatic lipid accumulation due to the formation of large lipid droplets.[88] Moreover, knockout mice for both Cidea and Cidec exhibited decreased hepatic lipid accumulation and increased insulin sensitivity when subjected to dietary challenges or a genetically obese background.[88,89]

In the context of metabolic diseases, dysregulated lipolysis leads to an increase in circulating FFAs, which in turn promotes ectopic fat deposition and hepatic steatosis. These events contribute to insulin resistance, thereby playing a role in the pathogenesis of T2D.

1.3 Sphingolipid Metabolism

Metabolic syndrome is characterized by disruptions in lipid and glucose metabolism. Beyond classical regulators, sphingolipids have emerged as bioactive lipids that not only fulfill structural functions but also actively modulate signaling pathways in liver and adipose tissue, emphasizing their functional relevance in this study.

Sphingolipids represent a significant class of eukaryotic lipids and were first described by J. L. W. Thudichum in 1884 in his “Treatise on the chemical constitution of the brain”.[90] Therein, he reported his identification of sphingosine in brain extracts and named it after the Greek mythological creature Sphinx, due to the many enigmas it posed until its discovery.[90] Sphingolipids are amphipathic molecules that, serve as structural components of the plasma membrane of eukaryotic cells, thereby influencing a plethora of cellular processes.[91] All sphingolipids consist of a sphingoid backbone

arising from the condensation of a fatty acyl-CoA and an amino acid. The most abundant long chain sphingoid base in mammalian cells, sphingosine, is composed of 18 carbon atoms. It serves as a backbone for the synthesis of complex sphingolipids, including ceramide (Cer), where it is amide-linked to fatty acyl chains of varying length and degree of saturation and may undergo further modification via an O-linkage to different polar head groups.[92] Due to their structural diversity, sphingolipids are the most structurally diverse lipid class. They are ubiquitously distributed throughout the body, with distinct tissue-specific sphingolipid profiles resulting from different head groups as well as variations in fatty acyl chain length and saturation. These structural variations contribute to the unique functional roles of sphingolipids in different tissues.[93] Research focusing on sphingolipids has revealed their involvement in numerous processes related to proliferation, differentiation, migration, and apoptosis.[94] Thus, the multifunctional nature of sphingolipids in mammalian cells has led to the discovery that alterations in their profiles can result in the development of various diseases.

1.3.1 *De Novo* Synthesis and Recycling Pathway of Sphingolipids

As key players in lipid metabolism, sphingolipids originate from *de novo* synthesis pathways that incorporate palmitate, thereby directly linking sphingolipid metabolism to overall lipid homeostasis. The pathway is initiated in the endoplasmic reticulum (ER), where serine palmitoyltransferase (SPT), a (PLP)-dependent membrane-bound heterodimer, catalyzes the first and rate-limiting step by condensing serine with fatty acyl-CoA to form 3-keto-dihydrosphingosine (Figure 2a, page 12).[95,96] Substrates for SPT are L-serine and palmitoyl-CoA (16:0), one of the most abundant acyl-CoA species in mammalian cells.[97] The carbonyl group of 3-ketodihydrosphingosine undergoes a rapid reduction to dihydrosphingosine (sphinganine) by NADPH-dependent enzyme 3-ketodihydrosphingosine reductase (KDSR), which is subsequently N-acylated to produce dihydroceramide.[98] The acylation of the amino group of sphinganine is mediated by (dihydro)ceramide synthase and occurs via the addition of acyl-CoA esters derived from unsaturated or saturated fatty acids. Six ceramide synthases (CerS1-6), each with distinct acyl-CoA preferences, generate dihydroceramides of varying chain lengths (C14 to C26) with specific subcellular localizations and tissue distributions.[99,100] Finally, dihydroceramide is converted to ceramide by dihydroceramide desaturase 1 (DEGS1) which introduces a 4-5 trans double bond into the sphingoid backbone.[101]

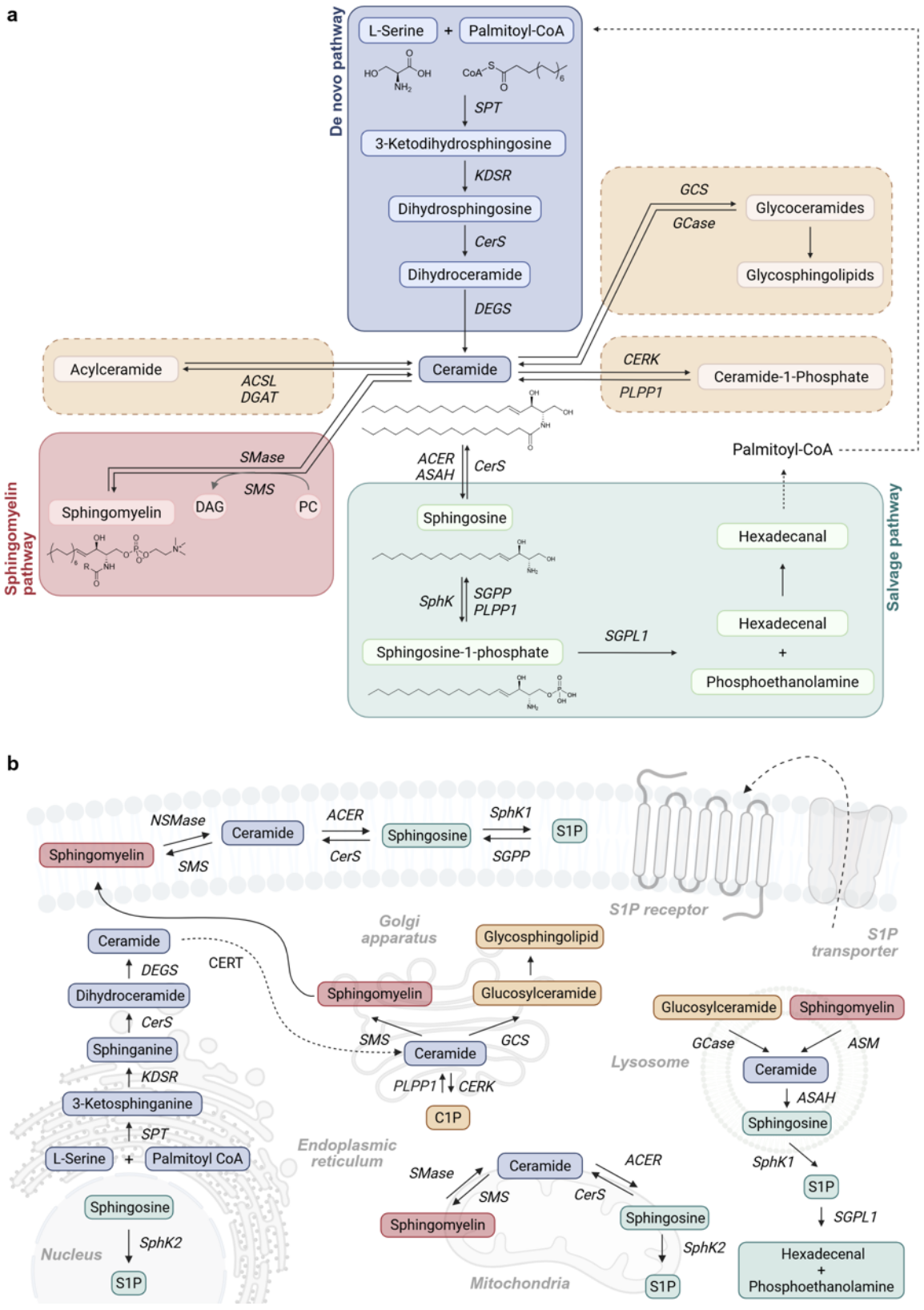

Figure 2. Sphingolipid metabolic pathway. Schematic overview of the a) sphingolipid pathway and b) the subcellular localization of the involved enzymes and intermediates. *De novo* sphingolipid synthesis initiates with the condensation of L-serine and palmitoyl-CoA, a reaction catalyzed by serine palmitoyl transferase at the endoplasmic reticulum. Subsequent reactions result in the formation of ceramide. Within the Golgi apparatus, ceramides may be incorporated into various complex sphingolipids or converted to sphingomyelin. Ultimately, in the salvage

pathway, ceramide is transformed into S1P, which is irreversibly degraded by S1P lyase. ACER, alkaline ceramidase; ACSL, acyl-CoA synthetase long chain; ASAH; acid ceramidase; ASM, acid sphingomyelinase; CERK, ceramide kinase; CerS, ceramide synthase; CERT, ceramide transfer protein; DAG, diacylglycerol; DEGS1, dihydroceramide desaturase 1; DGAT, Diacylglycerol O-Acyltransferase; GCase, glucosyl ceramidase; GCS, glucosylceramide synthase; KDSR, 3-ketodihydrosphingosine reductase; NSMase, neutral sphingomyelinase; PC, phosphatidylcholine; PLPP1, phospholipid phosphatase 1; S1P; sphingosine-1-phosphate; SGPL1, S1P lyase; SGPP, sphingosine-1-phosphate phosphatase; SMS, sphingomyelin synthase; SphK, sphingosine kinase; SPT, serine palmitoyl transferase. Adapted from published work by Kuo and Hla (2024), Hannun and Obeid (2018), and Lee et al. (2023).[94,102,103] Created with BioRender.com. Published under BioRender Publication License.

Ceramide is then transported to the Golgi, where it can translocate between the membrane leaflets.[104] From there, it reaches the *cis*-Golgi either via vesicular transport or by non-vesicular trafficking mediated by ceramide transfer protein (CERT), delivering ceramides to *trans*-Golgi contact sites (Figure 2b, page 12).[105]

As the fundamental precursor of all complex sphingolipids, ceramide undergoes modifications at the 1-hydroxyl position, thus making it a key component in sphingolipid metabolism. For instance, the direct phosphorylation of ceramide by ceramide kinase converts ceramide to ceramide-1-phosphate (C1P), a reaction that can be reversed by ceramide-1-phosphate phosphatase.[106] Additionally, ceramide can be N-acetylated to form 1-*O*-acylceramides, which are incorporated and stored within lipid droplets. This process primarily takes places in the liver and is catalyzed by the triacylglycerol-forming enzyme DGAT2 and involves the formation of a multienzyme complex consisting of DGAT2, CerS, and long-chain fatty acid CoA-ligase 5 (ACSL5).[107]

Acylceramides, in turn, can be hydrolyzed back into ceramide through cleavage of their ester bonds.[107] Alternatively, ceramide can be converted into glucosylceramide at the cytosolic side of the Golgi by the sequential addition of sugar groups, catalyzed by UDP-glucose ceramide glycosyltransferase (UGCG).[108,109] This provides the core structure for more complex glycosphingolipids. In the lysosome, various glycosidases typically cleave the sugar moieties from glycosphingolipids, thereby releasing ceramide (Figure 2a+b, page 12).[110]

Furthermore, within the Golgi lumen, sphingomyelin synthases (SMSs) transfer the phosphocholine group of phosphatidylcholines (PC) to ceramide, thereby generating SM and DAG.[111,112] SM is then transported to the outer leaflet of the plasma membrane or the lysosome via vesicular transport.[113] Both neutral- and acid sphingomyelinase (NSMase and ASM) catalyze the release of ceramide. ASM is located in the lysosomal membrane, where it degrades SM from endocytosed membranes, while NSMase is mainly found in the plasma membrane of neural tissues.[114] The regenerated ceramide

can subsequently be further catabolized by ceramidases, which deacetylate ceramide to produce Sph.[115] Acid ceramidase 1 (ASAH1) is predominantly localized within lysosomes, operating under acidic conditions, while neutral ceramidase (ACER2) is mainly present in mitochondria and plasma membranes.[116] Alkaline ceramidases 1-3 (ACER1-3), which function in high pH environments, are distributed across different subcellular locations: ACER1 in the ER, ACER2 in the Golgi complex, and ACER3 in both the ER and Golgi.[116] Consequently, two isoenzymes, known as sphingosine kinase 1 (SphK1) and sphingosine kinase 2 (SphK2), catalyze the phosphorylation of sphingosine to produce sphingosine-1-phosphate (S1P).[117,118]

From this point onwards, S1P can follow one of two distinct routes: it may either be dephosphorylated and recycled via the salvage pathway, which begins with the dephosphorylation of S1P or undergo irreversible degradation. In the salvage pathway, S1P is first dephosphorylated back to Sph, which can then be re-acetylated by CerSs to regenerate ceramide (Figure 2a, page 12).[119] This reaction is catalyzed by two S1P phosphohydrolases, SGPP1 and SGPP2, which share similar localization but differ in expression, both exhibiting high levels in placenta and kidney.[120,121] Furthermore, three lipid phosphate phosphohydrolases (LPP1-3) can also dephosphorylate S1P. These enzymes hydrolyze various phospholipids, including phosphatidic acid (PA), lysophosphatidic acid (LPA), C1P and diacylglycerol pyrophosphate.[122]

The terminal cleavage of S1P is catalyzed by sphingosine-1-phosphate lyase (SGPL1), which cleaves the bond between C2 and C3, producing ethanolamine phosphate and 2-*trans*-hexadecenal (Figure 2, page 12).[123] While ethanolamine phosphate can be utilized to form phospholipids, 2-*trans*-hexadecenal is converted to hexadecenoic acid by fatty aldehyde dehydrogenase (FALDH) and subsequently activated by long-chain ACSL to hexadecenoyl-CoA. This intermediate can then be further metabolized to palmitoyl-CoA, which can re-enter the *de novo* sphingolipid biosynthesis.[124]

1.3.2 Ceramide as a Central Hub in Sphingolipid Metabolism

The dynamic equilibrium between intracellular concentrations of the bioactive sphingolipids S1P, ceramide, and Sph, collectively referred to as the sphingolipid rheostat, is a critical determinant of cellular fate.[125,126] While S1P is known to exert pro-survival and pro-proliferative effects by promoting cell growth, migration, angiogenesis, and survival, ceramide and Sph tend to have more pro-apoptotic and anti-proliferative functions, including cell cycle arrest, apoptosis and other stress-related responses.[126,127]

The tight regulation of the canonical *de novo* synthesis of sphingolipids, the sphingomyelin hydrolysis pathway, and the salvage pathway ensures the homeostasis of sphingolipids, with ceramide serving as a central metabolic hub. It is noteworthy that the enzymes that facilitate the interconversion of ceramides play a pivotal role in determining the amount of ceramide, while also indirectly influencing the concentrations of complex sphingolipids.[128] Furthermore, ceramide itself functions as a key regulator of the *de novo* synthesis of sphingolipids mediated by three orosomucoid-like (ORMDL) proteins. By sensing ceramide pools in the ER membrane, they inhibit the *de novo* sphingolipid synthesis through interaction and modulation of the rate-limiting enzyme SPT.[129-131] Interestingly, cytosolic S1P, synthetized by SphK1, has been demonstrated to inhibit CerS2, thus representing an additional feedback inhibition loop.[132]

In ceramide catabolic pathways, the SMS enzyme is hypothesized to play a central role in maintaining sphingolipids and cellular homeostasis, as DAG, an important intermediate in lipid metabolism, is formed as a byproduct of this reaction[112]. In contrast to the pro-apoptotic effects of ceramide, DAGs exert mitogenic effects by activating various isoforms of protein kinase C (PKC).[133] Alternatively, ceramide undergoes catabolic breakdown to form Sph, S1P or other derivatives, which may either be resynthesized into ceramide or result in terminal cleavage by S1P lyase to generate hexadecenal and ethanolamine (Figure 2, page 12). The latter serves as a precursor in phospholipid metabolism, thereby occupying a crucial position at the intersection of these pathways and representing another critical regulatory node in sphingolipid metabolism.[134]

As previously stated, enzymes involved in ceramide/sphingolipid turnover exhibit distinct subcellular localizations, which result in corresponding local differences in sphingolipid concentrations. This enables second messenger actions on a multitude of cellular compartments.[135]

Ceramides have been shown to target serine/threonine protein phosphatases, including protein phosphatase 1 (PP1) and protein phosphatase 2A (PP2A), both of which are crucial regulators of apoptosis.[136,137] Mechanistically, PP2A promotes apoptosis by dephosphorylating and inactivating the pro-survival protein B-cell lymphoma-2 (BCL-2).[138] Ceramide-induced apoptosis can also occur through the formation of ceramide channels, the membrane permeability of which enables the release of proapoptotic cytochrome c and other intermembrane proteins into the cytosol.[139] Further, ceramide

has been shown to colocalize with voltage-dependent anion channel 2 in the mitochondrial membrane, leading to recruitment of Bcl-2-associated X protein (Bax) and Bcl-2 homologous antagonist/killer proteins (Bak) into the mitochondria. This enhances the permeability of the outer mitochondrial membrane and facilitates the release of cytochrome c.[140] Additionally, ceramide has been found to activate protein kinase C zeta (PKCζ), which, like PP2A, deactivates the pro-survival protein AKT through dephosphorylation.[141]

1.3.3 Sphingosine Kinases

Ceramide-derived sphingosine serves as the exclusive substrate for sphingosine kinases, the sole enzymes catalyzing its phosphorylation to sphingosine-1-phosphate (S1P), a crucial regulatory step in sphingolipid metabolism. Both kinases are encoded by distinct genes, each of which contains five conserved domains. The C4 domain of both enzymes is unique for SphKs, while the C1-C3 domains exhibit substantial homology with protein kinases and the C5 not only is conserved in SphKs but also in enzymes such as ceramide kinases and diacylglycerol kinases.[142]

Sphingosine kinases are activated through phosphorylation in response to extracellular signals, including growth factors (VEGF, EGF, and PGDF), which signal via receptor tyrosine kinases that activate downstream kinases, such as ERK1/2.[143,144] Inflammatory stimuli, such as TNF-α, also contribute to SphK activation.[145] SphK1 is commonly activated by protein kinase C (PKC) and triggered by phorbol esters such as phorbol 12-myristate 13-acetate (PMA).[146] G-protein-coupled receptors also contribute to SphK activation via second messengers (see Section 1.3.4).

This phosphorylation enhances the enzymatic activity of SphKs and can influence their subcellular localization, thereby regulating S1P production and its involvement in numerous cellular processes. SphK1 primarily resides in the cytosol but can translocate to the plasma membrane upon phosphorylation at Ser225 by PKC in response to stimuli such as PMA.[146] In contrast, SphK2 is localized within the nucleus and is also found in other organelles, including the ER and mitochondria.[147,148] In addition, SphK2 activity has been associated with the incorporation of palmitate into ceramide, suggesting isoenzyme-specific functions in sphingolipid metabolism.[148]

Although ubiquitously present, SphKs display distinct expression profiles across tissues. In murine tissues, SphK1 expression was found to be the highest in the lung and spleen, whereas SphK2 expression was highest in the liver and heart.[117,118] However,

total sphingosine kinase activity was found in all tissues, with SphK1 accounting for the largest proportion in most tissues, especially the brain, heart and colon.[149] Both sphingosine kinases have been demonstrated to exhibit redundant functions, with the deletion of a single kinase failing to result in a significant reduction in S1P levels or apparent phenotype in various mouse models. Notably, the concurrent deletion of both kinases has been shown to cause a deficiency of S1P, leading to severe developmental hemorrhaging and high lethality.[150] This finding indicates that total SphK activity and SphK-generated S1P are essential for viability.

Furthermore, SphKs have been implicated in several pathological conditions, particularly in cancer formation. Elevated SphK1 expression in various tumor types promotes cancer cell proliferation and migration.[151] This correlates with a higher severity, poor prognosis and chemotherapy resistance.[152-154] SphK2 serves as a prognostic biomarker of non-small cell lung cancer (NSCLC), where its overexpression is linked to disease progression.[155] In colorectal cancer, high SphK2 expression levels are also correlated with cell proliferation and migration.[156]

Given the critical roles of SphKs and S1P, the SphK/S1P pathway has emerged as a promising and innovative therapeutic target for various diseases. Over the past decade, there has been notable interest in developing novel SphK inhibitors, with a focus on their potential clinical applications. SphK inhibitors typically target either the sphingosine-binding pocket in the C4 region or ATP-binding site in the C2 region of the enzyme.[142] Common inhibitors, such as DMS or SKI-II, block both SphK1 and SphK2, although they also affect off-targets such as PKC and Degs1.[157,158] For 5c, a selective inhibitor of SphK1, anti-sickling properties have been demonstrated.[159] PF-543, which is also an SphK1 inhibitor, is 100-fold more selective for SphK1 than for SphK2 and exhibits anti-fibrotic, anti-inflammatory, and anti-cancer effects.[160,161] K145, selective for SphK2, shows anti-tumor properties *in vivo* and *in vitro*, whereas ABC294640, another potent SphK2 inhibitor, promotes tumor cell autophagy.[162,163] Despite receiving FDA orphan drug designation as opaganib for neuroblastoma treatment, ABC294640's inhibition of DEGS1 limits its suitability as a specific SphK2 inhibitor.[164] In response to the non-specific inhibition observed with ABC294640, researchers like Webster Santos and colleagues are focusing on the design and synthesis of novel SphK2 inhibitors to enhance specificity and therapeutic efficacy.[165]

1.3.4 The Intricate Dynamics of S1P Homeostasis and Signaling

Maintaining the Crucial Balance of S1P

The SphKs described above are the exclusive source of S1P, whose levels are tightly controlled by synthesis, degradation, and transport. This balance sustains the sphingolipid rheostat and supports several essential physiological processes. The presence of high S1P levels in plasma and lymph, reaching micromolar concentrations, contrasts sharply with nanomolar S1P levels in tissue interstitial fluids, creating a crucial S1P gradient.[166] This gradient is vital for the egress of hematopoietic and progenitor cells from extramedullary hematopoietic tissues to the lymph, as well as for lymphocyte migration from lymphoid organs to the bloodstream.[167,168] The establishment and maintenance of this gradient depend on S1P biosynthesis, storage, and release by three major cell types: erythrocytes, which lack S1P-degrading enzymes;[169,170] platelets, which release S1P upon activation;[171] and endothelial cells.[172] Erythrocytes play a key role in regulating plasma S1P levels. Blocking S1P export from erythrocytes can reduce plasma S1P levels by up to 50%.[173] Interestingly, vascular endothelial cells, but not hepatocytes, have been shown to secrete S1P *in vitro*, thereby directly contributing to the plasma S1P pool.[172] Once in the bloodstream, S1P has two major fates, as it undergoes rapid turnover in the plasma with a half-life of approximately 15 minutes.[172] Extracellular S1P can be reabsorbed by cells, where it is initially dephosphorylated by nonspecific plasma membrane phosphatases, facilitating its uptake as sphingosine, which is then converted back to S1P.[174,175] While cellular S1P reuptake typically reduces circulating S1P, loss of SphK2 impairs the uptake of S1P from the bloodstream into lymphoid tissues, resulting in paradoxically elevated plasma S1P levels.[176] Additionally, in a carrier-mediated route, S1P binds to and is transported by lipoproteins, which act as acceptors and chaperones for other lipids, including cholesterol and triglycerides. Notably, more than 60% of circulating S1P is bound to HDL and, to a lesser extent, low-density lipoproteins (LDL), while approximately 30% is associated with albumin.[177] Apolipoprotein M (ApoM), expressed in liver hepatocytes and tubular epithelial cells of the kidney bound to HDL, is essential for facilitating S1P binding to HDL, as evidenced by the absence of S1P in the HDL fraction of ApoM-deficient mice, a finding that may be reversed by ApoM overexpression.[178,179]

Specialized S1P export proteins are crucial for maintaining the S1P gradient and supporting extracellular signaling functions.

The major facilitator superfamily transporter 2b (MFSD2B) enables S1P efflux from erythrocytes and platelets in a proton gradient-dependent manner.[173,180] This dependency is evidenced by high S1P concentrations in erythrocytes and a marked decrease in plasma S1P levels in MFSD2B knockout mice.[173] The transporter spinster homolog 2 (SPNS2), initially identified in zebrafish, also functions as an S1P transporter. It is expressed in vascular endothelial cells with SPNS2 knockout studies revealing a significant reduction in plasma S1P levels.[181,182]

ATP-binding cassette (ABC) transporters also play a key role in facilitating S1P efflux in specific cell types. For instance, ABCC1 mediates S1P release in mast cells,[183] Langerhans cells,[184] brain and spinal cord endothelial cells,[185] and fibroblasts.[186] Conversely, ABCA1 has been shown to facilitate S1P efflux from erythrocytes and astrocytes. These findings were validated in a rat model using the ABCA1 inhibitor glyburide.[187,188]

In summary, S1P pools and gradients are essential not only for cellular homeostasis and various physiological processes but also for maintaining the balance of sphingolipid metabolism.

G Protein-Coupled S1P Receptor Signaling

S1P can act as an intracellular second messenger or, once exported to the extracellular space, exert pleiotropic autocrine and paracrine effects through binding to its five specific G protein-coupled receptors (S1PR1–5), thereby initiating diverse downstream signaling pathways. This “inside-out” signaling is mediated by five specific S1P receptors (S1PR1-5).[189] S1PRs, which belong to the GPCR family, were first identified and characterized by Lee and colleagues in 1998 and are differentially expressed across various tissues.[190] The receptors are ubiquitously expressed and, upon binding to S1P, couple to heterotrimeric G-protein complexes composed of three distinct G_{α} subunits: $G_{\alpha i}$, $G_{\alpha 12/13}$ and $G_{\alpha q}$ (Figure 3).[191] S1PR1 exclusively couples to $G_{\alpha i}$, while S1PR2 and S1PR3 can interact with all three G_{α} subunits.[192,193] S1PR4 and S1PR5 primarily signal through $G_{\alpha i}$ and $G_{\alpha 12/13}$.[194,195] Each G_{α} subunit then undergoes conformational change and propagates the ligand-binding signal by activating several classical downstream signaling pathways:

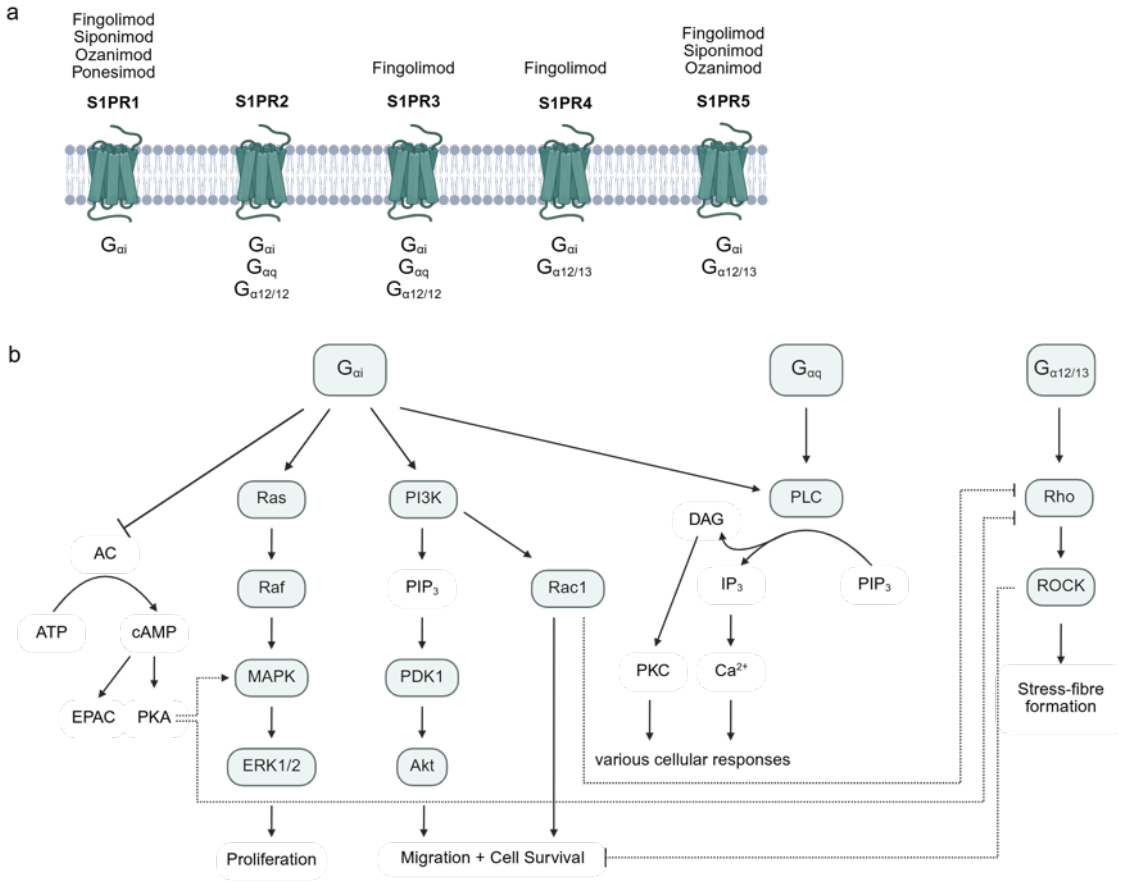

Figure 3. S1P signaling through five specific G-protein coupled receptors. G-protein coupled S1P receptors (S1PR) are activated upon the binding of S1P, initiating downstream signaling cascades through Gα subunits. a) Interaction of S1P receptor subtypes with S1PR modulators and their respective downstream cellular Gα subunit targets. b) Downstream signaling pathways of $G_{\alpha i}$, $G_{\alpha q}$, and $G_{\alpha 12/13}$ subunits. Signaling through $G_{\alpha i}$ promotes proliferation through activation of small GTPase Ras and ERK. Activated $G_{\alpha i}$ inhibits adenylyl cyclase (AC), thereby reducing cAMP levels. Additionally, the activation of PI3K, which subsequently activates Akt and the small GTPase Rac. promotes migration and cell survival. Both $G_{\alpha i}$ and $G_{\alpha q}$ activate PLC, which in turn leads to the activation of PKC and the release of intracellular free Ca^{2+}, ultimately triggering various cellular responses. $G_{\alpha 12/13}$ signaling activates the small GTPase Rho and ROCK, leading to stress-fiber formation and thus inhibiting migration. Adapted from published work by Chun et al. (2021).[196] Created with BioRender.com. Published under BioRender Publication License.

$G_{\alpha i}$ triggers the activation of small GTPase Ras and PI3K, which subsequently induces the MAPK signaling pathway as well as PKB/Akt and the small GTPase Rac, promoting cellular processes like proliferation, migration, and cell survival.[192,197] It also activates phospholipase C (PLC), leading to elevated intracellular calcium (Ca^{2+}) levels and activation of PKC, essential for various cellular responses.[198] Additionally, $G_{\alpha i}$ signaling inhibits AC, thereby reducing cAMP levels.[199] $G_{\alpha q}$ primarily activates PLC pathways and $G_{\alpha 12/13}$ signaling activates the small GTPase Rho and ROCK, which inhibits cellular migration, reduces endothelial barrier function and to induce vasoconstriction (Figure 3).[200-202]

Thus, S1PRs enable the heterogeneous regulation of various physiological processes, including the above-mentioned, contingent upon the distinct distribution and relative expression patterns of both S1PRs and G_α proteins.

Intracellular S1P Signaling

Beyond its well-established receptor-mediated functions, compartmentalized intracellular pools of S1P act as second messengers that directly engage distinct molecular targets, thereby regulating diverse signaling pathways independently of S1PR activation.

S1P, generated by SphK1, participates in TNFα-induced NF-κB activation, where it serves as a cofactor for the E3 ubiquitin ligase TRAF2. TRAF2 mediates lysine-63-linked polyubiquitination of receptor-interacting protein 1 (RIP1), leading to the activation of nuclear factor kappa-light-chain-enhancer of activated β-cells (NF-κB). This highlights S1P's role in inflammatory, antiapoptotic and immune processes.[203] Another cytoplasmic target of S1P is atypical protein kinase C (aPKC), which S1P directly binds at its kinase domain, thereby protecting cells from apoptosis, as demonstrated in HeLa cells.[204] Additionally, S1P interacts with peroxisome proliferator-activated receptor gamma (PPARγ), where its phosphate head group binds to His322 within the PPARγ ligand-binding pocket. This binding induces PPARγ expression and complex formation with peroxisome proliferator-activated receptor-γ coactivator 1 (PGC1β). *In vitro* studies have shown that the PPARγ:PGC1β complex translocates to the nucleus in endothelial cells, contributing to angiogenesis and vascular development.[205] Moreover, intercellular S1P triggers calcium mobilization from thapsigargin-sensitive stores in an S1PR-independent manner, demonstrated through photolysis of caged-S1P in HEK-293, SKNMC and HepG2 cells.[206]

Within the nucleus, SphK2-derived S1P directly targets and inhibits histone deacetylases (HDACs), specifically HDAC1 and HDAC2, leading to enhanced histone acetylation and consequent epigenetic regulation of gene expression.[207] Additionally, S1P interacts with human telomerase reverse transcriptase (hTERT), mimicking hTERT phosphorylation at Ser921. This interaction prevents ubiquitination, of hTERT ultimately promoting cell proliferation and preventing senescence.[208]

In mitochondria, SphK2/S1P colocalizes with prohibitin 2 (PHB2) at the inner mitochondrial membrane, where it facilitates complex IV assembly, thus modulating mitochondrial respiration.[209] This mechanism has shown cardioprotective effects in ischemic preconditioning models in SphK2-deficient and control mice.[210]

1.3.5 Therapeutic Implications in Sphingolipid-Related Pathologies

Dysregulation of sphingolipid metabolism is known to correlate with the development of a range of diseases, which has led to the implementation of several therapeutic approaches.

Sphingolipidoses are a prevalent group of lipid storage disorders characterized by deficiencies in enzymes essential for sphingolipid catabolism, leading to the pathological accumulation of these lipids.[211] An example is Niemann-Pick disease, an autosomal recessive disorder marked by sphingomyelinase-deficiency.[212] Sphingolipidoses generally affect the immune and nervous systems, and current treatment options are limited. Available therapies include enzyme replacement therapy, enzyme enhancement/chaperone therapy, and bone marrow or stem cell transplantation.[211]

Multiple sclerosis (MS), a neurodegenerative disorder driven by lymphocyte infiltration of the central nervous system, has also been associated with S1P. Fingolimod (FTY720; Gilenya®), an antagonist of S1PR1, S1PR3, S1PR4, and S1PR5, is a prodrug that requires phosphorylation *in situ* and is an in-class orally active drug approved for relapsing-remitting MS.[213] It acts by preventing lymphocyte egress from lymph nodes, thereby reducing the formation of focal lesions.[214] Additional S1PR modulators, including Siponimod (Mayzent®), Ozanimod (Zeposia®) and Ponesimod (Ponvory®), have been developed and approved for specific forms of MS.[215-217]

Furthermore, already approved drugs are increasingly being investigated for potential additional therapeutic indications. For instance, Ozanimod is being assessed as a potential treatment for inflammatory bowel conditions like Crohn's disease and ulcerative colitis.[218] Due to its immunomodulatory properties, Ponesimod is being tested for treatment of psoriasis.[219] Similarly, ABC294640, an orally available and the first in-class SphK2 inhibitor originally assessed for advanced solid tumors, is undergoing clinical trials for various cancer types.[220]

Additionally, a broad range of sphingolipid metabolic enzyme inhibitors, although not yet approved, are being tested for their efficacy in treating sphingolipid-related disor-

ders. Notable examples include the highly selective SPT inhibitor myriocin, amitriptyline as an effective ASM inhibitor, and the (dihydro)ceramide synthase inhibitor Fumonisin B1.[221]

1.4 The Role of Sphingolipids in the Development of Metabolic Disorders

Numerous studies have demonstrated that sphingolipid mediators, including ceramide and S1P, play a critical role in regulating obesity and glucose homeostasis with distinct regulatory roles in various metabolic tissues, including the liver, adipose tissue, and muscle. To date, significant progress has been made in elucidating the complex links between sphingolipid metabolism and the pathogenesis of metabolic diseases, identifying potential therapeutic targets. However, some findings within this body of research remain partially contradictory.

1.4.1 Ceramide Drives the Development of Metabolic Diseases

Sphingolipid accumulation can occur through endogenous *de novo* biosynthesis, the sphingolipid salvage pathway, or the sphingomyelin pathway. By increasing substrate supply to SPT, excess palmitate thereby stimulates sphingolipid synthesis.[222] In parallel, when serine availability declines, as reported in obesity and T2D, SPT can condense alanine and glycine yielding 1-deoxysphingolipids that have been implicated in diabetic neuropathy.[223,224] Consequently, although *de novo* sphingolipid synthesis and substrate availability influence ceramide accumulation, dietary ceramides are not directly absorbed in the gastrointestinal tract. Instead, they are hydrolyzed into FFAs, such as palmitate. However, dietary sphingosine, can be utilized by gastrointestinal microbiota to generate sphingolipids, which subsequently enter systemic circulation and reach organs like the liver.[225] Importantly, dietary FFAs directly fuel *de novo* ceramide synthesis, and the composition of dietary fatty acids critically determines the extent of ceramide production. For instance, individuals consuming diets rich in saturated fats, as opposed to polyunsaturated fats, exhibit higher plasma and liver ceramide levels and increased hepatic lipid accumulation.[226,227]

Furthermore, circulating FFAs released from fat depots during inflammation and insulin resistance, driven by enhanced adipocyte lipolysis, are taken up by ectopic tissues to serve as substrates for ceramide synthesis.[228] However, the ceramide precursor palmitate not only functions as a substrate but has also been demonstrated to increase

both mRNA levels and the activity of the ceramide-forming enzyme Degs1 in myotubes. Consequently, palmitate promotes ceramide synthesis and induces insulin resistance by diminishing Akt phosphorylation, which can be mitigated by knockdown of Degs1.[229] *In vivo* studies have confirmed this by using either Fenretinide, a DEGS1 inhibitor, to pharmacologically block DEGS1, or by employing heterozygous and inducible liver-specific, adipose-specific, as well as global Degs1 knockout strategies. All approaches led to a reduction in ceramide levels ($Cer_{16:0}$–$Cer_{24:0}$ and $Cer_{24:1}$) within tissues, which is associated with enhanced insulin sensitivity and improved liver steatosis.[230-232]

Other studies aimed at lowering global ceramide levels have targeted the rate-limiting step in sphingolipid synthesis in diet-induced or genetically obese (ob/ob) rodent models through the administration of Myriocin, an inhibitor of SPT. The therapeutic application of Myriocin, dependent on both time span and dosage, resulted in a reduction in body weight, amelioration of hepatic lipid accumulation, and improvement in insulin resistance, as well as enhanced glucose homeostasis.[233,234] The improvement in glucose homeostasis was evidenced by enhanced insulin signaling, as indicated by increased Akt phosphorylation in skeletal muscle and liver tissues.[235]

Interestingly, the levels of the endogen inhibitors of SPT, ORMDLs, exhibit an inverse correlation with the expression of obesity-related genes in human subcutaneous WAT.[236] This relationship is further corroborated by the observation of higher ceramide levels in HFD-fed ORMDL3-deficient mice, which is associated with increased body weight and insulin resistance.[237]

While the majority of studies indicate a beneficial role in reducing ceramide levels, the adipose tissue-specific deletion of either *Sptlc1* or *Sptlc2* impaired adipose tissue function, led to a lipodystrophic phenotype and the development of hepatosteatosis, systemic insulin resistance, and hyperglycemia.[238,239] This underscores the critical importance of tightly regulated *de novo* sphingolipid synthesis for maintaining normal metabolic function.

Research efforts have focused on directly targeting ceramide biosynthetic genes, specifically ceramide synthases. It has been demonstrated that in murine livers, ceramide species $Cer_{16:0}$ and $Cer_{18:0}$ increase after 16 weeks on a high-fat high-cholesterol diet (HFHCD), with $Cer_{16:0}$ and $Cer_{24:1}$ further elevated during disease progression from MASLD to MASH.[240] An increase in $Cer_{16:0}$ has also been observed in both visceral and subcutaneous WAT in mice and humans, correlating with the mRNA levels of the

$Cer_{16:0}$-producing enzyme CerS6, BMI, insulin resistance, and adipocyte size.[241] Consistent with these findings, the use of CerS6 antisense oligonucleotide in ob/ob mice and the global knockout of CerS6 in a HFD model resulted in reduced hepatic $Cer_{16:0}$ levels and prevention of diet-induced obesity (DIO) and its consequences, such as glucose intolerance and insulin resistance. A liver-specific knockout improved glucose tolerance and hepatic insulin sensitivity.[241,242] Hammerschmidt *et al.* demonstrated significant differences between CerS5 and CerS6-derived ceramides in the liver. While a knockout of either CerS5 or CerS6 reduced $Cer_{16:0}$ levels in hepatocytes, only the CerS6 knockout prevented diet-induced metabolic deterioration. This distinction is attributed to CerS6-deficiency reducing $Cer_{16:0}$ in hepatic mitochondria, thereby protecting against mitochondrial fragmentation and enhancing hepatic mitochondrial respiration, a benefit not observed in CerS5-deficient livers, highlighting the cellular localization of CerS6.[243]

Similarly, inhibition of the $Cer_{18:0}$-producing enzyme CerS1 in skeletal muscle, achieved through the administration of inhibitor P053 to HFD-fed mice, resulted in increased fatty acid oxidation and reduced TAG levels. However, this intervention did not confer protection against insulin resistance. In contrast, both global and muscle-specific knockout of CerS1 were effective in protecting against insulin resistance, attributed to an increase in muscle-derived Fgf21.[244,245] In INS-1 β-cells, CerS4 has been identified as a critical regulator of apoptosis. It has been demonstrated that the upregulation of CerS4, induced by palmitate- and glucose, elevates levels of $Cer_{18:0}$, $Cer_{22:0}$ and $Cer_{24:1}$, leading to cell death. Conversely, siRNA-mediated downregulation of CerS4 partially mitigated apoptosis.[246] Notably, haploinsufficiency of the enzyme CerS2, responsible for producing very-long-chain ceramides ($Cer_{20:0}$–$Cer_{26:0}$),[132] resulted in a significant reduction of long-chain ceramides in the liver. This was accompanied by a compensatory increase in $Cer_{16:0}$, which heightened the susceptibility to $Cer_{16:0}$-mediated exacerbation of steatohepatitis and insulin resistance upon dietary induction.[247]

However, during progression and development of obesity and metabolic diseases even more factors control ceramide accumulation. For instance, obesity-induced overexpression and release of pro-inflammatory cytokines, such as TNF-α, IL-1β or IL-6 further exacerbate ceramide synthesis by upregulating SPT in macrophages and stimulating ASM activity.[248,249] Of note, ceramides amplify inflammatory signaling through a

feedback mechanism, activating the transcription factor NF-κB and promoting expression of inflammatory genes.[250]

Interestingly, reduced adiponectin levels in obesity contribute to ceramide accumulation, as adiponectin enhances ceramide degradation via adiponectin receptor (AdipoR1 and AdipoR2)-mediated ACER activation.[251] Holland and colleagues demonstrated, that in a leptin-deficient mouse model, overexpression of AdipoRs in adipose and liver tissues restored ceramidase activity, reducing ceramide levels and alleviating hepatic steatosis.[252] Similarly, the overexpression of ACER specifically in adipocytes and hepatocytes both resulted in decreased ceramide levels in hepatocytes, reduced hepatic steatosis, and enhanced systemic insulin tolerance and glucose utilization.[253]

Furthermore, the dynamic turnover between SM and ceramide has been implicated in the regulation of hepatic lipid metabolism and steatosis. While liver-specific overexpression of SMS2 promoted SM accumulation, ceramide reduction in the liver, fatty acid uptake, and liver steatosis, a global SMS2 knockout challenged with a HFHCD, accompanied by elevated ceramide and reduced SM levels, abrogated hepatic steatosis. *In vitro*, ceramide treatment of Huh7 cells resulted in a reduction of PPARγ2 and its target genes *Cd36* and *Fsp27*.[254] Although a SMS2 deficiency was shown to alleviate hepatic steatosis, fibrotic lesions in the liver persist.[255] Additionally, in a 12-week HFD model, inhibition by SMS2 inhibitor LY93 (40 mg/kg/d) in parallel with HFD, led to the abolishment of insulin resistance, as demonstrated by intraperitoneal ITT and increase in IRS-1, Akt, and GSK-3β phosphorylation in the liver.[256]

In line with this, ceramides have also been reported to exhibit beneficial effects. In studies involving T1D and DIO mouse models, it was observed that $Cer_{24:1}$ levels were lower in plasma and liver.[257] However, supplementation of nervonic acid (C24:1) ameliorated body weight gain, glucose tolerance, and insulin sensitivity by enhancing expression of peroxisome proliferator-activated receptor alpha (PPARα) and Peroxisome proliferator-activated receptor gamma coactivator-1 alpha (PGC1α) expression.[258] Furthermore, the deletion of Acer3 resulted in elevated hepatic $Cer_{18:1}$ level in mice subjected to a palmitate-enriched western diet (PEWD), conferring protection against early inflammation and fibrosis by suppressing oxidative stress in hepatocytes.[259]

1.4.2 The S1P/SphK/S1PR Axis in the Context of Metabolic Diseases

S1P, its synthesizing enzymes SphK1/2, and its signaling via S1PR1–5 receptors and intracellular targets form a complex regulatory axis within the sphingolipid metabolic pathway, contributing to the development and progression of metabolic disorders.

Elevated plasma S1P levels have been documented in diabetic, diet-induced or genetically obese rodent models, as well as in human obese subjects, in comparison to their lean counterparts.[257,260] In diet-induced obese mice, liver S1P levels were similarly elevated, accompanied by an increase in Sph.[240] Regarding disease progression, in a cohort of human patients with cirrhosis and HCC, matched for age and sex, serum levels of S1P, Sph, and ceramide were significantly higher in HCC patients.[261] Consistent with this, SphK1 has been shown to contribute to disease progression in a MASLD mouse model, where global SphK1 knockout mice were protected from pro-inflammatory cytokine production in response to high-fat feeding, thus implicating a role in the progression from MASLD to MASH.[262] Indeed, SphK1 levels were found to be higher in HCC tissue and were associated with tumor size and stage, whereas low SphK1 expression correlated with overall survival.[263]

Mechanistically, intracellular S1P in various cell types has been shown to activate aPKCs, mediate profibrotic expression of Col α1(I) and Col α1(III) in human hepatogenic profibrotic cells (hHPCs) activated by TGF-β1, regulate glucose-stimulated insulin-secretion in pancreatic β-cells, and to promote release of proinflammatory cytokines TNFα, IL-6, MCP-1 in adipose tissue.[204,264-266] In line with its β-cell-specific effects, enhanced intracellular S1P degradation via SGPL1 overexpression in pancreatic β-cells conferred protection against cytokine-induced toxicity.[267]

Sphingosine kinases, which regulate S1P levels in cells, are expressed at higher levels in the terminal stage of 3T3-L1 differentiation, resulting in higher S1P levels.[268] SphK1 expression and activation may be promoted by TGF-β1 via TGF-βR as well as glucocorticoids and consequently were found to be elevated in the adipose tissue of ob/ob, diet-induced obese (DIO) mice and obese T2D humans.[264,266,268,269] Concomitantly, siRNA-mediated suppression of SphK1 in adipocytes attenuated lipid droplet accumulation and adipocyte marker gene expression, while a global SphK1 deficiency, despite higher adipose tissue mass, led to improved systemic insulin sensitivity and reduced

inflammation, both accompanied by a reduction of functional PPARγ.[264,268] Furthermore, overexpression of SphK1 or treatment with S1P promoted hepatic lipid storage in a PPARγ-dependent manner.[270]

Notably, while diet-induced obese SphK1 knockout mice developed diabetes due to β-cell death, adipocyte-specific loss of SphK1 promoted adipocyte hypertrophy, hepatic TAG accumulation, and systemic glucose intolerance.[271,272] Similarly, in KK/Ay diabetic mice and C2C12 cells, adenoviral SphK1 overexpression increased insulin signaling and glucose uptake, thereby lowering plasma glucose, insulin, NEFA and TAG levels and hyperglycemia-induced liver injury.[273] Consistently, SphK1 overexpression in mice subjected to a HFD protected against HFD-induced insulin resistance by promoting ceramide clearance in skeletal muscle and reducing JNK signaling.[274]

In contrast to SphK1, the data concerning SphK2 exhibit partial inconsistency. While SphK2 has been demonstrated to enhance glucose-stimulated insulin secretion through S1P production in pancreatic β-cells, its chronic activation under lipotoxic conditions induces β-cell apoptosis by initiating mitochondrial apoptotic signaling via Bcl-xL interaction. Furthermore, genetic deletion of SphK2 mitigated the loss of β-cell mass and improved the diabetic phenotype in a HFD plus streptozotocin (STZ)-induced mouse model.[265,275] Aged SphK2 deficient mice exhibit protection against age-related obesity and insulin resistance, along with elevated adiponectin levels and increased *Atgl* expression in adipose tissue.[276] Conversely, a liver-specific knockout of SphK2 exacerbated glucose intolerance and insulin resistance, attributed to Sph accumulation, whereas its global deletion has been reported to result in higher energy expenditure, protecting mice from DIO and glucose intolerance.[277,278] Contrarily, short term HFD-feeding of SphK2-deficient mice was associated with MASLD development.[279]

These findings underscore the tissue-specific and context-dependent roles of SphK2 in metabolic regulation, as its overexpression in mice and primary hepatocytes was shown to reduce hepatic lipid accumulation and enhance glucose tolerance and insulin sensitivity likely through SphK2-mediated upregulation of FAO genes.[280]

In the context of liver disorders, a 16-week western diet plus sugar water (WDSW)-induced mouse model of early MASH in SphK2-deficient mice, demonstrated upregulation of proinflammatory gene expression, hepatic lipid deposition and impairment of oxidative phosphorylation.[281] However, in a long-term HFD plus sugar water model, SphK2 ablation protected male mice from HCC.[282,283]

As the sole source of S1P, sphingosine kinases play a crucial role in determining the availability of S1P. This availability, in turn, influences the extracellular functions of S1P, which are mediated through its receptors and are integral to various aspects of metabolic regulation. Studies utilizing the S1P antagonist FTY720, which targets S1R1 and S1PR3-5, demonstrated reduced hepatic TAG levels as well as decreased hepatic steatosis, liver injury, and inflammation in mouse models of MASLD and MASH.[284,285] Estrasimod, which binds with high affinity to S1PR1, S1PR4, and S1PR5, has been shown to ameliorate liver injury and inflammation in a murine MASH model.[286] Recent findings indicate that the deletion of S1PR1 in myeloid cells mitigated murine MASH by reducing monocyte-derived macrophage infiltration.[287]

Beyond immune cells, S1P signaling is implicated in adipocyte differentiation. Treatment with the S1PR2 inhibitor JTE-013 inhibited adipogenic differentiation of 3T3-L1 preadipocytes, whereas the S1PR1/3 antagonist VPC-23019 also inhibited this process.[288] This suggests that S1P receptor subtypes exert opposing effects on adipocyte differentiation, with S1PR2 inhibiting and S1PR1/3 promoting adipogenesis. Similarly, selective blockade of S1PR2/3 by JTE-013, VPC-23019, or siRNA reduced lipid accumulation in Huh7 hepatocytes.[270] Additionally, S1PR2 signaling was also implicated in the apoptotic control of β-cells, where S1PR2-deficiency attenuated STZ-induced β-cell death.[289] In hepatocytes, elevated S1P signaling via S1PR2, similar to palmitate, inhibits insulin signaling, an effect that can be reversed by JTE-013.[290]

In the context of cholestasis-induced liver fibrosis, there is an observed increase in the expression levels of S1PR2. Consistent with this, conjugated bile acids activate S1PR2 in rodent primary hepatocytes, potentially promoting fibrogenic and inflammatory responses via AKT and ERK signaling pathways.[291] Notably, both the genetic S1PR2 knockout and its pharmacological inhibition with JTE-013 confer protection against fibrosis and result in a reduction of fibrosis, as evidenced by decreased expression of alpha smooth muscle actin (α-SMA).[292,293] Similarly, S1PR3 was found to be upregulated and involved in HSC activation, further promoting the recruitment of bone marrow-derived cells to fibrotic liver tissue, which is demonstrated by the observed decrease in α-SMA expression upon S1PR3 inhibition in the human HSC cell line LX-2.[294,295] In contrast, hepatic steatosis, impaired glucose tolerance, adipose tissue inflammation, and reduced levels of adiponectin mRNA, was not improved in HFD-challenged S1PR3-knockout mice.[296]

2 Research Aim

The metabolic syndrome, characterized by multiple risk factors that contribute to comorbidities such as MASLD, T2D, CVD, and hypertension, has reached epidemic proportions. This increase is driven by sedentary lifestyles and dietary changes. In clinical practice, addressing or preventing obesity and its comorbidities has proven challenging, as pharmacological interventions often lack long-term efficacy. Consequently, it is imperative to elucidate the underlying mechanisms linking these interrelated pathologies to develop targeted therapeutic interventions.

Emerging evidence suggests that sphingolipid signaling plays a significant role in lipid and energy metabolism, potentially driving the development and progression of various metabolic abnormalities. These abnormalities ultimately result in dysfunctional adipose tissue and impaired glucose and insulin homeostasis. However, the precise contributions of distinct enzymes regulating S1P turnover, as well as its bioactive properties and impact on signaling pathways, are not yet fully understood.

The primary objective of this study is to investigate the role of S1P turnover in the development of metabolic disorders such as obesity, MASLD, and T2D by using genetic and pharmacological strategies. A high-fat diet mouse model is utilized to characterize the metabolic phenotype of mice deficient in one of the sphingosine kinases responsible for S1P production, focusing on hepatic lipid metabolism. A second approach evaluates pharmacological SphK2 inhibition and its therapeutic potential to influence systemic metabolism and liver function in treating established MASLD, comparable to the genetic model. As a third approach, an alternative therapeutic strategy targeting the S1P-degrading enzyme S1P lyase is applied to increase S1P levels, combining phenotype and hepatic lipid metabolism assessment with a detailed analysis of adipose tissue function, particularly white adipose tissue lipolysis. Liver and plasma sphingolipid profiles are systematically examined across all approaches to reveal links between modifications in sphingolipid metabolism and systemic or tissue-specific outcomes.

This strategy aims to elucidate the impact of interventions in S1P metabolism on liver and adipose tissue homeostasis in cases of diet-induced obesity with MASLD and T2D. The objective is to uncover mechanisms of hepatic sphingolipid remodeling that may identify therapeutic targets.

3 Material and Methods

3.1 Material

3.1.1 Devices

Device and Model Name	Manufacturer
BZ-X microscope	Keyence Corporation, Osaka, Japan
C1000 Touch™ Thermal Cycler	Bio-Rad Laboratories, Hercules, USA
Centrifuge 5430 R	Eppendorf SE, Hamburg, Germany
Centrifuge 5810 R	Eppendorf SE, Hamburg, Germany
CFX96™ Real-Time System	Bio-Rad Laboratories, Hercules, USA
ChemiDoc™ XRS+ Imaging System	Bio-Rad Laboratories, Hercules, USA
Climate cabinet (MKKL1200)	Flohr Instruments, Nieuwegein, The Netherlands
Drying oven	Memmert GmbH & Co. KG, Schwabach, Germany
Gel Doc XR+ Gel Imaging System	Bio-Rad Laboratories, Inc., Hercules, USA
Ismatec Reglo Digital Pump (ISM834C)	Cole-Parmer, Vernon Hills, USA
KERN ADJ200-4 analytical balance	Kern & Sohn GmbH, Balingen, Germany
Kern EMB 500-1 small pet scale	Kern & Sohn GmbH, Balingen, Germany
LCMS-8050 triple quadrupole mass spectrometer	Shimadzu Deutschland GmbH, Duisburg, Germany
Leica EG1150H embedding station	Leica Microsystems GmbH, Wetzlar, Germany
MD 4C NT vacuum pump	Vacuubrand GmbH + Co. KG, Wertheim, Germany
Microplate Reader CLARIOstar Plus	BMG Labtech, Ortenberg, Germany
Mini PROTEAN® Tetra Cell	Bio-Rad Laboratories, Inc., Hercules, USA
Mini Trans-Blot® Cell	Bio-Rad Laboratories, Inc., Hercules, USA
Multi-Tube Vortex Mixer (VXMTAL)	Ohaus Europe GmbH, Greifensee, Switzerland
Multipette E3	Eppendorf, Hamburg, Germany
NanoDrop One	Thermo Fisher Scientific, Waltham, USA

Device and Model Name	Manufacturer
Nexera UHPLC system (Solvent Delivery Unit LC-40D X3, System Controller SCL-40, Autosampler SIL-40C X3, Column Oven CTO-40C, Degassing Unit DGU-405)	Shimadzu Deutschland GmbH, Duisburg, Germany
Nitrogen Generator NGM 22-LC/MS	cmc Instruments GmbH, Eschborn, Germany
Power PAC 200	Bio-Rad Laboratories, Hercules, USA
RVC 2.25 CDplus rotary vacuum concentrator	Martin Christ Gefriertrocknungsanlagen GmbH, Osterode am Harz, Germany
Sliding Microtome Microm HM 430	Thermo Fisher Scientific, Waltham, USA
Spotchem™ EZ SP-4430	Axon Lab AG, Reichenbach, Germany
StatStrip Xpress2	Nova Biomedical Corporation, Waltham, USA
Thermomixer	Eppendorf, Hamburg, Germany
Tissue float bath Hydro H2P	LAUDA Dr. R. Wobser GmbH & Co. KG, Lauda-Königshofen, Germany
TissueRuptor®	Qiagen GmbH, Hilden, Germany
Ultrapure water system	Stakpure GmbH, Niederahr, Germany
Vacuum infiltration tissue processor Tissue-Tek® VIP™5Jr.	Sakura Finetek Europe B.V., Alphen aan den Rijn, The Netherlands

3.1.2 Consumables

Product	Manufacturer
26G x ½“ needle (303800)	Becton, Dickinson and Company, Franklin Lakes, USA
Cell Strainer, 100µm (83.3945.100)	Sarstedt, Nümbrecht, Germany
Cell Strainer, 40µm (83.3945.040)	Sarstedt, Nümbrecht, Germany
Filtropur S 0.2 sterile filter (83.1826.001)	Sarstedt, Nümbrecht, Germany
Filtropur S 0.45 sterile filter (83.1826)	Sarstedt, Nümbrecht, Germany
Immobilon®-P PVDF membrane (IPVH00010)	Merck Millipore (Merck KGaA), Darmstadt, Germany

Product	Manufacturer
Microscope Slides 26 x 76mm	Engelbrecht Medizin- und Labortechnik GmbH, Edermünde, Germany
Microseal® B Adhesive Sealer for PCR plates (MSB-1001)	Bio-Rad Laboratories, Hercules, USA
Microtest Plate 96 Well, F (82.1581)	Sarstedt, Nümbrecht, Germany
Omnifix®-F syringe 1 mL (9161406V)	B. Braun SE, Melsungen, Germany
PCR plate full skirt LP transp. (72.1980)	Sarstedt, Nümbrecht, Germany
QIAshredder (79656)	Qiagen GmbH, Hilden, Germany
SPOTCHEM™ II Liver-1 profile (77182)	Arkray, Inc., Kyoto, Japan
StatStrip Xpress Glucose Strips (42214)	Nova Biomedical Corporation, Waltham, USA
Swingsette™ embedding cassettes (XY25.1)	Carl Roth GmbH + Co. KG, Karlsruhe, Germany
TC plate 6 well, Standard, F (83.3920)	Sarstedt, Nümbrecht, Germany
TC plate 6-well, Cell+, F (83.3920.300)	Sarstedt, Nümbrecht, Germany
Tissue Ruptor Disposable Probes (990890)	Qiagen GmbH, Hilden, Germany
Vasofix® Safety IV catheter 18G	B. Braun, Melsungen, Germany
Vicryl™ *Plus* 4-0, P3 (MPVCP494)	Ethicon, Inc., Raritan, NJ, USA
Whatman Paper 3mm (3030-672)	Cytvia, Marlborough, USA

3.1.3 Chemicals and Reagents

Basic Laboratory Chemicals

Product	Manufacturer
[gamma-32P]ATP	Hartmann Analytic, Braunschweig, Germany
Adenosine 5’-triphosphate (ATP) (A-2383)	Sigma-Aldrich, Merck KGaA, Darmstadt, Germany
Albumin bovine Fraction V, pH 7.0 (11930.04)	Serva Electrophoresis GmbH, Heidelberg, Germany

Product	Manufacturer
Ammonium chloride (A9434)	Sigma-Aldrich, Merck KGaA, Darmstadt, Germany
Ammoniumpersulfat (APS) (A3678)	Sigma-Aldrich, Merck KGaA, Darmstadt, Germany
Calcium chloride dihydrate (A3587)	AppliChem GmbH, Darmstadt, Germany
Coomassie brilliant blue R250 (1.12553)	Sigma-Aldrich, Merck KGaA, Darmstadt, Germany
D-glucose (G-7021)	Sigma-Aldrich, Merck KGaA, Darmstadt, Germany
D-Saccharose (4621.1)	Carl Roth GmbH + Co. KG, Karlsruhe, Germany
Dansyl Hydrazine for HPLC (A5552)	Tokyo Chemical Industry Co., Ltd, Zwijndrecht, Belgium
Dipotassium hydrogen phosphate (P3786)	Sigma-Aldrich, Merck KGaA, Darmstadt, Germany
Disodium hydrogen phosphate (A1372)	PanReac AppliChem, Darmstadt, Germany
DTT (A1101)	PanReac AppliChem, Darmstadt, Germany
EDTA (8043.2)	Carl Roth GmbH + Co. KG, Karlsruhe, Germany
EGTA (3054.3)	Carl Roth GmbH + Co. KG, Karlsruhe, Germany
Glycine PUFFERAN® ≥99%, p.a. (3908.2)	Carl Roth GmbH + Co. KG, Karlsruhe, Germany
HATU (C01011)	Carbolution Chemicals GmbH, St. Ingbert, Germany
HEPES (6763.3)	Carl Roth GmbH + Co. KG, Karlsruhe, Germany
Hydrochloric acid (182883)	PanReac AppliChem, Darmstadt, Germany
IGEPAL® CA-630 (I3021)	Sigma-Aldrich, Merck KGaA, Darmstadt, Germany
L-(-)-Malic acid (M1000)	Sigma-Aldrich, Merck KGaA, Darmstadt, Germany
L-glutamic acid monosodium salt hydrate (G1626)	Sigma-Aldrich, Merck KGaA, Darmstadt, Germany
Magnesium acetate (63052)	Sigma-Aldrich, Merck KGaA, Darmstadt, Germany
Magnesium chloride (208337)	Sigma-Aldrich, Merck KGaA, Darmstadt, Germany
Magnesium sulfate heptahydrate (63138)	Sigma-Aldrich, Merck KGaA, Darmstadt, Germany
NADH (N7004)	Sigma-Aldrich, Merck KGaA, Darmstadt, Germany
Non-fat dried milk powder (A0830)	AppliChem GmbH, Darmstadt, Germany

Product	Manufacturer
Potassium chloride (P5405)	Sigma-Aldrich, Merck KGaA, Darmstadt, Germany
Potassium dihydrogen phosphate (1.04873)	Sigma-Aldrich, Merck KGaA, Darmstadt, Germany
Pyruvic acid sodium salt (106619)	Sigma-Aldrich, Merck KGaA, Darmstadt, Germany
ROTIPHORESE® Gel30 (37.5:1) (3029.1)	Carl Roth GmbH + Co. KG, Karlsruhe, Germany
Sodium chloride (P029)	Carl Roth GmbH + Co. KG, Karlsruhe, Germany
Sodium deoxycholate (D6750)	Sigma-Aldrich, Merck KGaA, Darmstadt, Germany
Sodium dihydrogen phosphate (1.06370)	Supelco (Merck), Darmstadt, Germany
Sodium dodecyl sulfate (20765)	Serva Electrophoresis GmbH, Heidelberg, Germany
Sodium hydroxide pellets (131687)	PanReac AppliChem, Darmstadt, Germany
TEMED (1.107322.0100)	Sigma-Aldrich, Merck KGaA, Darmstadt, Germany
TRIS Hydrochlorid PUFFERAN® ≥99%, p.a. (9090)	Carl Roth GmbH + Co. KG, Karlsruhe, Germany
TRIS PUFFERAN® ≥99.9%, p.a. (4855)	Carl Roth GmbH + Co. KG, Karlsruhe, Germany
Tween®20 (polyoxyethylene sorbitan monolaurate) (63158)	Honeywell Riedel-de Haën, Seelze, Germany
β-Mercaptoethanol (A1108)	AppliChem GmbH, Darmstadt, Germany

Histological Reagents

Product	Manufacturer
Vitro-Clud® mounting medium (04-0001)	R Langenbrinck GmbH, Emmendingen, Germany
Erythrosine, bluish (1B-255)	Waldeck GmbH & Co. KG, Division Chroma, Münster, Germany
Sirius Red F3BA (1A280)	Waldeck GmbH & Co. KG, Division Chroma, Münster, Germany
Picric acid (74069)	Honeywell Fluka, Seelze, Germany

Animal Use Compounds

Product	Manufacturer
Ketamine 500 mg/10mL	Panpharma, Luitré, France
Xylazine 20 mg/mL	WDT, Garbsen, Germany
Huminsulin® Normal 100 (HI0210)	Eli Lilly and Company, Indianapolis, USA

Recombinant Proteins and Enzymes

Product	Manufacturer
Collagenase type II, CLS (C2-22)	Sigma-Aldrich, Merck KGaA, Darmstadt, Germany
Cozy™ Hi Prestained Protein Ladder (PRL0102)	HighQu GmbH, Kraichtal, Germany
Precision Plus Protein Dual Color Standards (1610374)	Bio-Rad Laboratories, Inc., Hercules, USA
Recombinant dephosphorylated MBP (13-110)	Sigma-Aldrich, Merck KGaA, Darmstadt, Germany
Recombinant human PKCζ protein (ab60848)	Abcam, Cambridge, UK
Glycerol-3-Phosphate Dehydrogenase (GDH) (47962023)	Roche Diagnostics GmbH, Mannheim, Germany
Glycerokinase from Cellumonas sp. (G6142)	Sigma-Aldrich, Merck KGaA, Darmstadt, Germany

Small Molecule Inhibitors and Modulators

Product	Manufacturer
4-deoxypyridoxine hydrochloride (D0501)	Sigma-Aldrich, Merck KGaA, Darmstadt, Germany
AUY954 (9000548)	Cayman Chemical, Ann Arbor, USA
Bisindolylmaleimide I (203290)	Sigma-Aldrich, Merck KGaA, Darmstadt, Germany
C2-ceramide (860502P)	Avanti Polar Lipids, Inc., Alabaster, USA
C17-sphingosine (860640P)	Avanti Polar Lipids, Inc., Alabaster, USA
CYM5520 (17638)	Cayman Chemical, Ann Arbor, USA

Product	Manufacturer
CYM5541 (15190)	Cayman Chemical, Ann Arbor, USA
Dexamethasone (D4902)	Sigma-Aldrich, Merck KGaA, Darmstadt, Germany
Fumonisin B1 (62580)	Cayman Chemical, Ann Arbor, USA
IBMX (I5879)	Sigma-Aldrich, Merck KGaA, Darmstadt, Germany
Isoproterenol (I6504)	Sigma-Aldrich, Merck KGaA, Darmstadt, Germany
Ly93 (MCE-HY-114307)	MedChemExpress LLC, Monmouth Junction, USA
PC 18:1-18:0 (850476)	Avanti Polar Lipids, Inc., Alabaster, USA
PD98059 (S1177)	Selleck Chemicals LLC, Houston, USA
Phosphatidy-L-serine (2TAT)	Carl Roth GmbH + Co. KG, Karlsruhe, Germany
PKCζ pseudo-substrate inhibitor (sc-3098)	Santa Cruz Biotechnology, Dallas, USA
Rosiglitazone (R2408)	Sigma-Aldrich, Merck KGaA, Darmstadt, Germany
S1PL-IN-1 (HY-115566)	MedChemExpress, Monmouth Junction, USA
Small molecule HSL-inhibitor (NNC0076-0079)	Novo Nordisk, Bagsværd, Denmark
Sphingosine-1-Phosphate, D-erythro (BML-SL140)	Enzo Life Sciences, Farmingdale, USA
SQ22536 (S8283)	Selleck Chemicals LLC, Houston, USA
Wortmannin (S2758)	Selleck Chemicals LLC, Houston, USA

Solvents

Product	Manufacturer
Acetic acid 99-100%, GPR RECTA-PUR® (20103)	VWR Chemicals (Avantor), Radnor, USA
Acetonitrile for LC-MS (701881)	AppliChem GmbH, Darmstadt, Germany
Chloroform ROTISOLV HPLC (7331.1)	Carl Roth GmbH + Co. KG, Karlsruhe, Germany
Dimethyl sulfoxide (D8418)	Sigma-Aldrich, Merck KGaA, Darmstadt, Germany
Ethanol ROTIPURAN® ≥99.8%, p.a. (9065.2)	Carl Roth GmbH + Co. KG, Karlsruhe, Germany

Product	Manufacturer
Formic acid ≥98% ROTIPURAN® (4724)	Carl Roth GmbH + Co. KG, Karlsruhe, Germany
Hydrazine Hydrate (225819)	Sigma-Aldrich, Merck KGaA, Darmstadt, Germany
Methanol CHROMASOLV™ LC-MS ≥99.9% (34966)	Honeywell Riedel-de Haën, Seelze, Germany
Triethylamine ≥99% (T0886)	Carl Roth GmbH + Co. KG, Karlsruhe, Germany
Xylene (4436.2)	Carl Roth GmbH + Co. KG, Karlsruhe, Germany

3.1.4 Commercial Kits

Product	Manufacturer
Free Fatty Acid Assay Kit (ab65341)	Abcam, Cambridge, United Kingdom
innuPREP DNase I Digest Kit (845-KS-5200250)	IST Innuscreen GmbH, Berlin, Germany
innuPREP RNA Mini Kit 2.0 (845-KS-2040250)	IST Innuscreen GmbH, Berlin, Germany
Pierce™ BCA Protein Assay Kit (23225)	Thermo Fisher Scientific, Waltham, USA
PowerTrack™ SYBR™ Green Master Mix (A46109)	Applied Biosystems (Thermo Fisher Scientific), Waltham, USA
RevertAid TM First Strand cDNA Synthesis Kit (K1691)	Thermo Fisher Scientific, Waltham, USA
Ultra-Sensitive Rat Insulin ELISA (90060)	CrystalChem, IL, USA

3.1.5 Primer Sequences for Quantitative Real-Time PCR

Table 1. Primer sequences

Target	5' to 3' Sequence	
Acc1	forward	ACATTCCGAGCAAGGGATAAG
	reverse	GGGATGGCAGTAAGGTCAAA
B2m	forward	GAGCCCAAGACCGTCTACTG
	reverse	GCTATTTCTTTCTGCGTGCAT
Cd36	forward	AGATGACGTGGCAAAGAACAG
	reverse	CCTTGGCTAGATAACGAACTCTG

Target	5' to 3' Sequence	
Cidea	forward	CTTAAGGGACAACACGCATTTC
	reverse	CGAAGGTGACTCTGGCTATTC
Cidec	forward	TGTTCATGGTCCTGCTGAAG
	reverse	TCTTAGTTGGCTTCTGGGAAAG
Fasn	forward	CTCATTGGTGGTGTGGACAT
	reverse	TTGGAGAGATCCTTCAGCTTTC
Lipe	forward	CCAGCCTGAGGGCTTACTG
	reverse	CTCCATTGACTGTGACATCTCG
Plin2	forward	AAGAGCCAGGAGACCATTTC
	reverse	CCACGAGACATAGAGCTTATCC
Pnpla2	forward	TCCGTGGCTGTCTACTAAAGA
	reverse	TGGGATATGATGACGTTCTCTCC
Tbp	forward	AGAACAATCCAGACTAGCAGCA
	reverse	GGGAACTTCACATCACAGCTC
Pparg	Mm_Pparg_1_SG QuantiTect Primer Assay, *QT00100296,* Qiagen, Hilden, Germany	

All oligonucleotides specific to *Mus musculus* were obtained from Eurofins Genomics Europe Shared Services GmbH (Ebersberg, Germany) unless stated otherwise.

3.1.6 Antibodies

Primary Antibodies

Target	Dilution	Manufacturer
phospho-HSL (Ser660) *(45804)*	1:1000	Cell Signaling Technology, Danvers, USA
CD36	1:500	not determined
HSL *(4107)*	1:1000	Cell Signaling Technology, Danvers, USA
PKCζ (H-1) *(sc-17781)*	1:200	Santa Cruz Biotechnology, Dallas, USA
p-PKCζ (H-2) *(sc-271962)*	1:100	Santa Cruz Biotechnology, Dallas, USA
GAPDH *(5G4cc)*	1:2000	HyTest Ltd., Turku, Finland
β-Actin (ACTB) *(a1978)*	1:1000	Sigma-Aldrich, Merck KGaA, Darmstadt, Germany
phospho-p44/42 MAPK (Erk1/2) (Thr202/Tyr204) *(9101)*	1:1000	Cell Signaling Technology, Danvers, USA
p44/42 MAPK (Erk1/2) *(9102)*	1:1000	Cell Signaling Technology, Danvers, USA

Secondary Antibodies

Target	Dilution	Manufacturer
Horse Anti-Mouse IgG (H+L), Peroxidase *(PI-2000)*	1:5000	Vector Laboratories, Newark, USA
Goat Anti-Rabbit IgG (H+L), Peroxidase *(PI-1000)*	1:5000	Vector Laboratories, Newark, USA

Conjugated Antibodies

Target	Dilution	Manufacturer
PKCζ (H-1) agarose-conjugated (AC) *(sc-17781)*	1:50	Santa Cruz Biotechnology, Dallas, USA

3.1.7 Media, Buffer and Solutions

Commercial Buffers

Product	Manufacturer
DPBS (1X) *(14190)*	Gibco (Thermo Fisher Scientific), Waltham, USA
Sodium chloride solution 0.9%	Fresenius Kabi, Bad Homburg, Germany
UltraPure™ TM Distilled Water DNase/RNase free *(10977)*	Invitrogen (Thermo Fisher Scientific), Waltham, USA
BD Pharm Lyse™ Lysing Buffer *(555899)*	Becton, Dickinson and Company, Franklin Lakes, USA
ROTI®Histofix 4% *(P087)*	Carl Roth GmbH + Co. KG, Karlsruhe, Germany
Paraplast® R embedding medium *(X880.1)*	Carl Roth GmbH + Co. KG, Karlsruhe, Germany
Hemalum solution acid acc. to Mayer *(T865.2)*	Carl Roth GmbH + Co. KG, Karlsruhe, Germany
HBSS calcium, magnesium *(14025)*	Gibco (Thermo Fisher Scientific), Waltham, USA
HBSS *(14175-095)*	Gibco (Thermo Fisher Scientific), Waltham, USA
Antibiotic-antimycotic *(15240-062)*	Gibco (Thermo Fisher Scientific), Waltham, USA
L-Glutamine 200 mM *(25030-081)*	Gibco (Thermo Fisher Scientific), Waltham, USA
Gentamicin 10mg/mL *(15710-049)*	Gibco (Thermo Fisher Scientific), Waltham, USA

Product	Manufacturer
Fetal Bovine Serum Value FBS *(A5256701)*	Gibco (Thermo Fisher Scientific), Waltham, USA
4x Laemmli Sample Buffer *(1610747)*	Bio-Rad Laboratories, Inc., Hercules, USA
M-PER™ Mammalian Protein Extraction Reagent *(78501)*	Thermo Fisher Scientific, Waltham, USA
Halt™ Phosphatase Inhibitor *(78428)*	Thermo Fisher Scientific, Waltham, USA
Halt™ Protease & Phosphatase Inhibitor Cocktail *(78442)*	Thermo Fisher Scientific, Waltham, USA
Halt™ Protease Inhibitor *(1860932)*	Thermo Fisher Scientific, Waltham, USA
Insulin solution human *(I9278)*	Sigma-Aldrich, Merck KGaA, Darmstadt, Germany
Mammalian Cell Lysis Buffer, 5X *(ab179835)*	Abcam, Cambridge, United Kingdom
Collagen I, Rat Tail *(10483-01)*	Gibco (Thermo Fisher Scientific), Waltham, USA
Insulin-Transferrin-Selenium 100X *(41400-045)*	Gibco (Thermo Fisher Scientific), Waltham, USA
DMEM, high glucose *(41965)*	Gibco (Thermo Fisher Scientific), Waltham, USA
William’s Medium E *(P04-29510)*	PAN-Biotech GmbH, Aidenbach, Germany
Stable Glutamine 200mM *(P04-82100)*	PAN-Biotech GmbH, Aidenbach, Germany
Trypsin-ETDA, 0.05% *(11580626)*	Gibco (Thermo Fisher Scientific), Waltham, USA

Western Blot Buffers

RIPA buffer	0.1% (w/v)	SDS
	1% (v/v)	NP-40 (IGEPAL)
	0.5% (w/v)	Sodium deoxycholate
		in PBS, add 1X Halt™ Protease & Phosphatase Inhibitor
Stacking gel buffer	1M	TRIS
	0.74% (w/v)	SDS
		in ddH_2O, set to pH 6.8 with HCl
Separating gel buffer	1.5 M	TRIS
	0.386% (w/v)	SDS
		in ddH2O, set to pH 8.8 with HCl
Stacking gel	68% (v/v)	ddH_2O
	17% (v/v)	Acrylamide (30%)
	14% (v/v)	Stacking gel buffer
	1% (v/v)	APS (10%)
	0.001% (v/v)	TEMED
Separation gel	ad 100%	ddH_2O
	*%	Acrylamide (30%)
	26%	Separation gel buffer
	1%	APS (10%)
	0.001%	TEMED
		*depending on required gel percentage
Running buffer	192 mM	Glycine
	25 mM	TRIS
	0.1% (w/v)	SDS
		in ddH_2O, set to pH 8.3 – 8.6
Transfer buffer	192 mM	Glycine
	25 mM	TRIS
	20% (v/v)	Methanol
		in ddH_2O, set pH 8.3 – 8.6
Wash buffer (PBS-T)	0.1% (v/v)	Tween-20
		in PBS

Primary Hepatocyte Isolation and Culture

Primary Hepatocyte Medium	1%	Antibiotic-Antimycotic
	1%	L-glutamine
	0.1%	Gentamicin
	0.1 µM	Dexamethasone
	0.001%	ITS Liquid Media supplement (100X)
	10%	FCS*
		in 500 mL William's Medium E
		*only added for cell plating
KH buffer (10x)	1.03 M	NaCl
	23.5 mM	KCl
	1.76 mM	KH_2PO_4
		in ddH_2O, set pH 7.4 with NaOH, sterile
Glucose solution	50 mM	D-Glucose in ddH_2O, sterile
Glutamine solution	47.9 mM	Glutamine in ddH_2O, sterile
HEPES solution (10x)	250 mM	HEPES in ddH_2O, sterile
		set pH 8.5 or pH 7.6 with NaOH
Amino acid solution (6.5x)	0.14 g/L	L-aspartic acid, L-cysteine
	0.27 g/L	L-alanine, L-citrulline
	0.4 g/L	L-asparagine, L-isoleucine
	0.55 g/L	L-methionine, L-phenylalanine, L-proline, L-tyrosine
	0.65 g/L	L-ornithine, L-serine, L-tryptophan
	0.8 g/L	L-leucine, L-valine
	1.0 g/L	L-histitine, L-glutamic acid, L-glycine
	1.3 g/L	L-lysine, L-threonine
		(all Sigma-Aldrich, Merck KGaA, Darmstadt, Germany)
		dissolve in 4M NaOH
		set pH to 7.6 by 2N HCl, sterile
EGTA solution	124.9 mM	EGTA (dissolve with NaOH) in ddH_2O
		set pH to 7.6 with HCl, sterile
$MgSO_4$ solution	99.8 mM	$MgSO_4 \times 7\ H_2O$ in ddH_2O, sterile
$CaCl_2$ solution	129.23 mM	$CaCl_2 \times 2\ H_2O$ in ddH_2O, sterile

EGTA perfusion buffer	63% (v/v)	Glucose solution
	10.2% (v/v)	KH buffer
	10.2% (v/v)	10x HEPES solution (25 mM)
	15.2% (v/v)	Amino acid solution
	1% (v/v)	Glutamine solution
	add fresh:	0.4% (v/v) EGTA solution
Collagenase perfusion buffer	62.6% (v/v)	Glucose solution
	10.1% (v/v)	KH buffer
	10.1% (v/v)	HEPES solution
	12.1% (v/v)	Amino acid solution
	1% (v/v)	Glutamine solution
	add fresh:	4% (v/v) $CaCl_2$ solution + 0.323 mg/mL (≈ 40 U/mL) Collagenase
Suspension buffer	62.5% (v/v)	Glucose
	10.1% (v/v)	KH buffer
	10.1% (v/v)	HEPES (pH 7.6)
	15.1% (v/v)	Amino acid solution
	1% (v/v)	Glutamine solution
	0.4% (v/v)	$MgSO_4$ solution
	add fresh:	0.8% (v/v) $CaCl_2$ solution + 0.2% (w/v) BSA

3T3-L1 Cell Culture and Differentiation

Growth Medium	10% (v/v)	FCS
	1% (v/v)	Antibiotic-Antimycotic
	1 mM	Sodium pyruvate
	2 mM	L-glutamine in DMEM, high glucose
Differentiation Medium I	1 µg/mL	Insulin
	2 µM	Rosiglitazone
	0.25 µM	Dexamethasone
	0.5 mM	IBMX in Growth Medium
Differentiation Medium II	1 µg/mL	Insulin in Growth Medium

Adipocyte Isolation and Culture

Collagenase Solution	1% (v/v)	Antibiotic-Antimycotic
	2.5% (w/v)	BSA
	0.2% (w/v)	Collagenase type II
		in HBSS calcium, magnesium
		set to pH 7.4, sterile filtered
Wash buffer	3.5% (w/v)	BSA
	1% (v/v)	Antibiotic-Antimycotic
		in HBSS
Erythrocyte lysis buffer	154 mM	NH_4Cl
	10 mM	K_2HPO_4
	0.1 mM	EDTA
		in ddH_2O, set to pH7.4, sterile filtered
Growth Medium	10% (v/v)	FCS
	1% (v/v)	Antibiotic-Antimycotic
		in DMEM high glucose
Induction Medium	850 nM	Insulin
	1 µm	Rosiglitazone
	1 mM	Dexamethasone
	0.5 mM	IBMX
		in Growth Medium
Differentiation Medium	850 nM	Insulin
		in Growth Medium

Assay Buffers

SMS Assay *Homogenization Buffer*	50 mM	TRIS-HCl
	5%	Sucrose
	1 mM	EDTA
		in ddH_2O
		adjust pH to 7.4
		add fresh:1X Halt™ Protease Inhibitor
SMS Assay *10X Reaction Buffer*	500 mM	TRIS-HCl
	250 mM	KCl
		in ddH_2O
		adjust pH to 7.4

Lipolysis Assay	50 mM	Glycine (pH 9.8)
Hydrazine Buffer	0.05%	Hydrazine Hydrate
	1 mM	$MgCl_2$
	0.75 mg/mL	ATP
	0.375 mg/mL	NADH
	25 µg/mL	GDH (95 µM)
	0.5 µg/mL	Glycerokinase
Kinase Assay	140 µM	Phosphatidylserine
Reaction Buffer	2 µM	ATP
	10 µCi	[gamma-32P]ATP
	2.5 mM	TRIS-HCl (pH 7.5)
	5 µM	EGTA
	50 µM	DTT
	3.75 mM	$Mg(CH_3COO)_2$

3.1.8 Mouse Strains and Diets

Table 2. Mouse strains

Strain	International Nomenclature	Origin
WT	C57BL/6J	The Jackson Laboratory, Bar Harbor, USA
SphK1$^{-/-}$	B6J.129S6(B6N)-Sphk1^{tm1Rpl}/J	Richard Proia (National Institutes of Health, Bethesda, USA).
SphK2$^{-/-}$	B6J.129S6(B6N)-Sphk2^{tm1Rpl}/J	Richard Proia (National Institutes of Health, Bethesda, USA).
SMS2$^{-/-}$	C57BL/6;129-Sgms2^{tm1Jia}	Xian-Cheng Jiang, SUNY Downstate Medical Center, Division of Comparative Medicine, New York, USA

Wild-Type C57BL/6J Mice

For wild-type experiments, male adult B6, Cg-S1pr2tm1Jch (Cg = B6J.129(B6N) x B6N;129 x B6;Cg) mice, originally obtained from Jackson Laboratory, were used. All knockout strains used in this study were generated on a C57BL/6J background. Accordingly, C57BL/6J were designated as wild-type controls and henceforth referred to as wild type (WT).

Sphingosine Kinase 1 and 2 Knockout Mice (SphK1$^{-/-}$ and SphK2$^{-/-}$)

Sphingosine kinase 1 knockout mice (B6J.129S6(B6N)-Sphk1$^{tm1Rpl/J}$) and sphingosine kinase 2 knockout mice (B6J.129S6(B6N)-Sphk2$^{tm1Rpl/J}$) were generated and kindly provided by Richard Proia (National Institutes of Health, Bethesda, USA).[150,297]

Sphingomyelin Synthase 2 Knockout Mice (SMS2$^{-/-}$)

Sphingomyelin synthase 2 knockout mice (C57BL/6;129-Sgms2^{tm1Jia}) were generated and kindly provided by Xiang-Cheng Jiang (SUNY Downstate Medical Center, Division of Comparative Medicine, New York, USA).[298]

Mouse Diets

Mice received either a maintenance diet (NC; V1534; ssniff Spezialdiäten GmbH, Soest, Germany) or a high-fat diet (HFD; C1090-60; Altromin Spezialfutter GmbH & Co. KG, Lage, Germany). Table 3 provides overview of the dietary composition.

Table 3. Composition of Mouse Diets.

	Maintenance diet (NC) (V1534, ssniff)	**High fat-diet (HFD)** (C1090-60, Altromin)
Gross Energy (kcal)	3.893	6.658
Metabolizable Energy (kcal)	3.057	5.228
Macronutrients (kcal + % of energy)		
Fat	275 (9%)	3,151 (60%)
Protein	1,009 (33%)	842 (16%)
Carbohydrates	1,773 (58%)	1,236 (24%)
Raw Nutrients & Moisture (mg/kg; %)		
Moisture	28,679 (1.23%)	28,679 (2.87%)
Crude ash	32,308 (0.64%)	32,308 (3.23%)
Crude fibre	47,433 (0.49%)	47,433 (4.74%)
Crude fat	350,363 (0.33%)	350,063 (35.01%)
Crude protein	210,400 (1.90%)	210,400 (21.04%)
Nitrogenfree extractives	331,118 (5.41%)	331,118 (35.00%)
Fatty Acids (mg/kg + % of mg)		
Arachidic acid C-20:0	100 (0.01%)	3,791 (0.38%)
Eicosenoic acid C-20:1	200 (0.02%)	1,706 (0.17%)
α-Linolenic acid C-18:3	2,300 (0.23%)	3,129 (0.31%)
Linolenic acid C-18:2	18,000 (1.80%)	22,119 (2.21%)
Palmitic acid C-16:0	4,700 (0.47%)	56,559 (5.66%)
Stearic acid C-18:0	800 (0.08%)	37,173 (3.72%)
Oleic acid C-18:1	6,200 (0.62%)	111,563 (11.16%)
C16:1	100 (0.01%)	–
C14:0	100 (0.01%)	–

3.1.9 Software

Software Product	Company/Developer
BioRender.com*	BioRender Inc., Toronto, Canada
BZ-X800 Viewer	Keyence Corporation, Osaka, Japan
CFX Maestro	Bio-Rad Laboratories, Hercules, USA
ChatGPT** (Version GPT-5, Sep 2025)	OpenAI, San Francisco, USA
CLARIOstar® MARS version 3.42 R3	BMG Labtech, Ortenberg, Germany
CLARIOstar® version 5.70	BMG Labtech, Ortenberg, Germany
Fiji - Is Just ImageJ (1.54p)	Fiji developer community (https://fiji.sc)
Graphpad Prism version 10.4.2	Graphpad Software, LLC, San Diego, USA
GSEA version 4.3.2	UC San Diego and Broad Institute
HALO Image Analysis Platform (4.0.5107) + HALO® Vacuole Quantification module	IndicaLabs, New Mexico, USA
Image Lab 3.0.1 (Beta 2)	Bio-Rad Laboratories, Hercules, USA
Oroboros DatLab version 7.4.0.4	Oroboros Instruments GmbH, Innsbruck, Austria
Paperpal**	Cactus Communications, Mumbai, India
R version 4.2.2	The R Foundation for Statistical Computing, Vienna, Austria

* BioRender.com was used to create graphical illustrations. Published under Bioren-der.com publication license.

** ChatGPT and Paperpal were used for linguistic refinement and stylistic improvements.

3.2 Methods

3.2.1 Animal Experiments

Animal Housing and Legal Provisions

All mouse experiments were performed with the approval of the Landesamt für Verbraucherschutz und Ernährung Nordrhein-Westfalen (LAVE NRW; State Office for Consumer Protection and Food Safety of North Rhine-Westphalia) in accordance with directive 2010/63/EU of the European Parliament and the Council on the protection of animals used for scientific purposes (81-02.04.2022.A03; 84-02.04.2016.A547).
Animals were housed and bred in the animal facility of the Heinrich Heine University Düsseldorf (ZETT, Zentrale Einrichtung für Tierforschung und wissenschaftliche Tierschutzaufgaben). The mice were maintained at 22 °C, a relative humidity of 55%, and a 12-hour light/dark cycle. Normal chow diet and water were provided *ad libitum*.

High-Fat Diet-Induced Obesity Model

Male mice aged 16 ± 2 weeks were fed a high-fat diet (60% kcal from fat) for 12 weeks. Control groups were fed a standard maintenance diet (Table 3). Body weight was determined weekly during the feeding period. Glucose and insulin tolerance tests were carried out at 10 and 11 weeks of feeding, respectively. At the end of the 12-week trial, the mice were weighed, and food was withdrawn overnight. Before dissection, mice were euthanized by anesthesia (10 mg/kg ketamine and 10 mg/kg xylazine) administered by intraperitoneal injection and subsequent blood withdrawal following successful verification and the absence of righting and pedal reflexes. The mice were placed in a supine position and the surgical field was disinfected with 70% ethanol, and the heart was exposed by carefully opening the thoracic cavity. Blood was then collected from the heart prior to exsanguination through transcardial perfusion with phosphate-buffered saline (PBS). Liver, gonadal, and inguinal white adipose tissues were harvested and weighed. The organs were either snap-frozen and stored at -80 °C or transferred to 4% formaldehyde (PFA). For liver studies, the liver was divided into individual lobes, with the median, lower right, and caudal lobes for cryopreservation and the left and upper right lobes for histology.

SLS1081832 Treatment

SLS1081832, a sphingosine kinase 2 inhibitor, was used to characterize the effects of sphingosine kinase 2 deficiency in obese mice. For that, male 15 ± 1 weeks old C57BL/6J mice were subjected to a high-fat diet (60% kcal from fat) for a duration of 16 weeks. After 10 weeks, mice were randomly divided into two groups. The first group received daily intraperitoneal injections of 10 mg/kg SLS1081832 in 36.1% PEG-400, 9.1% ethanol (70%), 4.6% solutol, and 50% *aqua ad iniectabilia*, for the remaining 6 weeks, during which the high-fat diet was continued. The other group served as the vehicle control group. Glucose and insulin tolerance tests were performed after 14 and 15 weeks of feeding, respectively. At the end of the 16-week period, the mice were euthanized as previously described, and tissues were collected for subsequent analysis. The inhibitor SLS1081832 was synthesized and kindly provided by Webster Santos and colleagues (Department of Chemistry, Virginia Tech, Virginia, USA).

4-Deoxypyridoxine Treatment

S1P levels were elevated by pharmacological inhibition of the S1P-degrading enzyme, S1P lyase, using 4-deoxypyridoxine (DOP), which was administered via drinking water. In a therapeutic approach, mice were subjected to a HFD (60% kcal from fat) for 10 weeks. Subsequently, the mice were randomly assigned to two groups, and the HFD-feeding was continued for an additional 6 weeks, with one group receiving a treatment of 180 mg/L (equivalent to 30 mg per kg body weight per day) SGPL1 inhibitor DOP.

Glucose Tolerance Test

Intraperitoneal glucose tolerance tests (ipGTT) were performed using the modified protocol of Zhang (2011).[299] The test was conducted following an overnight fasting period in new cages with a normal water supply. On the day of the assay, mice were weighed, and a drop of blood was collected by tail vein puncture to determine basal blood glucose level using the StatStrip Xpress®2 glucose/ketone meter prior to intraperitoneal injection of 2 g/kg glucose from a 30% glucose solution in sterile filtered PBS. Blood glucose levels were measured at 15, 30, 60, 90, and 120 minutes after the initial glucose injection under constant observation.

Insulin Tolerance test

Intraperitoneal insulin tolerance tests (ipITT) have been used to assess insulin resistance. The test was conducted according to the modified protocol described by Vinué and Gonzalez-Navarro (2015).[300] After a fasting period of four hours, the mice were weighed, and basal blood glucose levels were determined by tail vein puncture using the StatStrip Xpress®2 Glucose/Ketone Meter. An insulin bolus of 1 IU/kg was injected intraperitoneally from a solution of 0.25 U insulin in 0.9% NaCl. Blood glucose levels were measured 15, 30, 45, 60, 90, and 120 minutes after insulin administration. Throughout the test, the mice were closely monitored to identify signs of hypoglycemia such as tremors and inactivity. A glucose dosage (1 g/kg body weight) was kept ready for rapid administration if necessary.

3.2.2 Plasma Biochemical Analyses

Collection of Blood Samples

Whole blood was collected from euthanized mice as described before and transferred into tubes coated with 0.5 M EDTA in 0.9% NaCl to a final EDTA concentration of 20 mM per milliliter of blood. Plasma was separated from whole blood by centrifugation (1,500 × g, 10 min, 4 °C) and used for subsequent analyses, including insulin ELISA, assessment of liver injury markers, and LC-MS/MS (for sample preparation, see Section 3.2.12).

Assessment of Liver Injury Markers in Plasma

The quantitative determination of alanine aminotransferase (GPT/ALT) and aspartate aminotransferase (GOT/AST) in the plasma, was conducted using Spotchem™ Liver-1 profile strips from Arkray on a Spotchem™EZ SP-4430 by Axonlab.

Quantification of Plasma Insulin by ELISA

Plasma insulin was measured in 5 µL of undiluted mouse plasma using Ultra-Sensitive Rat Insulin ELISA kit according to the manufacturer's Wide Range Assay (0.1 – 12.8 ng/mL) protocol.

3.2.3 Histology

Tissue samples from liver, gWAT and iWAT were harvested and fixed in ROTI®Histofix 4% for two weeks. Prior to embedding in paraffin, the tissues were dehydrated through an ascending graded ethanol series (50%, 40 °C, ≥15 min; 2×70%, 40 °C, 1 h; 2×96%, 40 °C, 1 h; 3×99.5%, 40 °C, 1 h; 2×NeoClear, 40 °C, 1 h; 4×paraffin, 60 °C, 1 h) performed in the Central Unit for Animal Research and Animal Welfare Affairs of the Heinrich Heine University Düsseldorf using an automated vacuum infiltration tissue processor. The dehydrated tissues were subsequently embedded in paraffin. The embedded tissues were sectioned at a thickness of 5 µm for liver tissue and 6 µm for gWAT and iWAT using a sliding microtome. These sections were subsequently stained and imaged using the Keyence BZ-X microscope.

Hematoxylin-Eosin Staining

To examine the morphology of liver and adipose tissues, hematoxylin and eosin (H&E) staining was performed to visualize basophilic structures, including cell nuclei and the endoplasmic reticulum (blue), as well as eosinophilic structures, such as the cytoplasm (red). Briefly, tissue sections were first deparaffinized using a xylene series (3×10 minutes), followed by rehydration using a descending ethanol series (2×100%, 2×96%, 1×70%). The sections were then transferred to distilled water for one minute. Next, the sections were incubated in Mayer's hemalaun solution for 5 minutes and developed under running tap water for 10 minutes. After a brief rinse in distilled water, eosin staining was performed for 30 seconds using a 1% erythrosine solution in distilled water. The sections were then washed briefly in distilled water and dehydrated using an ascending ethanol series (3x70%, 2x96%, 2x100%), followed by a final xylene step. The sections were then covered with coverslips by using Vitro-Clud® for long-term storage.

Sirius Red Staining

Hepatic fibrosis was evaluated by Sirius Red staining, which enables the visualization of collagen fibers within tissue sections. Liver sections were deparaffinized using a xylene series (2x 10 minutes, 2x 1 minute) and rehydrated in a descending ethanol series (2x 100%, 1x 96%, 1x 70%). After transferring the sections to distilled water, they were incubated in Mayer´s hemalaun for 10 minutesfollowed by a development step under running tap water. Subsequently, the sections were incubated in a 0.1%

Picro-Sirius Red solution in saturated aqueous picric acid for 30 minutes. The sections were quickly dehydrated in ethanol (3x 100%), cleared in xylene, and mounted in Vitro-Clud® for long-term storage.

Image Quantification

To quantify vacuole area in H&E-stained liver sections, HALO Image Analysis Platform version 4.0.5107 (Indica Labs, Inc.) was employed to accurately assess the vacuolar area per image. Vessel containing areas have been removed from the total area analyzed. See appendix (Appendix Figure 1) for an example of image analysis. Results are presented as vacuole area per total analyzed area.
The diameter and area of the adipocytes were determined by calculating the mean of at least three fields of view at 100-fold magnification using Adiposoft plugin in Fiji.

3.2.4 Primary Mouse Hepatocyte Isolation and Cell Culture

Primary mouse hepatocytes were isolated from C57BL/6J and SphK2$^{-/-}$ mice by the two-step collagenase perfusion method first described by Seglen in 1976 which is based on the previous work of Berry and Friend.[301,302] In this study, a modified protocol described by Godoy and colleagues was employed.[303]
The EGTA perfusion buffer, collagenase perfusion buffer, and suspension buffer were prepared and pre-warmed to 37 °C (refer to Section 3.1.7). Additionally, 6-well cell culture plates were pre-coated with collagen I at a concentration of 5 µg/cm^2 following the manufacturer's instructions. Mice were anesthetized via intraperitoneal injection of ketamine/xylazine (10 mg/kg ketamine and 10 mg/kg xylazine). Upon successful verification of anesthesia, indicated by the and absence of righting and pedal reflexes, the mice were positioned supine. The surgical field was prepared with 70% ethanol to ensure aseptic conditions before performing a longitudinal incision from caudal to cranial in the upper abdominal wall without penetrating the peritoneum. Subsequently, the peritoneum was carefully excised without damaging the surrounding viscera, allowing for relocation of the intestines to the left side of the abdominal cavity. This procedure exposed the inferior *vena cava* (abdominal artery) and the portal vein. A loose ligature was placed around the *vena cava*, followed by a minor diagonal incision into the vein, which facilitated the insertion of a 18G Vasofix® Safety intravenous catheter at a flat angle into the blood vessel. Following the correct placement of the needle, the ligature was secured, ensuring effective perfusion with the perfusion buffer as indicated by the

immediate blanching of the liver. A relief incision was made in the portal vein, and the liver was perfused with EGTA perfusion buffer at a flow rate of 15mL/minutes. After 10 to 15 minutes, warm collagenase perfusion buffer was infused via a three-way valve while maintaining the flow rate. The digestion step, depending on collagenase activity, lasted 5 to 10 minutes. A comprehensive digestive process was confirmed when the liver exhibited a malleable consistency. The liver was gently excised and transferred into a petri dish containing suspension buffer, after which the liver capsule was carefully opened with forceps under sterile conditions. Primary hepatocytes were released into suspension buffer until only liver capsule remained. To eliminate tissue debris, the cell suspension was filtered through a 100 µM cell strainer into a 50 mL tube. Non-parenchymal cells were removed by centrifuging the cell suspension at 50 × g and 4 °C for 5 minutes, followed by discarding of the supernatant. After a second washing and centrifugation step, the cell pellet was carefully resuspended in 10 mL suspension buffer and placed on ice. The cell number and viability of the obtained primary hepatocytes was determined using Trypan blue. Finally, the cells were plated in Primary Hepatocyte Medium (see Section 3.1.7) supplemented with 10% fetal calf serum (FCS) at a density of 50.000 cells/cm^2. The cells were allowed to adhere for 2 to 3 hours before a washing step with PBS and medium exchange to Primary Hepatocyte Medium. The following day, medium was changed to remove cell debris before performing further experiments.

3.2.5 C17-Sphingosine Kinase Activity Assay

An assay to assess sphingosine kinase activity was conducted in primary mouse hepatocytes one day after isolation and plating. Two hours before the assay, the medium was replaced with Primary Hepatocyte Medium devoid of FCS. A concentration of 5 µM C17-sphingosine or ethanol as vehicle was added to the medium for a duration of 30 minutes. Subsequently, the cells were harvested using Trypsin-EDTA solution. The trypsinized cells were then divided into two equal parts and centrifuged at 100 × g and 4 °C for 3 minutes. The supernatant was discarded, and the pellets from the same wells were split and utilized for both protein concentration determination (refer to Section 3.2.11) and methanol precipitation for LC-MS/MS measurement of C17-S1P (refer to Section 3.2.12).

3.2.6 Cell Culture and Differentiation of Primary and 3T3-L1 Adipocytes

Primary Mouse Adipocyte Isolation and Differentiation

Murine primary adipocytes were isolated from mouse gonadal white adipose tissue as described in Weske *et al.*[304] by using a modified protocol by Oeckl *et al.*[305] Initially, the tissue was dissected and washed with PBS, then placed into a 15 mL tube containing 5 mL collagenase solution. The digestion was performed for 1 hour at 37 °C, with the tube being vigorously shaken by hand every 10 minutes. The digested tissue was passed through a 100 µM cell strainer and the tube was rinsed with an equal amount of wash buffer, which was also filtered through the strainer. The cells were then centrifuged at 250 × g for 5 minutes at room temperature. The tube was gently inverted several times before a second centrifugation step was performed. Following this, the fat layer and supernatant were discarded, and erythrocyte lysis was conducted using 1 mL of erythrocyte lysis buffer for 5 minutes at room temperature. The reaction was halted by adding 10 mL of wash buffer and the cells were centrifuged at 500 × g for 5 minutes. The supernatant was removed, cells were resuspended in 10 mL of growth medium, and the cell suspension was filtered through a 40 µM cell strainer before seeding into cell culture plates. Cells were incubated at 37 °C and 5% CO_2 overnight to allow adherence and the medium was changed the following day. Growth medium was changed every other day until cells reached 80%–100% confluency. To initiate differentiation, the medium was changed to double the volume of induction medium. On day 3 of differentiation, the medium was switched to differentiation medium, which was changed every other day until the cells were fully differentiated on day 8. For media and buffer formulations refer to Section 3.1.7.

3T3-L1 Cell Culture and Differentiation

3T3-L1 cell culture and differentiation was performed by Dr. Sarah Weske. The 3T3-L1 preadipocytes were obtained from the European Collection of Cell Culture (86052701, ECACC, Salisbury, UK) and maintained in T-175 flasks containing growth medium at 37 °C, 5% CO_2, and 90% humidity. For the differentiation experiments, the cells were seeded in growth medium onto Cell+ 6-well plates to a density of 96,000 per well. Differentiation was induced when the cells reached 80% confluence by replacing the medium with differentiation medium I. After 2 days, differentiation medium was replaced by differentiation medium II for an additional 2 days. Thereafter, the medium

was changed to growth medium, which was refreshed every two days until cells were fully differentiated on day 14. For details on the composition of the cell culture medium, refer to Section 3.1.7

3.2.7 Lipolysis Assay

The lipolysis assay was performed by Dr. Sarah Weske. Glycerol release from differentiated 3T3-L1 cells and primary adipocytes was measured 16 hours after induction of lipolysis in the presence or absence of 10 µM S1P, 10 µM AUY954, 10 µM CYM5520, 10 µM CYM5541, 1 µM VD-78, or 1 µM isoproterenol. In some conditions, cells were pre-incubated for 1 hour with 3 µM Bisindolylmaleimide I, 10 µM PKCζ pseudo-substrate inhibitor, 25 µM small molecular HSL inhibitor, 10 µM PD98059, 100 nM Wortmannin, 100 µM SQ22536 or 25 µM Fumonisin B1. Following incubation, cell culture supernatants were collected, and 80 µL of supernatant was incubated with 250 µL Hydrazine buffer (for composition see Section 3.1.7) for 2 hours at room temperature. Absorbance was measured at 340 nm using a microplate reader. Glycerol concentrations were determined based on a glycerol standard curve with known glycerol concentrations.

3.2.8 Kinase Assays

In Vitro Kinase Assays with Recombinant or Immunoprecipitated PKCζ

The *in vitro* kinase assay was performed by Lea Esser (Institute of Molecular Medicine I, Heinrich Heine University Düsseldorf). For the *in vitro* kinase assays using recombinant enzyme, 150 ng recombinant human PKCζ protein was incubated with 5 µg recombinant dephosphorylated myelin basic protein (MBP) and 10 µM S1P or methanol (vehicle control) in reaction buffer (for composition see Section 3.1.7) at 30 °C for 30 minutes. The reaction was terminated by the addition of Laemmli sample buffer, and the samples were subjected to SDS-PAGE. Gels were stained with Coomassie brilliant blue, followed by autoradiography.

For assays using immunoprecipitated PKCζ, 250 mg frozen gWAT was homogenized in 2 mL M-PER Mammalian Protein Extraction Reagent + Halt Protease- and Phosphatase Inhibitor Cocktail. Homogenates were incubated on ice for 30 min, then centrifuged at 16,000 × g for 15 minutes. The supernatant was transferred to fresh tubes,

and protein concentration was determined using the BCA protein assay. Immunoprecipitation was carried out overnight at 4 °C using 750 µg of total protein and 10 µg agarose-conjugated PKCζ (H-1) antibody. Beads were washed three times with extraction buffer and centrifuged at 2,000 × g for 1 minute. Kinase assays were then performed as described for recombinant protein.

Multiplex Kinome Activity Profiling

Protein extraction was performed in accordance with the “Protocol for Preparation of Lysates of Tissue sections” by PamGene (PamGene International, ‘s-Hertongenbosch, The Netherlands). Briefly, protein extraction from 10 × 10 µm liver tissue sections per sample on ice was initiated by adding pre-cooled M-PER™ Mammalian Protein Extraction Reagent (100 µL per 60 µm frozen tissue sections), supplemented with Halt™ Protease and Halt™ Phosphatase Inhibitor. The lysis process was facilitated by gently pipetting the mixture up and down ten times every ten minutes during a 30-minute incubation period on ice, ensuring the pipette tip remained in the solution throughout incubation. After 30 minutes, the homogeneity of the lysis was assessed, and if necessary, the mixture was further homogenized using a disposable pestle. Subsequently, the lysates were centrifuged at > 10,000 × g and 4 °C for 15 minutes, and the supernatant of each sample was transferred into several pre-cooled vials. Protein concentration was determined using the BCA assay (3.2.11).

Multiplex kinome activity profiling was conducted by the group of Emiel van der Vorst at the Institute for Molecular Cardiovascular Research (IMCAR, Aachen). The study involved determining protein tyrosine kinases (PTK) and serine- threonine kinase (STK) profiles using the PamChip® microarray platform with the PamStation®12 (PamGene International). This research specifically focuses on STK profiles. For these analyses, 2 µg of protein and 400 µM ATP were applied to the STK-PamChip®, which comprises 144 individual phospho-sites. An antibody mix was also added to detect the phosphorylated Ser/Thr. Following a 1-hour incubation at 30 °C, during which the sample was continuously pumped through the porous material to optimize binding kinetics, phosphorylation intensity was quantified using a secondary FITC-conjugated antibody. A LED imaging system was employed for imaging and background correction, and the spot intensity was quantified using the BioNavigator software (version 6.3, PamGene). Upstream Kinase Analysis (PamGene International) served as a functional scoring method to rank kinases based on combined specificity scores (peptides linked to a

kinase, derived from six databases) and sensitivity scores (treatment-control differences). A heatmap displays the median final scores of kinases that exceed 1.2, with adjusted P-values for multiple comparisons by the false discovery rate (FDR) being less than 0.05.

3.2.9 Quantitative Reverse Transcriptase Polymerase Chain Reaction

RNA-Isolation from Liver Tissue

RNA from liver tissue was isolated using the innuPREP RNA Mini Kit 2.0 according to the manufacturer's instructions. Briefly, 15-20 mg tissue was homogenized in 450 µL lysis buffer RL by using the TissueRuptor II and QIAshredder homogenizer. Afterwards, the homogenized tissue lysate was subjected to the extraction protocol. RNA concentration and purity were measured by NanoDrop One.

Synthesis of First Strand Complementary DNA

Complementary DNA (cDNA) was obtained from extracted RNA via reverse transcription by using the RevertAid TM First Strand cDNA Synthesis Kit. The reaction was performed in a thermocycler using 2000 ng RNA and Oligo(dT)18 primers according to the manufacturer's First Strand cDNA synthesis protocol.

Real-Time Quantitative Polymerase Chain Reaction

Real-time quantitative PCR (qPCR) was performed using PowerTrack™ SYBR Green Mastermix (Thermo Fisher Scientific, Waltham, USA). The individual reactions were prepared as shown in Table 4 and carried out on the CFX96™ Real-Time System (Bio-Rad Laboratories, Hercules, USA) with the thermal profile depicted in Table 5. Table 1 on page 38 provides the sequences of the primers utilized in this study.

Table 4. Reaction mixture for qRT-PCR

Component	Final concentration	Volume
cDNA		1 µL
5' Primer	10 pmol/mL	0.5 µL
3' Primer	10 pmol/mL	0.5 µL
SYBR green powertrack	1X	10 µL
Nuclease-free water		ad 20 µL

Table 5. Thermal profile for qRT-PCR "Fast cycling mode"

Step	1 Enzyme activation	2 Denaturation	3 Annealing/ Extension	4 Step to 65 °C	5 Melting curve
Temperature (°C)	95.0	95.0	60.0	65.0	65.0 – 95.0
Time (min)	2:00	0:05	0:30	0:05	0.5 °C/s
Number of cycles	1x	40x		1x	

3.2.10 RNA Sequencing

Sample Preparation

To prepare samples for RNA-sequencing (RNA-seq), total RNA was extracted from liver tissue as described in Section 3.2.9. Additionally, a DNA digestion step was performed to remove potential DNA contaminations using the innuPREP DNase I Digest Kit which is embedded in the first washing step of the RNA isolation protocol.

Quality Control and 3'Prime RNA Sequencing

RNA-seq, including initial quality control and first-level analysis of the sequencing data, was performed by the team at the Genomics & Transcriptomics Laboratory (GTL) from Biologisch-Medizinisches Forschungszentrum (BMFZ) of the Heinrich Heine University Düsseldorf.

Total RNA quantification was performed by fluorometric measurements with the Qubit device and the RNA High Sensitivity assay (Thermo Fisher Scientific Inc., MA, USA). RNA integrity was assessed via capillary electrophoresis using the Fragment Analyzer and the DNF-471 Total High Sensitivity Assay (Agilent Technologies Inc., Santa Clara, USA). Only samples with an RNA Quality Number (RQN) within the acceptable range (7.4–9.5) were selected for library preparation.

For library preparation, 50 ng of total RNA per sample was processed according to the manufacturer's protocol using the QuantSeq 3' mRNA-Seq V2 Library Prep Kit with UDI and UMI Second Strand Synthesis Module for QuantSeq FWD (Lexogen GmbH, Vienna, Austria). The resulting libraries were bead-purified, normalized, and subjected to 3'-mRNA sequencing on the NextSeq2000 system (Illumina Inc., SD, USA), using single-end sequencing with a read length of over 75 base pairs. Each sample generated an output of approximately 5 million reads. Conversion of raw sequencing data (bcl files) to fastq format, adapter trimming, and demultiplexing were performed using the bclconvert tool.

Data Processing and Initial Statistical Analysis

Fastq files were processed using CLC Genomics Workbench (version 24.0.1, QIAGEN, Venlo, NL). The first UMI tag was extracted from all reads and annotated accordingly, while reads lacking UMI were discarded. Adapter sequences and low-quality bases were trimmed using default parameters, removing bases below Q13 from the read ends and allowing a maximum of two ambiguous nucleotides. The filtered reads were mapped to the reference genome GRCm39 (*Mus musculus*). Samples were grouped based on their experimental conditions and biological replicates (n=4) before performing multigroup comparisons. Differential expression analysis was conducted using the built-in RNA-seq analysis workflow in CLC, and p-values were adjusted for multiple testing using both the false discovery rate (FDR) and Bonferroni correction.

Visualization and Functional Assessment of RNA Sequencing Data

The results of the differential expression analysis were visualized using Principal Component Analysis (PCA), as a heatmap that included only genes with Bonferroni-corrected p-values <0.05 and a fold change (FC) > 1.5, or as volcano plots displaying log2 fold changes (> 1.5) against –log10 of FDR-adjusted p-values (FDR p-value <0.05). Further data processing was performed using the Gene Set Enrichment Analysis (GSEA) software, following the standard parameters recommended in the software's guidelines. GSEA was conducted using the GOCC_LIPID_DROPLET gene set from the Molecular Signatures Database (MSigDB) and a custom gene set comprising genes associated with MASLD.[306] The results were visualized as normalized enrichment plots using R (version 4.2.2) with the clusterProfiler and enrichplot packages.

3.2.11 Protein Analyses

Protein Extraction from Tissue

Protein extraction from 15 mg liver and 40 mg gWAT tissue was achieved by homogenization in 500 µL RIPA buffer (see Section 3.1.7) using the TissueRuptor II. Afterwards, samples were centrifuged (max. speed, 4 °C, 5 min). Protein concentration of the supernatant was determined using the microplate-based Thermo Scientific™ Pierce BCA Protein Assay Kit and the standard protocol with a working range of 25 to 2,000 µg/mL. The protein concentration was then detected by OD determination at 562 nm in a plate reader.

SDS-PAGE

Extracted proteins from gWAT and liver were separated by sodium dodecyl sulfate-polyacrylamide gel electrophoresis (SDS-PAGE). A sample of 25 µg protein for liver and 30 µg for gWAT was prepared using 4x Laemmli buffer and ddH_2O, boiled at 95 °C for 5 min, and subsequently loaded on a 1.5 mm 4–20% gel. Depending on the experiment, either the Precision Plus Protein Dual Color Standard or the Cozy™ Hi Prestained Protein Ladder was used as a molecular weight standard. The electrophoresis was carried out in Running buffer (see Section 3.1.7) at constant voltage of 70 V for 30 min, followed by 130 V, until the dye front reached the end of the gel.

Western Blot

Proteins were transferred to a polyvinylidene difluoride membrane (PVDF; Merck Millipore, Burlington, USA) using a wet blot method. The transfer was conducted for 16 hours at a constant voltage of 30 V and 4 °C in a transfer buffer (see Section 3.1.7). Afterwards, the blotting construction was disassembled, and membrane was briefly washed in Wash buffer (see Section 3.1.7), followed by blocking in 5% non-fat dried milk powder in Wash buffer for 1 hour. After blocking, membrane was washed (3×10 min) in Wash buffer and subsequently incubated with primary antibody diluted in 5% BSA in Wash buffer overnight at 4 °C sealed with parafilm. The following day, the membrane was washed (3×10 min) in PBS-T and afterwards incubated with secondary antibody diluted in 0.5% non-fat dried milk powder in Wash buffer at room temperature for 1 hour. Subsequently, the membrane was washed (3×10 min) in Wash buffer. Development of the membrane was performed using 500 µL Immobilon Forte Western HRP-Substrate and imaging on a ChemiDoc XRS (Bio-Rad Laboratories, Hercules, USA). The primary and secondary antibodies as well as used dilutions of this study are listed in Section 0.

3.2.12 LC-MS/MS

Liquid Sample Preparation for LC-MS/MS Measurements

Lipids were extracted from plasma using methanol precipitation. Plasma samples (e.g. 50 µL) were diluted 1:10 with distilled methanol (LCMS grade). An internal standard (10 µL) was added, and the samples were precipitated at -80 °C. After overnight precipitation, the tubes were centrifuged at the maximum speed (21,460 × g) for five

minutes at 4 °C. The supernatant was transferred into 1.5 mL LCMS-certified glass vials with a screw neck, and the samples were stored at -80 °C until measurement.

Tissue Sample Preparation for LC-MS/MS Measurements

For lipid measurements in liver and gWAT tissue, about 5 mg and 25 mg , respectively, was supplemented with 500 µL distilled methanol (LCMS grade) and 10 µL of internal standard. The tissue was homogenized using the TissueRuptor II, and the resulting homogenates were added to 1 mL and subjected to methanol precipitation overnight at -80 °C. After precipitation, the tissue homogenate was centrifuged at the maximum speed (21,460 × g) and 4 °C for five minutes and the supernatant was transferred into a new vial. Following evaporation in a SpeedVac at 16 bar for 60 to 90 minutes, the residue was dissolved in 300 µL distilled methanol by vortexing at 2,400 rpm. The dissolved sample was transferred into 1.5 mL LCMS-certified glass vials with a screw neck, and the samples were stored at -80 °C until measurement.

Derivatization of Fatty Acids with Dansyl Hydrazine

Prior to measurement, fatty acids were derivatized with dansyl hydrazine in acetonitrile (ACN) to enhance ionization efficiency. To achieve this, 20 – 300 µL aliquots yielding 1-2 mg of tissue were taken from LC-MS/MS samples prepared as described above. The remaining methanol contained in the sample aliquots was evaporated using the SpeedVac. To ensure derivatization quality, an external standard prepared in serial dilution (10 nM, 30 nM, 0.1 µM, 0.3 µM, 1 µM, 3 µM, 10 µM and 30 µM) was derivatized in parallel with the samples. Samples were redissolved in 170 µL distilled ACN and vortexed for 2 minutes. Derivatization of the samples was carried out by adding 30 µL dansyl hydrazine (75 mM in ACN, 2.25 µmol, 1.50 equiv.), 30 µL HATU (51 mM in ACN, 1.00 equiv.), and 30 µL triethylamine (3 mM in ACN) followed by a two-hour incubation at room temperature under continuous agitation. Afterwards, 3 µL formic acid (79.5 µmol, 1.56 equiv.) was added followed by a second incubation step for 30 minutes under continuous agitation. Then, the organic solvent was evaporated using the SpeedVac before the residue was dissolved by adding 300 µL distilled ACN. The samples were vortexed and transferred into LCMS-certified glass vials with an inlay and a screw neck and stored at -80 °C until measurement.

LC-MS/MS Measurements

LC-MS/MS measurements were performed by Dr. Philipp Wollnitzke. Sphingolipids, phospholipids, and fatty acids were detected through positive electrospray ionization (ESI) or atmospheric pressure chemical ionization (APCI) depending on method of measurement using and LCMS-8050 triple quadrupole mass spectrometer connected to a Dual Ion Source and a Nexera X3 front-end-system. The ion source and gas settings were as follows: Interface Temperature: 300 °C, Desolvation Temperature: 526 °C, DL temperature: 250 °C, and Heat Block Temperature: 400 °C. For detailed account of the configuration options for each measuring procedure see table below.

Table 6. LC-MS/MS configuration

	S1P/Sph	Cer	LPC/PC/SM	FFA
Interface	ESI	APCI	ESI	ESI
Nebulizing gas flow (L/min)	3	2.4	2	3
Heating gas flow (L/min)	10	3	10	10
Drying gas flow (L/min)	10	3	10	10

Gradient separation of lipids was carried out with Nexera X3 UHPLC system from Shimadzu Deutschland GmbH. High-performance liquid chromatography (HPLC)/Chromatographic separation was performed with varying columns in accordance with the specific measurement method. Appendix Table 1 provides a comprehensive overview of the mobile phase utilized for each method, including the corresponding gradient settings for gradient elution, flow rate, injection volume and oven temperature.

LC-MS/MS Data Analysis and Quantification

Multiple Reaction Monitoring (MRM) was used to collect data for further qualitative analysis and quantification. External standard curves were generated by measuring increasing amounts of analyte (for details on internal and external standards, see Appendix Table 2). The fragment ions (m/z) used for each analyte are listed in Appendix Table 3. Linear regression analysis was used to determine standard curve linearity and correlation coefficients. Peak areas were normalized to the corresponding internal standard peak areas and external standard curve. All LC-MS/MS analyses were performed using LabSolutions 5.114 and analyzed using LabSolutions Insight (Shimadzu, Kyoto, Japan). The initial data analysis was performed by Dr. Philipp Wollnitzke. Additional processing of the collected data was performed using Excel.

3.2.13 Sphingomyelin Synthase Activity Assay

The activity of sphingomyelin synthase was assessed using a modified method previously described by Jiang and colleagues.[298] In this procedure, liver tissue was homogenized in homogenization buffer (see Section 3.1.7). Subsequently, the homogenate was centrifuged at 3,000 × g for 10 minutes and the protein content of the supernatant was determined using the BCA assay. Next, 100 µg protein of each tissue sample was prepared in 10x reaction buffer (see Section 3.1.7) containing 30 µM C2-ceramide (20:0 - 18:1/2:0), 50 µM PC (36:1 - 18:1/18:0) with ddH2O to a final reaction volume of 600 µL. Optionally, adjusted C2-ceramide concentrations or SMS2 inhibitor LY93 may be added to the reaction mixture. The samples were then incubated at 37 °C for 1 hour with continuous gentle shaking. The reaction was terminated by the addition of 800 µL distilled chloroform/methanol (2:1/v:v) plus 10 µL ISTD and vigorous vortexing. To initiate phase separation, the samples were centrifuged at 7,200 × g for 10 minutes, and the organic phase was transferred to a new tube. Finally, the samples were concentrated by vacuum centrifugation and redissolved in 300 µL distilled methanol before being transferred into 1.5 mL LCMS certified glass vials with an inlay and screw neck and stored at -80 °C until analysis. The C2-SM content in the samples was determined using the LC/MS-MS protocol for LPC, PC, and SM measurements. This content was subsequently normalized to LPC 17:0, as its retention time was the closest and the transition is also identical. Conclusions regarding the activity of sphingomyelin synthase were derived through a comparative analysis with the respective control groups.

3.2.14 Statistics

Data are presented as mean ± standard deviation (SD). Statistical analysis was performed using a two-tailed Student's *t*-test (paired or unpaired), one-way ANOVA, or two-way ANOVA followed by appropriate post hoc tests using GraphPad Prism® 10. Statistical significance was set at $P \leq 0.05$. Further information regarding the statistical data is available in the respective caption.

4 Results

4.1 A Global Knockout of Sphingosine Kinase 2, but Not 1, Mitigates the Metabolic Phenotype Induced by a High-Fat Diet

An initial approach for understanding the role of sphingolipids in the common symptoms of MetS, particularly obesity and MASLD, involves examining the influence of S1P-producing enzymes SphK1 and SphK2, as well as the alterations in the plasma and liver sphingolipidome associated with the knockout of these enzymes.

To investigate the effect of a high-fat diet (HFD; 60% kcal from fat) on mouse strains with different sphingolipid profiles, male SphK1 and SphK2 knockout (SphK1$^{-/-}$ and SphK2$^{-/-}$) mice, along with their corresponding controls (wild-type C57BL/6J mice also referred to as WT), were fed either a HFD or normal chow diet (NC) for 12 weeks. At the end of the 12-week period, mice were euthanized after an overnight fast, and blood, liver and adipose tissues, specifically gWAT and iWAT, were collected.

4.1.1 SphK2-Deficient Mice Are Protected from High-Fat Diet-Induced Fat Deposition and Metabolic Dysfunction

To evaluate the metabolic phenotype and differentiate between diet-induced effects and genotype-specific variations, control groups of all genotypes were maintained on a NC diet. SphK2$^{-/-}$ mice exhibited a significantly lower body weight at both the start and end of the experiment compared to the remaining two groups, as confirmed by a separate analysis using one-way ANOVA with Tukey's post hoc test for multiple comparisons. This observation did not extend to the liver, gWAT, and iWAT weight parameters of NC-fed mice. However, the gWAT of SphK1$^{-/-}$ mice was significantly increased compared to both other groups (Figure 4).

Following the administration of a high-fat diet, both WT and SphK1$^{-/-}$ mice exhibited a 30% increase in body weight (Figure 4a). In contrast, SphK2-deficient mice did not exhibit any increase in body weight despite being subjected to a high-fat diet for 12 weeks (Figure 4b). While the livers of SphK1$^{-/-}$ mice exhibited a modest increase in weight upon HFD, no such changes in liver weight were noted in the other mouse strains (Figure 4c). Consistent with body weight observations, SphK2$^{-/-}$ did not demonstrate an HFD-induced increase in adipose tissue mass in two representative fat depots, gWAT and iWAT. Both fat depots showed an increase in mass of up to 4.9- and

2.8-fold, respectively, in both WT and SphK1$^{-/-}$ mice (Figure 4d+e). Notably, SphK1$^{-/-}$ mice on a control diet display a 40% higher fat mass compared to WT controls.

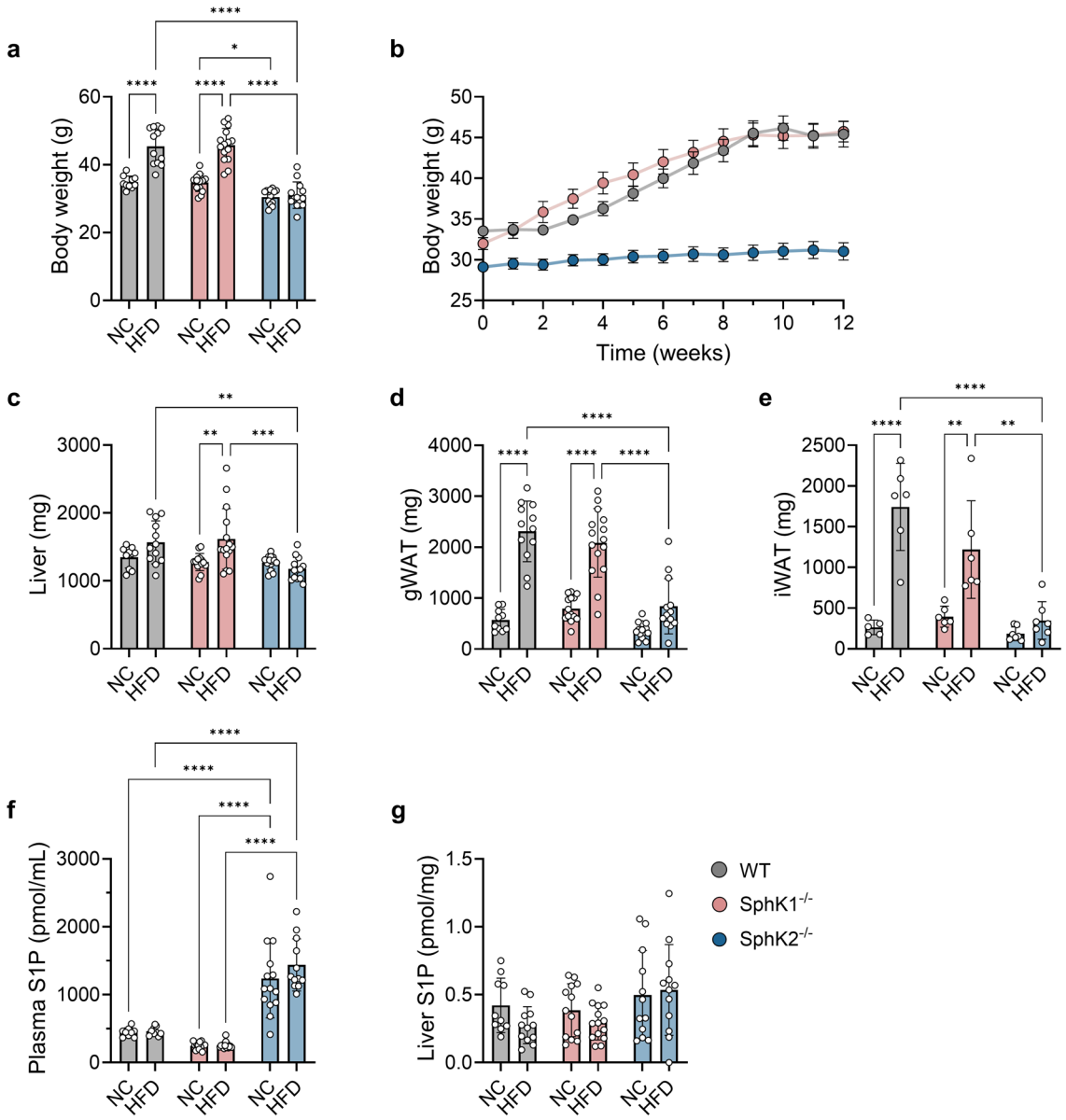

Figure 4. SphK2 knockout mice are protected from diet induced weight gain. WT, SphK1$^{-/-}$ and SphK2$^{-/-}$ mice were fed either a NC or high-fat diet (60% kcal from fat) for 12 weeks. Mice were sacrificed after an overnight fast. (a) Final body weight of all groups. (b) Body weight development of HFD-fed mice over 12 weeks. Organ weights of (c) liver, (d) gWAT, and (e) iWAT (n = 5–7 per group). LC-MS/MS measurements of S1P levels in (f) plasma and (g) liver. Data are presented as mean ± SD. n_{WT+NC} = 9–10, n_{WT+HFD} = 9–12, $n_{SphK1^{-/-}+NC}$ = 13–14, $n_{SphK1^{-/-}+HFD}$ = 14–15, $n_{SphK2^{-/-}+NC}$ = 12–14, $n_{SphK2^{-/-}+HFD}$ = 12–13 unless otherwise stated. Statistical analysis was performed using two-way ANOVA with Tukey's post hoc test for multiple comparisons. Statistical significance is indicated as follows: * p <0.05, ** p <0.01, *** p <0.001, **** p <0.0001.

To assess the impact of global deletion of SphK1 or SphK2 on sphingolipid metabolism, particularly S1P synthesis, LC-MS/MS analyses were performed (Figure 4f+g). SphK1-deficient mice showed a slight reduction in plasma S1P levels, whereas SphK2$^{-/-}$ mice

exhibited pronounced, diet-independent increases of 2.8-fold. The association between SphK2 deficiency and elevated plasma S1P levels is well documented.[174,176] Conversely, hepatic S1P levels remained unchanged in both knockout models.

Following the significant accumulation of adipose tissue observed in both representative fat depots under HFD conditions, an analysis of liver tissue was conducted to assess lipid deposition. Histological examination of H&E-stained liver sections revealed evident lipid deposition in livers from HFD-fed WT and SphK1$^{-/-}$ mice (Figure 5a+b). In contrast, SphK2$^{-/-}$ mice subjected to a HFD did not demonstrate an increase in fat vacuole area.

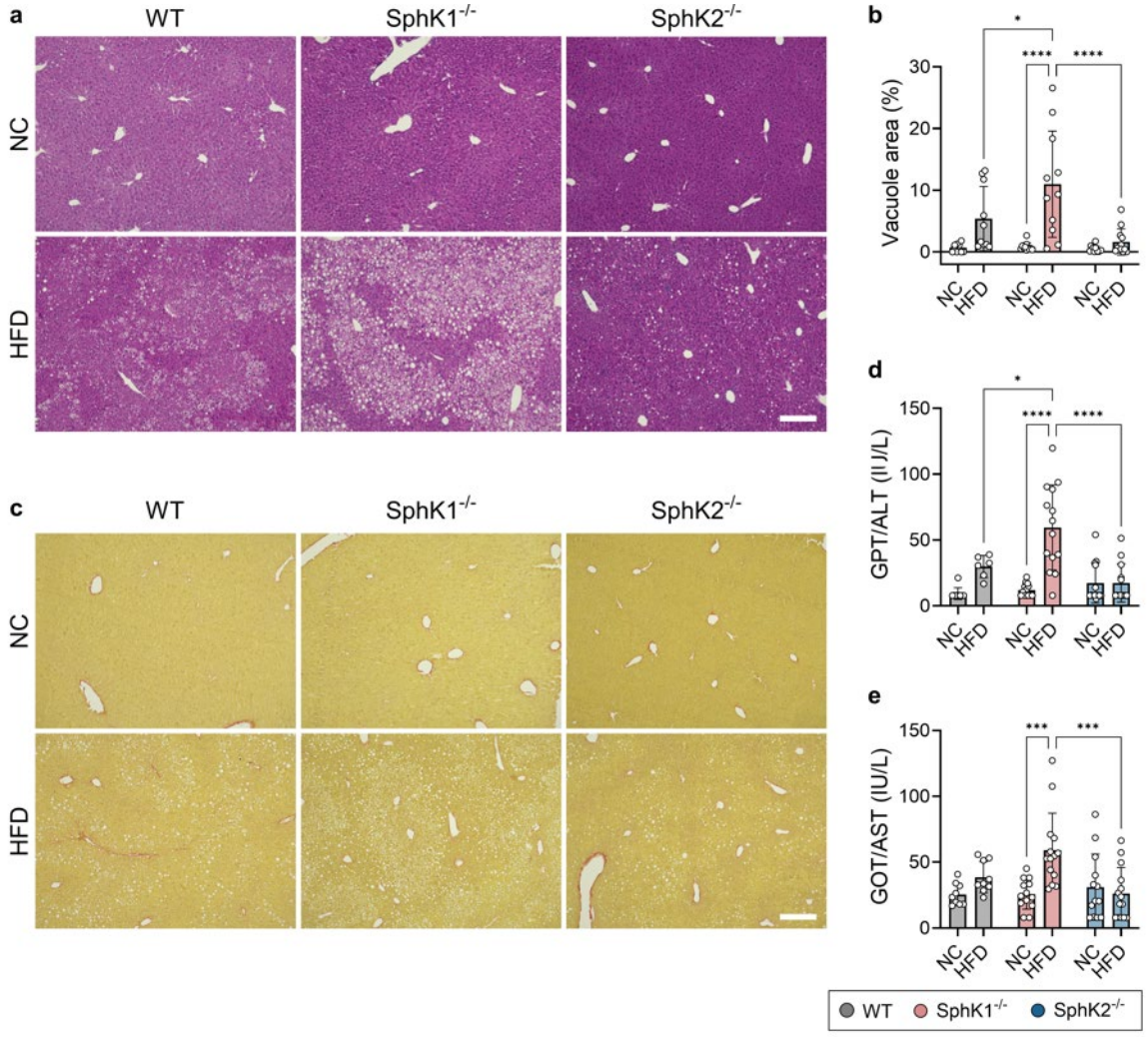

Figure 5. Hepatic lipid accumulation is reduced in livers of SphK2$^{-/-}$ mice. WT, SphK1$^{-/-}$ and SphK2$^{-/-}$ mice were fed NC or HFD for 12 weeks. (a) Representative H&E-stained liver sections (scale bar: 200 µM) and (b) quantification of vacuole area per total area. (c) Sirius Red staining of representative liver sections from all groups (scale bar: 200 µM). Plasma levels of (d) GOT/AST and (e) GPT/ALT. Data are presented as mean ± SD. n_{WT+NC} = 9–10, n_{WT+HFD} = 9–11, $n_{SphK1^{-/-}+NC}$ = 11–13, $n_{SphK1^{-/-}+HFD}$ = 11–14, $n_{SphK2^{-/-}+NC}$ = 12–13, $n_{SphK2^{-/-}+HFD}$ = 12–14. Statistical analysis was performed using two-way ANOVA with Tukey's post hoc test for multiple comparisons. Statistical significance is indicated as follows: * p <0.05, ** p <0.01, *** p <0.001, **** p <0.0001.

Sirius Red staining of liver sections was conducted to evaluate fibrotic changes in hepatic tissue, revealing an absence of fibrotic lesions irrespective of genotype or dietary conditions (Figure 5c). Relevant plasma parameters indicative of liver damage, specifically GOT/AST and GPT/ALT, were measured, showing an elevation in SphK1$^{-/-}$ mice fed an HFD, whereas WT and SphK2$^{-/-}$ mice did not exhibit a significant increase in liver injury markers.

Given the frequent co-occurrence of obesity with T2D, fasting blood glucose levels were assessed prior to conducting an ipGTT. Elevated fasting blood glucose levels were observed in both the HFD-fed WT and SphK1$^{-/-}$ mice, whereas the SphK2$^{-/-}$ mice did not exhibit such elevations (Figure 6a).

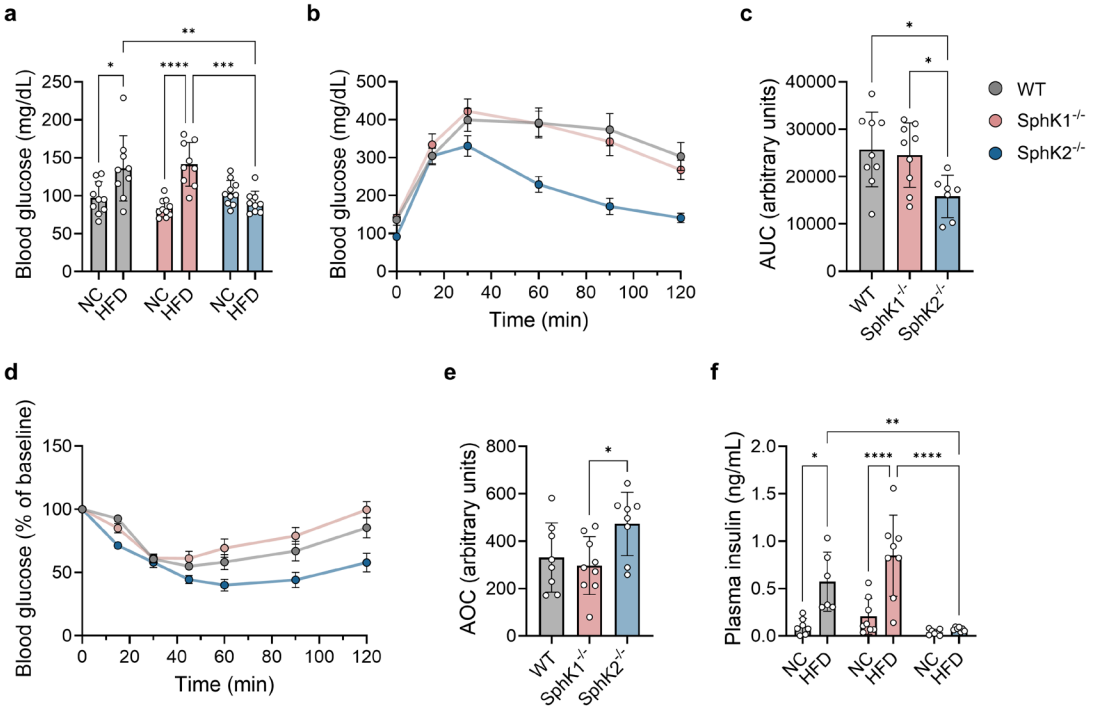

Figure 6. SphK2-deficient mice display improved glucose tolerance and insulin sensitivity. WT, SphK1$^{-/-}$ and SphK2$^{-/-}$ mice were fed NC or HFD for 12 weeks. (a) Fasting blood glucose levels. (b) Intraperitoneal glucose tolerance test (ipGTT) at 10 weeks of HFD using a glucose dose of 2 mg/kg with quantification of (c) area under curve (AUC). (d) Intraperitoneal insulin tolerance test (ipITT) at 11 weeks of HFD mice using an insulin dose of 1 U/kg with quantification of (e) area over curve (AOC). (f) Fasting plasma insulin levels. Data are presented as mean ± SD. n_{WT+NC} = 7–10, n_{WT+HFD} = 6–9, $n_{SphK1^{-/-}+NC}$ = 8–10, $n_{SphK1^{-/-}+HFD}$ = 8–9, $n_{SphK2^{-/-}+NC}$ = 7–10, $n_{SphK2^{-/-}+HFD}$ = 7–9. Statistical analysis was performed using one-way or two-way ANOVA followed by Tukey's post hoc test for multiple comparisons. Statistical significance is indicated as follows: * p <0.05, ** p <0.01, *** p <0.001, **** p <0.0001.

In contrast, no significant changes were detected in groups maintained on a normal chow diet. This observation aligns with the enhanced glucose tolerance observed in the SphK2$^{-/-}$ mice compared with the WT and SphK1$^{-/-}$ mice on HFD (Figure 6b+c).

Mice on the control diet demonstrated comparable glucose tolerance across all groups (Appendix Figure 2a, page 145).

To comprehensively assess the metabolic phenotype, an ipITT was performed to examine changes in peripheral insulin sensitivity. Prior to the ipITT, mice were subjected to a four-hour fasting period. Among all groups fed an HFD, SphK2$^{-/-}$ mice exhibited significantly enhanced insulin tolerance compared to SphK1$^{-/-}$ mice (Figure 6d+e). Furthermore, all strains of mice on a control diet displayed comparable levels of insulin tolerance (Appendix Figure 2b, page 145).

Consequently, fasting plasma insulin levels were assessed at the end of the 12-week feeding period. The results indicated a significant increase in insulin levels in both the WT and SphK1$^{-/-}$ groups subjected to a high-fat diet (HFD), whereas SphK2$^{-/-}$ mice maintained low insulin levels (Figure 6f).

These findings collectively suggest that the global knockout of SphK2 provides protection against DIO and the progression of hepatic steatosis. This is further supported by the observation that these animals do not exhibit a diabetic phenotype, but instead show enhanced glucose tolerance and insulin sensitivity under HFD conditions.

4.1.2 Genetic Interventions in the Sphingolipid Metabolism Result in Distinct Sphingolipid Profiles

Sphingolipid concentrations in plasma and liver were assessed through LC-MS/MS analysis, revealing distinct sphingolipidomic patterns dependent on genotype and diet (Figure 7a). In a more detailed examination, not only S1P (Figure 4f) but also sphingosine levels were found elevated to be elevated in plasma. Plasma sphingosine levels were elevated 3-fold, with an additional increase in Sph levels observed upon HFD in both kinase-deficient strains, but not in WT, where levels were significantly reduced (Figure 7b). Furthermore, Sph levels in the livers of SphK2$^{-/-}$ mice demonstrated an increase of at least 7-fold compared to the livers of SphK1$^{-/-}$ and WT mice (Figure 7c). Hepatic ceramide levels in SphK2$^{-/-}$ mice exhibited 5.3-fold and 3.7-fold higher levels under NC and HFD conditions, respectively, in comparison to WT (Figure 7d). In SphK1$^{-/-}$mice subjected to HFD, total SM level in the liver were reduced upon HFD. Similarly, hepatic SM level in SphK2$^{-/-}$ were also lower under HFD conditions, corresponding with the observed reduced hepatic ceramide levels during HFD (Figure 7e).

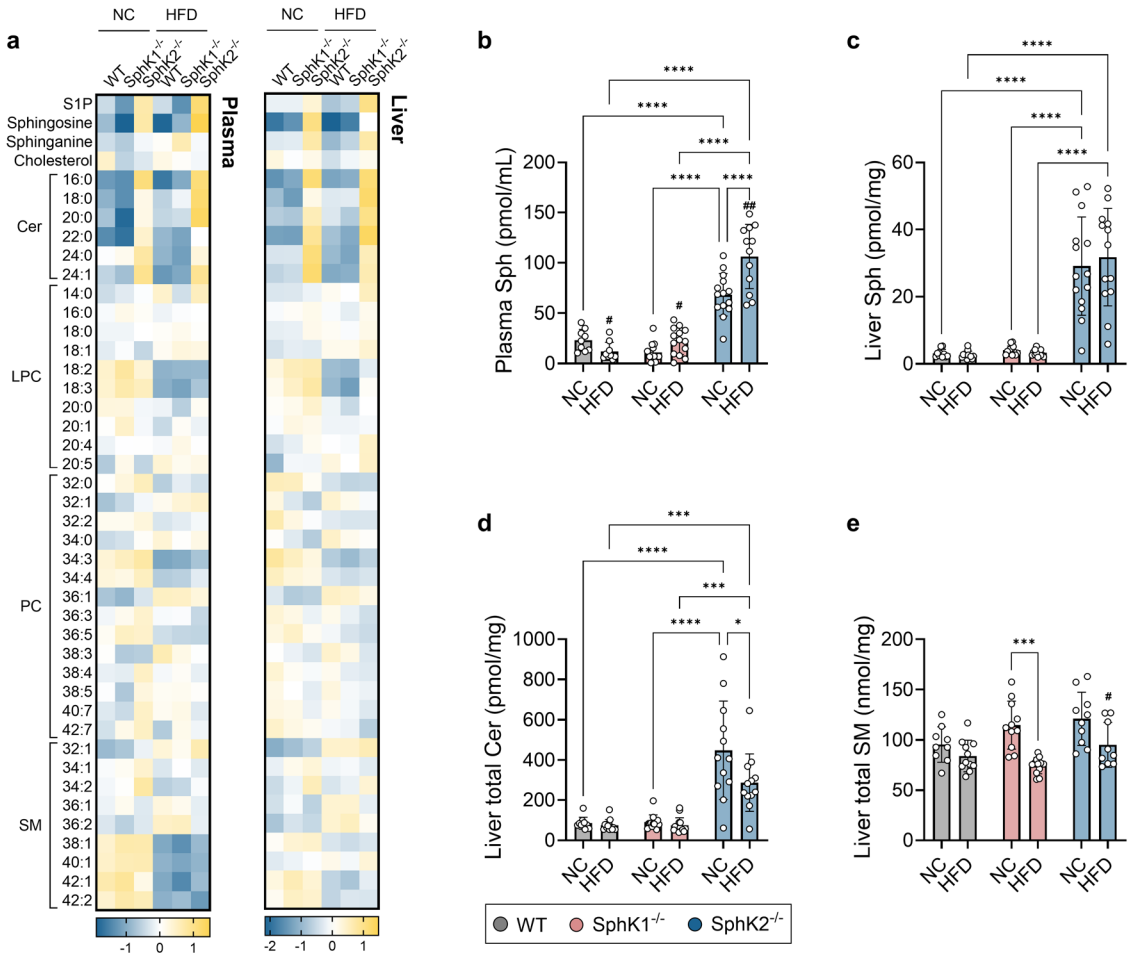

Figure 7. Diet- and genotype-dependent alterations in lipidomic profiles. WT, SphK1$^{-/-}$ and SphK2$^{-/-}$ mice were fed NC or HFD for 12 weeks. LC-MS/MS analysis was performed in plasma and liver tissue. (a) Heatmaps of selected lipid species in plasma and liver. Levels of (b) plasma sphingosine, (c) liver sphingosine, (d) liver ceramide, and (e) liver sphingomyelin. Data are presented as mean ± SD. n_{WT+NC} = 9–10, n_{WT+HFD} = 9–12, $n_{SphK1^{-/-}+NC}$ = 11–13, $n_{SphK1^{-/-}+HFD}$ = 12–14, $n_{SphK2^{-/-}+NC}$ = 10–14, $n_{SphK2^{-/-}+HFD}$ = 9–13. Statistical analysis was performed using two-way ANOVA followed by Tukey's post hoc test for multiple comparisons. Statistical significance is indicated as follows: * p <0.05, *** p <0.001, **** p <0.0001. Additional pairwise comparisons between grouped bars were analyzed using paired, two-tailed t-tests and are indicated with: # p <0.05, ## p <0.01.

Total ceramide and SM levels were quantified across defined acyl-chain lengths (C16:0, C18:0, C20:0 C22:0, C24:0, and C24:1), encompassing long- and very-long-chain species. Figure 8 (page 71) displays chain length-resolved hepatic ceramide and SM levels.

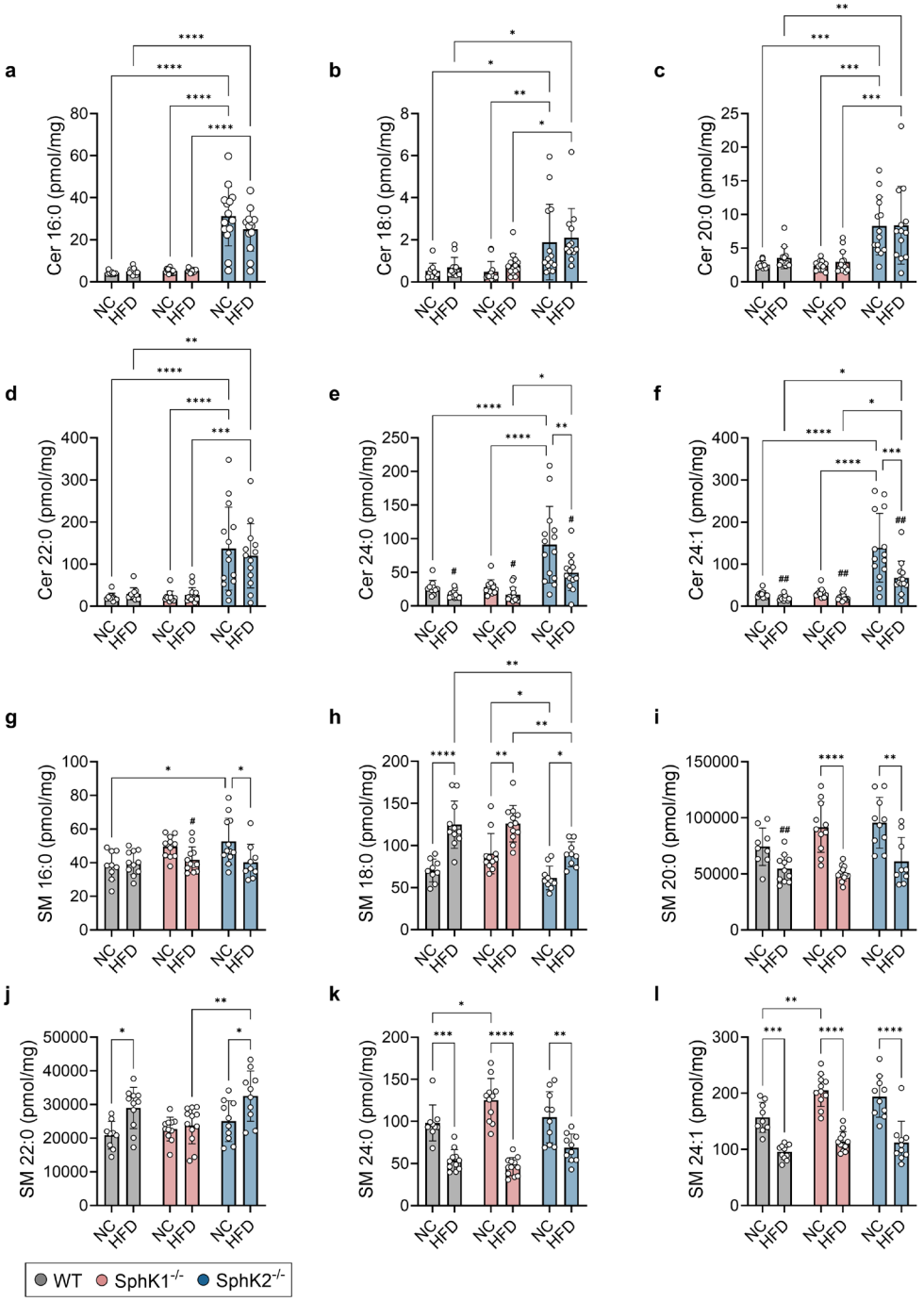

Figure 8. SphK2$^{-/-}$ mice exhibit higher hepatic ceramide levels. WT, SphK1$^{-/-}$ and SphK2$^{-/-}$ mice were fed NC or HFD for 12 weeks. LC-MS/MS analysis was performed on liver tissue. Ceramide levels were measured for individual long-chain fatty acid (LCFA) species (a) C16:0, (b) 18:0, (c) C20:0, and (d) C22:0 as well as very long-chain fatty acid (VLCFA) species (e) 24:0, and (f) 24:1. SM levels were measured for individual LCFA species (g) C16:0, (h) 18:0, (i) C20:0, and (j) C22:0 as well as VLCFA species (k) 24:0, and (l) 24:1. Data are presented as mean ± SD. n_{WT+NC} = 10, n_{WT+HFD} = 12, $n_{SphK1^{-/-}+NC}$ = 11–13, $n_{SphK1^{-/-}+HFD}$ = 12–14, $n_{SphK2^{-/-}+NC}$ = 12–14, $n_{SphK2^{-/-}+HFD}$ = 9–13. Statistical analysis was performed using two-way ANOVA followed by Tukey's post hoc test for multiple comparisons. Statistical significance is indicated as follows: * p <0.05, ** p <0.01, *** p <0.001, **** p <0.0001. Additional pairwise comparisons between grouped bars were analyzed using paired t-tests and are indicated with: # p <0.05, ## p <0.01.

Elevated ceramide levels, particularly of those containing long-chain fatty acids (LCFA) such as C16:0 and C22:0, were detected in the livers of SphK2$^{-/-}$, but not SphK1$^{-/-}$ or WT mice, fed a control diet. The LCFA concentrations were observed to be up to 7.8- and 6.5-fold higher, respectively, compared to WT mice (Figure 8a-d). Notably, no HFD-dependent increase in ceramide levels was observed across all groups. Conversely, ceramides containing very-long chain fatty acids (VLCFA), namely C24:0 and C24:1, exhibited an increase of 3.3- and 4.9-fold, respectively, in the livers of SphK2$^{-/-}$ mice compared the WT group on a normal chow diet (Figure 8e+f). The observed increase was mitigated by a reduction attributable to HFD, which was consistent across all groups. However, levels in SphK2$^{-/-}$ mice consistently exceeded those in WT and SphK1$^{-/-}$ mice.

Hepatic levels of SM species bearing C16:0 and C20:0 acyl chains (Figure 8g+i), as well as VLCFA ceramides C24:0 and 24:1 (Figure 8k+l), were reduced by HFD across nearly all genotypes. Conversely, hepatic SMs with acyl chain lengths of 18:0 and 22:0 were increased (Figure 8h+j).

However, VLCFA levels of SM 36:1 (18:1/18:0) were lower in the livers of SphK2$^{-/-}$ mice on a HFD compared to those in WT and SphK1$^{-/-}$ mice. For SMs with fatty acid chains of 20:0 and longer, a decrease was also observed in the plasma (Figure 7a). Despite the diet-specific alterations in the SM levels, it is noteworthy that the total concentration of SMs in the liver was consistent for all three groups (Figure 7e, page 70).

In summary, in addition to some diet-specific changes, the global deficiency of sphingosine kinases, particularly in the SphK2$^{-/-}$ mice, is the primary cause of altered sphingolipid profiles. Of note are the increases in sphingosine and various ceramide species observed in both plasma and liver in SphK2$^{-/-}$ mice, along with the lack of HFD-induced ceramide elevation, despite pronounced obesity and MASLD in WT controls.

4.1.3 SphK2 Deficiency Modulates Hepatic Transcriptome and Suppresses MASLD-Associated Responses

To get further insight into the phenotypic variations observed, liver gene expression patterns were examined through RNA-seq. With this approach, transcriptional alterations influenced by genotype and treatment, that might reveal pathways that are potentially involved, should be identified.

Principal component analysis of the six experimental groups, comprising three genotypes under two dietary conditions, revealed that the samples clustered according to their respective group (Figure 9a). Interestingly, while most groups exhibited distinct separation in the PCA, the WT NC, SphK2$^{-/-}$ NC, and SphK2$^{-/-}$ HFD groups formed an overlapping cluster. This suggests shared underlying biological characteristics across both genotype and dietary conditions.

A heatmap depicts the top 50 differentially expressed genes, identified through ANOVA analysis and Bonferroni correction, between the livers of NC- and HFD-fed SphK2$^{-/-}$ and WT mice (Figure 9b). Distinct clustering patterns between NC and HFD in the livers of WT mice indicate a HFD-induced response. In contrast, no such clustering difference is observed for SphK2$^{-/-}$ mice, suggesting that the HFD-induced effect is attenuated or absent. The SphK2$^{-/-}$ group closely aligns with both untreated groups, reflecting a similar expression profile.

Gene Set Enrichment Analyses (GSEA) was conducted to compare the HFD treatment effects between the SphK2$^{-/-}$ and WT groups (Figure 9c). A negative enrichment of the GOCC_LIPID_DROPLET gene set with a normalized enrichment score (NES) of -1.48, highlighted a WT-specific transcriptional response, contrasting with SphK2$^{-/-}$ mice. To further explore phenotypic differences, GSEA was performed using a gene set comprising genes upregulated in fatty livers of mice (Figure 9d).[306]

The analysis revealed a significant negative enrichment (NES = -1.89), indicating that this gene set is underrepresented in SphK2$^{-/-}$ livers compared to WT. Upregulated and downregulated genes from this gene set are depicted in green and red, respectively, in a volcano plot visualizing differentially expressed genes (grey, red, green) filtered for a false discovery rate (FDR) < 0.05 and fold change > 1.5. (Figure 9e).

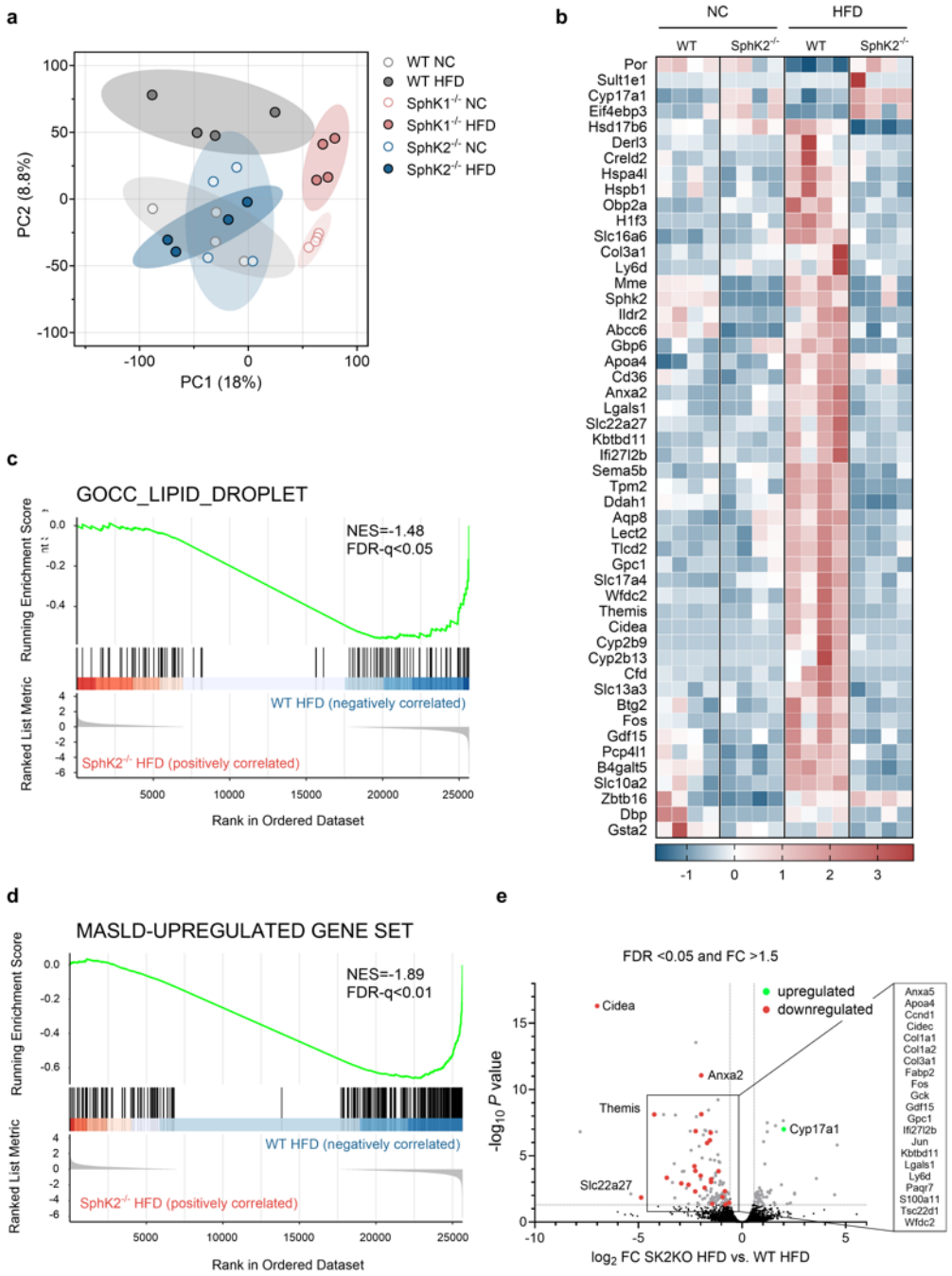

Figure 9. SphK2 deficiency is associated with negative enrichment of lipid-associated gene signatures under high-fat diet conditions. WT, SphK1$^{-/-}$ and SphK2$^{-/-}$ mice were fed either NC or HFD for 12 weeks RNA-seq of total RNA from moue liver tissues of all groups (n = 4 per group) was performed by the Genomics & Transcriptomics Laboratory (GTL) of the Heinrich Heine University. (a) Principal component analysis (PCA) based on variance-filtered TPM (transcripts per million) values. (b) Heatmap of Bonferroni-corrected differentially expressed genes in SphK2$^{-/-}$ and WT livers from both NC- and HFD-fed mice. (c) Gene set enrichment analysis (GSEA) of the GOCC_LIPID_DROPLET gene set comparing SphK2$^{-/-}$+HFD to WT+HFD. (d) GSEA of fatty liver disease-associated genes comparing SphK2$^{-/-}$+HFD to WT+HFD. (e) Volcano plot of differentially expressed genes comparing SphK2$^{-/-}$+HFD to WT+HFD. Grey, red, and green dots indicating significantly regulated genes (FDR <0.05, fold change > 1.5); green and red dots represent upregulated and downregulated genes from the “NAFLD gene set”, respectively; black dots represent non-significant genes. NES, normalized enrichment score; FDR-q, FDR-corrected p-value; FC, fold change.

The RNA-seq analysis comparing hepatic gene expression profiles between the HFD-fed SphK2$^{-/-}$ group and the HFD-fed WT control group demonstrated a negative enrichment of gene sets associated with lipid deposition and MASLD-related genes.
The RNA-seq analysis identified distinct gene expression profiles between the HFD-fed SphK2$^{-/-}$ and control groups, emphasizing significant gene sets associated with lipid deposition and MASLD-related genes, which do not align with the typical hepatic gene expression profile of a metabolically impaired phenotype. These findings support the hypothesis that SphK2 deficiency alters the global and local sphingolipidome in a way that prevents HFD-induced transcriptional activation of genes linked to metabolic dysfunction may contribute to the absence of metabolic changes that the HFD was intended to induce.

Subsequent analysis focused on canonical PPARγ target genes involved in uptake and storage (*Cd36*, *Cidea*, *Cidec/Fsp27*, *Plin2*), as well as markers of lipolysis (*Pnpla2*, *Lipe*) and lipogenesis (*Acc1*, *Fasn*). In hepatocytes, PPARγ predominantly regulates the uptake/storage, whereas *Acc1* and *Fasn* are mainly controlled by SREBP1c.[307]
The gene expression analysis revealed that neither *Pparg* itself nor the PPARγ-induced genes *Cidea*, *Cidec*, and *Perilipin 2* (*Plin2)* exhibited any changes in expression levels. However, a lower expression of *Cd36* expression, coding for fatty acid translocase, was observed (Figure 10a). Notably, there was a higher expression of *Pnpla2*, which catalyzes the first and rate-limiting step in lipolysis, while *Lipe* expression remained constant (Figure 10b). The expression of lipogenesis-associated genes, *Acc1* and *Fasn*, was unaltered in the livers of HFD-fed SphK2-deficient mice (Figure 10c). Consistent with the lower gene expression of *Cd36* mRNA, CD36 protein levels were lower in the livers of SphK2$^{-/-}$ mice, with a 61% relative to WT as determined by Western blot analysis (Figure 10d).
Additionally, kinase activity profiling (see Section 3.2.8, page 57) in the livers of HFD-fed SphK2$^{-/-}$ mice compared to WT controls revealed marked differences in the signaling activity of protein serine/threonine kinases (Figure 10e). Interestingly, these activity changes were dependent on the kinase family, with the activity of several kinases from the Cdk, MAPK, GSK, and Cdk-like related group (CMGC) being lower, whereas the Ca^{2+}/calmodulin-dependent kinase group (CaMK) and the Protein kinase A/G/C related group (AGC) exhibited increased activity in contrast to WT.

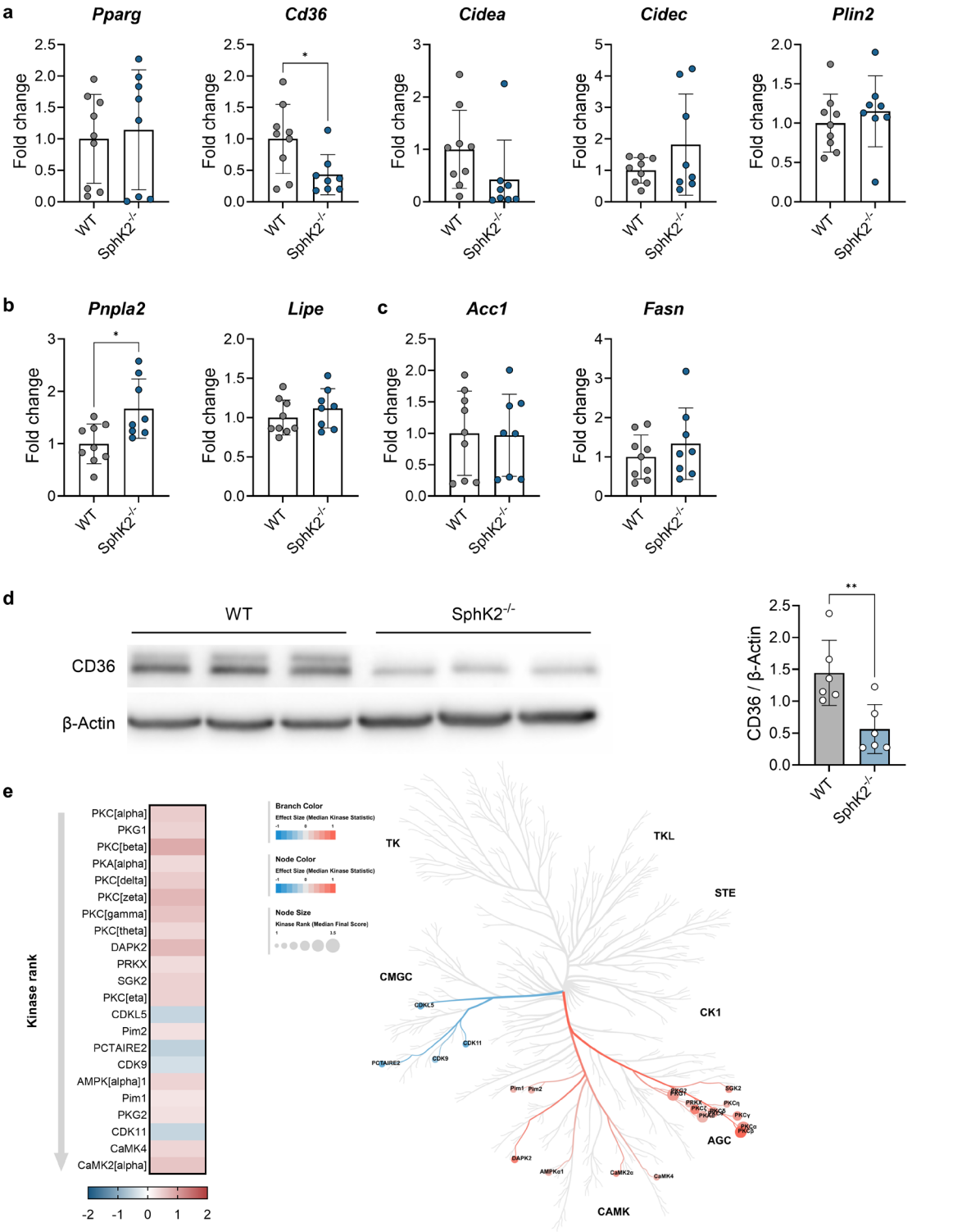

Figure 10. Obstruction of hepatic lipid accumulation in SphK2 deficient mice is associated with downregulation of CD36, upregulation of Pnpla2, and altered kinase signaling. RNA and protein from livers of HFD-fed WT and SphK2–/– mice was isolated. Gene expression of (a) PPARγ- (*Pparg*, *Cd36*, *Cidea*, *Cidec*, and *Plin2*), (b) lipolysis- (*Pnpla2* and *Lipe*), and (c) lipogenesis-associated genes (*Acc1* and *Fasn*) assessed via qRT-PCR (n_{WT} = 9, $n_{SphK2^{-/-}}$ = 8). (d) Representative Western Blot of CD36 and β-Actin and relative quantification of CD36/β-Actin (n = 6 for both groups). (e) Serin-tyrosine kinase activity in livers of SphK2$^{-/-}$ mice compared to WT mice, both fed an HFD (n = 4 per group). Only significantly regulated kinases are shown. The coral tree depicts the degree of sequence similarity among the analyzed kinases, with kinases showing significant activity changes highlighted. Data are presented as mean ± SD. Statistical analysis was performed using an unpaired, two-tailed *t*-test. Statistical significance is indicated as follows: * p <0.05, ** p <0.01.

Notably, within the AGC kinase group, phosphorylation of PKC isoforms was observed to be higher. While both classical and novel PKCs can be activated by DAG, PKCζ, an atypical PKC, is activated by phospholipids rather than DAG. PKCζ is recognized for its significant role in metabolic regulation.[308]

In conclusion, a deficiency in SphK2, as opposed to SphK1 and the WT, correlates with the absence of HFD-induced hepatic lipid accumulation, improved systemic glucose regulation, and enhanced insulin sensitivity. Besides markedly elevated levels of S1P in the plasma, this condition is characterized by higher levels of hepatic ceramide and sphingosine, lower expression of Cd36, higher expression of Pnpla2, and greater activation of PKCs. Together, these findings highlight that SphK2 deficiency triggers hepatic adaptations that render mice less susceptible to diet-induced metabolic dysfunction.

4.2 Therapeutic Intervention by Sphingosine Kinase 2 Inhibitor SLS1081832 Restores Metabolic Balance in HFD-Induced Metabolic Dysregulation

Based on the observation that sphingosine kinase 2 deficiency protects mice from diet-induced obesity and associated metabolic complications, including impaired glucose homeostasis and reduced insulin sensitivity, subsequent testing aimed to determine whether established MASLD and insulin resistance could also be ameliorated by pharmacological SphK2 inhibition. To this end, SLS1081832, a potent inhibitor for sphingosine kinase 2, synthetized and provided by Webster Santos and colleagues, was employed as a pharmacological tool.[165]

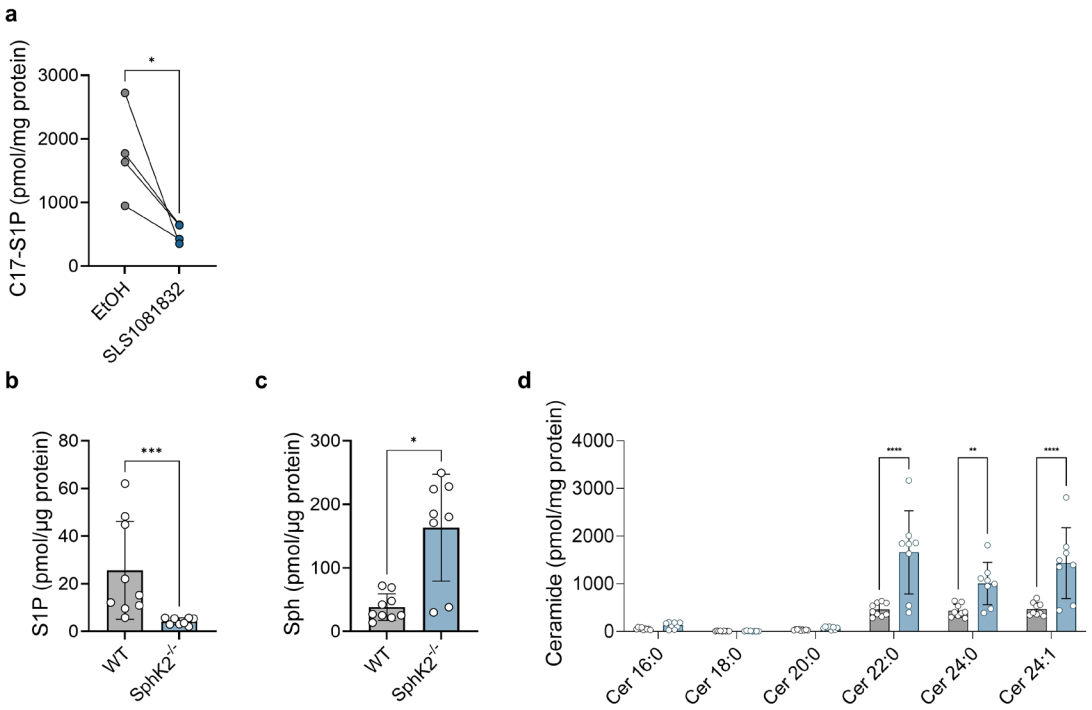

Figure 11. SphK2 absence reduces S1P and increases sphingosine and ceramide in primary mouse hepatocytes. Primary mouse hepatocytes were isolated from mice utilizing a two-step collagenase perfusion method. (a) 10 µM SLS1081832 was added to the culture medium of WT hepatocytes 30 minutes prior to conducting a sphingosine kinase assay with 5 µM C17-sphingosine. The cells were subsequently harvested and analyzed for C17-S1P reaction product via LC-MS/MS (n = 4). Statistical analysis was performed using a paired, two-tailed t-test. (b) S1P, (c) sphingosine, and (d) ceramide levels in primary hepatocytes of WT and SphK2$^{-/-}$ mice were evaluated using LC-MS/MS (n_{WT} = 9, $n_{SphK2^{-/-}}$ = 8). Data are presented as mean ± SD. Statistical analysis was performed using an unpaired, two-tailed t-test unless otherwise stated. Statistical significance is indicated as follows: * p <0.05, ** p <0.01, *** p <0.001, **** p <0.0001.

To evaluate the functional efficacy of the inhibitor SLS1081832, an assay utilizing C17-sphingosine was conducted on primary mouse hepatocytes. The results indicated that SLS1081832 is able to decrease S1P production by an average of 71% within 30 minutes (Figure 11a). This finding is in line with the significantly lower S1P levels (84%)

in primary hepatocytes of SphK2$^{-/-}$ compared WT mice (Figure 11b), while perfused whole-liver homogenates showed no reduction, likely due to the presence of residual S1P originating from plasma (Figure 4f, page 66). In support, SphK2$^{-/-}$ mice exhibit 4.3-fold higher sphingosine levels and a 2.3- to 3.6-fold higher levels of (very) long-chain fatty acid-associated ceramide species, as detected by LC-MS/MS in primary hepatocytes (Figure 11c+d).

4.2.1 SphK2 Inhibition Reduces MASLD and Associated Metabolic Impairments

Based on these findings, the SphK2 inhibitor was tested in a therapeutic approach. Male WT mice were subjected to a HFD (60% kcal from fat) for 10 weeks prior to receiving daily intraperitoneal injections of 10 mg/kg SLS1081832 or the corresponding vehicle control for an additional 6 weeks, while continuing the HFD.

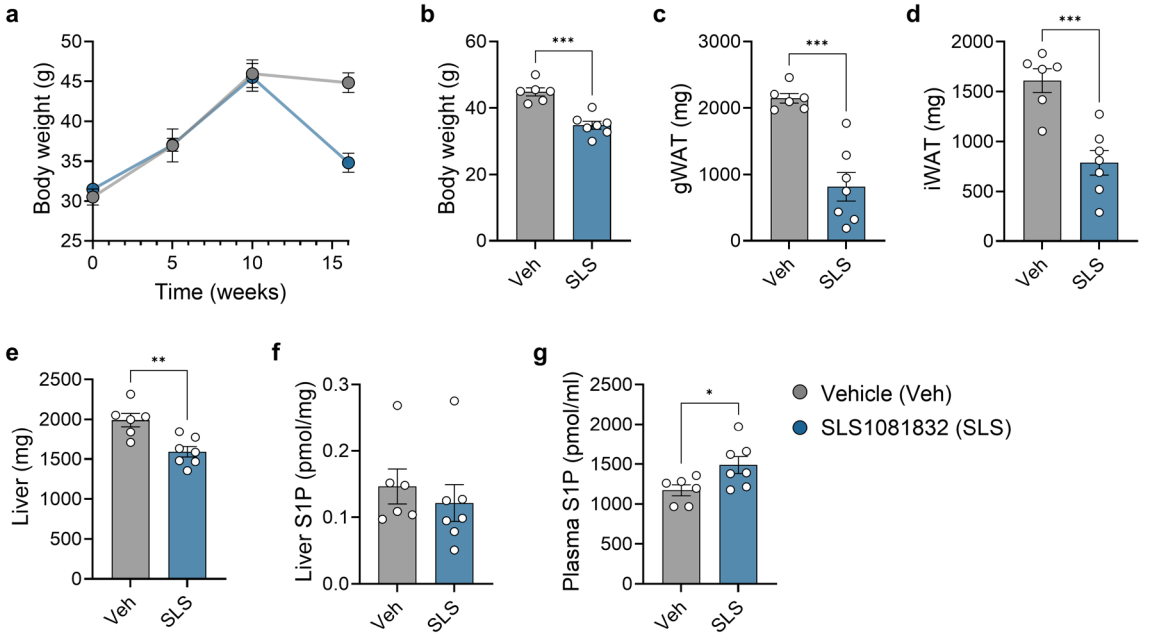

Figure 12. SLS1081832 treatment improves HFD-induced lipid deposition in adipose tissues and liver. WT mice were subjected to a HFD for 10 weeks prior to daily intraperitoneal injections of 10 mg/kg SLS1081832, a specific SphK2 inhibitor, or respective vehicle control under continuous HFD-feeding for 6 weeks. Mice were sacrificed after a 4-hour fast. (a) Body weight development of SLS1081832 and vehicle-treated group over 16 weeks. (b) Final body weight. (c) gWAT, (d) iWAT, and (e) liver weight. LC-MS/MS measurements of S1P levels in (f) liver and (g) plasma. Data are presented as mean ± SD. n_{Veh} = 6, n_{SLS} = 7. Statistical analysis was performed using an unpaired, two-tailed *t*-test. Statistical significance is indicated as follows: * p <0.05, ** p <0.01, *** p <0.001

After an initial comparable increase in body weight over the first 10 weeks of HFD feeding, the SLS1081832 treated group exhibited a reduction in body weight despite continued HFD consumption. Consequently, the treated group displayed a 22% lower final body weight compared to the control group at the conclusion of the experiment

(Figure 12a+b). Additionally, treatment with SLS1081832 resulted in a reduction in the weights of gWAT, iWAT, and liver by 62%, 51%, and 20%, respectively (Figure 12c-e). Additional LC-MS/MS measurements confirmed that hepatic S1P levels remained unchanged following SphK2 inhibition, whereas SLS1081832-treated mice showed a 1.3-fold increase in plasma S1P (Figure 12f+g), mirroring the liver and plasma S1P levels observed in global SphK2 knockout mice (Figure 4f+g, page 66).

To further evaluate the therapeutic efficacy of SLS1081832, liver sections were stained with H&E and Sirius Red (Figure 13a+b). Histological analysis indicated reduced fat accumulation by 42% in the treatment group compared to controls, while no differences in fibrotic potential were observed. (Figure 13b+c). However, the treatment did not affect hepatic enzyme levels compared to the vehicle group, as plasma GOT/AST and GPT/ALT remained unchanged (Figure 13d+e).

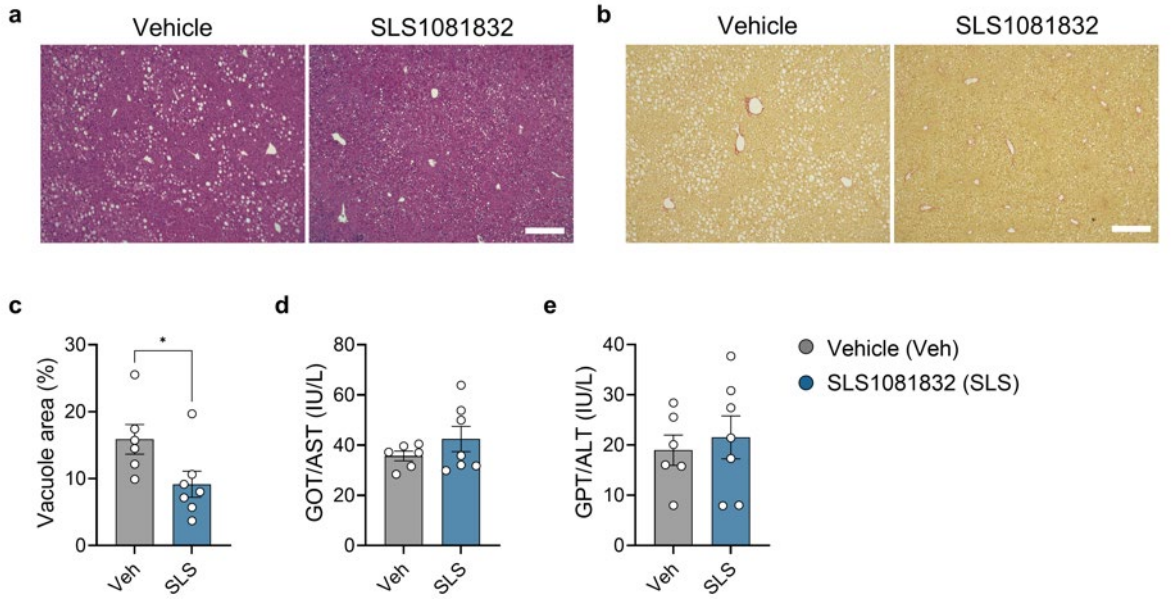

Figure 13. Inhibition of SphK2 improves HFD-induced hepatic lipid deposition. WT mice were subjected to a HFD for 10 weeks prior to daily intraperitoneal injections of 10 mg/kg SLS1081832, a specific SphK2 inhibitor, or respective vehicle control under continuous HFD-feeding for 6 weeks. Mice were sacrificed after a 4-hour fast. (a) H&E and (b) Sirius Red staining of representative liver sections (scale bar: 200 µM) and (c) quantification of vacuole area per total area of H&E-stained sections. Plasma levels of (d) GOT/AST and (e) GPT/ALT. Data are presented as mean ± SD. n_{Veh} = 6, n_{SLS} = 7. Statistical analysis was performed using an unpaired, two-tailed *t*-test. Statistical significance is indicated as follows: * p <0.05.

To assess the effects of SphK2 inhibitor treatment on glucose regulation, an ipGTT was conducted. Fasting blood glucose levels, measured after six hours of fasting, were

already lower in the treatment group compared to the control group (Figure 14a). Furthermore, the quantification of the ipGTT by area under the curve confirmed the enhanced glucose regulation in mice treated with SLS1081832 (Figure 14b+c).

Considering the improved glucose regulation in the ipGTT, an ipITT was performed to further evaluate insulin sensitivity. In comparison to HFD-fed control group, which demonstrated a rebound in blood glucose levels as early as 45 minutes after insulin injection, the treated group exhibited a delayed increase, suggesting a prolonged insulin response relative to the control group, consistent with their lower fasting plasma insulin levels. (Figure 14d-f). Assessment of metabolic function revealed that SLS1081832-treated mice, similar to SphK2-deficient mice, displayed reduced body weight, improved glucose tolerance and insulin sensitivity under HFD conditions. Furthermore, they show enhanced glucose tolerance and insulin sensitivity under these dietary conditions.

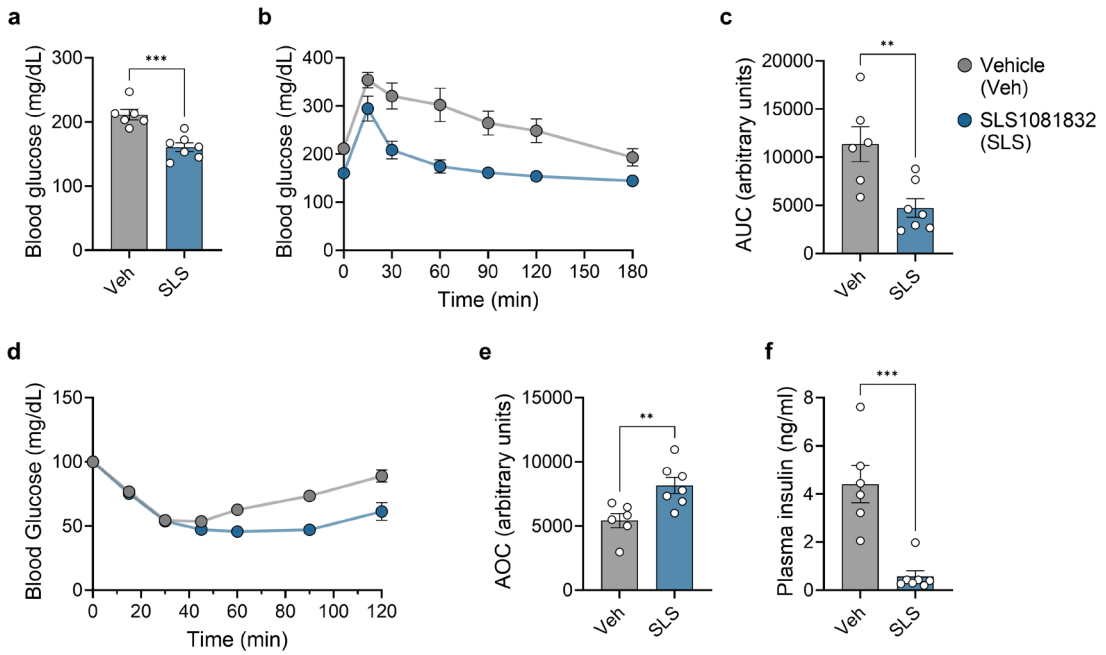

Figure 14. SLS1081832-treatment improves glucose handling. WT mice were subjected to a high-fat diet (60% kcal from fat) for 10 weeks prior to daily intraperitoneal injections of 10 mg/kg SLS1081832, a specific SphK2 inhibitor, or respective vehicle control under continuous HFD-feeding. a) Fasting blood glucose levels. (b) ipGTT at 14 weeks of treatment using a glucose dose of 2 mg/kg with quantification of (c) AUC. (d) ipITT at 15 weeks of treatment using an insulin dose of 1 U/kg with quantification of (e) AOC. (f) Fasting plasma insulin levels. Data are presented as mean ± SD. Statistical analysis was performed using an unpaired, two-tailed *t*-test. n_{Veh} = 6, n_{SLS} = 7. Statistical significance is indicated as follows: ** p <0.01, *** p <0.001.

4.2.2 SphK2 Inhibition Mimics the Hepatic Lipidome of SphK2 Deficiency

To comprehensively evaluate the phenotype of mice treated with SLS1081832, LC-MS/MS analyses were conducted on plasma and liver samples. These analyses revealed a pattern in global and local sphingolipid levels (Figure 15a) analogous to the SphK2$^{-/-}$ phenotype (Figure 7a). Plasma sphingosine levels exhibited a 1.7-fold increase (Figure 15b), while total plasma ceramide levels ($C_{16:0}$, $C_{18:0}$, $C_{20:0}$, $C_{22:0}$, $C_{24:0}$, and $C_{24:1}$) were significantly elevated, as illustrated in Figure 15a. $C_{24:0}$ and $C_{24:1}$ were notably elevated, although the respective statistical test is not shown in the heatmap.

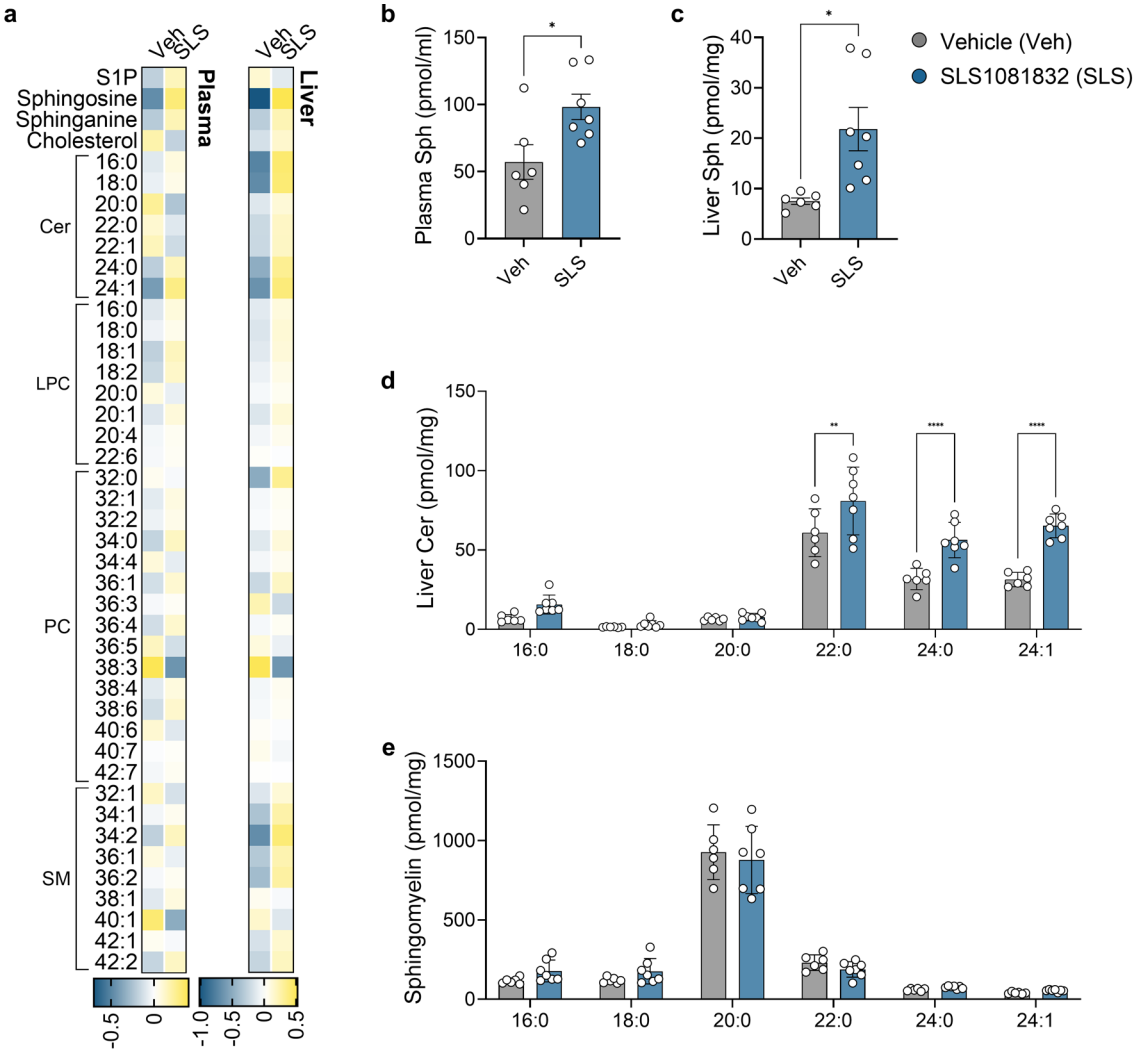

Figure 15. SLS1081832 treatment results in increasing sphingosine and ceramide levels of (V)LCFA in the liver. WT mice were subjected to a high-fat diet (60% kcal from fat) for 10 weeks prior to daily intraperitoneal injections of 10 mg/kg SLS1081832, a specific SphK2 inhibitor, or respective vehicle control under continuous HFD-feeding. Sphingolipidomic analysis was performed on plasma and liver tissue. (a) Heatmaps of selected sphingolipid species in plasma and liver. Sphingosine levels in (b) plasma and (c) liver. (d) Ceramide and (e) sphingomyelin levels in the liver were measured for individual fatty acid species (C16:0, C18:0, C20:0 C22:0, C24:1, and C24:1). Statistical analysis was performed using two-way ANOVA with Tukey's post hoc test for multiple comparisons. Data are presented as mean ± SD. n_{Veh} = 6, n_{SLS} = 7. Statistical significance is indicated as follows: * p <0.05, ** *p* <0.01, **** p <0.0001.

Alterations in local sphingolipid levels were also observed in liver tissue between groups. While hepatic S1P levels remained unchanged following SphK2 inhibition (Figure 12f, page 79), sphingosine levels increased by 2.9-fold (Figure 15c). Notably, ceramide levels in the liver were markedly upregulated by SLS1081832 treatment, with the most prevalent ceramide species ($C_{16:0}$, $C_{22:0}$, $C_{24:0}$, and $C_{24:1}$) increasing up to 2.3-fold (Figure 15d). In contrast, hepatic SM levels remained stable upon SLS1081832 treatment (Figure 15e).

When comparing the sphingolipid profiles of SLS1081832-treated mice to SphK2-deficient mice, a similar trend is observed in the elevation of plasma and liver metabolite levels, particularly S1P, sphingosine and ceramide, mirroring the phenotype of global SphK2$^{-/-}$ mice relative to their respective control groups (refer to Figure 4, page 66). These findings underscore that treatment with SLS1081832 can replicate the phenotype observed in SphK2-deficient mice subjected to a high-fat diet (HFD) by modulating overall sphingolipid levels.

4.2.3 Inhibition of SphK2 Reduces Lipid Droplet-Associated Gene Expression and Modulates Kinase Activity in the Liver

Consistent with the knockout mice models, the livers of mice treated with SLS1081832, and their respective controls were analyzed for expression changes related to lipid accumulation and lipid droplet formation. The expression of Pparγ-induced genes, specifically *Cd36*, *Cidec*, and *Plin2*, was significantly downregulated to about 0.5-fold, in SLS1081832 treated mice, indicating a reduction in hepatic lipid droplet formation (Figure 16a). In contrast, genes linked to lipogenesis, *Acc1* and *Fasn,* showed significant upregulation by 1.4 and 2-fold, respectively, while lipolytic expression remained unchanged (Figure 16b+c). Notably, the protein levels of CD36 did not mirror the mRNA-expression changes, as revealed by Western Blot analysis (Figure 16d). Similar to findings in SphK2-deficient mice fed an HFD, SLS1081832 treatment led to an 20% increase in PKCζ phosphorylation, suggesting enhanced activity (Figure 16e).

Collectively, these findings indicate that therapeutic inhibition of SphK2 in HFD-fed mice improves their metabolic status and demonstrates a clear trend towards reduced lipid accumulation. This is consistent with results observed in SphK2-deficient mice subjected to a high-fat diet. Of particular significance is the observation that both

SphK2 deficiency and SphK2 inhibition led to similar alterations in the local hepatic sphingolipidome, alongside elevated circulating S1P. These changes were consistently accompanied by reduced obesity, improved glucose homeostasis, and amelioration of MASLD.

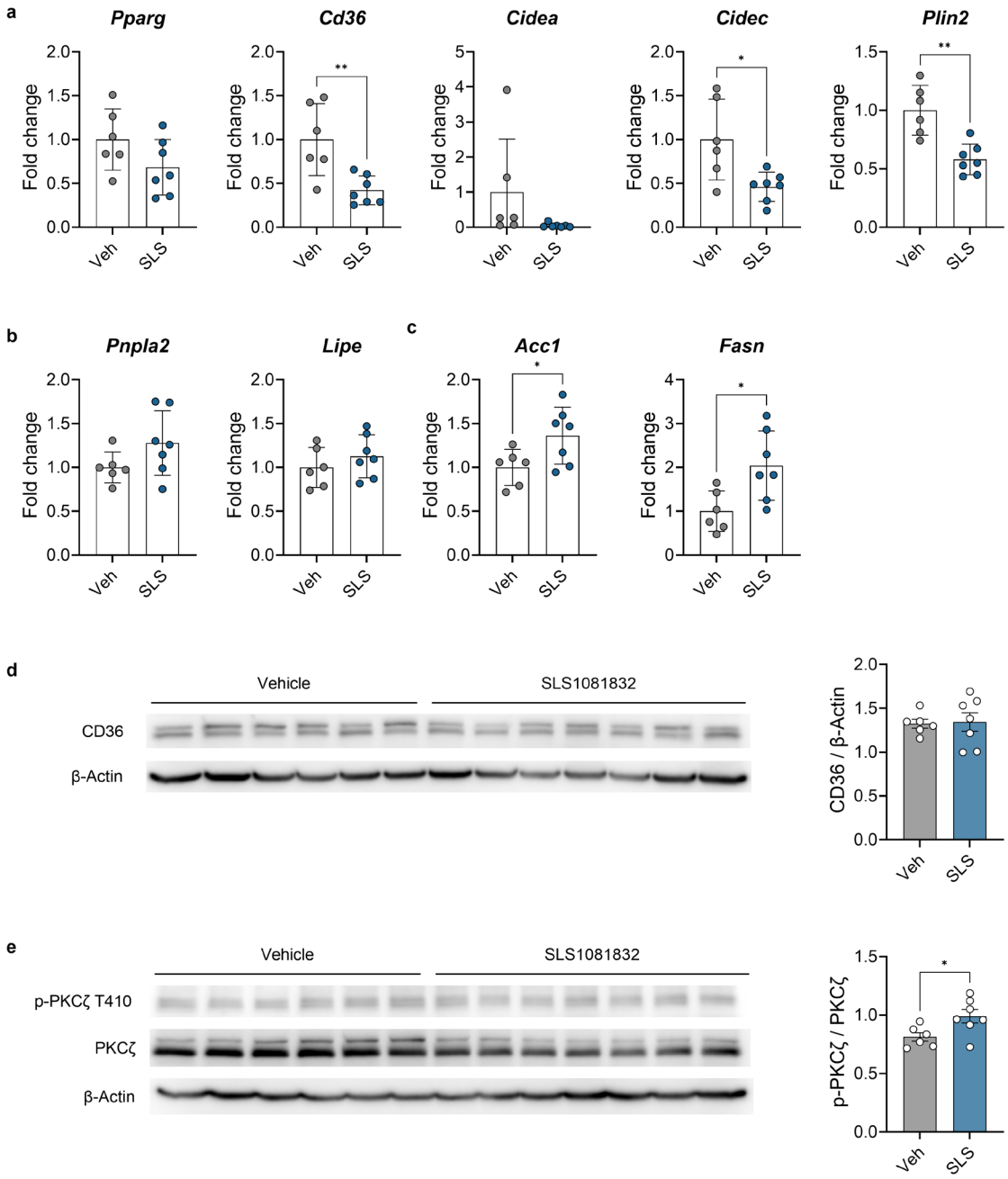

Figure 16. SphK2 inhibition shifts expression towards reduced lipid accumulation RNA and protein from livers of SLS1081832-treated and control mice was isolated. Gene expression of (a) PPARγ- (*Pparg*, *Cd36*, *Cidea*, *Cidec*, and *Plin2*), (b) lipolysis- (*Pnpla2* and *Lipe*), and (c) lipogenesis-associated genes (*Acc1* and *Fasn*) assessed via qRT-PCR (n_{WT} = 9, $n_{SphK2^{-/-}}$ = 8). (d) Western Blot of CD36 and β-Actin and relative quantification of CD36/ β-Actin. (e) Western Blot of p-PKCζ T410, PKCζ, and β-Actin and relative quantification of p-PKCζ/PKCζ. Data are presented as mean ± SD. n_{Veh} = 6, n_{SLS} = 7. Statistical analysis was performed using an unpaired, two-tailed *t*-test. Statistical significance is indicated as follows: * p <0.05, ** *p* <0.01.

4.3 S1P Lyase Inhibition using 4-Deoxypyridoxine Improves High-Fat Diet-Induced Obesity and Restores Glycemic Control

Among sphingolipids, circulating S1P exhibited a substantial increase in the plasma of mice either genetically deficient in SphK2 or subjected to SphK2 inhibition. To test, whether this increase is causally involved in SphK2-dependent resistance to obesity, MASLD, and impaired glucose homeostasis, a secondary therapeutic approach was implemented. This strategy involved inhibiting S1P lyase, the enzyme responsible for the irreversible degradation of S1P. In this approach, male WT mice were initially fed either a HFD (60% kcal from fat) or normal chow (NC). After a period of 10 weeks, each group was further divided into control and treatment subgroups. The treatment subgroups were administered 180 mg/L of the S1P lyase inhibitor 4-deoxypyridoxine (DOP) administered via drinking water, as previously described,[309] for an additional 6 weeks. At the conclusion of the treatment period, the mice were fasted overnight and subsequently euthanized for the collection of blood, liver, gWAT, and iWAT samples, in order to elucidate the DOP-mediated alterations in the sphingolipidome, especially S1P levels, and its impact on HFD treatment.

4.3.1 DOP-Treatment Leads to Weight Loss and Metabolic Improvements

WT mice were fed either a HFD or NC for 16 weeks, while collecting weight parameters. The body weight of groups subjected to a high-fat diet exhibited an increase over time until the initiation of the treatment at 10 weeks. DOP-treated mice demonstrated a reduction in body weight, whereas the high-fat control group continued to gain weight until reaching the endpoint of the study at 16 weeks (Figure 17a). In comparison to the groups on the control diet, both high-fat groups exhibited a significant weight gain from the initial weight. However, the group receiving DOP for the last 6 weeks of the study gained 23% less weight than the group on the high-fat diet alone, which is reflected in the final body weight (Figure 17b+c). Beyond the increase in body weight, a 16-week HFD resulted in a 1.8-fold increase in liver weight, a change not observed in the group receiving both HFD and DOP (Figure 17d). Furthermore, the high-fat diet induced a significant increase in the weights of adipose tissue gWAT and iWAT, by 2.6- and 8-fold, respectively (Figure 17e+f). Mice that received additional DOP treatment demonstrated a reduction in gWAT and iWAT weight by 20% and 30%, respectively, in comparison to the group subjected solely to a HFD. Notably, both the NC and HFD groups

that underwent treatment with the S1P lyase inhibitor exhibited less adipose tissue mass in both gWAT and iWAT compared to their respective untreated control groups.

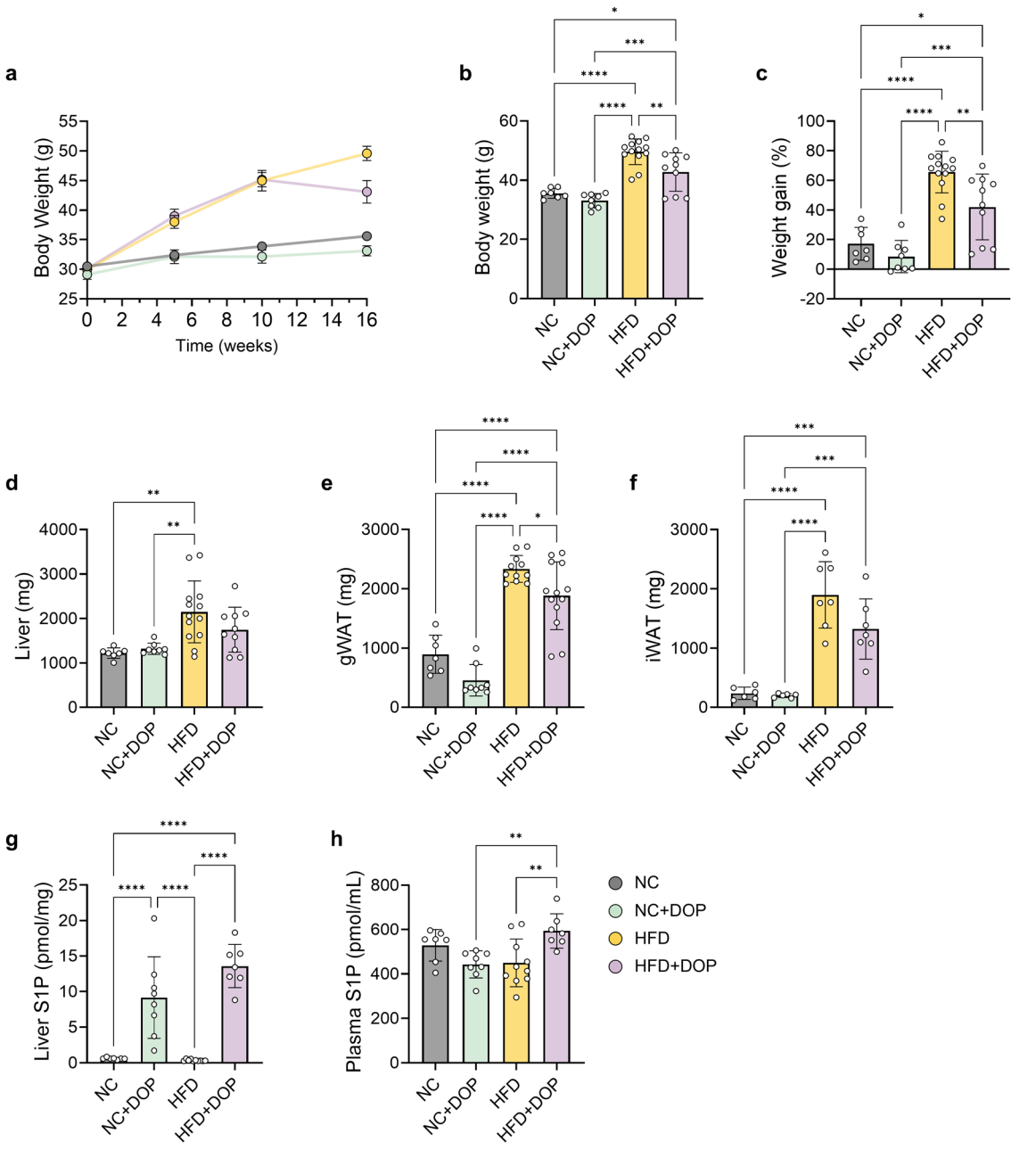

Figure 17. Treatment with S1P lyase inhibitor 4-deoxypyridoxine reduced body weight of obese mice. WT mice were subjected to either a normal chow or high-fat diet (60% kcal from fat) for a 10-week period. Subsequently, each group was divided into two subgroups: one control group and the other receiving treatment with 180 mg/L S1P lyase inhibitor 4-Deoxypyridoxine (DOP) administered via drinking water for an additional 6 more weeks. Mice were sacrificed after an overnight fast. (a) Body weight development of all groups treated over 16 weeks. (b) Final body weight. (c) Body weight gain in percent from starting weight. Organ weights of (d) liver, (e) gWAT, and (f) iWAT. LC-MS/MS measurements of S1P levels in (g) liver and (h) plasma. Data are presented as mean ± SD. n_{NC} = 6–7, n_{NC+DOP} = 6–8, n_{HFD} = 7–13, $n_{HFD+DOP}$ = 7–13. Statistical analysis was performed using one-way ANOVA followed by Tukey's post hoc test for multiple comparisons. Statistical significance is indicated as follows: * p <0.05, ** *p* <0.01, *** *p* <0.001, **** p <0.0001.

To assess the effect of DOP, S1P levels in liver and plasma were quantified by LC-MS/MS. In the liver, DOP treatment resulted in a 9.1-fold increase in S1P in control NC-fed mice and 13.6-fold increase in those on a HFD (Figure 17g). In contrast, in mice maintained on a control diet, plasma S1P levels remained stable despite DOP treatment. Conversely, a 30% increase was noted in mice subjected to a HFD and DOP challenge, in comparison to the HFD control group without DOP. (Figure 17h).

Subsequent histological analysis of liver sections was conducted to comprehensively assess potential morphological alterations. As expected, the NC groups exhibited neither lipid depositions in the H&E-stained liver sections nor fibrotic lesions in Sirius Red staining (Figure 18a). In contrast, the high-fat groups, both demonstrated hepatic lipid depositions (Figure 18a+b), whereas no fibrotic lesions were observed by Sirius Red staining (Figure 18a).

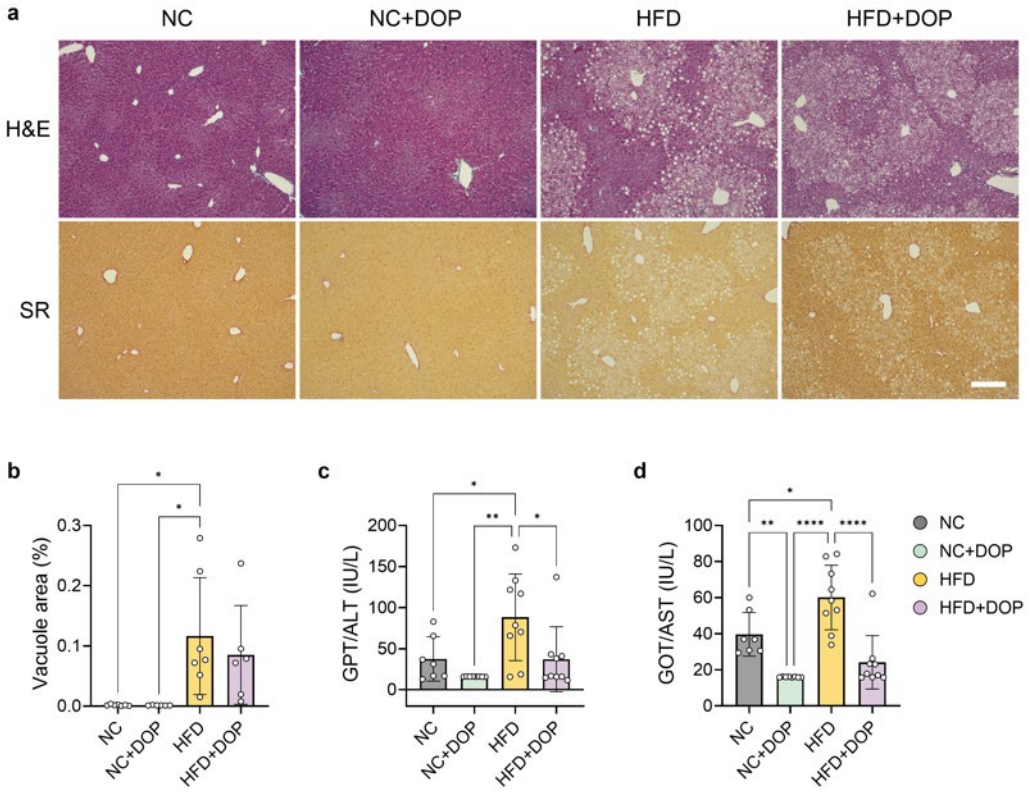

Figure 18. DOP-treatment improves liver injury parameters despite present lipid deposition. WT mice were fed NC or a HFD for 10 weeks, then split into control or DOP treatment for an additional 6 weeks. (a) H&E and Sirius Red staining of representative liver sections (scale bar: 200 µM) and (b) quantification of vacuole area per total area. Plasma levels of (c) GOT/AST and (d) GPT/ALT. Data are presented as mean ± SD. n_{NC} = 7, n_{NC+DOP} = 6–8, n_{HFD} = 7–9, $n_{HFD+DOP}$ = 6–9. Statistical analysis was performed using one-way ANOVA followed by Tukey's post hoc test for multiple comparisons. Statistical significance is indicated as follows: * p <0.05, ** p <0.01, **** p <0.0001.

Notably, GPT/ALT and GOT/AST levels significantly increased following high-fat diet treatment (Figure 18c+d). In contrast, the values in the DOP-treated groups were approximately 60% lower than those observed in their respective diet control group.

To complete metabolic characterization, glucose and insulin tolerance tests were conducted. Fasting blood glucose levels were equally elevated in both HFD-fed groups (Figure 19a). However, glucose tolerance tests indicated that 14 weeks of HFD resulted in impaired glucose tolerance compared to the DOP-treated mice, which aligned with the mice in both normal chow groups (Figure 19b+c). A similar pattern was observed in the insulin tolerance tests, where all groups, including the HFD+DOP group, exhibited improved insulin sensitivity compared to the HFD-only group (Figure 19d+e). Consistently, fasting plasma insulin levels were highest in the HFD group, suggesting a DOP-induced enhancement in glucose handling and peripheral insulin sensitivity (Figure 19f).

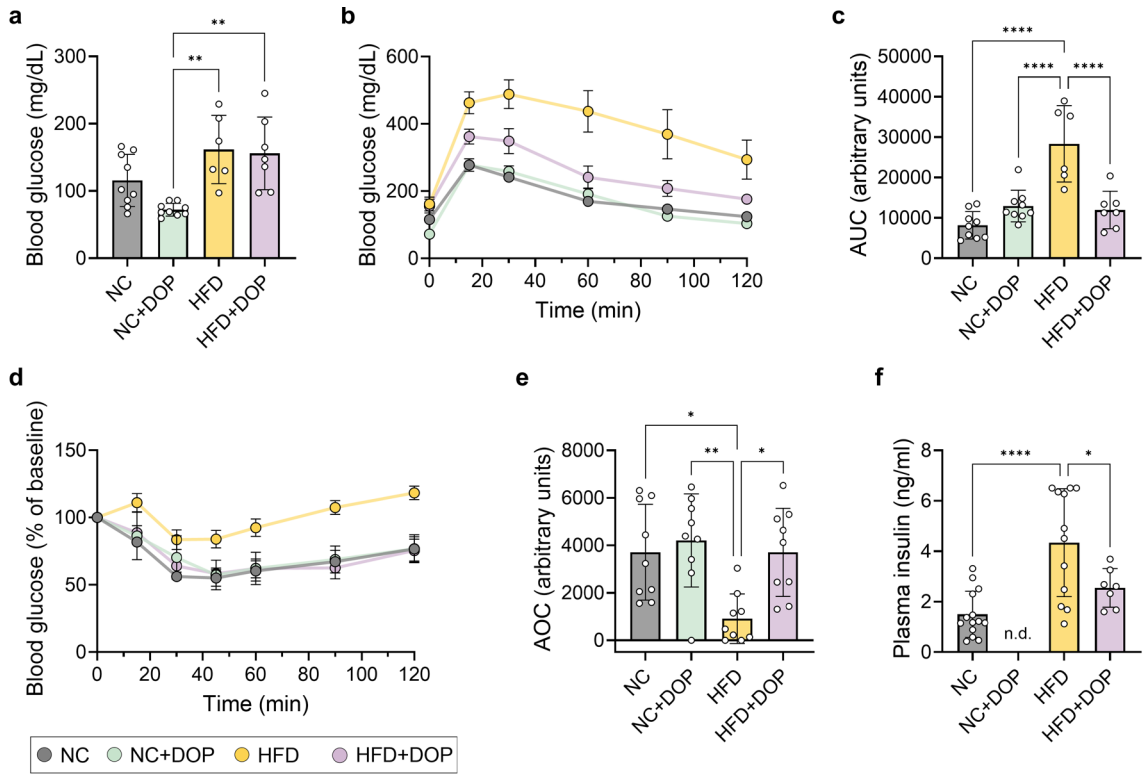

Figure 19. DOP-treatment improves glucose homeostasis and insulin sensitivity in high-fat diet-fed mice. WT mice were fed NC or a HFD for 10 weeks, then split into control or DOP treatment for an additional 6 weeks. (a) Fasting blood glucose levels. (b) ipGTT at 14 weeks of feeding using a glucose dose of 2 mg/kg with quantification of (c) AUC. (d) ipITT at 15 weeks into the experiment using an insulin dose of 1 U/kg with quantification of (e) AOC. (f) Fasting plasma insulin levels of NC, HFD, and the HFD+DOP group at the end of the experiment. Data are presented as mean ± SD. n_{NC} = 9-14, n_{NC+DOP} = 8–9, n_{HFD} = 6–12, $n_{HFD+DOP}$ = 7–9. Statistical analysis was performed using one-way ANOVA followed by Tukey's post hoc test for multiple comparisons. Statistical significance is indicated as follows: * p <0.05, ** p <0.01, **** p <0.0001. n.d., not determined.

4.3.2 S1P Lyase Inhibition Is Associated with Sphingolipidome and Gene Expression Alterations in the Livers of HFD-Fed Mice

Plasma and liver sphingolipidome analysis showed unique sphingolipid patterns, influenced by dietary changes or shifts in sphingolipid metabolism (Figure 20a).

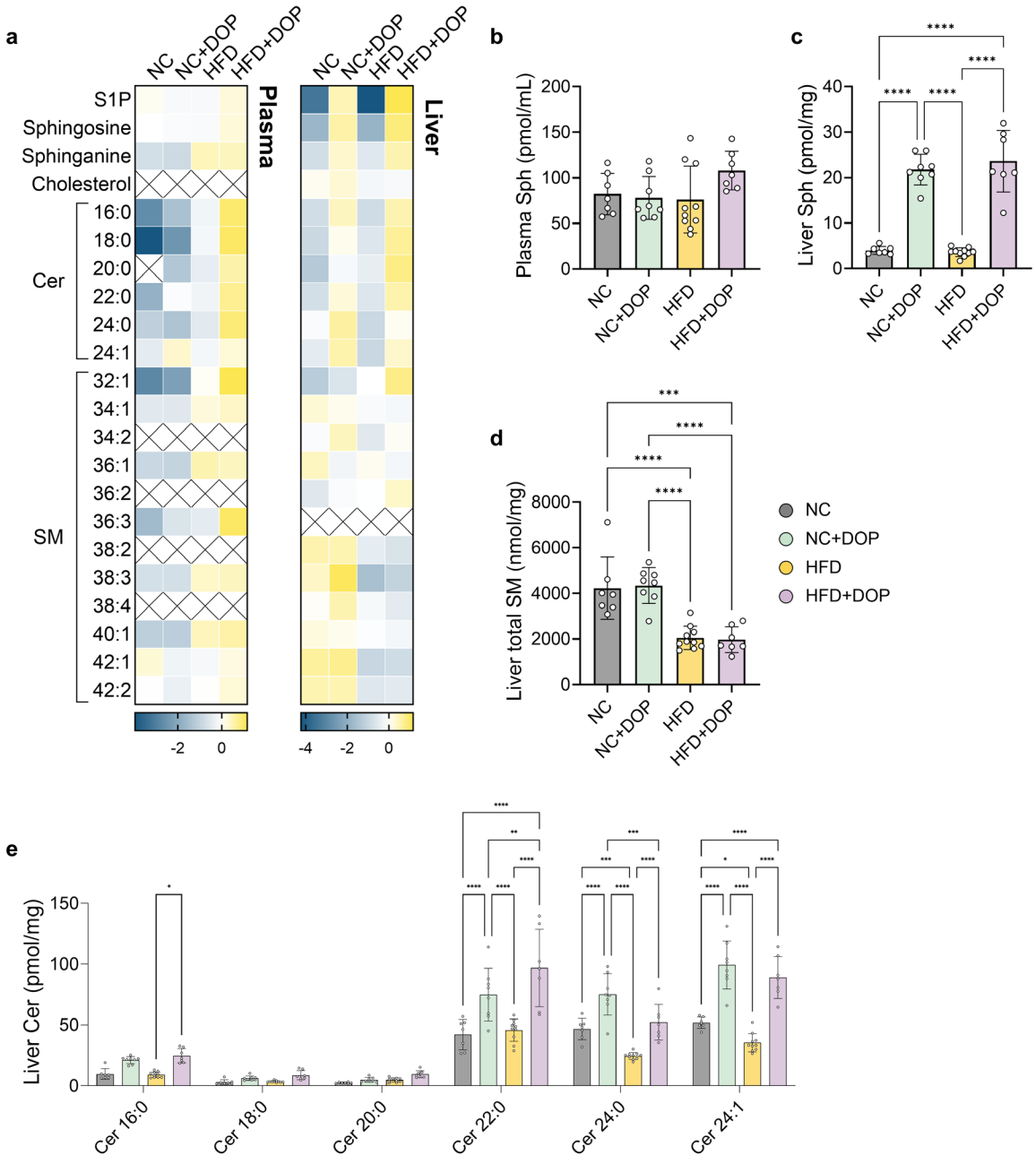

Figure 20. Inhibition of S1P lyase mediates alterations in global and local sphingolipid profiles. WT mice were fed NC or a HFD for 10 weeks, then split into control or DOP treatment for an additional 6 weeks. LC-MS/MS analysis was performed in plasma and liver tissue. (a) Heatmap of selected lipid species in plasma and liver. Sphingosine levels in (b) plasma and (c) liver. (d) Total liver SM levels and (e) liver ceramide levels were measured for individual fatty acid species (C16:0, C18:0, C20:0 C22:0, C24:0, and C24:1). Data are presented as mean ± SD. n_{NC} = 7, n_{NC+DOP} = 8, n_{HFD} = 10, $n_{HFD+DOP}$ = 7. Statistical analysis was performed using one-way or two-way ANOVA followed by Tukey's post hoc test for multiple comparisons. Statistical significance is indicated as follows: * p <0.05, ** p <0.01, *** p <0.001, **** p <0.0001. The species that are crossed out could not be detected. Plasma cholesterol levels were not assessed.

As mentioned earlier, DOP treatment increased plasma S1P levels, whereas hepatic S1P levels increased tenfold (Figure 17g+h, page 86). Similarly, sphingosine levels in the plasma were unaffected by diet or S1P lyase inhibition, yet a 9.5-fold and 6.7-fold increase was detected in the liver of control diet and HFD-fed mice with DOP treatment, respectively (Figure 20b+c). Additionally, ceramide levels in the liver increased between 1.6- to 1.9-fold in control diet-fed mice and by 2.1- to 2.5-fold in HFD-fed mice due to S1P lyase inhibition by DOP (Figure 20e). No DOP-dependent alterations were observed (Figure 20d) in SM levels. However, a reduction in SM levels by 50% due to a high-fat diet, previously observed in plasma (Figure 20a) and in the most abundant SM species in WT mice, was apparent (refer to Figure 8).

Altogether, the sphingolipid alterations observed upon DOP treatment closely resembled those seen in sphingosine kinase knockout mice and following therapeutic inhibition of SphK2 using SLS1081832. The only notable difference was that inhibition of S1P lyase by DOP led to increases in hepatic S1P levels.

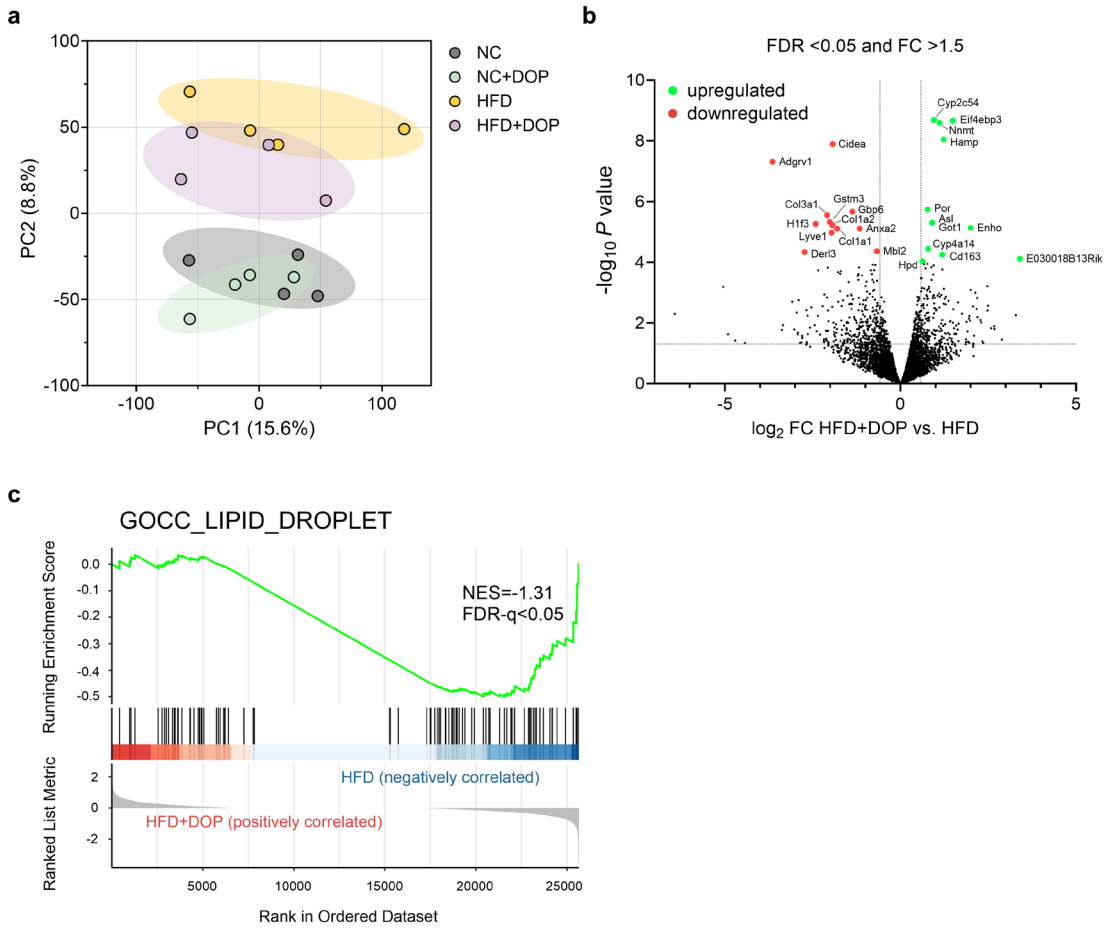

Figure 21. DOP-mediated transcriptional shifts involve suppression of lipid droplet genes. WT mice were fed NC or a HFD for 10 weeks, then split into control or DOP treatment for an additional 6 weeks. RNA-seq of total RNA from mouse liver tissues of all groups (n = 4 per group) was performed by the Genomics & Transcriptomics

Laboratory (GTL) of the Heinrich Heine University. (a) Principal component analysis (PCA) based on variance-filtered TPM (transcripts per million) values. (b) Volcano plot of differentially expressed genes comparing HFD+DOP to HFD. Red and green indicate significantly downregulated and upregulated genes, respectively (FDR <0.05, fold change > 1.5); black dots represent non-significant genes. (c) Gene set enrichment analysis (GSEA) of the GOCC_LIPID_DROPLET gene set comparing HFD+DOP-treated mice to HFD control. NES, normalized enrichment score; FDR-q, FDR-corrected p-value; FC, fold change.

RNA-seq analysis was conducted to elucidate transcriptional alterations resulting from DOP treatment, which led to the phenotypic observations. Principal component analysis of all four experimental groups demonstrated distinct clustering based on the administered diet, with the HFD+DOP group clustering between the NC and HFD groups (Figure 21a). A volcano plot further visualized prevailing differential expression between HFD+DOP- and HFD-treated mice (Figure 21b). GSEA revealed a clear negative enrichment (NES = -1.31) of the GOCC_LIPID_DROPLET gene set (Figure 21c). The underrepresentation of this gene set in the livers of HFD-fed mice treated with DOP indicated transcriptional changes favoring reduced lipid accumulation compared to the HFD only group.

Subsequently, a more comprehensive examination was conducted on the gene expression of individual genes implicated in lipid droplet formation, lipolysis and lipogenesis in the livers of the HFD-fed groups. As shown in Figure 22b+c, DOP treatment led to a concurrent upregulation of genes involved in both lipolysis (*Pnpla2*, *Lipe*) and lipogenesis (*Acc1*, *Fasn*), whereas the expression of lipid droplet–associated genes such as *Pparg* and *Cidea* (Figure 22a) was significantly reduced, suggesting an imbalance between lipid storage and metabolic turnover.
Although the mRNA expression of *Cd36* remained unchanged with DOP treatment, Western Blot analysis indicated a 31% reduction in CD36 protein levels (Figure 22d). Kinase activity profiling in these livers revealed a downregulation of kinases from the CMGC group, whereas AGC kinases, particularly PKC isoforms, exhibited significantly enhanced activity, with PKCζ being the most prominent (Figure 22e).

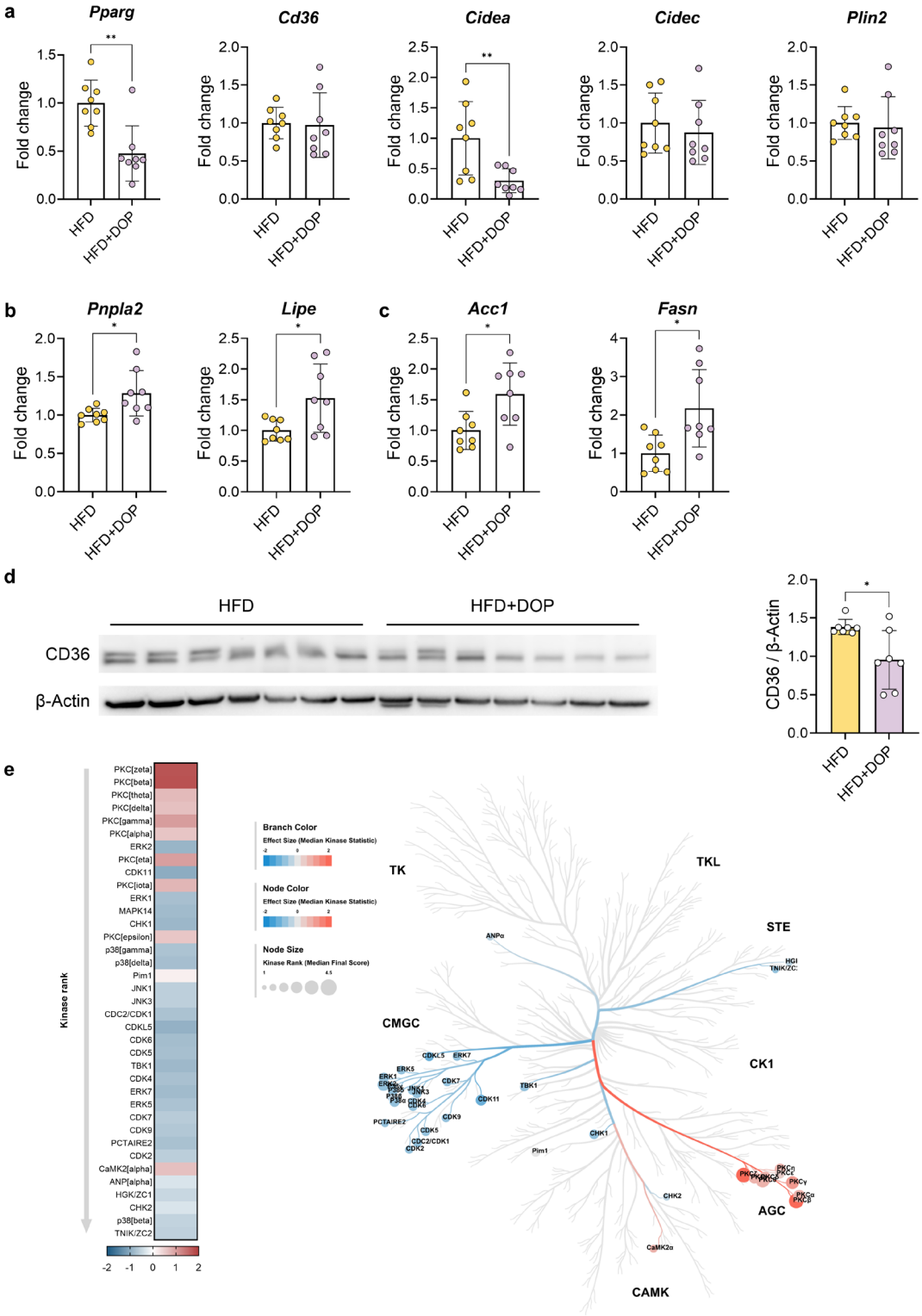

Figure 22. S1P lyase inhibition alters lipid metabolism gene expression. RNA and protein from livers of HFD-fed mice treated with 180 mg/L S1P lyase inhibitor DOP and respective control group was isolated. Gene expression of (a) PPARγ- (*Pparg*, *Cd36*, *Cidea*, *Cidec*, and *Plin2*), (b) lipolysis- (*Pnpla2* and *Lipe*), and (c) lipogenesis-associated genes (*Acc1* and *Fasn*) assessed via qRT-PCR (n = 8 per group). (d) Western Blot of CD36 and β-Actin and relative quantification of CD36/ β-Actin. e) Serin-tyrosine kinase activity in livers of HFD+DOP mice compared to HFD mice (n = 4 per group). Only significantly regulated kinases are shown. The coral tree depicts the degree of sequence similarity among the analyzed kinases, with kinases showing significant activity changes highlighted. Data are presented as mean ± SD. Statistical analysis was performed using an unpaired, two-tailed t-test. Statistical significance is indicated as follows: * p <0.05, ** p <0.01.

In conclusion, like a genetic SphK2 knockout or pharmacological SphK2 inhibition in mice, therapeutic DOP-treatment led to comparable improvements, including reduced weight gain, a tendency towards decreased hepatic lipid accumulation, and enhanced glucose tolerance and peripheral insulin sensitivity. This connection was substantiated by the corresponding sphingolipid profiles in both plasma and liver, with the distinction that S1P lyase inhibition led to an elevation in hepatic S1P levels. In the liver, in addition to elevated S1P and Sph, ceramides were notably elevated in all experimental setups.

4.4 Ceramide Elevation Correlates with Reduced Sphingomyelin Synthase Activity in the Liver

In all interventions targeting the salvage pathway of sphingolipid metabolism, hepatic ceramide levels were consistently elevated, while total SM levels remained unchanged. Yet, given the association between ceramides and lipotoxicity and their conversion to S1P or SM, SMS2 activity was evaluated to determine its role in the disproportionate ceramide increase and whether S1P signaling might mitigate ceramide-driven effects.[310,311]

The relative SMS-activity was assessed using an SMS activity assay on liver homogenates. The assay's validity was confirmed by comparing livers of SMS2$^{-/-}$ with WT mice, additionally employing the selective SMS2 inhibitor LY93 (Figure 23a+b). The livers of SMS2$^{-/-}$ exhibited a 93% reduction in SMS2 activity, indicating SMS2 as the predominant liver isoform. LY93 decreased SMS2 activity in WT mice livers by 46%.

Interestingly, lower SMS activity was also observed in the livers of SphK2-deficient mice (Figure 23c). An equal reduction is present in DOP-treated mice compared to controls (Figure 23d), suggesting a correlation between elevated ceramide levels and decreased SMS activity.

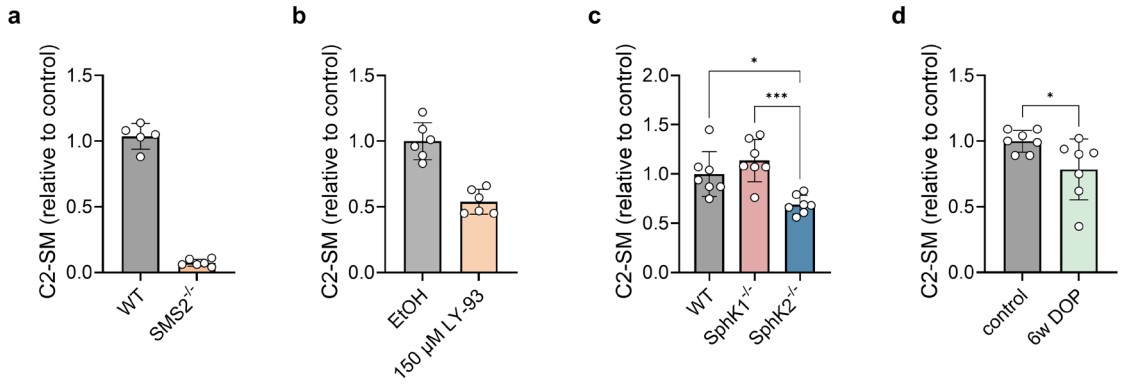

Figure 23. Ceramide-rich livers feature reduced SMS2 activity. SMS activity in liver tissues was measured by adding 30 µM C2-ceramide and PC36:0 to 100 µg protein of each liver homogenate in assay buffer. C2-SM content after 1 hour was measured by LC-MS/MS and normalized to respective control. (a) SMS2–/– versus WT. (b) WT with additional treatment of 150 µM SMS2 inhibitor LY-93 and respective control. (c) SMS activity in livers of WT versus SphK1$^{-/-}$ and SphK2$^{-/-}$. (d) Six-week treatment with 180 mg/L DOP versus control. Data are presented as mean ± SD (n = 6–7 per group). Statistical analysis was performed using paired or unpaired, two-tailed t-test or one-way repeated measures ANOVA followed by Tukey's post hoc test for multiple comparisons. Statistical significance is indicated as follows: * p <0.05, *** p <0.001, **** p <0.0001.

To investigate ceramide's effect on SMS activity, concentrations of C2-ceramide, ranging from 0.03 to 300 µM, were tested in the assay. The results showed rising ceramide concentrations enhanced SMS activity, peaking at 30 µM, with higher concentrations

causing decreased activity, yielding a bell-shaped dose-response curve (Figure 24a). Importantly, the assay reflects catalytic potential under defined assay conditions and cannot be equated 1:1 with ceramide concentrations in 1 mg of intact liver tissue. Comparing these with ceramide concentrations in liver tissues of WT, Sphk1$^{-/-}$, SphK2$^{-/-}$, and DOP-treated mice shows that local ceramide levels ($C_{16:0}$, $C_{18:0}$, $C_{20:0}$, $C_{22:0}$, $C_{24:0}$, and $C_{24:1}$) in livers of SphK2$^{-/-}$ and DOP mice reached 408 µM and 282 µM, respectively (Figure 8 and Figure 20d). In contrast, control groups showed lower total ceramide levels, with 85 µM and 152 µM, as did SphK1$^{-/-}$ mice at 90 µM. This indicates that higher levels of total ceramide in the liver correlate with reduced SMS activity, particularly where total ceramide levels approach or exceed 300 µM.

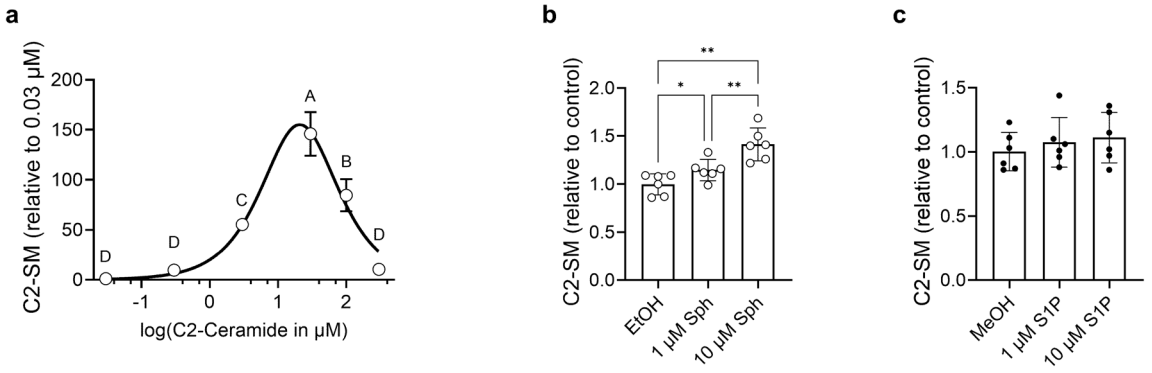

Figure 24. Increased ceramide, but not sphingosine or S1P, levels inhibit SMS2 activity. SMS activity in liver tissues was measured by adding 30 µM C2-ceramide and PC36:0 to 100 µg protein of each liver homogenate in assay buffer. C2-SM content after 1 hour was measured by LC-MS/MS and normalized to respective control. (a) WT liver homogenates with rising C2-ceramide concentrations (0.03, 0.3, 3, 30, 100, 300 µM). Statistical analysis was performed using nonlinear regression with substrate inhibition model to analyze concentration-response relationship. The model fit was evaluated using the R2 value (R2 = 0.9352), indicating a good fit to the data. Additionally, differences between conditions were assessed using repeated measures one-way ANOVA followed by Tukey's post hoc test for pairwise comparisons. Groups sharing a letter in Compact Letter Display (CLD) are not significantly different, while groups with different letters indicate significant differences. All significant comparisons showed at least p< 0.01, with most comparisons at p< 0.001. (b) WT with additional treatment of 1 and 10 µM Sph and respective control (EtOH; ethanol). (c) WT with additional treatment of 1 and 10 µM S1P and respective control (MeOH; methanol). Data are presented as mean ± SD (n = 6 per group). Statistical analysis was performed using one-way repeated measures ANOVA followed by Tukey's post hoc test for multiple comparisons unless otherwise stated. Statistical significance is indicated as follows: * p <0.05, ** p <0.01.

In contrast, Sph and S1P concentrations up to 10 µM did not inhibit SMS activity at 30 µM C2-ceramide (Figure 24b+c). Instead, sphingosine increased SMS activity.

It is important to note that the experiments were conducted using liver cell homogenate from C57BL/6J mice, which inherently possess specific ceramide levels. Consequently, the concentrations employed in the experiment are cumulative and cannot be directly equated in a 1:1 ratio. Nevertheless, these results suggest a ceramide-dependent inhibition of SMS2 activity in the liver, consistent with substrate inhibition kinetics.

4.5 Sphingosine-1-Phosphate Promotes Lipolysis in Adipose Tissue via Activation of PKCζ

In HFD-fed mice, SphK2 knockout and pharmacological inhibition of both SphK2 or S1P lyase showed a consistent trend towards reduced hepatic lipid droplet formation, supported by histological and gene expression readouts. Besides lower hepatic lipid deposition in these interventions, another notable observation was the reduction in adipose tissue mass. Subsequently, the potential contribution of enhanced lipolysis to the observed reduction in adipose tissue mass was examined.

Previous research in our group demonstrated that S1P signaling through S1PR2 inhibits adipogenesis in mesenchymal progenitor cells by suppressing PPARγ-dependent gene expression.[309] Similarly, studies conducted by the Park group revealed that S1PR2 stimulation inhibited 3T3-L1 differentiation by downregulating adipogenic transcription factors and inactivating JNK and p38 MAPK signaling pathways.[312,313] Intracellular S1P has also been considered, as other studies have shown that the S1P-producing enzymes SphK1 and SphK2 are induced during adipogenic differentiation of 3T3-L1.[268]

4.5.1 PKCζ Activation by Intracellular Action of S1P Stimulates Lipolysis

To investigate the role of S1P as a potential inducer of lipolysis, differentiated 3T3-L1 adipocytes were exposed to gradually increasing concentrations of S1P. Only concentrations equal to or exceeding 10 µM, 100-fold above S1PR activation thresholds, resulted in a two- to three-fold increase in glycerol release in the lipolysis assay. In contrast, at equimolar concentrations, the S1PR1-3 agonists AUY954, CYM5520, and CYM5541 did not induce lipolysis (Figure 25a+b), thereby excluding the three major S1PRs as mediators of the S1P effect. To examine whether intracellular S1P may be involved, cellular uptake of S1P in differentiated 3T3-L1 cells treated with 10 µM S1P was measured. After 30 minutes, intracellular S1P levels increased by up to 19.3-fold, equivalent to 0.17 µM, accompanied by a 5.9-fold increase in Sph levels, while ceramide levels remained constant (Figure 25c). Adenylate cyclase and phosphatidylinositol 3-kinase (PI3K) were excluded as potential intracellular targets for S1P, as their respective inhibitors, SQ22536 and Wortmannin, did not suppress lipolysis in the presence of S1P (Figure 25d+e).

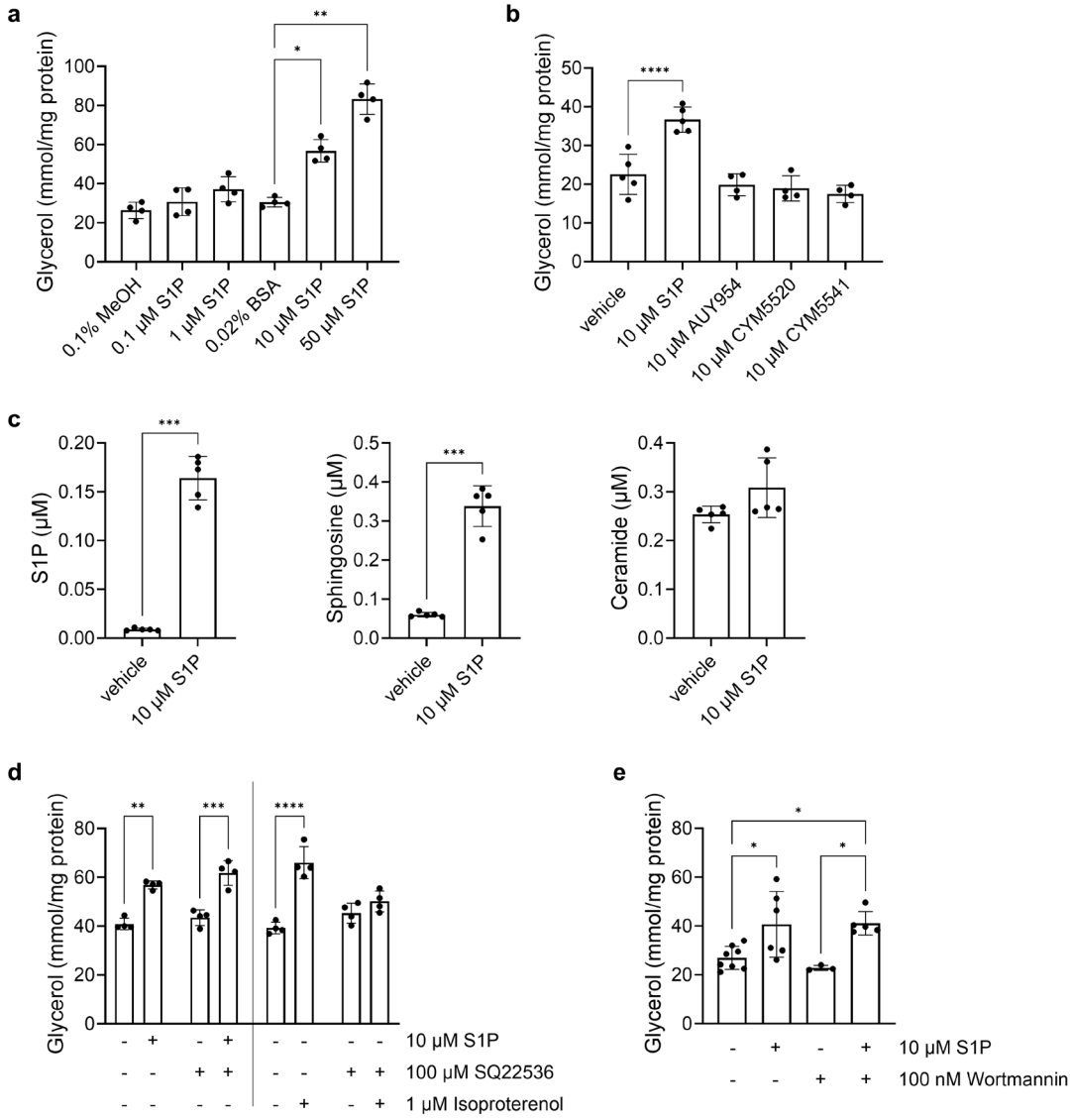

Figure 25. Intracellular S1P induces lipolysis through PKCζ in differentiated 3T3-L1 adipocytes. (a) Glycerol release of differentiated 3T3-L1 cells after treatment with 0.1, 1, 10 and 50 µM S1P or respective vehicle for 16 hours (*n* = 4 per group). (b) Glycerol release of differentiated 3T3-L1 cells after treatment with 10 µM of each S1P or S1PR1-3 agonists AUY954, CYM5520, and CYM5541 or vehicle control (0.1% DMSO) for 16 hours (*n* = 4–5 per group). (c) LC-MS/MS measurements of adipocyte-associated S1P, Sph, and ceramide (Cer14:0, 16:0, 18:0, 22:0, 24:0, and 24:1) after incubating differentiated 3T3-L1 cells with 10 µM S1P for 30 minutes (*n* = 5 per group). (d) Glycerol release of differentiated 3T3-L1 cells after treatment with 10 µM S1P and 1 µM Isoproterenol in presence and absence of 100 µM adenylate cyclase inhibitor SQ22536 and respective vehicle controls for 16 hours (*n* = 4 per group). (e) Glycerol release of differentiated 3T3-L1 cells with 10 µM S1P and/or 100 nM PI3K inhibitor Wortmannin and respective control for 16 hours (*n* = 3–8 per group). Data are presented as mean ± SD. Statistical analysis was performed using a one-way ANOVA (A,B,E) or a repeated measures one-way ANOVA, with treatment as the within-subject (paired) factor (D) followed by Tukey's multiple comparison test (A,B,E) or a paired, two-tailed *t*-test (C). Statistical significance is indicated as follows: * p <0.05, ** *p* <0.01, *** *p* <0.001, **** p <0.0001.

PKCζ, known to be allosterically bound and activated by S1P, was investigated as another potential intracellular target.[204] Figure 26a illustrates a significant stimulation of PKCζ activity by 10 µM S1P in differentiated 3T3-L1 cells, as demonstrated in a PKCζ

activity assay. Furthermore, S1P induced phosphorylation at Thr410, located in the PKCζ activation loop (Figure 26b).[314]

To ascertain whether S1P-induced lipolysis is dependent on PKCζ activity, lipolysis was induced by S1P in the presence and absence of either the general PKC inhibitor bisindolylmaleimide I (Bis) or a PKCζ-specific pseudo-substrate inhibitor (PSI), resulting in the complete abolition of the S1P-stimulating effect on lipolysis (Figure 26c+d).

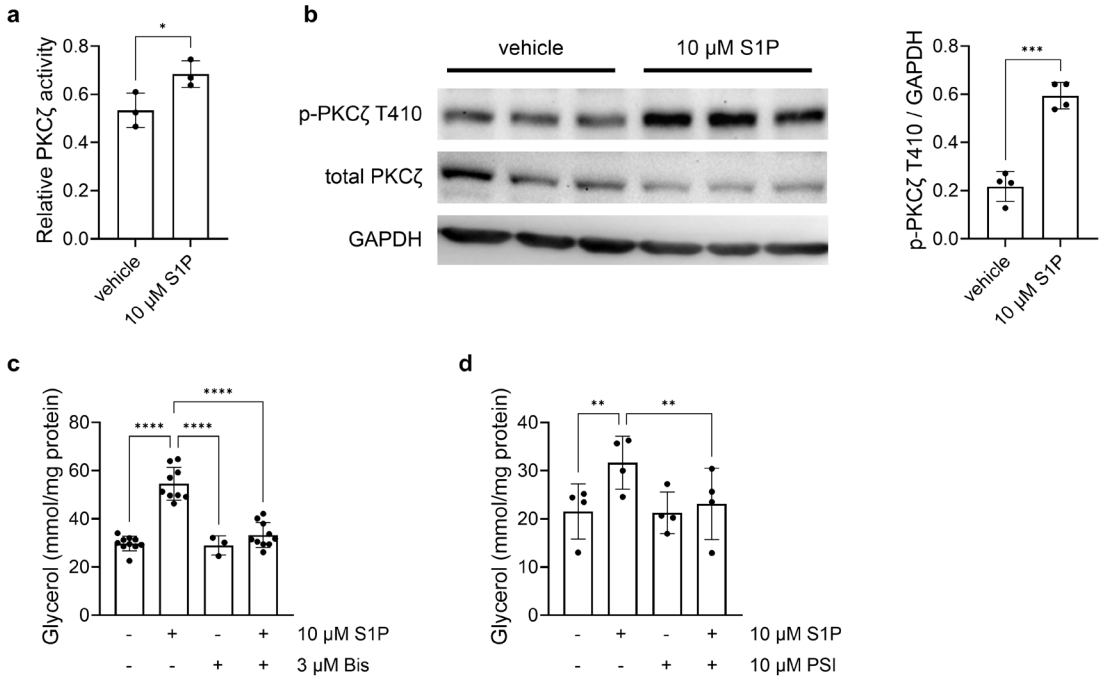

Figure 26. S1P induces lipolysis through PKCζ in differentiated 3T3-L1 cells. (a) Relative kinase activity of recombinant PKCζ treated with 10 µM S1P and respective vehicle (*n* = 3 per group). (b) Representative Western Blots of phosphorylated PKCζ (Thr410), total PKCζ, and GAPDH in differentiated 3T3-L1 adipocytes treated with 10 µM S1P and respective vehicle for 15 minutes and relative quantification of p-PKCζ T410 to GAPDH loading control (*n* = 4 per group). (c) Glycerol release of differentiated 3T3-L1 cells after treatment with 10 µM S1P and/or 3 µM PKC inhibitor bisindolylmaleimid (Bis) for 16 hours (*n* = 3–10 per group). (d) Glycerol release of differentiated 3T3-L1 cells after treatment with 10 µM S1P and/or 10 µM PKCζ pseudo-substrate inhibitor (Psi) for 16 hours (*n* = 4 per group). Data are presented as mean ± SD. Statistical analysis was performed using a paired, two-tailed *t*-test (A,B) or a repeated measures one-way ANOVA followed by Tukey's multiple comparisons test (C,D). Statistical significance is indicated as follows: * p <0.05, ** *p* <0.01, *** *p* <0.001, **** p <0.0001.

4.5.2 S1P Induces Lipolysis Dependent on a PKCζ/MAPK/HSL Pathway

To elucidate the downstream signaling mechanisms by which S1P induces lipolysis, adipose HSL was inhibited using a small molecule HSL inhibitor (smHSLi). This revealed an inhibition of the S1P-activated lipolysis pathway under investigation (Figure 27a). Given that mitogen-activated protein kinases (MAPK) have been demonstrated to activate HSL through Ser660 phosphorylation in mature 3T3-L1 adipocytes, the inhibition of MAPK was tested using the ERK inhibitor PD98059.[315]

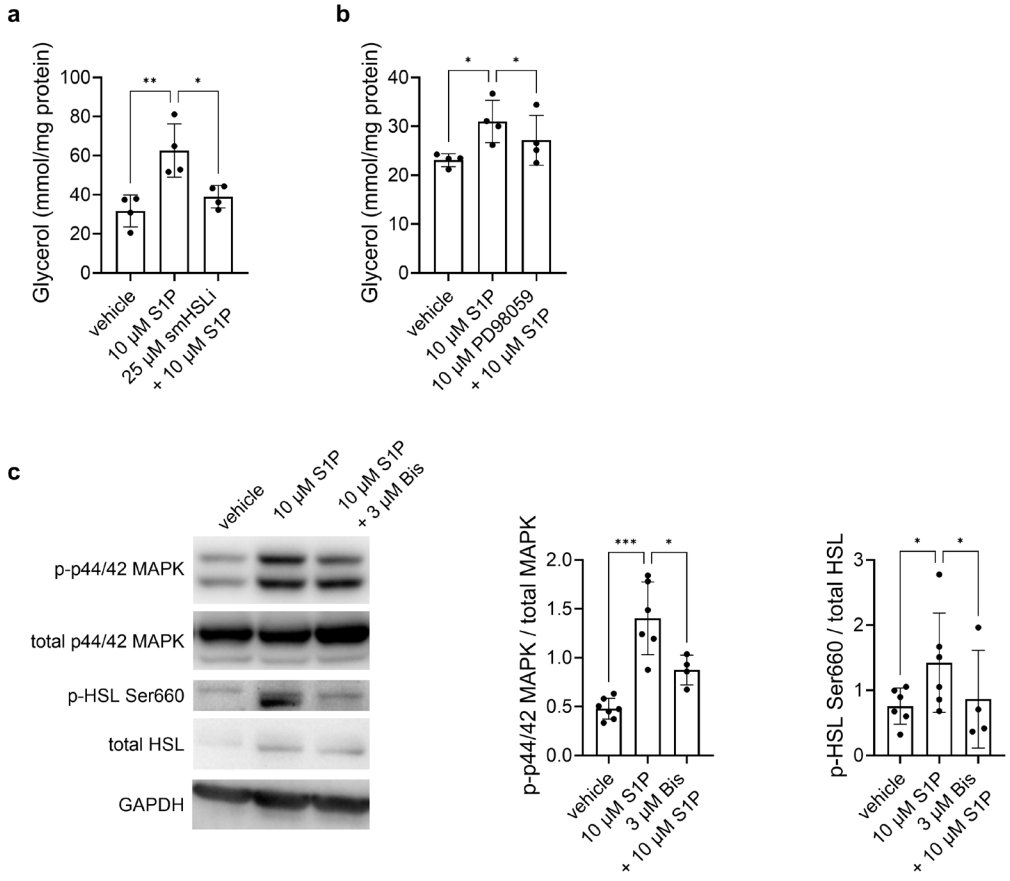

Figure 27. S1P-induced lipolysis via activation of PKCζ is dependent on MAPK/ERK pathway. (a) Glycerol release of differentiated 3T3-L1 adipocytes after treatment with 10 µM S1P in presence or absence of 10 µM ERK inhibitor PD98059 for 16 hours (*n* = 4 per group). (b) Glycerol release of differentiated 3T3-L1 cells after treatment with 10 µM S1P in presence or absence of 25 µM small molecule HSL inhibitor (smHSLi) for 16 hours (*n* = 4 per group). (c) Representative Western Blots of phosphorylated p44/42 MAPK, total-p44/42 MAPK, phosphorylated HSL (Ser660), total HSL, and GAPDH in differentiated 3T3-L1 adipocytes treated with 10 µM S1P in presence and absence of 3 µM bisindolylmaleimide I (Bis) for 15 minutes (*n* = 4–7 per group) and relative quantification of p-p44/42 MAPK to total MAPK or p-HSL to total HSL. Data are presented as mean ± SD. Statistical analysis was performed using a one-way ANOVA followed by Tukey's multiple comparisons test. Statistical significance is indicated as follows: * p <0.05, ** *p* <0.01, *** *p* <0.001.

Indeed, MAPK inhibition resulted in the suppression of S1P-stimulated lipolysis (Figure 27b). Consistently, Western Blot analysis of differentiated 3T3-L1 adipocytes treated with 10 µM S1P, with or without 3 µM of the PKCζ inhibitor bisindolylmaleimide I, indicated that the PKCζ inhibition prevents the downstream phosphorylation of HSL and MAPK, even in the presence of S1P stimulation (Figure 27c). These findings suggest that S1P induces lipolysis via the PKCζ/HSL/MAPK signaling pathway.

4.5.3 Inhibition of S1P Lyase Promotes Lipolysis *in vitro* and *in vivo*

In accordance with the proposed mechanism whereby S1P enters the cell and activates the PKCζ/HSL/MAPK pathway intracellularly, subsequent experiments were conducted by inhibiting S1P lyase to elevate intracellular S1P levels. This was achieved using 1 µM of the S1P lyase inhibitor S1PL-IN-1. The application of S1PL-IN-1 resulted in a successful increase in glycerol levels by up to 20% in both differentiated 3T3-L1 cells and primary murine adipocytes, as demonstrated in a lipolysis assay (Figure 28a).

Subsequently, a therapeutic intervention was employed to pharmacologically elevate S1P levels in mice, aiming to assess whether increased S1P levels would influence lipolysis *in vivo*. For this purpose, mice were subjected to an initial HFD for 10 weeks, followed by the administration of 180 mg/L DOP via drinking water for an additional 6 weeks of HFD for both the treatment and control groups (refer to Section 4.3). Notably, a ~2-fold increase in plasma S1P levels was observed, while a 92-fold increase was detected in gWAT in the DOP-treated group compared to the control group (Figure 28b). Concurrently, reductions in body weight and gWAT mass were observed, as previously mentioned in Section 4.3.1 (Figure 28c). Histomorphometric analyses of two representative adipose tissue depots, gWAT and iWAT, revealed that the treatment group exhibited smaller adipocyte size (mean diameter and area) and a significant shift towards smaller cells compared to the group receiving only HFD (Figure 28d-f).

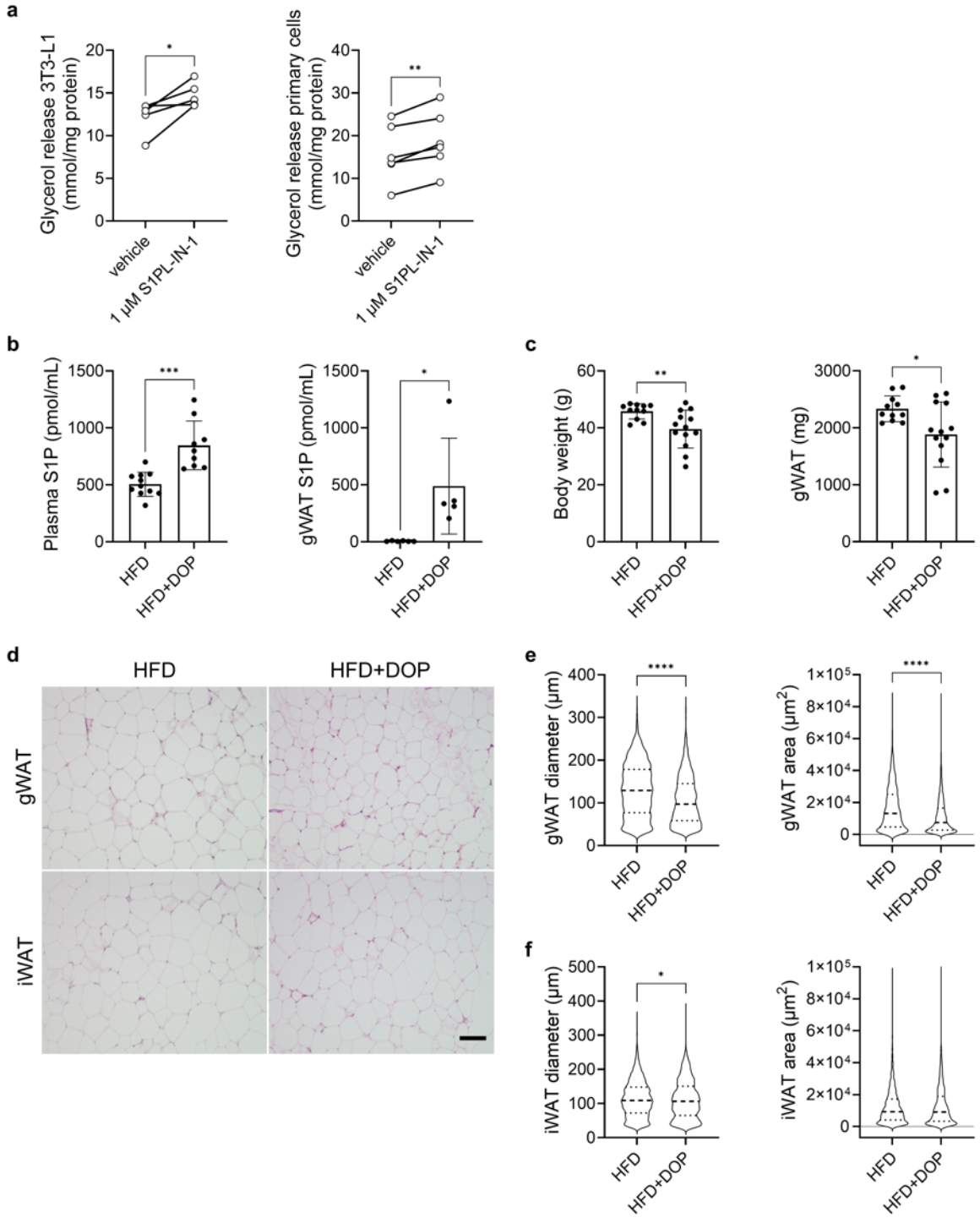

Figure 28. S1P lyase inhibition increases S1P levels in vitro and in vivo leading to reduced adipose tissue mass in HFD-fed mice. (a) Glycerol release of differentiated 3T3-L1 adipocytes and differentiated primary mouse adipocytes after treatment with 1 µM S1P lyase inhibitor S1PL-IN-1 or respective vehicle for 16 hours (n = 5–6 per group). (b) LC-MS/MS measurements of S1P in plasma and gWAT of mice fed a HFD for 16 weeks versus additional DOP-treatment for 6 weeks (n = 5–11 per group). (c) Body and gWAT weight of mice fed a HFD for 16 weeks versus additional DOP-treatment for 6 weeks (n = 11–13 per group). (f) Representative H&E staining of of gWAT and iWAT of mice fed a HFD for 16 weeks versus additional DOP-treatment for 6 weeks (Scale bar: 100 µM) and quantification of adipocyte diameter and area in (e) gWAT (n = 11–13) and (f) iWAT (n = 4–5 per group). Data are presented as mean ± SD. Statistical analysis was performed using a paired or unpaired, two-tailed t-test. Statistical significance is indicated as follows: * p <0.05, ** p <0.01, *** p <0.001, **** p <0.0001.

To evaluate whether the elevated S1P levels and reduced adipose tissue mass were associated with increased lipolysis *in vivo*, FFAs were measured in plasma and gWAT. Elevated FFA levels in the DOP group indicated enhanced lipolytic activity (Figure 29a). To further investigate the proposed PKCζ/HSL/MAPK pathway *in vivo*, PKCζ activity in gWAT was assessed by measuring PKCζ T410 phosphorylation via western blotting and an *in vitro* kinase assay using immunoprecipitated PKCζ. Both relative PKCζ activity and T410 phosphorylation were elevated in the gWAT tissue of mice with increased S1P levels due to DOP treatment (Figure 29b+c). Finally, phosphorylation of HSL at Ser660 was increased in the group receiving additional DOP-treatment, in contrast to the HFD group (Figure 29d).

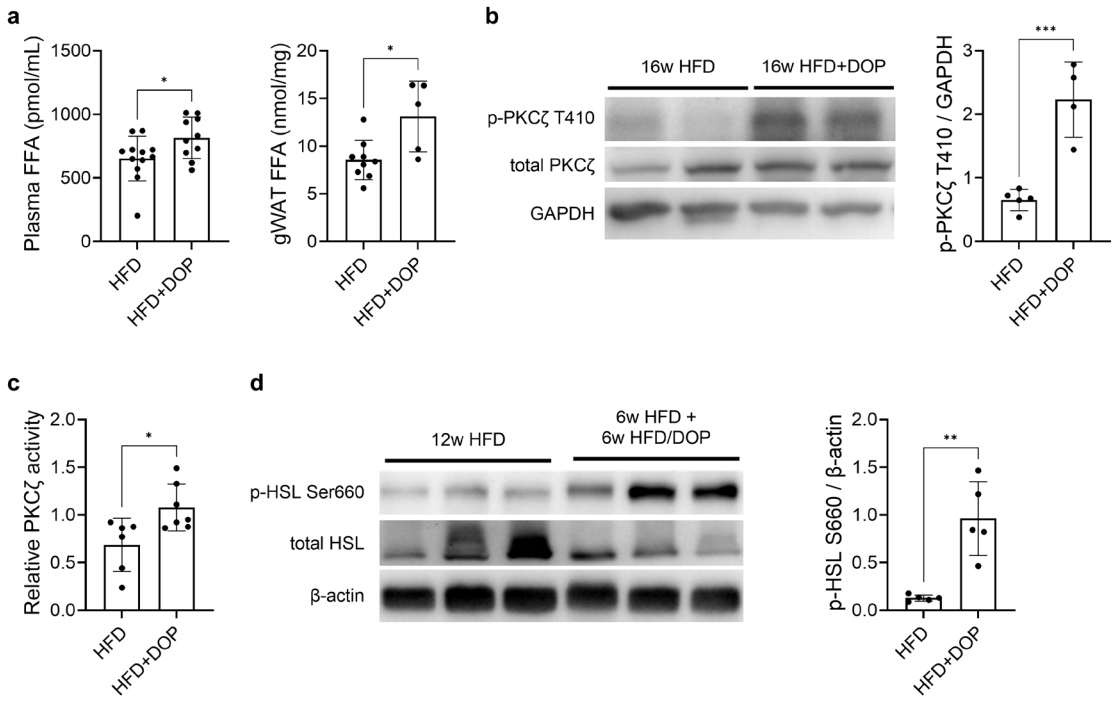

Figure 29. S1P increases lipolysis in vivo through PKCζ activation. Mice were fed a HFD for 16 weeks with or without supplementation of S1P lyase inhibitor DOP via drinking water during the last 6 weeks of the diet. (a) FFA in plasma and gWAT (*n* = 5–12 per group). (b) Representative Western Blots of phosphorylated PKCζ (Thr410), and total PKCζ and relative quantification of p-PKCζ in gWAT to GAPDH loading control (*n* = 4–5 per group). (c) PKCζ kinase activity as measured by in vitro phosphorylation assay with immunoprecipitated PKCζ in gWAT (*n* = 6–7 per group). (d) Representative Western Blots of p-HSLSer660 and total HSL in gWAT and relative quantification of p-HSL to beta-actin loading control (*n* = 5 per group). Data are presented as mean ± SD. Statistical analysis was performed using an unpaired, two-tailed *t*-test. Statistical significance is indicated as follows: * p <0.05, ** *p* <0.01, *** *p* <0.001.

These findings suggest that the elevation of S1P levels *in vivo*, achieved through therapeutic intervention in obese mice, induce lipolysis via the same mechanism postulated *in vitro*, leading to a reduction in adiposity and improvement in metabolic state

indicators, as described in Section 4.3. In the livers of DOP-treated mice, elevated PKCζ activity is associated with increased levels of S1P, Sph, and ceramide. In contrast, in the livers of SphK2-deficient mice, elevated levels were observed only for Sph and ceramide, despite a similar increase in PKCζ activity.

5 Discussion

This study aimed to elucidate the role of S1P turnover in the development and progression of obesity-related complications and evaluate whether targeting this pathway can modulate tissue-specific responses. By employing both genetic and pharmacological interventions, this study investigated the impact of altered S1P turnover on lipid handling and systemic metabolic regulation, integrating liver and plasma sphingolipid profiling to link functional changes with the underlying lipid remodeling. Consistent with this objective, this study identified a range of phenotypic and functional changes that depended on either genotype or treatment:

1. A global knockout of SphK2, but not SphK1, confers protection against weight gain induced by a high-fat diet and subsequent metabolic complications such as MASLD and insulin resistance. The observed reduction in body and adipose tissue weight is associated with enhanced systemic glucose tolerance and insulin sensitivity. In the liver, gene expression analysis indicated a negative enrichment of genes linked to lipid droplets and MASLD in mice, alongside lower expression of CD36, higher expression of the lipolysis gene *Pnpla2*, and elevated kinase activity of PKCs, including atypical PKCζ.
2. Therapeutic inhibition of SphK2 in HFD-fed mice replicates the SphK2-deficient phenotype and reverses metabolic deterioration by reducing lipid deposits in adipose and the liver, improving glucose tolerance and enhancing insulin sensitivity. This is facilitated by lower expression of genes involved in lipid deposition and higher PKCζ.
3. Therapeutic inhibition of S1P lyase results in reduced body and gWAT weight in DIO mice, reduced transaminase levels, and enhanced glucose tolerance and insulin sensitivity. Further functional characterization in the liver revealed a negative enrichment of genes associated with lipid droplets and fatty acid uptake, increased expression of lipolytic and lipogenic genes, and elevated PKC activity, including PKCζ.
4. Sphingomyelin synthase 2 activity is lower in in livers of mice exhibiting a SphK2-deficiency or treated with S1P lyase inhibitor DOP, both of which have high hepatic ceramide levels.

5. In gWAT of DOP-treated animals, S1P directly activated PKCζ, which mediated activation of HSL-dependent lipolysis, leading to a reduction in adipose tissue mass and decreased cell diameter of fat cells in both gWAT and iWAT. This mechanism was linked to an cAMP/PKA-independent pathway involving MAPK/ERK signaling directly activating HSL.

In this study, sphingolipid metabolism was deliberately altered either by genetic deletion of SphK2 or by pharmacological inhibition of SphK2 and S1P lyase. Across all these models, the induced changes in sphingolipid profiles within plasma, liver, and adipose tissue were consistently associated with metabolic improvements, including reduced body and adipose tissue weight, enhanced glucose tolerance, and improved insulin sensitivity. Notably, plasma levels of S1P, ceramide, and sphingosine were elevated, whereas liver-specific changes more distinctly reflected the effects of the respective interventions.

In examining the intricate role of bioactive sphingolipids, specifically S1P and ceramide, within the context of MetS *in vivo*, researchers encounter significant challenges. Associated comorbidities, including obesity, hypertension, MASLD, and T2D, frequently coexist and influence each other.[316,317] For example, studies investigating S1P in humans often measure circulating S1P, resulting in varied conclusions, as they reported that S1P is positively correlated with a high BMI as well as exhibiting curvilinear associations.[260,309,318]

Different species of ceramides, distinguished solely by acyl chain length, assume distinct roles in MASLD and MASH. Ceramides $C_{16:0}$ and $C_{20:0}$, but not $C_{24:0}$, have been found to positively correlate with MASLD as well as with lipotoxicity, inflammation, oxidative stress, and insulin resistance in both mice and humans.[310] Consequently, while ceramide $C_{16:0}$ and $C_{18:0}$ accumulate during the progression from hepatic steatosis to MASH, ceramides $C_{16:0}$, $C_{22:0}$ and $C_{24:1}$ were elevated in patients with MASH compared to those with MASLD.[240,319]

This highlights not only the complexity of these interconnected disorders, but also the importance of subtle variations in sphingolipid profiles in different organs and plasma, with their detection being a key objective of this study.

5.1 Interventions in Sphingolipid Metabolism Ameliorate Metabolic Dysfunction

In this study, knockout of either SphK1 or SphK2 had distinct effects on the development of metabolic diseases, including obesity, T2D, and MASLD, in an HFD-induced mouse model. To investigate this, both SphK1 and SphK2 knockout mice and WT control mice were subjected to a 12-week high-fat diet regimen and subsequently examined for key metabolic parameters such as insulin sensitivity, glucose tolerance, adiposity, and hepatic lipid accumulation.

5.1.1 Global SphK1 Deficiency Fails to Protect Against Diet-Induced Metabolic Complications

SphK1-deficient mice exhibited severe obesity comparable to WT controls following 12 weeks of HFD feeding, with body weight increasing by over 40% and accompanied by an expansion of adipose tissue mass. Similar observations have been previously documented in global SphK1 knockout mice after extended HFD exposure.[264] Notably, hepatic fibrosis was not observed, acknowledging that no dedicated fibrosis model was employed. However, while earlier studies reported reduced hepatic lipid accumulation, lower fasting plasma insulin and glucose levels, and enhanced systemic insulin sensitivity in SphK1$^{-/-}$ mice, the findings in this study indicated impaired glucose tolerance and diminished insulin sensitivity under similar dietary conditions.

Prior research has demonstrated that SphK1 is upregulated in palmitate-treated adipocytes and hepatocytes, as well as in the adipose tissue of genetically or diet-induced obese mice and obese T2D humans.[264,268,270] Consistent with this, SphK1 overexpression was associated with hepatic lipid accumulation, whereas SphK1 deficiency ameliorated hepatic steatosis in a PPARγ-dependent manner.[270] Further evidence is provided by S1P lyase knockout models, which exhibited elevated hepatic sphingolipid levels, together with excessive lipid accumulation and increased hepatic PPARγ expression, yet paradoxically reduced adipose tissue mass.[320] These findings indicate a tissue-specific role of the S1P/SphK1 axis, a notion further supported by studies in adipocyte-specific SphK1 knockouts, which showed increased adiposity and hepatic lipid accumulation upon HFD feeding, along with impaired glucose tolerance.[271] Together, these observations suggest that SphK1 may exert distinct, even opposing, functions in liver and adipose tissue metabolism.

In the context of diabetes, prior research has demonstrated that SphK1 deficiency results in impaired glucose tolerance due to β-cell loss.[272] In the current study, fasting insulin levels were found to be elevated following 12 weeks of HFD feeding, which is consistent with the compensatory hyperinsulinemia observed in WT mice, preceding the onset of insulin resistance around week 11.[48] Furthermore, in this study SphK1-deficient mice exhibited impaired glucose tolerance and insulin sensitivity under HFD feeding, corroborating previous findings that reported impaired glucose tolerance as early as 8 weeks, with progressive deterioration characterized by reduced fasting insulin levels and β-cell loss by 24 weeks.[272] Mechanistically, treatment with S1P or overexpression of SphK1 in β-cell lines and isolated islets has been shown to confer protection against lipotoxicity and cell death. At the systemic level, systemic SphK1 overexpression improved insulin sensitivity and reduced steatosis in mouse models of diabetes and DIO.[272-274] Together, these findings outline a dynamic progression from early β-cell compensation to later stages of insulin resistance and β-cell failure, with SphK1 being crucial for sustaining metabolic balance. While β-cell function was not addressed within the framework of this study, it should be considered when interpreting the overall effects of S1P.

Taken together, the discrepancies with previously published studies may reflect differences in dietary composition and feeding duration, thereby underscoring the context-dependent nature of the metabolic consequences of global SphK1 deficiency.

5.1.2 Genetic and Pharmacological Targeting of SphK2 Counteracts Diet-Induced Manifestation of Metabolic Diseases

SphK2$^{-/-}$ mice exhibited lower body weight at the onset of the 12-week high-fat diet treatment and were consequently protected from diet-induced weight gain and metabolic deterioration. This included reduced hepatic lipid accumulation, improved glucose tolerance, and enhanced insulin sensitivity.

Consistent with the findings in this study, earlier work also documented the protection of SphK2$^{-/-}$ mice from age-related obesity and insulin resistance, partially attributed to elevated circulating adiponectin, enhanced lipolysis in WAT, and increased energy expenditure.[276] Another study employing a similar HFD regimen (60% kcal from fat for 8 weeks) also observed reduced body and adipose tissue weight in SphK2$^{-/-}$ mice, accompanied by improved glucose tolerance. These benefits were attributed to higher energy expenditure and increased *Ucp1* expression in inguinal WAT.[278] While these

studies primarily focused on WAT, a more liver-centric investigation found that liver-specific SphK2 deficiency exacerbated MASLD, with impaired glucose tolerance and reduced systemic insulin sensitivity. Mechanistically, defective hepatic insulin signaling and Sph-mediated inhibition of Akt phosphorylation contributed to this phenotype.[277] The study by Aji supports the paradigm of selective hepatic insulin resistance, where insulin fails to suppress gluconeogenesis but continues to promote lipogenesis, thereby fueling both steatosis and hyperglycemia.[321,322] However, transcriptomic analysis in the present study demonstrated reduced abundance of gene sets associated with fatty liver and lipid droplets in the livers of HFD-fed SphK2 knockout mice compared to WT controls, consistent with their non-steatotic phenotype. It is also important to consider that, beyond hepatic insulin signaling, other cell types such as adipocytes, skeletal muscle, and pancreatic β-cells significantly contribute to systemic metabolic homeostasis.

Indeed, SphK2 deficiency has been demonstrated to ameliorate the diabetic phenotype in a STZ-treated HFD mouse model by mitigating the reduction of β-cell mass, which may also contribute to the findings reported here.[265,275] Supporting this, the SphK2/S1P axis has been implicated in β-cell protection, mechanistically associated with decreased S1P levels that enhance PHB2 expression, thereby increasing ATP production and oxygen consumption and alleviating cytokine-induced ATP depletion and ER stress.[267] Consistent with the results of the present study, improved glucose tolerance indicates preserved insulin secretion in conjunction with peripheral insulin sensitivity.

In addition to these tissue-specific effects of SphK2 deficiency and the broader SphK2/S1P axis, dietary composition and treatment regimens appear to strongly influence the experimental outcome. Notably, a western diet (~42% kcal from fat and carbohydrates, respectively) has been reported to yield results that contrast with those observed under a classical HFD providing 60% of total energy from fat, such as increased hepatic fat accumulation.[279,281]

In the subsequent phase of this project, pharmacological SphK2 inhibition was evaluated in a therapeutic context. Mice were initially subjected to a HFD for ten weeks, followed by daily intraperitoneal injections of the specific SphK2 inhibitor SLS1081832 (10 mg/kg) for 6 weeks, while continuing the HFD. By the conclusion of this treatment,

the mice exhibited reduced body and adipose tissue weight, decreased hepatic lipid accumulation, and enhanced glucose tolerance and insulin sensitivity compared to vehicle controls. This closely mirrored the characteristics observed in the genetic SphK2 knockout model, which was already resistant to the pathological effects of HFD.

Consistent with these observations, SphK2 inhibitors like ABC294640 (opaganib) and K145 have been studied across various disease settings. Opaganib has progressed to clinical trials for conditions such as advanced solid tumors and COVID-19, whereas K145 has shown antitumor effects both *in vitro* and *in vivo*.[323,324] These compounds have also been tested in liver- and metabolism-related models. For example, opaganib was found to protect against hepatic mitochondrial dysfunction and inflammation, and to facilitate weight loss in obese mice with improved glucose tolerance, either alone or combined with the GLP-1 analogue semaglutide.[325,326] Similarly, K145 reduced hepatic steatosis and restored liver function in ob/ob mice, associated with the downregulation of lipogenic and upregulation of β-oxidation-related gene expression.[325] However, caution is advised, as both ABC294640 and K145 have been reported to exert off-target effects, including inhibition of Degs1 and apparent activation of KDSR, which in some cases resulted in elevated S1P levels.[327,328] In contrast, such alterations were not observed in the livers of mice in the present study, which complicates a direct comparison with published inhibitor data.

Beyond the protective effects of SLS1081832, analyses of liver expression and signaling showed significant similarities to the SphK2 knockout model. Transcriptomic profiling indicated a negative enrichment of gene sets associated with lipid droplets, along with decreased expression of *Cidec* and *Plin2* in mice treated with SLS1081832. In SphK2 knockout mice, *Pparg*, *Plin2*, and *Cidec* expression remained unchanged, likely due to the overnight fasting regimen before tissue collection. By contrast, SLS1081832-treated mice underwent a shorter fasting period, which may explain the differences observed between the groups, as fasting has been shown to attenuate diet-induced changes in these genes.[329]

Regarding lipid metabolism, SphK2$^{-/-}$ mice exhibited increased hepatic *Pnpla2* expression along with lower plasma insulin levels, aligning with previous findings of its suppression under hyperinsulinemic conditions.[330] Although *Pnpla2* overexpression alleviates hepatic steatosis, it does not restore systemic insulin sensitivity, underscoring its hepatoprotective but limited systemic impact.[331] Conversely, SLS1081832 treatment

led to an upregulation of lipogenic enzymes (*Acc1* and *Fasn*) despite a tendency for reduced lipid droplet formation. This contrasts with results in ob/ob mice, treated with the SphK2 inhibitor K145, where hepatic *Acc1* and *Fasn* expression decreased.[325] The differing regulation likely reflects model-specific variations as K145 reduces hyperinsulinemia and systemic insulin resistance in ob/ob mice and thus SREBP1c-driven lipogenesis, while HFD-fed mice develop selective insulin resistance and may activate compensatory lipogenic pathways upon SphK2.

A common feature in both pharmacological and genetic inhibition of SphK2 was the reduced *Cd36* expression, with knockout mice also showing decreases at the protein level. Since CD36 facilitates fatty acid uptake and promotes lipogenesis, its downregulation is consistent with reduced hepatic lipid accumulation in CD36-deficient mouse models.[332,333] Additionally, as CD36 expression is induced by insulin, the lower insulin levels in SphK2-deficient and inhibitor-treated models in this study provide a plausible explanation.[334] An alternative mechanism might involve the SphK2–S1P–HDAC pathway. When nuclear SphK2 is inhibited, the levels of nuclear S1P decrease, which in turn alleviates the S1P-induced suppression of HDAC1/2.[207,335] Given that HDAC1/2 activity suppresses the transcription of *Cd36*, as demonstrated by Li and colleagues, the lack of S1P-mediated inhibition of HDAC1/2 offers a reasonable explanation for the observed decrease in *Cd36* in this study.[336]
In addition, common observations associated with SphK2 knockout and pharmacologic SphK2 inhibition, which include elevated ceramide levels and PKCζ phosphorylation in the liver, as well as increased plasma S1P levels will, be discussed in detail in a subsequent Section (5.1.3).

5.1.3 Therapeutic Inhibition of S1P Lyase Ameliorates Obesity and Metabolic Decline

As a secondary approach, a therapeutic strategy was implemented, wherein mice were subjected to a 10-week HFD treatment and were subsequently treated with the S1P lyase inhibitor DOP (180 mg/L in drinking water) for an additional 6 weeks. Previous research has indicated that global Sgpl1 knockout mice typically survive only up to approximately six weeks of age.[337] Since this study focused on diet-induced metabolic abnormalities and a global knockout would have required a dietary regimen exceeding

the animals' lifespan, pharmacological inhibition of S1P lyase represented a feasible approach.

In HFD-fed mice, DOP administration resulted in lower body and WAT weight. Notably, although improved liver function was evidenced by decreased markers of hepatic injury, specifically GPT/ALT and GOT/AST, the levels of hepatic lipids remained largely unchanged. Indeed, Sgpl1$^{-/-}$ mice were shown to exhibit reduced postnatal growth and weight gain, characterized by decreased adipose tissue mass but an increased number and size of hepatic lipid droplets.[320,337] This observation supports the hypothesis that DOP treatment of adult mice does not alter hepatic lipid deposition, despite negative enrichment of lipid droplet-associated genes.[320] Additionally, elevations in sphingolipids, such as S1P and ceramide, were observed in both serum and liver, a finding replicated in the present study under HFD conditions with the additional application of the S1P lyase inhibitor DOP. An alternative method to reduce S1P lyase activity involved exposure to polycyclic aromatic hydrocarbons (PAH), which oxidize Cys317 of S1P lyase, thereby impairing lyase function and activating SphK1, ultimately increasing S1P levels.[338] In HFD-fed mice, PAH treatment exacerbated MASLD, whereas Sgpl1 knock-in mice were protected from PAH-induced exacerbation.[339] Thus, intrahepatic S1P accumulation may facilitate lipid deposition. Conversely, a recent study reported that HFD-fed Sgpl1 knock-in mice exhibited reduced circulating S1P levels but developed a higher MASLD score and worsened glucose intolerance.[340]

To mechanistically link hepatic steatosis and its underlying pathways, gene expressional analysis of key metabolic genes was conducted. Bektas *et al*. identified widespread transcriptional changes in Sgpl1$^{-/-}$ livers, including increased hepatic *Pparg* expression, while Kuo *et al.* corroborated that Sgpl1-deficient mice on a HFD exhibited increased elevated hepatic *Pparg and Cd36*, *Acc1*, and *Fasn*.[320,339] Conversely, liver-specific deletion of Sgpl1, which increased hepatic S1P and slightly augmented neutral lipid droplets, did not affect *Pparg* expression.[341]

In contrast to these models, the HFD+DOP model was applied in this study, which resulted in elevated systemic and hepatic S1P levels and led to a reduction in hepatic *Pparg* and its target gene *Cidea*, accompanied by decreased CD36 protein levels. Although discrepancies with published findings may partially be attributed to the overnight-fasted state of mice, the observed downregulation of *Pparg*, *Cidea*, and CD36 suggests a shift away from lipid storage, as these factors are typically elevated under

steatotic conditions.[342] Supporting this, high S1P levels in 3T3-L1 adipocytes and primary osteoblasts lead to downregulation of *Pparg*, thereby hindering adipogenic differentiation.[309,312] Concurrently, an upregulation of lipolytic genes (*Pnpla2* and *Lipe)* as well as lipogenic genes (*Acc1* and *Fasn*) was observed. While the upregulation of *Acc1* and *Fasn* aligns with reports of similar models, the simultaneous induction of *Fasn* and *Pnpla2* indicates an increased lipid turnover, a phenomenon known to occur during β-adrenergic stimulation in BAT.[343]

Further characterization of HFD-fed mice treated with the S1P lyase inhibitor DOP revealed altered glucose homeostasis. Despite elevated fasting glucose levels, these mice displayed improved systemic glucose tolerance and insulin sensitivity, along with reduced fasting insulin levels. Interestingly, studies in mouse embryonic fibroblasts (MEF) identified a potential mechanism, where S1P accumulation due to S1P lyase deficiency can enhance glucose uptake and aerobic glycolysis via S1PR1-3-mediated HIF-1 signaling, while autophagy is suppressed through the Akt/mTOR pathway.[344] Contrarily, earlier research from our group demonstrated that elevated circulating S1P, induced by Sgpl1 deficiency, Sgpl1 inhibition, or HFD, reduced red blood cell (RBC) glucose uptake in a PP2A-dependent manner.[345] In C2C12 myoblasts, S1P also increased S1PR-dependent intracellular Ca^{2+}, triggering ROS-mediated oxidation and inactivation of PTP1B, which subsequently trans-activated the insulin receptor promoting glucose uptake.[346] Since this study primarily focused on hepatic and adipose lipid metabolism, the S1P-dependent regulation of glucose handling in peripheral tissues such as skeletal muscle, which accounts for the majority of whole-body glucose disposal, may contribute to the improved systemic glucose tolerance reported here.[347] Collectively, these studies underscore the important tissue- and cell-type-specific functions of S1P.

Finally, further alterations in the hepatic sphingolipidome, including increased ceramides, S1P, and Sph, along with enhanced PKC phosphorylation, particularly of PKCζ, will be discussed in the context of preceding and following findings in Section 5.3.1.

5.2 Intracellular S1P Mediates Lipolytic Activity in Adipocytes via a PKCζ/MAPK/HSL Pathway

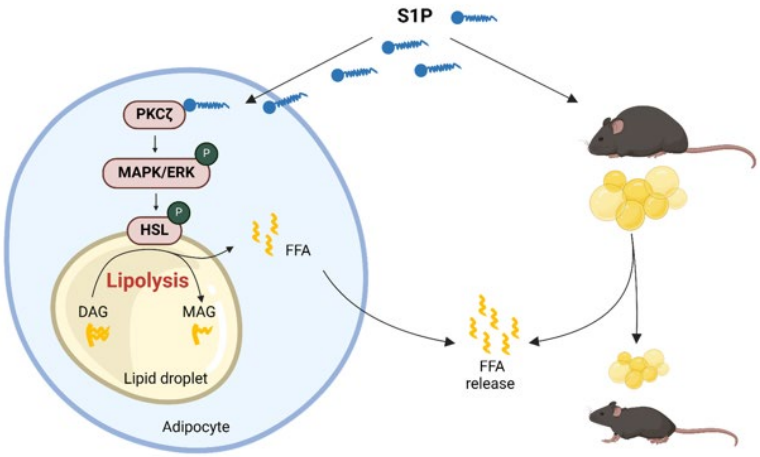

Figure 30. Proposed mechanism of intracellular S1P-mediated activation of lipolysis in adipocytes. Intracellular sphingosine-1-phosphate (S1P) directly activates PKCζ, which subsequently phosphorylates the MAPK/ERK pathway. This ultimately results in the phosphorylation of hormone-sensitive lipase (HSL) and the stimulation of lipolysis in 3T3-L1 cells. The inhibition of S1P degradation, achieved with S1PL-IN-1, further amplifies this effect in both 3T3-L1 cells and primary adipocytes *in vitro*. *In vivo* studies demonstrate that pharmacological inhibition of S1P lyase using 4-deoxypyridoxine (DOP) in HFD-fed mice enhances lipolytic activity, leading to a reduction in adipose tissue mass and increased activation of PKCζ. Parts of the figure were created with BioRender.com. Published under BioRender Publication License.

This study identified S1P as a potent intracellular activator of PKCζ, which subsequently initiates MAPK/ERK signaling and leads to the activation of the lipolytic pathway via HSL. The proposed mechanism shown in a graphical abstract in Figure 30 (page 113) contrasts with previous evidence suggesting that S1P activates PI3K signaling through S1P receptors, which can also activate PKCζ, indicating an extracellular mechanism.[196] However, the results demonstrated that neither inhibition of AC by SQ22536 nor PI3K signaling using Wortmannin abrogated the lipolytic effect of S1P, which is only effective at concentrations between 5 and 50 µM, exceeding the Kd of S1PRs.[190] Pointing to an intracellular mechanism, treatment with S1PR1-3 agonists AUY954, CYM5520, and CYM5541 failed to induce lipolysis, even at equimolar concentrations to S1P. Supporting this, S1PR-dependent activation of $G_{\alpha i}$ inhibits AC, thereby lowering cAMP levels and suppressing lipolysis. This mechanism resembles the antilipolytic action of insulin, which reduces cAMP signaling through activation of PDE3B.[199] Additionally, $G_{\alpha i}$-induced activation of PI3K engages the insulin-pathway and feeds into a non-canonical pathway described to Akt-independently interfere with PKA-mediated phosphorylation of perilipin, but not HSL.[192,348] These studies suggest

an opposite effect, further excluding receptor-mediated induction of lipolysis and shifting the focus to intracellular S1P.

Elevation of intracellular S1P levels in differentiated 3T3-L1 cells and murine primary adipocytes was achieved either by extracellular S1P supplementation, resulting in an intracellular increase by 19.3-fold after 30 minutes, or by inhibition of S1P lyase with the inhibitor S1PL-IN-1. *In vivo*, elevated S1P levels were attained through S1P lyase inhibition via DOP-treatment. Elevated S1P levels in the body, particularly within adipose tissue, correlated with the activation of PKCζ and HSL in adipose tissue. These changes were accompanied by physiological changes, including a reduction in adipocyte size, adipose tissue mass, and overall body weight, thereby substantiating the role of S1P in promoting lipolysis *in vivo*.

PKCζ is one of two atypical PKCs, with the other being PKC lambda in mice (iota in humans).[314] The activation of atypical PKCs is distinct in that it does not rely on DAG, but rather on binding to protein scaffolds and lipid mediators such as PA, phosphatidylserine, and the bioactive sphingolipids S1P and ceramide.[204,308] The involvement of ceramide in the proposed mechanism has been excluded, as S1P treatment of 3T3-L1 cells resulted in elevated intracellular S1P levels without a corresponding increase in ceramide levels. Supporting this mechanism, it has been documented that PMA induces aPKCs in differentiated 3T3-L1 cells, similarly stimulating lipolysis by activating HSL via MAPK/ERK, acting independently of cAMP/PKA-dependent activation of lipolysis.[349] Notably, the mechanistic insights of the present study are largely based on inhibitor studies. Genetic interference approaches, such as retroviral expression of dominant-negative PKCζ, were unsuccessful, due to the low transduction efficiency in 3T3-L1 cells.[350] Consequently, this study concludes that intracellular S1P promotes HSL-mediated lipolysis independently of cAMP/PKA by activating MAPK/ERK through direct activation of PKCζ.

5.3 Ceramides Exert Multifaceted Functions in Metabolic Health

Contrary to a plethora of prior studies, this investigation identified elevated hepatic ceramide levels concomitant with metabolic improvements. Ceramides are typically linked to negative outcomes such as obesity, T2D, MASLD-HCC progression, and heart failure.[240,242,351] In both humans and mice, ceramides of varying chain lengths accumulate in the liver and plasma under conditions of obesity, MASLD, and T2D.[240] Targeted downregulation of ceramides, particularly $Cer_{16:0}$ has been demonstrated to

reverse these effects.[242] However, beneficial effects have also been documented for $Cer_{24:1}$, for instance, in the context of T1D.[257,258]

Notably, the current study did not observe higher hepatic ceramide levels after 12 or 16 weeks of HFD compared with NC. Previous studies of modest increases in $Cer_{16:0}$ and total ceramides have typically utilized diets with a different composition, particularly those with a higher palmitate content, compared to the diet employed in this study.[231,240] Human biopsy studies similarly demonstrate yet moderate increases in hepatic ceramides in diabetic versus non-diabetic patients.[226,319]

In the present study, total hepatic ceramides ($Cer_{16:0}$, $Cer_{18:0}$, $Cer_{20:0}$, $Cer_{22:0}$, $Cer_{24:0}$, and $Cer_{24:1}$) were consistently elevated following either genetic ablation of SphK2 or pharmacological inhibition of SphK2 and S1P lyase compared to HFD-fed controls. Significantly, $Cer_{22:0}$, $Cer_{24:0}$, and $Cer_{24:1}$ demonstrated the highest concentrations in the liver. Notably, $Cer_{24:1}$ has been identified as having favorable impact on disease outcomes in the context of DIO and T1D.[257,258] Despite these significantly elevated hepatic ceramide levels, the beneficial effects observed in this study appear to be attributable to distinct underlying mechanisms.

5.3.1 Ceramide-Induced PKCζ Activation in Metabolic Regulation

Based on the findings from all experimental approaches, several observations across all interventions were noted, indicating metabolic improvements. These include reduced adipose lipid deposition, improved systemic insulin sensitivity, consistent upregulation of PKCζ activity, and decreased expression of CD36 together with increased expression of lipolytic genes. Ceramides have been identified as mechanistic suppressors of the β-adrenoreceptor-induced activation of HSL via PP2A in brown adipocytes, acting independently of atypical PKCs but involving the cAMP/PKA pathway.[352] Consistently, inhibition of AC with SQ22536 in this study excluded this route as a mediator of S1P's lipolytic effect in white adipose tissue.

Apart from this, ceramides have been shown to act as intermediates in G_i-coupled GPCR signaling, as seen in the activation of PKCζ through lipopolysaccharides (LPS).[353] Notably, ceramides can also directly activate PKCζ, enhancing kinase activity at sub-nanomolar concentrations by interacting with amino acids 405–592 in the C-terminal sequence.[354-356] Indeed, both SphK2-deficiency and DOP-treatment in HFD-fed mice, resulted in increased hepatic ceramide levels, whereas no changes were observed in WAT of SphK2-deficient mice (Appendix Figure 3). This was accompanied

by elevated activity of atypical PKCs, including PKCζ, suggesting ceramides may similarly modulate lipolysis activation through PKCζ in the liver. PI3K-mediated activation of PKCζ has further been reported to contribute to insulin-stimulated glucose uptake in metabolic studies involving white and brown adipocytes.[357,358]

However, excessive aPKC activation has been linked to aggravated insulin resistance. Mechanistically, two pathways have been proposed: Firstly, ceramide has been demonstrated to stimulate dephosphorylation of Akt by PP2A.[359] Secondly, increased ceramide levels displace Akt, thereby preventing its phosphorylation and subsequent binding to PIP_3.[360] As a result, FOXO1 remains transcriptionally active, which not only perpetuates impaired insulin signaling but also induces lipolysis in hepatocytes, including increased expression of *Pnpla2*.[361,362] In line with these reports, the concomitant increase in active PKCζ together with enhanced lipolysis and reduced CD36 expression observed in this study may indicate that ceramide-induced FOXO1 activity contributes to the reduced hepatic lipid burden, thereby providing a plausible mechanism to the findings.

Additionally, activation of aPKCλ/ζ through PI3K has been reported to induce insulin-dependent SREBP1c expression and CD36-mediated lipid uptake in the liver.[363] In line with this, lowering ceramide levels through ceramidase overexpression has been shown to reverse insulin resistance and hepatic steatosis by reducing PKCζ activtiy.[253] Together, these studies support a model in which ceramides promote PKCζ activation to enhance *CD36* expression and lipid accumulation. In contrast, despite markedly elevated ceramides and increased PKCζ activity within this study, *CD36* expression was consistently reduced. This was accompanied by improved insulin sensitivity and reduced hepatic lipid deposition, suggesting that ceramide levels may drive divergence from the canonical ceramide/PKCζ/CD36 axis.

These ceramide levels may reflect a chain length-defined ceramide increase rather than an increase of total ceramide levels. Alternatively, elevated plasma S1P could counteract negative ceramide effects reported in earlier studies. Together, these observations underscore the importance of the S1P/ceramide rheostat for elucidating cellular mechanisms. In this context, defining the net effect of S1P independent of ceramide elevation remains a key objective.

5.3.2 Elevated Hepatic Ceramide Correlates with Reduced SMS2 Activity

Considering the markedly elevated hepatic ceramide levels, the activity of SMS2 was subsequently investigated, given that SMS2 is the isoform responsible for the conversion of ceramide to SM in the liver.[364] SMS2 assays of ceramide-rich liver homogenates from SphK2$^{-/-}$ as well as DOP-treated mice demonstrated a reduction in SMS2 activity compared to controls. The dose-response curve turned out to be bell-shaped. Notably, S1P did not influence SMS2 activity, whereas Sph enhanced activity in WT liver homogenates. These findings provide the first evidence that ceramide may function as a substrate inhibitor of SMS2, a regulatory mode not previously described. Notably, SMS2 undergoes posttranslational modifications, such as C-terminal S-palmitoylation, which regulates its plasma membrane localization without affecting its catalytic activity.[365] Considering that substrate inhibition of SMS2 is expected to diminish SMS2-derived production of DAG, the conventional activator of classical PKCs, the current findings present a paradox:[366] despite reduced SMS2 activity, there is an increase in PKC phosphorylation, suggesting a DAG-independent PKC signaling pathway.

Nevertheless, reduced SMS2 activity has been consistently associated with favorable metabolic outcomes. SMS2-deficiency confers protection against atherosclerosis by promoting cholesterol efflux from macrophages, whereas liver-specific overexpression has the opposite effect.[311] Similarly, liver-specific overexpression of SMS2 increases fatty acid uptake and steatosis, while a global knockout prevents steatosis, albeit not preventing fibrotic lesions.[254,255] Pharmacological inhibition with LY93 under HFD conditions improved insulin sensitivity and enhanced Akt phosphorylation.[256] *In vitro*, ceramide treatment of Huh7 cells resulted in a reduction of *Pparg*, *Cd36,* and *Fsp27/Cidec* expression, consistent with the current study.[254] Additionally, in palmitate-treated MEFs, SMS2 knockout preserved insulin signaling, highlighting that GPCR5B-driven SMS2 activation promotes lipid-induced insulin resistance through DAG.[367]

In conclusion, although the reason or precise mechanism by which elevated ceramide inhibits SMS2 remains unclear, this effect may contribute to ceramide accumulation while simultaneously inducing protective metabolic adaptations evidenced by findings from SMS2-deficient models. Future studies should validate substrate inhibition of SMS2 in reconstituted membrane systems with defined, physiologically relevant lipid

compositions. Finally, this mechanism may contribute to the observed metabolic benefits, in addition to direct S1P effects and modulation of the S1P/ceramide axis, as well as potential effects of ceramides themselves.

5.4 Diagnostic and Regulatory Potential of Sphingolipid Metabolism in Metabolic Disease

Sphingolipids are recognized as pivotal regulators of lipid and glucose metabolism and insulin homeostasis, with even minor alterations exerting either detrimental or protective effects on the progression of metabolic diseases. Fatty acids such as palmitate disrupt the tightly regulated equilibrium, leading to tissue specific consequences.[295]

In the liver, ceramides[240,253,319] and S1P[261-263] have been implicated in disease progression, with elevated S1P promoting lipogenic expression (*Pparg*, *Cd36, Acc1*, and *Fasn*),[320,337-339] whereas reduced S1P correlates with enhanced lipolytic gene expression (*Pnpla2* and *Cd36*),[330] consistent with the present findings. Whereas low levels correlate with enhanced lipolytic gene expression, as observed in the present study. While elevations in hepatic Sph have been associated with systemic insulin resistance,[277] this study observed improved systemic insulin sensitivity. In line with this complexity, impaired insulin tolerance in HFD-fed SphK1$^{-/-}$ mice[271,272] aligning to the present study contrasts with improved insulin sensitivity reported in other studies.[264,270] Moreover, mitochondria-associated $Cer_{16:0}$ negatively influences lipid deposition and systemic glucose control,[241-243,247] whereas $Cer_{24:1}$ enhances hepatic β-oxidation and confers metabolic protection.[257,258] In this study, ceramides may exert beneficial effects by reducing SMS2 activity and activating of PKCζ, thus enhancing lipolytic potential.

In adipose tissue**,** S1P[264,309] and ceramide[232,238,239,253] are generally linked to adverse metabolic outcomes. Yet, while reduced S1P increased UCP1 expression in an earlier work,[278] the current findings indicate that elevated S1P can also stimulate lipolysis via a PKCζ/MAPK/HSL pathway. In β-cells, S1P has been reported to promote insulin secretion[265,267] and protect against β-cell loss,[272] whereas SphK2 deficiency was shown to prevent lipotoxic β-cell death.[275] In skeletal muscle, S1P enhances glucose uptake through S1PR signaling[344,346] and improves insulin sensitivity,[274] while intracellular S1P in RBCs reduces uptake.[345]

Collectively, these observations underscore the necessity of a tightly regulated sphingolipid metabolism to maintain tissue-specific functions.

Comprehensive understanding of this is from translational relevance in the development of diagnostic biomarkers and targeting strategies. A recent multi-omics study on MASLD-HCC progression identified dysregulated key sphingolipid genes (CerS6, SPTLC2, and S1PR1) accompanied by altered metabolite profiles in serum and liver, providing prognostic significance.[368] Dihydroceramides have similarly been proposed as early markers for T2D and MASLD.[369,370] Ratios such as circulating $Cer_{16:0}/Cer_{24:0}$ or $Cer_{16:0}/Cer_{24:1}$ were associated with the prediction of heart failure and insulin resistance, respectively.[371,372] Based on such concepts, the ceramide-based CERT1 (Ceramide test 1) score was developed to predict cardiovascular mortality using ceramide ratios to $Cer_{24:0}$, and further refined into CERT2 by incorporation of phosphatidylcholines.[373,374] Building on these concepts, a risk score derived from circulating dhS1P/dhSph (dihydro-S1P/dihydrosphingosine) ratios has been developed for the prediction of T2D, thereby highlighting the translational potential of sphingolipid-based models.[375] Similarly, serum C18:1-ceramide has recently been proposed as a potential biomarker for the early detection of gestational diabetes, further expanding the clinical spectrum of sphingolipid-based risk stratification.[376] Furthermore, a study that identified distinct plasma sphingolipid profiles in normal-weight and obese subjects proposed their use as a biochemical tool for diagnosing metabolic syndrome, thereby emphasizing the value of sphingolipid signatures beyond single lipid ratios.[377]

A key challenge remains the heterogeneity of metabolic diseases with variable stages, symptoms, and comorbidities, limiting the universal applicability of risk scores. Here, artificial intelligence (AI) and deep learning provide new opportunities.[378] For example, the MELD-Plus score, a machine-learning extension of the classical MELD score for end-stage liver disease (MELD), integrates additional clinical and laboratory parameters to improve prediction of 90-day mortality following hospital admission.[379]

Together, these advances suggest that integrating sphingolipid biology with data-driven approaches may enable more accurate diagnostics and enable personalized therapeutic strategies for MetS, obesity, MASLD, T2D, and cardiometabolic disease.

5.5 Outlook

This study offers significant insights into the role of sphingolipids in the development and progression of metabolic diseases. Specifically, S1P and ceramide, recognized as bioactive sphingolipids, exhibit tissue- and cell-type specific functions. By intervening in the tightly regulated sphingolipid metabolism, this study revealed that extensive changes in sphingolipid profiles ultimately lead to an improved metabolic status. Elevated levels of hepatic ceramides were shown to potentially contribute to protection from lipid accumulation and activation of lipolysis through PKCζ, while diverging from canonical mechanisms. Similarly, beyond established pathways, S1P mediated adipose tissue lipolysis via a PKCζ/MAPK/HSL signaling pathway. These findings underscore that subtle changes in the sphingolipid pathway may lead to tissue-related implications, thereby promoting broader variations impacting whole-body metabolism. As MetS comprises various diseases with rising incidences, affecting millions globally, the need for effective therapies to combat the associated metabolic complications becomes increasingly vital.

The results of this study, in conjunction with existing literature, highlight the challenges of developing targeting strategies. Bioactive sphingolipids exert broad and sometimes opposing effects, depending on the tissues and processes involved, which are often interrelated. Most studies that propose mechanisms are based on experiments in cell lines neglecting potential cell-type interactions. Nevertheless, from these initial insights further approaches might extend to combining this knowledge towards identifying potential global or tissue-specific targets. Although tissue-specific knockouts mainly capture organ-intrinsic aspects of disease development, they also allow for the exploration of inter-organ communication and its contribution to metabolic dysregulation.

As tissue-specific actions of bioactive sphingolipids are considered crucial in the overall picture of MetS development, this study lacks insights into the dual effects of β-cell insulin secretion and muscle glucose disposal. While S1P has been described to facilitate insulin secretion, hyperinsulinemic-euglycemic clamp studies in mice should be conducted in similar experimental and therapeutic setups, including examination of SphK2$^{-/-}$ deficiency and SGPL1 inhibition using DOP. This will provide insights into insulin sensitivity, endogenous glucose production, and tissue-specific glucose uptake. It is also crucial to include measurements of sphingolipid levels in skeletal muscle tissues to elaborate the influence of S1P and ceramide on the muscle, ultimately shaping

whole-body glucose metabolism, as systemic glucose uptake is primarily muscle-dependent. Moreover, energy expenditure should be characterized by indirect calorimetry, and brown adipose tissue function should be systematically assessed to clarify their contributions to the phenotype.

While this study proposed a mechanism, where S1P induces adipose tissue lipolysis through a PKCζ/MAPK/HSL signaling pathway, the actions of ceramide and ceramide-induced PKCζ in the liver contributing to a lipolytic rather than lipid-storing state remain to be elucidated. To dissect exact mechanisms underlying possible ceramide-dependent activation of lipolysis, potentially beyond established models, future studies should test varying ceramide doses. For example, overexpression of CerS2 in primary hepatocytes might be implemented to gain mechanistic insights and to evaluate the proposed mechanism.

It is evident that the sphingolipid rheostat, characterized by the dynamic equilibrium between intracellular concentrations of bioactive sphingolipids, particularly S1P and ceramide, holds significant potential for future therapeutic strategies. Minor modifications in this rheostat not only indicate metabolic changes but also affect circulating sphingolipid levels, thereby presenting diagnostic and therapeutic opportunities. Distinct sphingolipid patterns, which reflect various symptom constellations within the MetS, may assist in identifying specific signatures associated with the onset and progression of diseases such as T2D, MASLD or progressive liver disease. Translating these signatures into clinical manifestations in human patients could facilitate the definition of potential risk scores and expand diagnostic possibilities. Furthermore, pharmacological therapies developed concurrently may target these signatures and restore them to physiological levels.

This research thus lays the groundwork for identifying sphingolipid-based therapeutic targets and developing clinically applicable signatures to enhance diagnosis and risk prediction, ultimately enabling more targeted treatment strategies in metabolic disorders.

References

1. Chew, N.W.S., Ng, C.H., Tan, D.J.H.*, et al.* The global burden of metabolic disease: Data from 2000 to 2019. *Cell Metab* 35, 414-428 e413 (2023).
2. Reaven, G.M. Banting lecture 1988. Role of insulin resistance in human disease. *Diabetes* 37, 1595-1607 (1988).
3. Eckel, R.H., Grundy, S.M. & Zimmet, P.Z. The metabolic syndrome. *The Lancet* 365, 1415-1428 (2005).
4. Alberti, K.G., Zimmet, P. & Shaw, J. Metabolic syndrome - a new world-wide definition. A Consensus Statement from the International Diabetes Federation. *Diabet Med* 23, 469-480 (2006).
5. Grundy, S.M., Cleeman, J.I., Daniels, S.R.*, et al.* Diagnosis and management of the metabolic syndrome: an American Heart Association/National Heart, Lung, and Blood Institute Scientific Statement. *Circulation* 112, 2735-2752 (2005).
6. Alberti, K.G. & Zimmet, P.Z. Definition, diagnosis and classification of diabetes mellitus and its complications. Part 1: diagnosis and classification of diabetes mellitus provisional report of a WHO consultation. *Diabet Med* 15, 539-553 (1998).
7. Fathi Dizaji, B. The investigations of genetic determinants of the metabolic syndrome. *Diabetes Metab Syndr* 12, 783-789 (2018).
8. Matsuzawa, Y., Funahashi, T. & Nakamura, T. The Concept of Metabolic Syndrome: Contribution of Visceral Fat Accumulation and Its Molecular Mechanism. *Journal of Atherosclerosis and Thrombosis* 18, 629-639 (2011).
9. Trayhurn, P. & Wood, I.S. Adipokines: inflammation and the pleiotropic role of white adipose tissue. *Br J Nutr* 92, 347-355 (2004).
10. Juhan-Vague, I., Alessi, M.C., Mavri, A. & Morange, P.E. Plasminogen activator inhibitor-1, inflammation, obesity, insulin resistance and vascular risk. *J Thromb Haemost* 1, 1575-1579 (2003).
11. (WHO), W.H.O. Cardiovascular diseases. (2024, July 17).
12. WHO, I. Obesity and overweight. (2024).
13. Lingvay, I., Cohen, R.V., Roux, C.W.l. & Sumithran, P. Obesity in adults. *The Lancet* 404, 972-987 (2024).
14. Hales, C.M., Fryar, C.D., Carroll, M.D., Freedman, D.S. & Ogden, C.L. Trends in Obesity and Severe Obesity Prevalence in US Youth and Adults by Sex and Age, 2007-2008 to 2015-2016. *Jama* 319, 1723-1725 (2018).
15. Rubino, F., Batterham, R.L., Koch, M.*, et al.* Lancet Diabetes & Endocrinology Commission on the Definition and Diagnosis of Clinical Obesity. *The Lancet Diabetes & Endocrinology* 11, 226-228 (2023).
16. Haslam, D.W. & James, W.P.T. Obesity. *The Lancet* 366, 1197-1209 (2005).
17. Chater, A., Chadwick, P., Gillison, F.*, et al. BPS 2019 - Psychological Perspectives on Obesity - Addressing Policy, Practice, and Research Priorities*, (2019).
18. Locke, A.E., Kahali, B., Berndt, S.I.*, et al.* Genetic studies of body mass index yield new insights for obesity biology. *Nature* 518, 197-206 (2015).
19. Schwartz, M.W., Seeley, R.J., Zeltser, L.M.*, et al.* Obesity Pathogenesis: An Endocrine Society Scientific Statement. *Endocrine Reviews* 38, 267-296 (2017).
20. Alvarez-Llamas, G., Szalowska, E., de Vries, M.P.*, et al.* Characterization of the Human Visceral Adipose Tissue Secretome. *Molecular & Cellular Proteomics* 6, 589-600 (2007).
21. Börgeson, E., Boucher, J. & Hagberg, C.E. Of mice and men: Pinpointing species differences in adipose tissue biology. *Frontiers in Cell and Developmental Biology* Volume 10 - 2022(2022).
22. Matsuzawa, Y., Shimomura, I., Nakamura, T., Keno, Y. & Tokunaga, K. Pathophysiology and pathogenesis of visceral fat obesity. *Ann N Y Acad Sci* 676, 270-278 (1993).
23. Richard, D. & Picard, F. Brown fat biology and thermogenesis. *Front Biosci (Landmark Ed)* 16, 1233-1260 (2011).

24. Lafontan, M. Adipose tissue and adipocyte dysregulation. *Diabetes & Metabolism* 40, 16-28 (2014).
25. Birsoy, K., Festuccia, W.T. & Laplante, M. A comparative perspective on lipid storage in animals. *Journal of Cell Science* 126, 1541-1552 (2013).
26. McLaughlin, T., Craig, C., Liu, L.F.*, et al.* Adipose Cell Size and Regional Fat Deposition as Predictors of Metabolic Response to Overfeeding in Insulin-Resistant and Insulin-Sensitive Humans. *Diabetes* 65, 1245-1254 (2016).
27. Hirsch, J. & Batchelor, B. Adipose tissue cellularity in human obesity. *Clin Endocrinol Metab* 5, 299-311 (1976).
28. Lönn, M., Mehlig, K., Bengtsson, C. & Lissner, L. Adipocyte size predicts incidence of type 2 diabetes in women. *Faseb J* 24, 326-331 (2010).
29. Jamdar, S.C. & Fang Cao, W. Triacylglycerol biosynthetic enzymes in lean and obese Zucker rats. *Biochimica et Biophysica Acta (BBA) - Lipids and Lipid Metabolism* 1255, 237-243 (1995).
30. Chitraju, C., Walther, T.C. & Farese, R.V., Jr. The triglyceride synthesis enzymes DGAT1 and DGAT2 have distinct and overlapping functions in adipocytes. *J Lipid Res* 60, 1112-1120 (2019).
31. Weisberg, S.P., McCann, D., Desai, M.*, et al.* Obesity is associated with macrophage accumulation in adipose tissue. *J Clin Invest* 112, 1796-1808 (2003).
32. Lumeng, C.N., Bodzin, J.L. & Saltiel, A.R. Obesity induces a phenotypic switch in adipose tissue macrophage polarization. *J Clin Invest* 117, 175-184 (2007).
33. de Candia, P., Prattichizzo, F., Garavelli, S.*, et al.* The pleiotropic roles of leptin in metabolism, immunity, and cancer. *J Exp Med* 218(2021).
34. Coleman, D.L. Obese and diabetes: two mutant genes causing diabetes-obesity syndromes in mice. *Diabetologia* 14, 141-148 (1978).
35. Lee, Y.S. & Olefsky, J. Chronic tissue inflammation and metabolic disease. *Genes Dev* 35, 307-328 (2021).
36. Guilherme, A., Virbasius, J.V., Puri, V. & Czech, M.P. Adipocyte dysfunctions linking obesity to insulin resistance and type 2 diabetes. *Nat Rev Mol Cell Biol* 9, 367-377 (2008).
37. Virtue, S. & Vidal-Puig, A. Adipose tissue expandability, lipotoxicity and the Metabolic Syndrome — An allostatic perspective. *Biochimica et Biophysica Acta (BBA) - Molecular and Cell Biology of Lipids* 1801, 338-349 (2010).
38. Turner, N., Kowalski, G.M., Leslie, S.J.*, et al.* Distinct patterns of tissue-specific lipid accumulation during the induction of insulin resistance in mice by high-fat feeding. *Diabetologia* 56, 1638-1648 (2013).
39. Choi, S. & Snider, A.J. Sphingolipids in High Fat Diet and Obesity-Related Diseases. *Mediators Inflamm* 2015, 520618 (2015).
40. Chen, H.C., Stone, S.J., Zhou, P., Buhman, K.K. & Farese, R.V., Jr. Dissociation of obesity and impaired glucose disposal in mice overexpressing acyl coenzyme a:diacylglycerol acyltransferase 1 in white adipose tissue. *Diabetes* 51, 3189-3195 (2002).
41. Federation, I.D. IDF Diabetes Atlas. (Brussels, Belgium, 2025).
42. Roden, M. & Shulman, G.I. The integrative biology of type 2 diabetes. *Nature* 576, 51-60 (2019).
43. Ferrannini, E. & Mari, A. Beta cell function and its relation to insulin action in humans: a critical appraisal. *Diabetologia* 47, 943-956 (2004).
44. Saisho, Y., Butler, A.E., Manesso, E.*, et al.* β-cell mass and turnover in humans: effects of obesity and aging. *Diabetes Care* 36, 111-117 (2013).
45. Hanley, S.C., Austin, E., Assouline-Thomas, B.a.*, et al.* β-Cell Mass Dynamics and Islet Cell Plasticity in Human Type 2 Diabetes. *Endocrinology* 151, 1462-1472 (2010).
46. Hull, R.L., Kodama, K., Utzschneider, K.M.*, et al.* Dietary-fat-induced obesity in mice results in beta cell hyperplasia but not increased insulin release: evidence for specificity of impaired beta cell adaptation. *Diabetologia* 48, 1350-1358 (2005).

47. Jetton, T.L., Lausier, J., LaRock, K.*, et al.* Mechanisms of Compensatory β-Cell Growth in Insulin-Resistant Rats : Roles of Akt Kinase. *Diabetes* 54, 2294-2304 (2005).
48. Mosser, R.E., Maulis, M.F., Moullé, V.S.*, et al.* High-fat diet-induced β-cell proliferation occurs prior to insulin resistance in C57Bl/6J male mice. *Am J Physiol Endocrinol Metab* 308, E573-582 (2015).
49. Christensen, A.A. & Gannon, M. The Beta Cell in Type 2 Diabetes. *Curr Diab Rep* 19, 81 (2019).
50. Swisa, A., Glaser, B. & Dor, Y. Metabolic Stress and Compromised Identity of Pancreatic Beta Cells. *Front Genet* 8, 21 (2017).
51. Güemes, M., Rahman, S.A. & Hussain, K. What is a normal blood glucose? *Arch Dis Child* 101, 569-574 (2016).
52. Jiang, G. & Zhang, B.B. Glucagon and regulation of glucose metabolism. *Am J Physiol Endocrinol Metab* 284, E671-678 (2003).
53. Saltiel, A.R. & Kahn, C.R. Insulin signalling and the regulation of glucose and lipid metabolism. *Nature* 414, 799-806 (2001).
54. Tan, S.Y., Mei Wong, J.L., Sim, Y.J.*, et al.* Type 1 and 2 diabetes mellitus: A review on current treatment approach and gene therapy as potential intervention. *Diabetes & Metabolic Syndrome: Clinical Research & Reviews* 13, 364-372 (2019).
55. Quek, J., Chan, K.E., Wong, Z.Y.*, et al.* Global prevalence of non-alcoholic fatty liver disease and non-alcoholic steatohepatitis in the overweight and obese population: a systematic review and meta-analysis. *Lancet Gastroenterol Hepatol* 8, 20-30 (2023).
56. Younossi, Z.M., Golabi, P., Price, J.K.*, et al.* The Global Epidemiology of Nonalcoholic Fatty Liver Disease and Nonalcoholic Steatohepatitis Among Patients With Type 2 Diabetes. *Clin Gastroenterol Hepatol* 22, 1999-2010.e1998 (2024).
57. Rinella, M.E., Lazarus, J.V., Ratziu, V.*, et al.* A multisociety Delphi consensus statement on new fatty liver disease nomenclature. *J Hepatol* 79, 1542-1556 (2023).
58. Stefan, N., Yki-Järvinen, H. & Neuschwander-Tetri, B.A. Metabolic dysfunction-associated steatotic liver disease: heterogeneous pathomechanisms and effectiveness of metabolism-based treatment. *The Lancet Diabetes & Endocrinology* (2024).
59. Romeo, S., Kozlitina, J., Xing, C.*, et al.* Genetic variation in PNPLA3 confers susceptibility to nonalcoholic fatty liver disease. *Nat Genet* 40, 1461-1465 (2008).
60. Luukkonen, P.K., Qadri, S., Ahlholm, N.*, et al.* Distinct contributions of metabolic dysfunction and genetic risk factors in the pathogenesis of non-alcoholic fatty liver disease. *J Hepatol* 76, 526-535 (2022).
61. Smith, G.I., Shankaran, M., Yoshino, M.*, et al.* Insulin resistance drives hepatic de novo lipogenesis in nonalcoholic fatty liver disease. *J Clin Invest* 130, 1453-1460 (2020).
62. Kahn, C.R., Wang, G. & Lee, K.Y. Altered adipose tissue and adipocyte function in the pathogenesis of metabolic syndrome. *J Clin Invest* 129, 3990-4000 (2019).
63. Younossi, Z.M., Golabi, P., Paik, J.M.*, et al.* The global epidemiology of nonalcoholic fatty liver disease (NAFLD) and nonalcoholic steatohepatitis (NASH): a systematic review. *Hepatology* 77, 1335-1347 (2023).
64. Friedman, S.L., Neuschwander-Tetri, B.A., Rinella, M. & Sanyal, A.J. Mechanisms of NAFLD development and therapeutic strategies. *Nat Med* 24, 908-922 (2018).
65. Rao, G., Peng, X., Li, X.*, et al.* Unmasking the enigma of lipid metabolism in metabolic dysfunction-associated steatotic liver disease: from mechanism to the clinic. *Front Med (Lausanne)* 10, 1294267 (2023).
66. Bilzer, M., Roggel, F. & Gerbes, A.L. Role of Kupffer cells in host defense and liver disease. *Liver Int* 26, 1175-1186 (2006).
67. Tsuchida, T. & Friedman, S.L. Mechanisms of hepatic stellate cell activation. *Nat Rev Gastroenterol Hepatol* 14, 397-411 (2017).
68. Caldwell, S., Ikura, Y., Dias, D.*, et al.* Hepatocellular ballooning in NASH. *J Hepatol* 53, 719-723 (2010).
69. Lekakis, V. & Papatheodoridis, G.V. Natural history of metabolic dysfunction-associated steatotic liver disease. *European Journal of Internal Medicine* 122, 3-10 (2024).

70. Tsochatzis, E.A., Bosch, J. & Burroughs, A.K. Liver cirrhosis. *The Lancet* 383, 1749-1761 (2014).
71. McGlynn, K.A., Petrick, J.L. & El-Serag, H.B. Epidemiology of Hepatocellular Carcinoma. *Hepatology* 73 Suppl 1, 4-13 (2021).
72. Shi, J., Zhao, Y., Wang, K.*, et al.* Cleavage of GSDMD by inflammatory caspases determines pyroptotic cell death. *Nature* 526, 660-665 (2015).
73. Chen, J., Li, X., Ge, C., Min, J. & Wang, F. The multifaceted role of ferroptosis in liver disease. *Cell Death & Differentiation* 29, 467-480 (2022).
74. Schwabe, R.F. & Luedde, T. Apoptosis and necroptosis in the liver: a matter of life and death. *Nature Reviews Gastroenterology & Hepatology* 15, 738-752 (2018).
75. Murphy, J.M., Czabotar, P.E., Hildebrand, J.M.*, et al.* The pseudokinase MLKL mediates necroptosis via a molecular switch mechanism. *Immunity* 39, 443-453 (2013).
76. Vucur, M., Ghallab, A., Schneider, A.T.*, et al.* Sublethal necroptosis signaling promotes inflammation and liver cancer. *Immunity* 56, 1578-1595.e1578 (2023).
77. Mihm, S. Danger-Associated Molecular Patterns (DAMPs): Molecular Triggers for Sterile Inflammation in the Liver. *Int J Mol Sci* 19(2018).
78. Arner, P. Catecholamine-induced lipolysis in obesity. *International Journal of Obesity* 23, S10-S13 (1999).
79. Londos, C., Brasaemle, D.L., Schultz, C.J.*, et al.* On the control of lipolysis in adipocytes. *Ann N Y Acad Sci* 892, 155-168 (1999).
80. Carey, G.B. Mechanisms regulating adipocyte lipolysis. *Adv Exp Med Biol* 441, 157-170 (1998).
81. Brasaemle, D.L. Thematic review series: adipocyte biology. The perilipin family of structural lipid droplet proteins: stabilization of lipid droplets and control of lipolysis. *J Lipid Res* 48, 2547-2559 (2007).
82. Sztalryd, C. & Brasaemle, D.L. The perilipin family of lipid droplet proteins: Gatekeepers of intracellular lipolysis. *Biochim Biophys Acta Mol Cell Biol Lipids* 1862, 1221-1232 (2017).
83. Chen, X., Iqbal, N. & Boden, G. The effects of free fatty acids on gluconeogenesis and glycogenolysis in normal subjects. *J Clin Invest* 103, 365-372 (1999).
84. Kitamura, T., Kitamura, Y., Kuroda, S.*, et al.* Insulin-induced phosphorylation and activation of cyclic nucleotide phosphodiesterase 3B by the serine-threonine kinase Akt. *Mol Cell Biol* 19, 6286-6296 (1999).
85. Taschler, U., Radner, F.P.W., Heier, C.*, et al.* Monoglyceride Lipase Deficiency in Mice Impairs Lipolysis and Attenuates Diet-induced Insulin Resistance. *Journal of Biological Chemistry* 286, 17467-17477 (2011).
86. Schoiswohl, G., Stefanovic-Racic, M., Menke, M.N.*, et al.* Impact of Reduced ATGL-Mediated Adipocyte Lipolysis on Obesity-Associated Insulin Resistance and Inflammation in Male Mice. *Endocrinology* 156, 3610-3624 (2015).
87. Chen, F.J., Yin, Y., Chua, B.T. & Li, P. CIDE family proteins control lipid homeostasis and the development of metabolic diseases. *Traffic* 21, 94-105 (2020).
88. Zhou, L., Xu, L., Ye, J.*, et al.* Cidea promotes hepatic steatosis by sensing dietary fatty acids. *Hepatology* 56, 95-107 (2012).
89. Toh, S.Y., Gong, J., Du, G.*, et al.* Up-regulation of mitochondrial activity and acquirement of brown adipose tissue-like property in the white adipose tissue of fsp27 deficient mice. *PLoS One* 3, e2890 (2008).
90. Thudichum, J.L.W. *A Treatise on the Chemical Constitution of the Brain. Based Throughout upon Original Researches.*, (London: Bailliere, Tindall, and Cox, Royal College of Physicians of London, 1884).
91. Brown, D.A. & London, E. Structure and function of sphingolipid- and cholesterol-rich membrane rafts. *J Biol Chem* 275, 17221-17224 (2000).
92. Merrill, A.H., Jr., Wang, M.D., Park, M. & Sullards, M.C. (Glyco)sphingolipidology: an amazing challenge and opportunity for systems biology. *Trends Biochem Sci* 32, 457-468 (2007).

93. Muralidharan, S., Shimobayashi, M., Ji, S.*, et al.* A reference map of sphingolipids in murine tissues. *Cell Reports* 35, 109250 (2021).
94. Hannun, Y.A. & Obeid, L.M. Sphingolipids and their metabolism in physiology and disease. *Nat Rev Mol Cell Biol* 19, 175-191 (2018).
95. Mandon, E.C., Ehses, I., Rother, J., van Echten, G. & Sandhoff, K. Subcellular localization and membrane topology of serine palmitoyltransferase, 3-dehydrosphinganine reductase, and sphinganine N-acyltransferase in mouse liver. *Journal of Biological Chemistry* 267, 11144-11148 (1992).
96. Yard, B.A., Carter, L.G., Johnson, K.A.*, et al.* The Structure of Serine Palmitoyltransferase; Gateway to Sphingolipid Biosynthesis. *Journal of Molecular Biology* 370, 870-886 (2007).
97. DeMar, J.C. & Anderson, R.E. Identification and Quantitation of the Fatty Acids Composing the CoA Ester Pool of Bovine Retina, Heart, and Liver. *Journal of Biological Chemistry* 272, 31362-31368 (1997).
98. Merrill, A.H., Jr. & Wang, E. Biosynthesis of long-chain (sphingoid) bases from serine by LM cells. Evidence for introduction of the 4-trans-double bond after de novo biosynthesis of N-acylsphinganine(s). *J Biol Chem* 261, 3764-3769 (1986).
99. Levy, M. & Futerman, A.H. Mammalian ceramide synthases. *IUBMB Life* 62, 347-356 (2010).
100. Mullen, T.D., Hannun, Y.A. & Obeid, L.M. Ceramide synthases at the centre of sphingolipid metabolism and biology. *Biochem J* 441, 789-802 (2012).
101. Ternes, P., Franke, S., Zähringer, U., Sperling, P. & Heinz, E. Identification and characterization of a sphingolipid delta 4-desaturase family. *J Biol Chem* 277, 25512-25518 (2002).
102. Kuo, A. & Hla, T. Regulation of cellular and systemic sphingolipid homeostasis. *Nat Rev Mol Cell Biol* (2024).
103. Lee, M., Lee, S.Y. & Bae, Y.S. Functional roles of sphingolipids in immunity and their implication in disease. *Exp Mol Med* 55, 1110-1130 (2023).
104. López-Montero, I., Rodriguez, N., Cribier, S.*, et al.* Rapid transbilayer movement of ceramides in phospholipid vesicles and in human erythrocytes. *J Biol Chem* 280, 25811-25819 (2005).
105. Hanada, K., Kumagai, K., Yasuda, S.*, et al.* Molecular machinery for non-vesicular trafficking of ceramide. *Nature* 426, 803-809 (2003).
106. Sugiura, M., Kono, K., Liu, H.*, et al.* Ceramide kinase, a novel lipid kinase. Molecular cloning and functional characterization. *J Biol Chem* 277, 23294-23300 (2002).
107. Senkal, C.E., Salama, M.F., Snider, A.J.*, et al.* Ceramide Is Metabolized to Acylceramide and Stored in Lipid Droplets. *Cell Metab* 25, 686-697 (2017).
108. Ichikawa, S., Sakiyama, H., Suzuki, G., Hidari, K.I. & Hirabayashi, Y. Expression cloning of a cDNA for human ceramide glucosyltransferase that catalyzes the first glycosylation step of glycosphingolipid synthesis. *Proc Natl Acad Sci U S A* 93, 4638-4643 (1996).
109. Jeckel, D., Karrenbauer, A., Burger, K.N., van Meer, G. & Wieland, F. Glucosylceramide is synthesized at the cytosolic surface of various Golgi subfractions. *J Cell Biol* 117, 259-267 (1992).
110. Bourne, Y. & Henrissat, B. Glycoside hydrolases and glycosyltransferases: families and functional modules. *Current Opinion in Structural Biology* 11, 593-600 (2001).
111. Futerman, A.H., Stieger, B., Hubbard, A.L. & Pagano, R.E. Sphingomyelin synthesis in rat liver occurs predominantly at the cis and medial cisternae of the Golgi apparatus. *J Biol Chem* 265, 8650-8657 (1990).
112. Villani, M., Subathra, M., Im, Y.B.*, et al.* Sphingomyelin synthases regulate production of diacylglycerol at the Golgi. *Biochem J* 414, 31-41 (2008).
113. Lipsky, N.G. & Pagano, R.E. Intracellular translocation of fluorescent sphingolipids in cultured fibroblasts: endogenously synthesized sphingomyelin and glucocerebroside analogues pass through the Golgi apparatus en route to the plasma membrane. *J Cell Biol* 100, 27-34 (1985).

114. Stoffel, W. Functional analysis of acid and neutral sphingomyelinases in vitro and in vivo. *Chemistry and Physics of Lipids* 102, 107-121 (1999).
115. Mao, C. & Obeid, L.M. Ceramidases: regulators of cellular responses mediated by ceramide, sphingosine, and sphingosine-1-phosphate. *Biochim Biophys Acta* 1781, 424-434 (2008).
116. Parveen, F., Bender, D., Law, S.-H.*, et al.* Role of Ceramidases in Sphingolipid Metabolism and Human Diseases. *Cells* 8, 1573 (2019).
117. Kohama, T., Olivera, A., Edsall, L.*, et al.* Molecular cloning and functional characterization of murine sphingosine kinase. *J Biol Chem* 273, 23722-23728 (1998).
118. Liu, H., Sugiura, M., Nava, V.E.*, et al.* Molecular cloning and functional characterization of a novel mammalian sphingosine kinase type 2 isoform. *J Biol Chem* 275, 19513-19520 (2000).
119. Sribney, M. Enzymatic synthesis of ceramide. *Biochimica et Biophysica Acta (BBA) - Lipids and Lipid Metabolism* 125, 542-547 (1966).
120. Le Stunff, H., Peterson, C., Thornton, R.*, et al.* Characterization of Murine Sphingosine-1-phosphate Phosphohydrolase. *Journal of Biological Chemistry* 277, 8920-8927 (2002).
121. Ogawa, C., Kihara, A., Gokoh, M. & Igarashi, Y. Identification and Characterization of a Novel Human Sphingosine-1-phosphate Phosphohydrolase, hSPP2. *Journal of Biological Chemistry* 278, 1268-1272 (2003).
122. Brindley, D.N. & Pilquil, C. Lipid phosphate phosphatases and signaling. *J Lipid Res* 50 Suppl, S225-230 (2009).
123. Saba, J.D., Nara, F., Bielawska, A., Garrett, S. & Hannun, Y.A. The BST1 gene of Saccharomyces cerevisiae is the sphingosine-1-phosphate lyase. *J Biol Chem* 272, 26087-26090 (1997).
124. Nakahara, K., Ohkuni, A., Kitamura, T.*, et al.* The Sjögren-Larsson Syndrome Gene Encodes a Hexadecenal Dehydrogenase of the Sphingosine 1-Phosphate Degradation Pathway. *Molecular Cell* 46, 461-471 (2012).
125. Cuvillier, O., Pirianov, G., Kleuser, B.*, et al.* Suppression of ceramide-mediated programmed cell death by sphingosine-1-phosphate. *Nature* 381, 800-803 (1996).
126. Obeid, L.M., Linardic, C.M., Karolak, L.A. & Hannun, Y.A. Programmed cell death induced by ceramide. *Science* 259, 1769-1771 (1993).
127. Pyne, S. & Pyne, N.J. Sphingosine 1-phosphate signalling in mammalian cells. *Biochem J* 349, 385-402 (2000).
128. Merrill, A.H., Jr. De Novo Sphingolipid Biosynthesis: A Necessary, but Dangerous, Pathway. *Journal of Biological Chemistry* 277, 25843-25846 (2002).
129. Breslow, D.K., Collins, S.R., Bodenmiller, B.*, et al.* Orm family proteins mediate sphingolipid homeostasis. *Nature* 463, 1048-1053 (2010).
130. Davis, D.L., Gable, K., Suemitsu, J., Dunn, T.M. & Wattenberg, B.W. The ORMDL/Orm-serine palmitoyltransferase (SPT) complex is directly regulated by ceramide: Reconstitution of SPT regulation in isolated membranes. *J Biol Chem* 294, 5146-5156 (2019).
131. Green, C.D., Weigel, C., Oyeniran, C.*, et al.* CRISPR/Cas9 deletion of ORMDLs reveals complexity in sphingolipid metabolism. *J Lipid Res* 62, 100082 (2021).
132. Laviad, E.L., Albee, L., Pankova-Kholmyansky, I.*, et al.* Characterization of ceramide synthase 2: tissue distribution, substrate specificity, and inhibition by sphingosine 1-phosphate. *J Biol Chem* 283, 5677-5684 (2008).
133. Hampton, R.Y. & Morand, O.H. Sphingomyelin Synthase and PKC Activation. *Science* 246, 1050-1050 (1989).
134. Horibata, Y. & Hirabayashi, Y. Identification and characterization of human ethanolaminephosphotransferase1. *J Lipid Res* 48, 503-508 (2007).
135. Gault, C.R., Obeid, L.M. & Hannun, Y.A. An overview of sphingolipid metabolism: from synthesis to breakdown. *Adv Exp Med Biol* 688, 1-23 (2010).

136. Chalfant, C.E., Kishikawa, K., Mumby, M.C*., et al.* Long chain ceramides activate protein phosphatase-1 and protein phosphatase-2A. Activation is stereospecific and regulated by phosphatidic acid. *J Biol Chem* 274, 20313-20317 (1999).
137. Garcia, A., Cayla, X., Guergnon, J*., et al.* Serine/threonine protein phosphatases PP1 and PP2A are key players in apoptosis. *Biochimie* 85, 721-726 (2003).
138. Ruvolo, P.P., Deng, X., Ito, T., Carr, B.K. & May, W.S. Ceramide Induces Bcl2 Dephosphorylation via a Mechanism Involving Mitochondrial PP2A. *Journal of Biological Chemistry* 274, 20296-20300 (1999).
139. Siskind, L.J., Kolesnick, R.N. & Colombini, M. Ceramide Channels Increase the Permeability of the Mitochondrial Outer Membrane to Small Proteins. *Journal of Biological Chemistry* 277, 26796-26803 (2002).
140. Dadsena, S., Bockelmann, S., Mina, J.G.M*., et al.* Ceramides bind VDAC2 to trigger mitochondrial apoptosis. *Nature Communications* 10, 1832 (2019).
141. Bourbon, N.A., Sandirasegarane, L. & Kester, M. Ceramide-induced inhibition of Akt is mediated through protein kinase Czeta: implications for growth arrest. *J Biol Chem* 277, 3286-3292 (2002).
142. Yokota, S., Taniguchi, Y., Kihara, A., Mitsutake, S. & Igarashi, Y. Asp177 in C4 domain of mouse sphingosine kinase 1a is important for the sphingosine recognition. *FEBS Letters* 578, 106-110 (2004).
143. Shu, X., Wu, W., Mosteller, R.D. & Broek, D. Sphingosine kinase mediates vascular endothelial growth factor-induced activation of ras and mitogen-activated protein kinases. *Mol Cell Biol* 22, 7758-7768 (2002).
144. Pitson, S.M., Moretti, P.A., Zebol, J.R*., et al.* Activation of sphingosine kinase 1 by ERK1/2-mediated phosphorylation. *Embo j* 22, 5491-5500 (2003).
145. Xia, P., Wang, L., Gamble, J.R. & Vadas, M.A. Activation of Sphingosine Kinase by Tumor Necrosis Factor-α Inhibits Apoptosis in Human Endothelial Cells. *Journal of Biological Chemistry* 274, 34499-34505 (1999).
146. Johnson, K.R., Becker, K.P., Facchinetti, M.M., Hannun, Y.A. & Obeid, L.M. PKC-dependent activation of sphingosine kinase 1 and translocation to the plasma membrane. Extracellular release of sphingosine-1-phosphate induced by phorbol 12-myristate 13-acetate (PMA). *J Biol Chem* 277, 35257-35262 (2002).
147. Igarashi, N., Okada, T., Hayashi, S*., et al.* Sphingosine kinase 2 is a nuclear protein and inhibits DNA synthesis. *J Biol Chem* 278, 46832-46839 (2003).
148. Maceyka, M., Sankala, H., Hait, N.C*., et al.* SphK1 and SphK2, Sphingosine Kinase Isoenzymes with Opposing Functions in Sphingolipid Metabolism. *Journal of Biological Chemistry* 280, 37118-37129 (2005).
149. Fukuda, Y., Kihara, A. & Igarashi, Y. Distribution of sphingosine kinase activity in mouse tissues: contribution of SPHK1. *Biochemical and Biophysical Research Communications* 309, 155-160 (2003).
150. Mizugishi, K., Yamashita, T., Olivera, A*., et al.* Essential role for sphingosine kinases in neural and vascular development. *Mol Cell Biol* 25, 11113-11121 (2005).
151. Shida, D., Takabe, K., Kapitonov, D., Milstien, S. & Spiegel, S. Targeting SphK1 as a new strategy against cancer. *Curr Drug Targets* 9, 662-673 (2008).
152. Meng, X.-D., Zhou, Z.-S., Qiu, J.-H*., et al.* Increased SPHK1 expression is associated with poor prognosis in bladder cancer. *Tumor Biology* 35, 2075-2080 (2014).
153. Matula, K., Collie-Duguid, E., Murray, G*., et al.* Regulation of cellular sphingosine-1-phosphate by sphingosine kinase 1 and sphingosine-1-phopshate lyase determines chemotherapy resistance in gastroesophageal cancer. *BMC Cancer* 15, 762 (2015).
154. Ruckhäberle, E., Rody, A., Engels, K*., et al.* Microarray analysis of altered sphingolipid metabolism reveals prognostic significance of sphingosine kinase 1 in breast cancer. *Breast Cancer Res Treat* 112, 41-52 (2008).
155. Wang, Q., Li, J., Li, G*., et al.* Prognostic significance of sphingosine kinase 2 expression in non-small cell lung cancer. *Tumor Biology* 35, 363-368 (2014).

156. Zhang, L., Liu, X., Zuo, Z., Hao, C. & Ma, Y. Sphingosine kinase 2 promotes colorectal cancer cell proliferation and invasion by enhancing MYC expression. *Tumour Biol* 37, 8455-8460 (2016).
157. Igarashi, Y., Hakomori, S., Toyokuni, T.*, et al.* Effect of chemically well-defined sphingosine and its N-methyl derivatives on protein kinase C and src kinase activities. *Biochemistry* 28, 6796-6800 (1989).
158. Cingolani, F., Casasampere, M., Sanllehí, P.*, et al.* Inhibition of dihydroceramide desaturase activity by the sphingosine kinase inhibitor SKI II[S]. *J Lipid Res* 55, 1711-1720 (2014).
159. Darrow, M.C., Zhang, Y., Cinquin, B.P.*, et al.* Visualizing red blood cell sickling and the effects of inhibition of sphingosine kinase 1 using soft X-ray tomography. *Journal of cell science* 129, 3511-3517 (2016).
160. Schnute, M.E., McReynolds, M.D., Kasten, T.*, et al.* Modulation of cellular S1P levels with a novel, potent and specific inhibitor of sphingosine kinase-1. *Biochemical Journal* 444, 79-88 (2012).
161. Yi, X., Tang, X., Li, T.*, et al.* Therapeutic potential of the sphingosine kinase 1 inhibitor, PF-543. *Biomedicine & Pharmacotherapy* 163, 114401 (2023).
162. Liu, K., Guo, T.L., Hait, N.C.*, et al.* Biological Characterization of 3-(2-amino-ethyl)-5-[3-(4-butoxyl-phenyl)-propylidene]-thiazolidine-2,4-dione (K145) as a Selective Sphingosine Kinase-2 Inhibitor and Anticancer Agent. *PLOS ONE* 8, e56471 (2013).
163. Beljanski, V., Knaak, C. & Smith, C.D. A novel sphingosine kinase inhibitor induces autophagy in tumor cells. *J Pharmacol Exp Ther* 333, 454-464 (2010).
164. Venant, H., Rahmaniyan, M., Jones, E.E.*, et al.* The Sphingosine Kinase 2 Inhibitor ABC294640 Reduces the Growth of Prostate Cancer Cells and Results in Accumulation of Dihydroceramides In Vitro and In Vivo. *Molecular Cancer Therapeutics* 14, 2744-2752 (2015).
165. Pashikanti, S., Foster, D.J., Kharel, Y.*, et al.* Sphingosine Kinase 2 Inhibitors: Rigid Aliphatic Tail Derivatives Deliver Potent and Selective Analogues. *ACS Bio Med Chem Au* 2, 469-489 (2022).
166. Hla, T., Venkataraman, K. & Michaud, J. The vascular S1P gradient-cellular sources and biological significance. *Biochim Biophys Acta* 1781, 477-482 (2008).
167. Massberg, S., Schaerli, P., Knezevic-Maramica, I.*, et al.* Immunosurveillance by hematopoietic progenitor cells trafficking through blood, lymph, and peripheral tissues. *Cell* 131, 994-1008 (2007).
168. Pappu, R., Schwab, S.R., Cornelissen, I.*, et al.* Promotion of lymphocyte egress into blood and lymph by distinct sources of sphingosine-1-phosphate. *Science* 316, 295-298 (2007).
169. Hänel, P., Andréani, P. & Gräler, M.H. Erythrocytes store and release sphingosine 1-phosphate in blood. *The FASEB Journal* 21, 1202-1209 (2007).
170. Ito, K., Anada, Y., Tani, M.*, et al.* Lack of sphingosine 1-phosphate-degrading enzymes in erythrocytes. *Biochem Biophys Res Commun* 357, 212-217 (2007).
171. Yatomi, Y., Igarashi, Y., Yang, L.*, et al.* Sphingosine 1-phosphate, a bioactive sphingolipid abundantly stored in platelets, is a normal constituent of human plasma and serum. *J Biochem* 121, 969-973 (1997).
172. Venkataraman, K., Lee, Y.-M., Michaud, J.*, et al.* Vascular Endothelium As a Contributor of Plasma Sphingosine 1-Phosphate. *Circulation Research* 102, 669-676 (2008).
173. Vu, T.M., Ishizu, A.N., Foo, J.C.*, et al.* Mfsd2b is essential for the sphingosine-1-phosphate export in erythrocytes and platelets. *Nature* 550, 524-528 (2017).
174. Peest, U., Sensken, S.C., Andréani, P.*, et al.* S1P-lyase independent clearance of extracellular sphingosine 1-phosphate after dephosphorylation and cellular uptake. *J Cell Biochem* 104, 756-772 (2008).
175. Zhao, Y., Kalari, S.K., Usatyuk, P.V.*, et al.* Intracellular generation of sphingosine 1-phosphate in human lung endothelial cells: role of lipid phosphate phosphatase-1 and sphingosine kinase 1. *J Biol Chem* 282, 14165-14177 (2007).

176. Sensken, S.C., Bode, C., Nagarajan, M.*, et al.* Redistribution of sphingosine 1-phosphate by sphingosine kinase 2 contributes to lymphopenia. *J Immunol* 184, 4133-4142 (2010).
177. Murata, N., Sato, K., Kon, J.*, et al.* Interaction of sphingosine 1-phosphate with plasma components, including lipoproteins, regulates the lipid receptor-mediated actions. *Biochem J* 352 Pt 3, 809-815 (2000).
178. Christoffersen, C., Nielsen, L.B., Axler, O.*, et al.* Isolation and characterization of human apolipoprotein M-containing lipoproteins. *J Lipid Res* 47, 1833-1843 (2006).
179. Christoffersen, C., Obinata, H., Kumaraswamy, S.B.*, et al.* Endothelium-protective sphingosine-1-phosphate provided by HDL-associated apolipoprotein M. *Proc Natl Acad Sci U S A* 108, 9613-9618 (2011).
180. Nguyen, T.Q., Vu, T.M., Tukijan, F.*, et al.* Erythrocytes efficiently utilize exogenous sphingosines for S1P synthesis and export via Mfsd2b. *J Biol Chem* 296, 100201 (2021).
181. Kawahara, A., Nishi, T., Hisano, Y.*, et al.* The Sphingolipid Transporter Spns2 Functions in Migration of Zebrafish Myocardial Precursors. *Science* 323, 524-527 (2009).
182. Hisano, Y., Kobayashi, N., Yamaguchi, A. & Nishi, T. Mouse SPNS2 functions as a sphingosine-1-phosphate transporter in vascular endothelial cells. *PLoS One* 7, e38941 (2012).
183. Mitra, P., Oskeritzian, C.A., Payne, S.G.*, et al.* Role of ABCC1 in export of sphingosine-1-phosphate from mast cells. *Proc Natl Acad Sci U S A* 103, 16394-16399 (2006).
184. Japtok, L., Schaper, K., Bäumer, W.*, et al.* Sphingosine 1-Phosphate Modulates Antigen Capture by Murine Langerhans Cells via the S1P2 Receptor Subtype. *PLOS ONE* 7, e49427 (2012).
185. Cartwright, T.A., Campos, C.R., Cannon, R.E. & Miller, D.S. Mrp1 is essential for sphingolipid signaling to p-glycoprotein in mouse blood-brain and blood-spinal cord barriers. *J Cereb Blood Flow Metab* 33, 381-388 (2013).
186. Nieuwenhuis, B., Lüth, A., Chun, J.*, et al.* Involvement of the ABC-transporter ABCC1 and the sphingosine 1-phosphate receptor subtype S1P(3) in the cytoprotection of human fibroblasts by the glucocorticoid dexamethasone. *J Mol Med (Berl)* 87, 645-657 (2009).
187. Kobayashi, N., Kobayashi, N., Yamaguchi, A. & Nishi, T. Characterization of the ATP-dependent sphingosine 1-phosphate transporter in rat erythrocytes. *J Biol Chem* 284, 21192-21200 (2009).
188. Sato, K., Malchinkhuu, E., Horiuchi, Y.*, et al.* Critical role of ABCA1 transporter in sphingosine 1-phosphate release from astrocytes. *Journal of Neurochemistry* 103, 2610-2619 (2007).
189. Hla, T. Sphingosine 1-phosphate receptors. *Prostaglandins & Other Lipid Mediators* 64, 135-142 (2001).
190. Lee, M.J., Van Brocklyn, J.R., Thangada, S.*, et al.* Sphingosine-1-phosphate as a ligand for the G protein-coupled receptor EDG-1. *Science* 279, 1552-1555 (1998).
191. Oldham, W.M. & Hamm, H.E. Heterotrimeric G protein activation by G-protein-coupled receptors. *Nat Rev Mol Cell Biol* 9, 60-71 (2008).
192. Lee, M.-J., Evans, M. & Hla, T. The Inducible G Protein-coupled Receptor edg-1 Signals via the Gi/Mitogen-activated Protein Kinase Pathway. *Journal of Biological Chemistry* 271, 11272-11279 (1996).
193. Windh, R.T., Lee, M.J., Hla, T.*, et al.* Differential coupling of the sphingosine 1-phosphate receptors Edg-1, Edg-3, and H218/Edg-5 to the G(i), G(q), and G(12) families of heterotrimeric G proteins. *J Biol Chem* 274, 27351-27358 (1999).
194. Gräler, M.H., Grosse, R., Kusch, A.*, et al.* The sphingosine 1-phosphate receptor S1P4 regulates cell shape and motility via coupling to Gi and G12/13. *J Cell Biochem* 89, 507-519 (2003).
195. Im, D.S., Clemens, J., Macdonald, T.L. & Lynch, K.R. Characterization of the human and mouse sphingosine 1-phosphate receptor, S1P5 (Edg-8): structure-activity

relationship of sphingosine1-phosphate receptors. *Biochemistry* 40, 14053-14060 (2001).
196. Chun, J., Giovannoni, G. & Hunter, S.F. Sphingosine 1-phosphate Receptor Modulator Therapy for Multiple Sclerosis: Differential Downstream Receptor Signalling and Clinical Profile Effects. *Drugs* 81, 207-231 (2021).
197. Jaillard, C., Harrison, S., Stankoff, B.*, et al.* Edg8/S1P5: an oligodendroglial receptor with dual function on process retraction and cell survival. *J Neurosci* 25, 1459-1469 (2005).
198. Sato, K., Kon, J., Tomura, H.*, et al.* Activation of phospholipase C-Ca2+ system by sphingosine 1-phosphate in CHO cells transfected with Edg-3, a putative lipid receptor. *FEBS Lett* 443, 25-30 (1999).
199. Zondag, C.M.G., Postma, R.F., Etten, I.v., Verlaan, I. & Moolenaar, H.W. Sphingosine 1-phosphate signalling through the G-protein-coupled receptor Edg-1. *Biochemical Journal* 330, 605-609 (1998).
200. Malchinkhuu, E., Sato, K., Maehama, T.*, et al.* S1P(2) receptors mediate inhibition of glioma cell migration through Rho signaling pathways independent of PTEN. *Biochem Biophys Res Commun* 366, 963-968 (2008).
201. McVerry, B.J., Peng, X., Hassoun, P.M.*, et al.* Sphingosine 1-phosphate reduces vascular leak in murine and canine models of acute lung injury. *Am J Respir Crit Care Med* 170, 987-993 (2004).
202. Szczepaniak, W.S., Pitt, B.R. & McVerry, B.J. S1P2 receptor-dependent Rho-kinase activation mediates vasoconstriction in the murine pulmonary circulation induced by sphingosine 1-phosphate. *Am J Physiol Lung Cell Mol Physiol* 299, L137-145 (2010).
203. Alvarez, S.E., Harikumar, K.B., Hait, N.C.*, et al.* Sphingosine-1-phosphate is a missing cofactor for the E3 ubiquitin ligase TRAF2. *Nature* 465, 1084-1088 (2010).
204. Kajimoto, T., Caliman, A.D., Tobias, I.S.*, et al.* Activation of atypical protein kinase C by sphingosine 1-phosphate revealed by an aPKC-specific activity reporter. *Sci Signal* 12(2019).
205. Parham, K.A., Zebol, J.R., Tooley, K.L.*, et al.* Sphingosine 1-phosphate is a ligand for peroxisome proliferator-activated receptor-gamma that regulates neoangiogenesis. *Faseb J* 29, 3638-3653 (2015).
206. Meyer zu Heringdorf, D., Liliom, K., Schaefer, M.*, et al.* Photolysis of intracellular caged sphingosine-1-phosphate causes Ca2+ mobilization independently of G-protein-coupled receptors. *FEBS Lett* 554, 443-449 (2003).
207. Hait, N.C., Allegood, J., Maceyka, M.*, et al.* Regulation of Histone Acetylation in the Nucleus by Sphingosine-1-Phosphate. *Science* 325, 1254-1257 (2009).
208. Panneer Selvam, S., De Palma, R.M., Oaks, J.J.*, et al.* Binding of the sphingolipid S1P to hTERT stabilizes telomerase at the nuclear periphery by allosterically mimicking protein phosphorylation. *Sci Signal* 8, ra58 (2015).
209. Strub, G.M., Paillard, M., Liang, J.*, et al.* Sphingosine-1-phosphate produced by sphingosine kinase 2 in mitochondria interacts with prohibitin 2 to regulate complex IV assembly and respiration. *Faseb J* 25, 600-612 (2011).
210. Gomez, L., Paillard, M., Price, M.*, et al.* A novel role for mitochondrial sphingosine-1-phosphate produced by sphingosine kinase-2 in PTP-mediated cell survival during cardioprotection. *Basic Res Cardiol* 106, 1341-1353 (2011).
211. Abed Rabbo, M., Khodour, Y., Kaguni, L.S. & Stiban, J. Sphingolipid lysosomal storage diseases: from bench to bedside. *Lipids Health Dis* 20, 44 (2021).
212. Brady, R.O., Kanfer, J.N., Mock, M.B. & Fredrickson, D.S. The metabolism of sphingomyelin. II. Evidence of an enzymatic deficiency in Niemann-Pick diseae. *Proc Natl Acad Sci U S A* 55, 366-369 (1966).
213. Kappos, L., Antel, J., Comi, G.*, et al.* Oral fingolimod (FTY720) for relapsing multiple sclerosis. *N Engl J Med* 355, 1124-1140 (2006).
214. Chun, J. & Hartung, H.P. Mechanism of action of oral fingolimod (FTY720) in multiple sclerosis. *Clin Neuropharmacol* 33, 91-101 (2010).

215. Kappos, L., Bar-Or, A., Cree, B.A.C., *et al.* Siponimod versus placebo in secondary progressive multiple sclerosis (EXPAND): a double-blind, randomised, phase 3 study. *Lancet* 391, 1263-1273 (2018).
216. Kappos, L., Fox, R.J., Burcklen, M., *et al.* Ponesimod Compared With Teriflunomide in Patients With Relapsing Multiple Sclerosis in the Active-Comparator Phase 3 OPTIMUM Study: A Randomized Clinical Trial. *JAMA Neurol* 78, 558-567 (2021).
217. Brossard, P., Derendorf, H., Xu, J., *et al.* Pharmacokinetics and pharmacodynamics of ponesimod, a selective S1P1 receptor modulator, in the first-in-human study. *Br J Clin Pharmacol* 76, 888-896 (2013).
218. Danese, S., Abreu, M., Wolf, D., *et al.* DOP37 Efficacy and safety of 3 years of continuous ozanimod treatment: an interim analysis of the True North open-label extension study. *Journal of Crohn's and Colitis* 17, i101-i102 (2023).
219. Vaclavkova, A., Chimenti, S., Arenberger, P., *et al.* Oral ponesimod in patients with chronic plaque psoriasis: a randomised, double-blind, placebo-controlled phase 2 trial. *The Lancet* 384, 2036-2045 (2014).
220. French, K.J., Zhuang, Y., Maines, L.W., *et al.* Pharmacology and antitumor activity of ABC294640, a selective inhibitor of sphingosine kinase-2. *J Pharmacol Exp Ther* 333, 129-139 (2010).
221. Janneh, A.H. & Ogretmen, B. Targeting Sphingolipid Metabolism as a Therapeutic Strategy in Cancer Treatment. *Cancers* 14, 2183 (2022).
222. Zabielski, P., Błachnio-Zabielska, A.U., Wójcik, B., Chabowski, A. & Górski, J. Effect of plasma free fatty acid supply on the rate of ceramide synthesis in different muscle types in the rat. *PLOS ONE* 12, e0187136 (2017).
223. Bertea, M., Rütti, M.F., Othman, A., *et al.* Deoxysphingoid bases as plasma markers in Diabetes mellitus. *Lipids in Health and Disease* 9, 84 (2010).
224. Othman, A., Bianchi, R., Alecu, I., *et al.* Lowering plasma 1-deoxysphingolipids improves neuropathy in diabetic rats. *Diabetes* 64, 1035-1045 (2015).
225. Johnson, E.L., Heaver, S.L., Waters, J.L., *et al.* Sphingolipids produced by gut bacteria enter host metabolic pathways impacting ceramide levels. *Nature Communications* 11, 2471 (2020).
226. Luukkonen, P.K., Zhou, Y., Sädevirta, S., *et al.* Hepatic ceramides dissociate steatosis and insulin resistance in patients with non-alcoholic fatty liver disease. *J Hepatol* 64, 1167-1175 (2016).
227. Rosqvist, F., Kullberg, J., Ståhlman, M., *et al.* Overeating Saturated Fat Promotes Fatty Liver and Ceramides Compared With Polyunsaturated Fat: A Randomized Trial. *J Clin Endocrinol Metab* 104, 6207-6219 (2019).
228. Grabner, G.F., Xie, H., Schweiger, M. & Zechner, R. Lipolysis: cellular mechanisms for lipid mobilization from fat stores. *Nat Metab* 3, 1445-1465 (2021).
229. Hu, W., Ross, J., Geng, T., Brice, S.E. & Cowart, L.A. Differential regulation of dihydroceramide desaturase by palmitate versus monounsaturated fatty acids: implications for insulin resistance. *J Biol Chem* 286, 16596-16605 (2011).
230. Holland, W.L., Brozinick, J.T., Wang, L.-P., *et al.* Inhibition of Ceramide Synthesis Ameliorates Glucocorticoid-, Saturated-Fat-, and Obesity-Induced Insulin Resistance. *Cell Metabolism* 5, 167-179 (2007).
231. Bikman, B.T., Guan, Y., Shui, G., *et al.* Fenretinide prevents lipid-induced insulin resistance by blocking ceramide biosynthesis. *J Biol Chem* 287, 17426-17437 (2012).
232. Chaurasia, B., Tippetts, T.S., Mayoral Monibas, R., *et al.* Targeting a ceramide double bond improves insulin resistance and hepatic steatosis. *Science* 365, 386-392 (2019).
233. Chavez, J.A. & Summers, S.A. A ceramide-centric view of insulin resistance. *Cell Metab* 15, 585-594 (2012).
234. Kurek, K., Piotrowska, D.M., Wiesiołek-Kurek, P., *et al.* Inhibition of ceramide de novo synthesis reduces liver lipid accumulation in rats with nonalcoholic fatty liver disease. *Liver International* 34, 1074-1083 (2014).

235. Yang, G., Badeanlou, L., Bielawski, J.*, et al.* Central role of ceramide biosynthesis in body weight regulation, energy metabolism, and the metabolic syndrome. *Am J Physiol Endocrinol Metab* 297, E211-224 (2009).
236. Pan, D.Z., Garske, K.M., Alvarez, M.*, et al.* Integration of human adipocyte chromosomal interactions with adipose gene expression prioritizes obesity-related genes from GWAS. *Nature Communications* 9, 1512 (2018).
237. Song, Y., Zan, W., Qin, L.*, et al.* Ablation of ORMDL3 impairs adipose tissue thermogenesis and insulin sensitivity by increasing ceramide generation. *Mol Metab* 56, 101423 (2022).
238. Alexaki, A., Clarke, B.A., Gavrilova, O.*, et al.* De Novo Sphingolipid Biosynthesis Is Required for Adipocyte Survival and Metabolic Homeostasis. *J Biol Chem* 292, 3929-3939 (2017).
239. Lee, S.Y., Lee, H.Y., Song, J.H.*, et al.* Adipocyte-Specific Deficiency of De Novo Sphingolipid Biosynthesis Leads to Lipodystrophy and Insulin Resistance. *Diabetes* 66, 2596-2609 (2017).
240. Sanyal, A.J. & Pacana, T. A Lipidomic Readout of Disease Progression in A Diet-Induced Mouse Model of Nonalcoholic Fatty Liver Disease. *Trans Am Clin Climatol Assoc* 126, 271-288 (2015).
241. Turpin, S.M., Nicholls, H.T., Willmes, D.M.*, et al.* Obesity-induced CerS6-dependent C16:0 ceramide production promotes weight gain and glucose intolerance. *Cell Metab* 20, 678-686 (2014).
242. Raichur, S., Brunner, B., Bielohuby, M.*, et al.* The role of C16:0 ceramide in the development of obesity and type 2 diabetes: CerS6 inhibition as a novel therapeutic approach. *Mol Metab* 21, 36-50 (2019).
243. Hammerschmidt, P., Ostkotte, D., Nolte, H.*, et al.* CerS6-Derived Sphingolipids Interact with Mff and Promote Mitochondrial Fragmentation in Obesity. *Cell* 177, 1536-1552.e1523 (2019).
244. Turner, N., Lim, X.Y., Toop, H.D.*, et al.* A selective inhibitor of ceramide synthase 1 reveals a novel role in fat metabolism. *Nat Commun* 9, 3165 (2018).
245. Turpin-Nolan, S.M., Hammerschmidt, P., Chen, W.*, et al.* CerS1-Derived C(18:0) Ceramide in Skeletal Muscle Promotes Obesity-Induced Insulin Resistance. *Cell Rep* 26, 1-10.e17 (2019).
246. Véret, J., Coant, N., Berdyshev, E.V.*, et al.* Ceramide synthase 4 and de novo production of ceramides with specific N-acyl chain lengths are involved in glucolipotoxicity-induced apoptosis of INS-1 β-cells. *Biochem J* 438, 177-189 (2011).
247. Raichur, S., Wang, S.T., Chan, P.W.*, et al.* CerS2 haploinsufficiency inhibits β-oxidation and confers susceptibility to diet-induced steatohepatitis and insulin resistance. *Cell Metab* 20, 687-695 (2014).
248. Chang, Z.Q., Lee, S.Y., Kim, H.J.*, et al.* Endotoxin activates de novo sphingolipid biosynthesis via nuclear factor kappa B-mediated upregulation of Sptlc2. *Prostaglandins Other Lipid Mediat* 94, 44-52 (2011).
249. Jenkins, R.W., Canals, D., Idkowiak-Baldys, J.*, et al.* Regulated secretion of acid sphingomyelinase: implications for selectivity of ceramide formation. *J Biol Chem* 285, 35706-35718 (2010).
250. Kouba, D.J., Nakano, H., Nishiyama, T.*, et al.* Tumor necrosis factor-alpha induces distinctive NF-kappa B signaling within human dermal fibroblasts. *J Biol Chem* 276, 6214-6224 (2001).
251. Arita, Y., Kihara, S., Ouchi, N.*, et al.* Paradoxical decrease of an adipose-specific protein, adiponectin, in obesity. *Biochem Biophys Res Commun* 257, 79-83 (1999).
252. Holland, W.L., Xia, J.Y., Johnson, J.A.*, et al.* Inducible overexpression of adiponectin receptors highlight the roles of adiponectin-induced ceramidase signaling in lipid and glucose homeostasis. *Mol Metab* 6, 267-275 (2017).

253. Xia, J.Y., Holland, W.L., Kusminski, C.M., *et al.* Targeted Induction of Ceramide Degradation Leads to Improved Systemic Metabolism and Reduced Hepatic Steatosis. *Cell Metab* 22, 266-278 (2015).
254. Li, Y., Dong, J., Ding, T., *et al.* Sphingomyelin synthase 2 activity and liver steatosis: an effect of ceramide-mediated peroxisome proliferator-activated receptor γ2 suppression. *Arterioscler Thromb Vasc Biol* 33, 1513-1520 (2013).
255. Sugimoto, M., Hamada, T., Wakabayasi, M., *et al.* Sphingomyelin synthase 2 loss suppresses steatosis but exacerbates fibrosis in the liver of mice fed with choline-deficient, L-amino acid-defined, high-fat diet. *Biochem Biophys Res Commun* 533, 1269-1275 (2020).
256. Huang, Y., Huang, T., Zhen, X., *et al.* A selective sphingomyelin synthase 2 inhibitor ameliorates diet induced insulin resistance via the IRS-1/Akt/GSK-3beta signaling pathway. *Pharmazie* 74, 553-558 (2019).
257. Fox, T.E., Bewley, M.C., Unrath, K.A., *et al.* Circulating sphingolipid biomarkers in models of type 1 diabetes. *J Lipid Res* 52, 509-517 (2011).
258. Keppley, L.J.W., Walker, S.J., Gademsey, A.N., *et al.* Nervonic acid limits weight gain in a mouse model of diet-induced obesity. *Faseb J* 34, 15314-15326 (2020).
259. Wang, K., Li, C., Lin, X., *et al.* Targeting alkaline ceramidase 3 alleviates the severity of nonalcoholic steatohepatitis by reducing oxidative stress. *Cell Death Dis* 11, 28 (2020).
260. Kowalski, G.M., Carey, A.L., Selathurai, A., Kingwell, B.A. & Bruce, C.R. Plasma sphingosine-1-phosphate is elevated in obesity. *PLoS One* 8, e72449 (2013).
261. Grammatikos, G., Schoell, N., Ferreirós, N., *et al.* Serum sphingolipidomic analyses reveal an upregulation of C16- ceramide and sphingosine-1-phosphate in hepatocellular carcinoma. *Oncotarget* 7(2016).
262. Geng, T., Sutter, A., Harland, M.D., *et al.* SphK1 mediates hepatic inflammation in a mouse model of NASH induced by high saturated fat feeding and initiates proinflammatory signaling in hepatocytes. *J Lipid Res* 56, 2359-2371 (2015).
263. Uranbileg, B., Ikeda, H., Kurano, M., *et al.* Increased mRNA Levels of Sphingosine Kinases and S1P Lyase and Reduced Levels of S1P Were Observed in Hepatocellular Carcinoma in Association with Poorer Differentiation and Earlier Recurrence. *PLOS ONE* 11, e0149462 (2016).
264. Wang, J., Badeanlou, L., Bielawski, J., Ciaraldi, T.P. & Samad, F. Sphingosine kinase 1 regulates adipose proinflammatory responses and insulin resistance. *Am J Physiol Endocrinol Metab* 306, E756-768 (2014).
265. Cantrell Stanford, J., Morris, A.J., Sunkara, M., *et al.* Sphingosine 1-phosphate (S1P) regulates glucose-stimulated insulin secretion in pancreatic beta cells. *J Biol Chem* 287, 13457-13464 (2012).
266. Xiu, L., Chang, N., Yang, L., *et al.* Intracellular Sphingosine 1-Phosphate Contributes to Collagen Expression of Hepatic Myofibroblasts in Human Liver Fibrosis Independent of Its Receptors. *The American Journal of Pathology* 185, 387-398 (2015).
267. Hahn, C., Tyka, K., Saba, J.D., Lenzen, S. & Gurgul-Convey, E. Overexpression of sphingosine-1-phosphate lyase protects insulin-secreting cells against cytokine toxicity. *J Biol Chem* 292, 20292-20304 (2017).
268. Hashimoto, T., Igarashi, J. & Kosaka, H. Sphingosine kinase is induced in mouse 3T3-L1 cells and promotes adipogenesis. *J Lipid Res* 50, 602-610 (2009).
269. Lambert, J., Kovilakath, A., Jamil, M., *et al.* Sphingosine kinase 1 is induced by glucocorticoids in adipose derived stem cells and enhances glucocorticoid mediated signaling in adipose expansion. *bioRxiv* (2024).
270. Chen, J., Wang, W., Qi, Y., *et al.* Deletion of sphingosine kinase 1 ameliorates hepatic steatosis in diet-induced obese mice: Role of PPARγ. *Biochimica et Biophysica Acta (BBA) - Molecular and Cell Biology of Lipids* 1861, 138-147 (2016).
271. Anderson, A.K., Lambert, J.M., Montefusco, D.J., *et al.* Depletion of adipocyte sphingosine kinase 1 leads to cell hypertrophy, impaired lipolysis, and nonalcoholic fatty liver disease. *J Lipid Res* 61, 1328-1340 (2020).

272. Qi, Y., Chen, J., Lay, A.*, et al.* Loss of sphingosine kinase 1 predisposes to the onset of diabetes via promoting pancreatic β-cell death in diet-induced obese mice. *Faseb J* 27, 4294-4304 (2013).
273. Ma, M.M., Chen, J.L., Wang, G.G.*, et al.* Sphingosine kinase 1 participates in insulin signalling and regulates glucose metabolism and homeostasis in KK/Ay diabetic mice. *Diabetologia* 50, 891-900 (2007).
274. Bruce, C.R., Risis, S., Babb, J.R.*, et al.* Overexpression of sphingosine kinase 1 prevents ceramide accumulation and ameliorates muscle insulin resistance in high-fat diet-fed mice. *Diabetes* 61, 3148-3155 (2012).
275. Song, Z., Wang, W., Li, N.*, et al.* Sphingosine kinase 2 promotes lipotoxicity in pancreatic β-cells and the progression of diabetes. *Faseb J* 33, 3636-3646 (2019).
276. Ravichandran, S., Finlin, B.S., Kern, P.A. & Özcan, S. Sphk2−/− mice are protected from obesity and insulin resistance. *Biochimica et Biophysica Acta (BBA) - Molecular Basis of Disease* 1865, 570-576 (2019).
277. Aji, G., Huang, Y., Ng, M.L.*, et al.* Regulation of hepatic insulin signaling and glucose homeostasis by sphingosine kinase 2. *Proceedings of the National Academy of Sciences* 117, 24434-24442 (2020).
278. Zhao, J. & Lee, M.-J. Sphingosine Kinase 2 Knockout Mice Resist HFD-Induced Obesity Through Increasing Energy Expenditure. *International Journal of Endocrinology and Metabolism* 21(2023).
279. Nagahashi, M., Takabe, K., Liu, R.*, et al.* Conjugated bile acid-activated S1P receptor 2 is a key regulator of sphingosine kinase 2 and hepatic gene expression. *Hepatology* 61, 1216-1226 (2015).
280. Lee, S.-Y., Hong, I.-K., Kim, B.-R.*, et al.* Activation of sphingosine kinase 2 by endoplasmic reticulum stress ameliorates hepatic steatosis and insulin resistance in mice. *Hepatology* 62, 135-146 (2015).
281. Jackson, K.G., Zhao, D., Su, L.*, et al.* Sphingosine kinase 2 (SphK2) depletion alters redox metabolism and enhances inflammation in a diet-induced MASH mouse model. *Hepatology Communications* 8, e0570 (2024).
282. Liu, X.T., Chung, L.H., Liu, D.*, et al.* Ablation of sphingosine kinase 2 suppresses fatty liver-associated hepatocellular carcinoma via downregulation of ceramide transfer protein. *Oncogenesis* 11, 67 (2022).
283. Green, C.D., Brown, R.D.R., Uranbileg, B.*, et al.* Sphingosine kinase 2 and p62 regulation are determinants of sexual dimorphism in hepatocellular carcinoma. *Molecular Metabolism* 86, 101971 (2024).
284. Rohrbach, T.D., Asgharpour, A., Maczis, M.A.*, et al.* FTY720/fingolimod decreases hepatic steatosis and expression of fatty acid synthase in diet-induced nonalcoholic fatty liver disease in mice. *J Lipid Res* 60, 1311-1322 (2019).
285. Mauer, A.S., Hirsova, P., Maiers, J.L., Shah, V.H. & Malhi, H. Inhibition of sphingosine 1-phosphate signaling ameliorates murine nonalcoholic steatohepatitis. *American Journal of Physiology-Gastrointestinal and Liver Physiology* 312, G300-G313 (2017).
286. Liao, C.-Y., Barrow, F., Venkatesan, N.*, et al.* Modulating sphingosine 1-phosphate receptor signaling skews intrahepatic leukocytes and attenuates murine nonalcoholic steatohepatitis. *Frontiers in immunology* 14, 1130184 (2023).
287. Parthasarathy, G., Venkatesan, N., Sidhu, G.S.*, et al.* Deletion of sphingosine 1-phosphate receptor 1 in myeloid cells reduces hepatic inflammatory macrophages and attenuates MASH. *Hepatol Commun* 9(2025).
288. Kitada, Y., Kajita, K., Taguchi, K.*, et al.* Blockade of Sphingosine 1-Phosphate Receptor 2 Signaling Attenuates High-Fat Diet-Induced Adipocyte Hypertrophy and Systemic Glucose Intolerance in Mice. *Endocrinology* 157, 1839-1851 (2016).
289. Imasawa, T., Koike, K., Ishii, I., Chun, J. & Yatomi, Y. Blockade of sphingosine 1-phosphate receptor 2 signaling attenuates streptozotocin-induced apoptosis of pancreatic beta-cells. *Biochem Biophys Res Commun* 392, 207-211 (2010).

290. Fayyaz, S., Japtok, L. & Kleuser, B. Divergent Role of Sphingosine 1-Phosphate on Insulin Resistance. *Cellular Physiology and Biochemistry* 34, 134-147 (2014).
291. Studer, E., Zhou, X., Zhao, R.*, et al.* Conjugated bile acids activate the sphingosine-1-phosphate receptor 2 in primary rodent hepatocytes. *Hepatology* 55, 267-276 (2012).
292. Ikeda, H., Watanabe, N., Ishii, I.*, et al.* Sphingosine 1-phosphate regulates regeneration and fibrosis after liver injury via sphingosine 1-phosphate receptor 2. *J Lipid Res* 50, 556-564 (2009).
293. Sato, M., Ikeda, H., Uranbileg, B.*, et al.* Sphingosine kinase-1, S1P transporter spinster homolog 2 and S1P2 mRNA expressions are increased in liver with advanced fibrosis in human. *Sci Rep* 6, 32119 (2016).
294. Li, C., Jiang, X., Yang, L.*, et al.* Involvement of sphingosine 1-phosphate (SIP)/S1P3 signaling in cholestasis-induced liver fibrosis. *Am J Pathol* 175, 1464-1472 (2009).
295. Al Fadel, F., Fayyaz, S., Japtok, L. & Kleuser, B. Involvement of Sphingosine 1-Phosphate in Palmitate-Induced Non-Alcoholic Fatty Liver Disease. *Cellular Physiology and Biochemistry* 40, 1637-1645 (2016).
296. Chakrabarty, S., Bui, Q., Badeanlou, L.*, et al.* S1P/S1PR3 signalling axis protects against obesity-induced metabolic dysfunction. *Adipocyte* 11, 69-83 (2022).
297. Allende, M.L., Sasaki, T., Kawai, H.*, et al.* Mice deficient in sphingosine kinase 1 are rendered lymphopenic by FTY720. *J Biol Chem* 279, 52487-52492 (2004).
298. Hailemariam, T.K., Huan, C., Liu, J.*, et al.* Sphingomyelin Synthase 2 Deficiency Attenuates NFκB Activation. *Arteriosclerosis, Thrombosis, and Vascular Biology* 28, 1519-1526 (2008).
299. Zhang, P. Glucose Tolerance Test in Mice. *Bio-protocol* 1, e159 (2011).
300. Vinué, Á. & González-Navarro, H. Glucose and Insulin Tolerance Tests in the Mouse. *Methods Mol Biol* 1339, 247-254 (2015).
301. Seglen, P.O. Preparation of isolated rat liver cells. *Methods Cell Biol* 13, 29-83 (1976).
302. Berry, M.N. & Friend, D.S. High-yield preparation of isolated rat liver parenchymal cells: a biochemical and fine structural study. *J Cell Biol* 43, 506-520 (1969).
303. Godoy, P., Hewitt, N.J., Albrecht, U.*, et al.* Recent advances in 2D and 3D in vitro systems using primary hepatocytes, alternative hepatocyte sources and non-parenchymal liver cells and their use in investigating mechanisms of hepatotoxicity, cell signaling and ADME. *Arch Toxicol* 87, 1315-1530 (2013).
304. Weske, S., Nowak, M.K., Zaufel, A.*, et al.* Intracellular Sphingosine-1-Phosphate Induces Lipolysis Through Direct Activation of Protein Kinase C Zeta. *Faseb J* 39, e70528 (2025).
305. Oeckl, J., Bast-Habersbrunner, A., Fromme, T., Klingenspor, M. & Li, Y. Isolation, Culture, and Functional Analysis of Murine Thermogenic Adipocytes. *STAR Protoc* 1, 100118 (2020).
306. Hou, C., Feng, W., Wei, S.*, et al.* Bioinformatics Analysis of Key Differentially Expressed Genes in Nonalcoholic Fatty Liver Disease Mice Models. *Gene Expr* 19, 25-35 (2018).
307. Lee, Y.K., Park, J.E., Lee, M. & Hardwick, J.P. Hepatic lipid homeostasis by peroxisome proliferator-activated receptor gamma 2. *Liver Research* 2, 209-215 (2018).
308. Velnati, S., Centonze, S., Girivetto, F.*, et al.* Identification of Key Phospholipids That Bind and Activate Atypical PKCs. *Biomedicines* 9(2021).
309. Weske, S., Vaidya, M., Reese, A.*, et al.* Targeting sphingosine-1-phosphate lyase as an anabolic therapy for bone loss. *Nat Med* 24, 667-+ (2018).
310. Hammerschmidt, P. & Bruning, J.C. Contribution of specific ceramides to obesity-associated metabolic diseases. *Cell Mol Life Sci* 79, 395 (2022).
311. Liu, J., Zhang, H., Li, Z.*, et al.* Sphingomyelin synthase 2 is one of the determinants for plasma and liver sphingomyelin levels in mice. *Arterioscler Thromb Vasc Biol* 29, 850-856 (2009).
312. Moon, M.H., Jeong, J.K., Lee, Y.J., Seol, J.W. & Park, S.Y. Sphingosine-1-phosphate inhibits the adipogenic differentiation of 3T3-L1 preadipocytes. *Int J Mol Med* 34, 1153-1158 (2014).

313. Moon, M.H., Jeong, J.K. & Park, S.Y. Activation of S1P2 receptor, a possible mechanism of inhibition of adipogenic differentiation by sphingosine 1-phosphate. *Mol Med Rep* 11, 1031-1036 (2015).
314. Newton, A.C. Protein kinase C: poised to signal. *Am J Physiol Endocrinol Metab* 298, E395-402 (2010).
315. Greenberg, A.S., Shen, W.J., Muliro, K.*, et al.* Stimulation of lipolysis and hormone-sensitive lipase via the extracellular signal-regulated kinase pathway. *J Biol Chem* 276, 45456-45461 (2001).
316. Kajita, K., Ishii, I., Mori, I.*, et al.* Sphingosine 1-Phosphate Regulates Obesity and Glucose Homeostasis. *Int J Mol Sci* 25(2024).
317. Larsen, P.J. & Tennagels, N. On ceramides, other sphingolipids and impaired glucose homeostasis. *Mol Metab* 3, 252-260 (2014).
318. Völzke, H., Alte, D., Schmidt, C.O.*, et al.* Cohort profile: the study of health in Pomerania. *Int J Epidemiol* 40, 294-307 (2011).
319. Apostolopoulou, M., Gordillo, R., Koliaki, C.*, et al.* Specific Hepatic Sphingolipids Relate to Insulin Resistance, Oxidative Stress, and Inflammation in Nonalcoholic Steatohepatitis. *Diabetes Care* 41, 1235-1243 (2018).
320. Bektas, M., Allende, M.L., Lee, B.G.*, et al.* Sphingosine 1-phosphate lyase deficiency disrupts lipid homeostasis in liver. *J Biol Chem* 285, 10880-10889 (2010).
321. Brown, M.S. & Goldstein, J.L. Selective versus Total Insulin Resistance: A Pathogenic Paradox. *Cell Metabolism* 7, 95-96 (2008).
322. Samuel, Varman T. & Shulman, Gerald I. Mechanisms for Insulin Resistance: Common Threads and Missing Links. *Cell* 148, 852-871 (2012).
323. Britten, C.D., Garrett-Mayer, E., Chin, S.H.*, et al.* A Phase I Study of ABC294640, a First-in-Class Sphingosine Kinase-2 Inhibitor, in Patients with Advanced Solid Tumors. *Clin Cancer Res* 23, 4642-4650 (2017).
324. Smith, C.D., Maines, L.W., Keller, S.N.*, et al.* Recent Progress in the Development of Opaganib for the Treatment of Covid-19. *Drug Des Devel Ther* 16, 2199-2211 (2022).
325. Shi, Y., Wei, Q., Liu, Y. & Yuan, J. The alleviating effect of sphingosine kinases 2 inhibitor K145 on nonalcoholic fatty liver. *Biochemical and Biophysical Research Communications* 580, 1-6 (2021).
326. Maines, L.W., Keller, S.N., Smith, R.A. & Smith, C.D. Opaganib Promotes Weight Loss and Suppresses High-Fat Diet-Induced Obesity and Glucose Intolerance. *Diabetes Metab Syndr Obes* 18, 969-983 (2025).
327. McNaughton, M., Pitman, M., Pitson, S.M., Pyne, N.J. & Pyne, S. Proteasomal degradation of sphingosine kinase 1 and inhibition of dihydroceramide desaturase by the sphingosine kinase inhibitors, SKi or ABC294640, induces growth arrest in androgen-independent LNCaP-AI prostate cancer cells. *Oncotarget* 7, 16663-16675 (2016).
328. Prell, A., Wigger, D., Huwiler, A., Schumacher, F. & Kleuser, B. The sphingosine kinase 2 inhibitors ABC294640 and K145 elevate (dihydro)sphingosine 1-phosphate levels in various cells. *J Lipid Res*, 100631 (2024).
329. Li, H., Sun, J., Li, B.*, et al.* AMPK-PPARγ-Cidec Axis Drives the Fasting-Induced Lipid Droplet Aggregation in the Liver of Obese Mice. *Front Nutr* 9, 917801 (2022).
330. Kim, J.Y., Tillison, K., Lee, J.-H., Rearick, D.A. & Smas, C.M. The adipose tissue triglyceride lipase ATGL/PNPLA2 is downregulated by insulin and TNF-α in 3T3-L1 adipocytes and is a target for transactivation by PPARγ. *American Journal of Physiology-Endocrinology and Metabolism* 291, E115-E127 (2006).
331. Turpin, S.M., Hoy, A.J., Brown, R.D.*, et al.* Adipose triacylglycerol lipase is a major regulator of hepatic lipid metabolism but not insulin sensitivity in mice. *Diabetologia* 54, 146-156 (2011).
332. Wilson, C.G., Tran, J.L., Erion, D.M.*, et al.* Hepatocyte-Specific Disruption of CD36 Attenuates Fatty Liver and Improves Insulin Sensitivity in HFD-Fed Mice. *Endocrinology* 157, 570-585 (2016).

333. Zeng, H., Qin, H., Liao, M.*, et al.* CD36 promotes de novo lipogenesis in hepatocytes through INSIG2-dependent SREBP1 processing. *Mol Metab* 57, 101428 (2022).
334. Steneberg, P., Sykaras, A.G., Backlund, F.*, et al.* Hyperinsulinemia Enhances Hepatic Expression of the Fatty Acid Transporter Cd36 and Provokes Hepatosteatosis and Hepatic Insulin Resistance. *Journal of Biological Chemistry* 290, 19034-19043 (2015).
335. Kwong, E.K. & Zhou, H. Sphingosine-1-phosphate signaling and the gut-liver axis in liver diseases. *Liver Res* 3, 19-24 (2019).
336. Li, X., Yuan, B., Lu, M.*, et al.* The methyltransferase METTL3 negatively regulates nonalcoholic steatohepatitis (NASH) progression. *Nature Communications* 12, 7213 (2021).
337. Schmahl, J., Raymond, C.S. & Soriano, P. PDGF signaling specificity is mediated through multiple immediate early genes. *Nature Genetics* 39, 52-60 (2007).
338. Wang, H.-C., Wong, T.-H., Wang, L.-T.*, et al.* Aryl hydrocarbon receptor signaling promotes ORMDL3-dependent generation of sphingosine-1-phosphate by inhibiting sphingosine-1-phosphate lyase. *Cellular & Molecular Immunology* 16, 783-790 (2019).
339. Kuo, H.-R., Chung, Y.-F., Wang, L.-T.*, et al.* Polycyclic aromatic hydrocarbon aggravates high-fat diet-induced metabolic dysfunction-associated steatotic liver disease through disturbing hepatocyte sphingolipid metabolism. *Environmental Pollution* 383, 126846 (2025).
340. Hsu, S.C., Chen, C.L., Liu, C.T.*, et al.* Reduced Sphingosine-1-Phosphate Levels Exacerbate Type 2 Diabetes Mellitus and Associated Complications in a High-Fat Diet Mouse Model. *Endocrinol Metab (Seoul)* (2025).
341. Spohner, A.K., Jakobi, K., Trautmann, S.*, et al.* Mouse Liver Compensates Loss of Sgpl1 by Secretion of Sphingolipids into Blood and Bile. *Int J Mol Sci* 22(2021).
342. Zhou, J., Febbraio, M., Wada, T.*, et al.* Hepatic Fatty Acid Transporter Cd36 Is a Common Target of LXR, PXR, and PPARγ in Promoting Steatosis. *Gastroenterology* 134, 556-567.e551 (2008).
343. Yu, X.X., Lewin, D.A., Forrest, W. & Adams, S.H. Cold elicits the simultaneous induction of fatty acid synthesis and beta-oxidation in murine brown adipose tissue: prediction from differential gene expression and confirmation in vivo. *Faseb J* 16, 155-168 (2002).
344. Afsar, S.Y., Alam, S., Fernandez Gonzalez, C. & van Echten-Deckert, G. Sphingosine-1-phosphate-lyase deficiency affects glucose metabolism in a way that abets oncogenesis. *Mol Oncol* 16, 3642-3653 (2022).
345. Thomas, N., Schröder, N.H., Nowak, M.K.*, et al.* Sphingosine-1-phosphate suppresses GLUT activity through PP2A and counteracts hyperglycemia in diabetic red blood cells. *Nat Commun* 14, 8329 (2023).
346. Rapizzi, E., Taddei, M.L., Fiaschi, T.*, et al.* Sphingosine 1-phosphate increases glucose uptake through trans-activation of insulin receptor. *Cellular and Molecular Life Sciences* 66, 3207-3218 (2009).
347. DeFronzo, R.A., Jacot, E., Jequier, E.*, et al.* The effect of insulin on the disposal of intravenous glucose. Results from indirect calorimetry and hepatic and femoral venous catheterization. *Diabetes* 30, 1000-1007 (1981).
348. Choi, S.M., Tucker, D.F., Gross, D.N.*, et al.* Insulin regulates adipocyte lipolysis via an Akt-independent signaling pathway. *Mol Cell Biol* 30, 5009-5020 (2010).
349. Fricke, K., Heitland, A. & Maronde, E. Cooperative activation of lipolysis by protein kinase A and protein kinase C pathways in 3T3-L1 adipocytes. *Endocrinology* 145, 4940-4947 (2004).
350. Orlicky, D.J., DeGregori, J. & Schaack, J. Construction of stable coxsackievirus and adenovirus receptor-expressing 3T3-L1 cells. *J Lipid Res* 42, 910-915 (2001).
351. Havulinna, A.S., Sysi-Aho, M., Hilvo, M.*, et al.* Circulating Ceramides Predict Cardiovascular Outcomes in the Population-Based FINRISK 2002 Cohort. *Arterioscler Thromb Vasc Biol* 36, 2424-2430 (2016).
352. Chaurasia, B., Ying, L., Talbot, C.L.*, et al.* Ceramides are necessary and sufficient for diet-induced impairment of thermogenic adipocytes. *Mol Metab* 45, 101145 (2021).

353. Monick, M.M., Carter, A.B., Flaherty, D.M., Peterson, M.W. & Hunninghake, G.W. Protein kinase C zeta plays a central role in activation of the p42/44 mitogen-activated protein kinase by endotoxin in alveolar macrophages. *J Immunol* 165, 4632-4639 (2000).
354. Wang, Y., Seibenhener, M.L., Vandenplas, M.L. & Wooten, M.W. Atypical PKC ζ is activated by ceramide, resulting in coactivation of NF-κb/JNK kinase and cell survival. *Journal of Neuroscience Research* 55, 293-302 (1999).
355. Bourbon, N.A., Yun, J. & Kester, M. Ceramide directly activates protein kinase C zeta to regulate a stress-activated protein kinase signaling complex. *J Biol Chem* 275, 35617-35623 (2000).
356. Fox, T.E., Houck, K.L., O'Neill, S.M.*, et al.* Ceramide recruits and activates protein kinase C zeta (PKC zeta) within structured membrane microdomains. *The Journal of biological chemistry* 282, 12450-12457 (2007).
357. Bandyopadhyay, G., Sajan, M.P., Kanoh, Y.*, et al.* PKC-ζ Mediates Insulin Effects on Glucose Transport in Cultured Preadipocyte-Derived Human Adipocytes. *The Journal of Clinical Endocrinology & Metabolism* 87, 716-723 (2002).
358. Arribas, M., Valverde, A.M., Burks, D.*, et al.* Essential role of protein kinase C zeta in the impairment of insulin-induced glucose transport in IRS-2-deficient brown adipocytes. *FEBS Lett* 536, 161-166 (2003).
359. Stratford, S., Hoehn, K.L., Liu, F. & Summers, S.A. Regulation of insulin action by ceramide: dual mechanisms linking ceramide accumulation to the inhibition of Akt/protein kinase B. *J Biol Chem* 279, 36608-36615 (2004).
360. Powell, D.J., Hajduch, E., Kular, G. & Hundal, H.S. Ceramide disables 3-phosphoinositide binding to the pleckstrin homology domain of protein kinase B (PKB)/Akt by a PKCzeta-dependent mechanism. *Mol Cell Biol* 23, 7794-7808 (2003).
361. Sajan, M.P., Ivey, R.A., Lee, M.C. & Farese, R.V. Hepatic insulin resistance in ob/ob mice involves increases in ceramide, aPKC activity, and selective impairment of Akt-dependent FoxO1 phosphorylation. *J Lipid Res* 56, 70-80 (2015).
362. Chakrabarti, P. & Kandror, K.V. FoxO1 controls insulin-dependent adipose triglyceride lipase (ATGL) expression and lipolysis in adipocytes. *J Biol Chem* 284, 13296-13300 (2009).
363. Taniguchi, C.M., Kondo, T., Sajan, M.*, et al.* Divergent regulation of hepatic glucose and lipid metabolism by phosphoinositide 3-kinase via Akt and PKClambda/zeta. *Cell Metab* 3, 343-353 (2006).
364. Huitema, K., van den Dikkenberg, J., Brouwers, J.F. & Holthuis, J.C. Identification of a family of animal sphingomyelin synthases. *Embo j* 23, 33-44 (2004).
365. Tani, M. & Kuge, O. Sphingomyelin synthase 2 is palmitoylated at the COOH-terminal tail, which is involved in its localization in plasma membranes. *Biochem Biophys Res Commun* 381, 328-332 (2009).
366. Hannun, Y.A. & Bell, R.M. Functions of sphingolipids and sphingolipid breakdown products in cellular regulation. *Science* 243, 500-507 (1989).
367. Kim, Y.J., Greimel, P. & Hirabayashi, Y. GPRC5B-Mediated Sphingomyelin Synthase 2 Phosphorylation Plays a Critical Role in Insulin Resistance. *iScience* 8, 250-266 (2018).
368. Zeng, J., Way, G., Wu, N.*, et al.* Transcriptomics, lipidomics, and single-nucleus RNA sequencing integration: exploring sphingolipids in MASH-HCC progression. *Cell Biosci* 15, 34 (2025).
369. Wigger, L., Cruciani-Guglielmacci, C., Nicolas, A.*, et al.* Plasma Dihydroceramides Are Diabetes Susceptibility Biomarker Candidates in Mice and Humans. *Cell Rep* 18, 2269-2279 (2017).
370. Carlier, A., Phan, F., Szpigel, A.*, et al.* Dihydroceramides in Triglyceride-Enriched VLDL Are Associated with Nonalcoholic Fatty Liver Disease Severity in Type 2 Diabetes. *Cell Rep Med* 1, 100154 (2020).
371. Tippetts, T.S., Holland, W.L. & Summers, S.A. The ceramide ratio: a predictor of cardiometabolic risk. *J Lipid Res* 59, 1549-1550 (2018).

372. Griess, K., Rieck, M., Muller, N.*, et al.* Sphingolipid subtypes differentially control proinsulin processing and systemic glucose homeostasis. *Nat Cell Biol* 25, 20-29 (2023).
373. Rigamonti, A.E., Dei Cas, M., Caroli, D.*, et al.* Ceramide Risk Score in the Evaluation of Metabolic Syndrome: An Additional or Substitutive Biochemical Marker in the Clinical Practice? *Int J Mol Sci* 24(2023).
374. Hilvo, M., Meikle, P.J., Pedersen, E.R.*, et al.* Development and validation of a ceramide- and phospholipid-based cardiovascular risk estimation score for coronary artery disease patients. *European Heart Journal* 41, 371-380 (2019).
375. Chen, Q., Wang, W., Xia, M.-F.*, et al.* Identification of circulating sphingosine kinase-related metabolites for prediction of type 2 diabetes. *Journal of Translational Medicine* 19, 393 (2021).
376. Juchnicka, I., Kuźmicki, M., Zabielski, P.*, et al.* Serum C18:1-Cer as a Potential Biomarker for Early Detection of Gestational Diabetes. *J Clin Med* 11(2022).
377. Rigamonti, A.E., Dei Cas, M., Caroli, D.*, et al.* Identification of a Specific Plasma Sphingolipid Profile in a Group of Normal-Weight and Obese Subjects: A Novel Approach for a "Biochemical" Diagnosis of Metabolic Syndrome? *Int J Mol Sci* 24(2023).
378. Hasselgren, C. & Oprea, T.I. Artificial Intelligence for Drug Discovery: Are We There Yet? *Annu Rev Pharmacol Toxicol* 64, 527-550 (2024).
379. Kartoun, U., Corey, K.E., Simon, T.G.*, et al.* The MELD-Plus: A generalizable prediction risk score in cirrhosis. *PLoS One* 12, e0186301 (2017).

Appendix

A1 Supplementary Tables

Appendix Table 1. HPLC setup.

Method	Settings				
S1P + Cer	Column and pore size	MultoHigh 100 RP-18, 3µm, 60×2 mm			
	Mobile phase	A = Methanol B = aq. HCO_2H (1% *v/v*)			
	Gradient Settings	Time [min]	A [%]	B [%]	B curve
		0	10	90	-2
		3	100	0	0
		8	100	0	0
		8.01	10	90	0
		Stop time: 10 min			
	Flow rate	0.4 mL/min			
	Injection volume	10 µL (3µL for Liver samples)			
	Oven temperature	40 °C			
LPC PC SM	Column and pore size	Accucore Polar Premium, 2.6 µm, 150×3 mm			
	Mobile phase	A = ACN/1-Propanol (1:1) + 0.01% (*v/v*) HCO_2H B = 5 mM aq. ammonium formate + 0.01% (v/v) HCO_2H			
	Gradient Settings	Time [min]	A [%]	B [%]	B curve
		0	20	80	0
		1	20	80	0
		2	40	60	−3
		25	92.5	7.5	0
		26	100	0	0
		35	100	0	0
		35.1	20	80	0
		Stop time: 38 min			
	Flow rate	0.3 mL/min			
	Injection volume	1 µL			
	Oven temperature	45 °C			
FFA	Column and pore size	MultoHigh 100 RP-8, 3µm, 60×2 mm			
	Mobile phase	A = Methanol/^{i}1-Propanol (9:1) B = 5 mM aq. ammonium formate + 0.01% (v/v) HCO_2H			
	Gradient Settings	Time [min]	A [%]	B [%]	B curve
		0	40	60	-2
		9.5	95	5	0
		12	100	0	0
		13	100	0	0
		13.1	40	60	0
		Stop Time: 15 min			
	Flow rate	0.4 mL/min			
	Injection volume	3 µL			
	Oven temperature	40 °C			

Appendix Table 2. Internal and external standards and analytes used for standard curve generation.

Analyte	ISTD group	ISTD	ISTD (µM)	Ext. Std. conc.	Ext. standard
S1P	1	S1P-d_7	0.1	10 nM – 5 µM	S1P
C17-S1P	1	S1P-d_7	0.1	10 nM – 5 µM	C17-S1P
Sph	2	Sph-d_7	0.3	10 nM – 5 µM	Sph
C17-Sph	2	Sph-d_7	0.3	10 nM – 5 µM	C17-Sph
Spha	2	Sph-d_7	0.3	10 nM – 5 µM	Sph
Chol	3	Ergosterol	3.0	1 µM – 5 mM	Chol
Cer	4	Cer 15:0	3.0	10 nm – 5 µM	18:1/16:0 18:1/18:0 18:1/ 20:0 18:1/22:0 18:1/24:0 18:1/24:1
LPC	5	17:0	0.3	0.1 µM – 10 µM	14:0 16:0 18:0 18:1 22:6
PC	5	LPC 17:0	3	0.1 µM – 10 µM	32:0–16:0/16:0 34:0–18:0/16:0 36:1–18:1/18:0 36:4–16:0/20:4 38:4–18:0/20:4 38:6–18:0/22:6 40:6–18:0/22:6
SM	6	17:0	0.3	0.1 µM – 10 µM	32:1–18:1/14:0 34:1–18:1/16:0 36:1–18:1/18:1 38:1–18:1/20:0 40:1–18:1/22:0 42:1–18:1/24:0 42:2–18:1/24:1
FFA	7	d35-FA 18:0	30	0.1 µM – 10 µM	FA 14:0 FA 16:0 FA 18:0
	8	d9-FA 18:1	30		FA 18:1 FA 18:2 FA 20:3
	9	d8-FA 20:4	30		FA 20:3 FA 20:4 FA 20:5 FA 22:6

Appendix Table 3. MRM settings

Analyte	m/z (Q1)	m/z (Q3)	ISTD Group
S1P (d18:1)	380.3	264.1; 82.0	1
S1P (d17:1)	366.2	250.1; 268.3	1
S1P (d18:1)-d_7	387.2	271.25	1
Sphingosine (d18:1)	300.3	252.2	2
Sphingosine (d17:1)	286.3	268.2	2
Sphingosine (d18:1)-d_7	307.2	289.35	2
Sphinganine (d18:0)	302.3	254.3	2
Cholesterol	369.2	161.3	3
Ergosterol	379.2	69.2	3
Cer (d18:1/16:0)	538.5	264.2	4
Cer (d18:1/18:0)	566.6	264.5	4
Cer (d18:1/20:0)	594.5	264.5	4
Cer (d18:1/22:0)	622.7	264.5	4
Cer (d18:1/24:0)	650.7	264.4	4
Cer (d18:1/24:1)	648.7	264.54	4
LPC (14:0)	468.3	184.1	5
LPC (17:0)	510.35	184.1	5
LPC (16:0)	496.35	184.1	5
LPC (18:0)	524.35	184.1	5
LPC (18:1)	522.35	184.1	5
LPC (18:2)	520.35	184.1	5
LPC (18:3)	518.3	184.1	5
LPC (20:0)	552.4	184.1	5
LPC (20:1)	550.4	184.1	5
LPC (20:4)	544.35	184.1	5
LPC (20:5)	542.3	184.1	5
LPC (22:6)	568.35	184.1	5
PC (32:0)	734.55	184.1	5
PC (32:1)	732.55	184.1	5
PC (32:2)	730.55	184.1	5
PC (34:0)	762.6	184.1	5
PC (34:3)	756.55	184.1	5
PC (34:4)	754.55	184.1	5
PC (36:1)	788.6	184.1	5
PC (36:3)	784.6	184.1	5

Analyte	m/z (Q1)	m/z (Q3)	ISTD Group
PC (36:4)	782.55	184.1	5
PC (36:5)	780.55	184.1	5
PC (38:3)	812.6	184.1	5
PC (38:4)	810.6	184.1	5
PC (38:5)	808.6	184.1	5
PC (38:6)	806.55	184.1	5
PC (40:6)	834.6	184.1	5
PC (40:7)	832.6	184.1	5
PC (42:7)	860.6	184.1	5
SM (35:1-d18:1/17:0)	717.7	184.2	6
SM (20:1-d18:1/2:0)	507.35	184.1	5
SM (32:1-d18:1/14:0)	675.55	184.1	6
SM (34:1-d18:1/16:0)	703.6	184.1	6
SM (34:2-d18:1/16:1)	701.55	184.1	6
SM (36:1-d18:1/18:0)	731.6	184.1	6
SM (36:2-d18:1/18:1)	729.6	184.1	6
SM (38:1-d18:1/20:0)	759.65	184.1	6
SM (40:1-d18:1/22:0)	787.75	184.1	6
SM (42:1-d18:1/24:0)	815.8	184.1	6
SM (42:2-d18:1/24:1)	813.8	184.2	6
FA 14:0	476.2	171.2	7
FA 16:0	504.2	1713	7
FA 18:0-d_{35} [ISTD]	567.3	171.3	7
FA 18:0	532.3	171.3	8
FA 18:1-d_9 [ISTD]	539.2	171	8
FA 18:1	530.3	171.3	8
FA 18:2	528.3	170.5	8
FA 20:3	554.3	171.2	9
FA 20:4-d_8 [ISTD]	560.2	171.2	9
FA 20:4	552.2	171.3	9
FA 20:5	550.2	171.2	9
FA 22:6	576.3	171.2	9

A2 Additional Figures

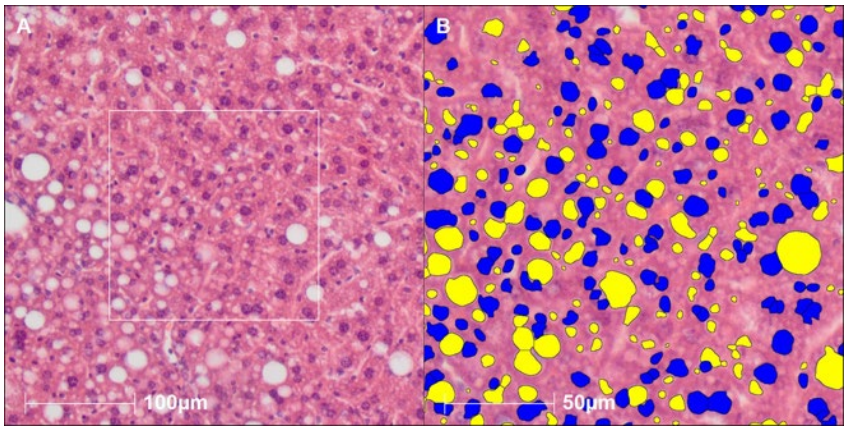

Appendix Figure 1. Example image for HALO Image Analysis Platform version 4.0.5107 (Indica Labs, Inc.). (a) Exemplary representation of a H&E-stained liver section. (b) Zoom-in view analyzed using HALO vacuole quantification module (Vacuole v3.2.2). Yellow, vacuole area; blue, nucleus.

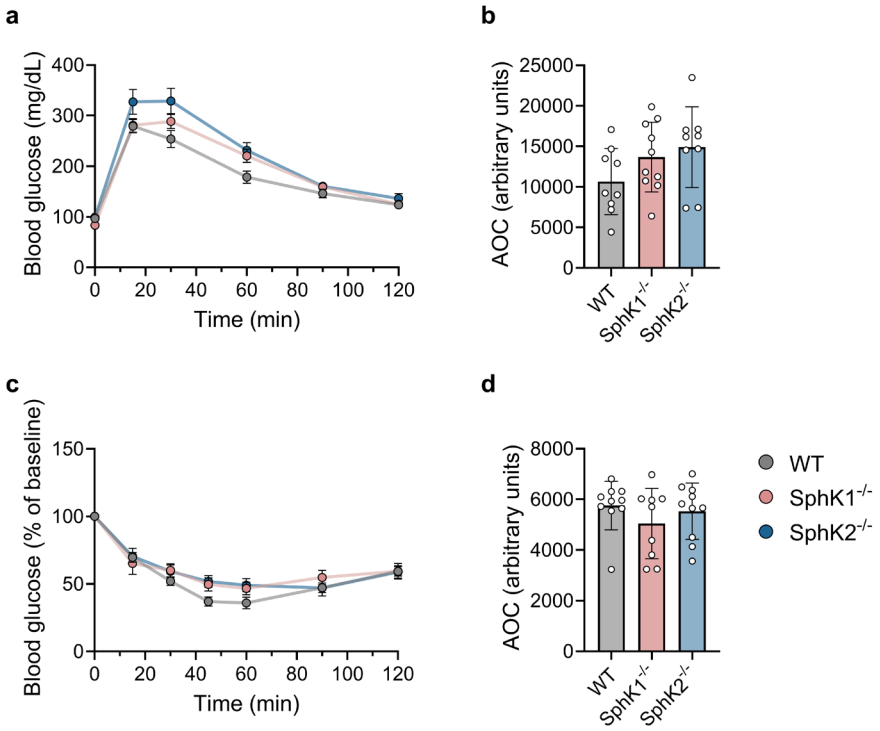

Appendix Figure 2. Glucose and insulin tolerance tests in mice fed a control diet. Mice were fed a control diet for 10 and 11 weeks, respectively. (a) ipGTT using a glucose dose of 2 mg/kg and (b) quantification of AUC. (c) ipITT using an insulin dose of 1 U/kg and (d) quantification of AOC. Data are presented as mean ± SD. Statistical analysis was performed using one-way ANOVA followed by Tukey's post-hoc test for multiple comparisons.

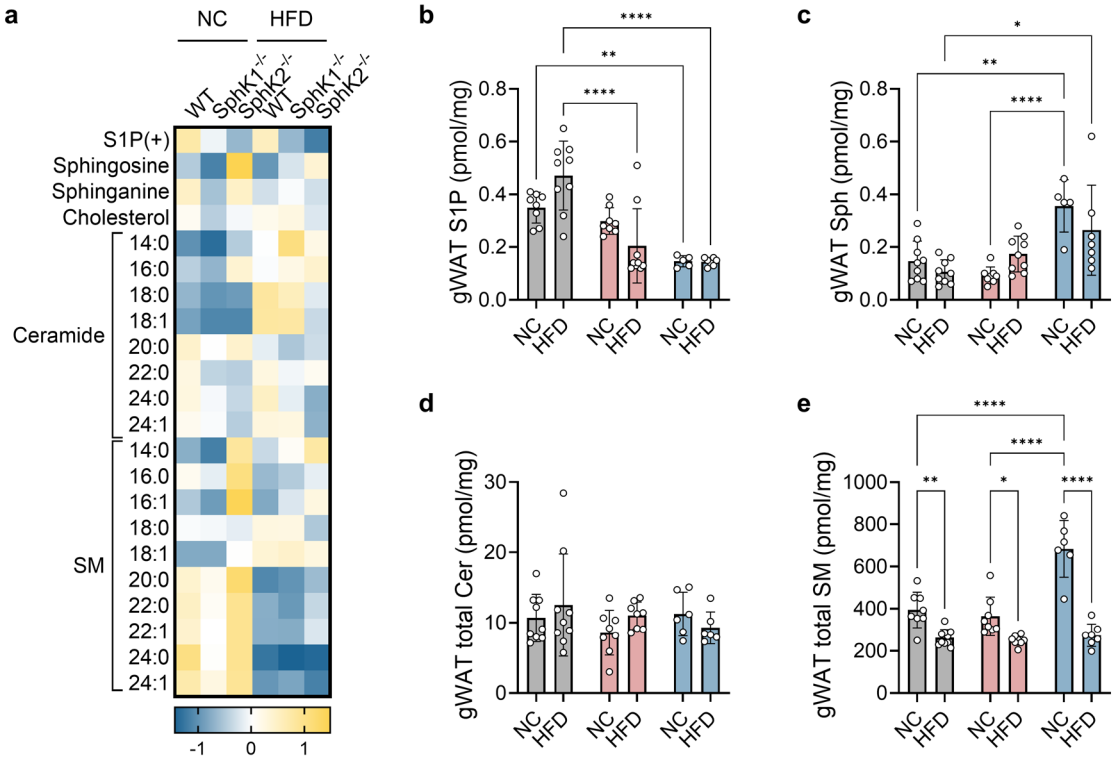

Appendix Figure 3. Sphingolipid profiles in white adipose tissue. WT, SphK1$^{-/-}$ and SphK2$^{-/-}$ mice were fed either a NC or high-fat diet (60% kcal from fat) for 12 weeks. LC-MS/MS analysis was performed in gonadal white adipose tissue. (a) Heatmap of selected lipid species in gWAT. Levels of (b) S1P and (c) Sph, (d) ceramide (sum), and (e) sphingomyelin (sum) in gWAT. Data are presented as mean ± SD. n_{WT+NC} = 8–9, n_{WT+HFD} = 9, $n_{SphK1^{-/-}+NC}$ = 8, $n_{SphK1^{-/-}+HFD}$ = 8–9, $n_{SphK2^{-/-}+NC}$ = 5–6, $n_{SphK2^{-/-}+HFD}$ = 6–7. Statistical analysis was performed using two-way ANOVA followed by Tukey's post hoc test for multiple comparisons. Statistical significance is indicated as follows: **** p <0.0001.

Author Contribution Statement

Melissa Nowak was responsible for the planning, designing, performing, analyzing, and interpreting of most of the experiments, under the supervision and guidance of Prof. Dr. Bodo Levkau. The research benefited from the contributions of other researchers, who provided their expertise and collaboration, as detailed below.

The samples for **RNA Sequencing** (3.2.10) were prepared by Melissa Kim Nowak. Quality control, 3′ RNA sequencing, including library preparation and initial data processing, was conducted by the team at the Genomics & Transcriptomics Laboratory (GTL) from Biologisch-Medizinisches Forschungszentrum (BMFZ) of the Heinrich Heine University Düsseldorf. Subsequent analysis, data visualization, and functional interpretation of the sequencing results were performed by Melissa Kim Nowak.

Melissa Kim Nowak was responsible for preparing the samples for **LC-MS/MS** (3.2.12). Philipp Wollnitzke managed the operation of the instrument, data acquisition, and initial data processing. Subsequently, Melissa Kim Nowak performed further data processing, statistical analysis, and interpretation.

Sample preparation for **multiplex kinome activtiy profiling** (3.2.8) was carried out by Melissa Kim Nowak. The assay as well as data analysis was conducted by the group of Emiel van der Vorst at the Institute for Molecular Cardiovascular Research (IMCAR) at the University Hospital Aachen.

Parts of this thesis are based on the following publication:

Sarah Weske*, **Melissa Kim Nowak***, Alex Zaufel, Lea Esser, Christoph Peter, Lisa Walz, Helena Kühn, Tsyon Wolde, Julia Hoppe, Nathalie Hannelore Schröder, Tobias Buschmann, Philipp Wollnitzke and Bodo Levkau. **Intracellular Sphingosine-1-Phosphate Induces Lipolysis Through Direct Activation of Protein Kinase C Zeta**. (2025). The FASEB Journal, 39: e70528. https://doi.org/10.1096/fj.202403272R

As a shared first author, Melissa Kim Nowak was responsible for investigation and methodology (including mouse models, isolation and differentiation of murine primary adipocytes, and LC-MS/MS sample preparation), as well as for data visualization, formal analysis and original draft preparation. The procedures for 3T3-L1 cell culture and differentiation (3.2.6), lipolysis assay (3.2.7), and *in vitro* kinase assay (3.2.8) were performed by Sarah Weske and co-authors and are comprehensively detailed in the Methods section to ensure completeness.

Publications

Weske S*, **Nowak MK***, Zaufel A, Esser L, Peter C, Walz L, Kühn H, Wolde T, Hoppe J, Schröder NH, Buschmann T, Wollnitzke P, Levkau B. Intracellular Sphingosine-1-Phosphate Induces Lipolysis Through Direct Activation of Protein Kinase C Zeta. FASEB J. 2025 Apr 15;39(7):e70528. doi: 10.1096/fj.202403272R. Erratum in: FASEB J. 2025 Jun 15;39(11):e70692. doi: 10.1096/fj.202501754. PMID: 40193069; PMCID: PMC11975168.

Duse DA, Schröder NH, Srivastava T, Benkhoff M, Vogt J, **Nowak MK**, Funk F, Semleit N, Wollnitzke P, Erkens R, Kötter S, Meuth SG, Keul P, Santos W, Polzin A, Kelm M, Krüger M, Schmitt J, Levkau B. Deficiency of the sphingosine-1-phosphate (S1P) transporter Mfsd2b protects the heart against hypertension-induced cardiac remodeling by suppressing the L-type-Ca^{2+} channel. Basic Res Cardiol. 2024 Oct;119(5):853-868. doi: 10.1007/s00395-024-01073-x. Epub 2024 Aug 7. PMID: 39110173; PMCID: PMC11461684.

Heller K, Flocke V, Straub T, Ding Z, Srivastava T, **Nowak M**, Funk F, Levkau B, Schmitt J, Grandoch M, Flögel U. Magnetic resonance reveals early lipid deposition in murine prediabetes as predictive marker for cardiovascular injury. Npj Imaging. 2024 Sep 23;2(1):36. doi: 10.1038/s44303-024-00044-0. PMID: 40604298; PMCID: PMC12118699.

Wille A, Weske S, von Wnuck Lipinski K, Wollnitzke P, Schröder NH, Thomas N, **Nowak MK**, Deister-Jonas J, Behr B, Keul P, Levkau B. Sphingosine-1-phosphate promotes osteogenesis by stimulating osteoblast growth and neovascularization in a vascular endothelial growth factor-dependent manner. J Bone Miner Res. 2024 Apr 19;39(3):357-372. doi: 10.1093/jbmr/zjae006. PMID: 38477738; PMCID: PMC11240155.

Thomas N, Schröder NH, **Nowak MK**, Wollnitzke P, Ghaderi S, von Wnuck Lipinski K, Wille A, Deister-Jonas J, Vogt J, Gräler MH, Dannenberg L, Buschmann T, Westhoff P, Polzin A, Kelm M, Keul P, Weske S, Levkau B. Sphingosine-1-phosphate suppresses GLUT activity through PP2A and counteracts hyperglycemia in diabetic red blood cells. Nat Commun. 2023 Dec 14;14(1):8329. doi: 10.1038/s41467-023-44109-x. PMID: 38097610; PMCID: PMC10721873.

Keul P, Peters S, von Wnuck Lipinski K, Schröder NH, **Nowak MK**, Duse DA, Polzin A, Weske S, Gräler MH, Levkau B. Sphingosine-1-Phosphate (S1P) Lyase Inhibition Aggravates Atherosclerosis and Induces Plaque Rupture in *ApoE–/–*Mice. Int J Mol Sci. 2022 Aug 24;23(17):9606. doi: 10.3390/ijms23179606. PMID: 36077004; PMCID: PMC9455951.

Stejskalová A, Fincke V, **Nowak M**, Schmidt Y, Borrmann K, von Wahlde MK, Schäfer SD, Kiesel L, Greve B, Götte M. Collagen I triggers directional migration, invasion and matrix remodeling of stroma cells in a 3D spheroid model of endometriosis. Sci Rep. 2021 Feb 18;11(1):4115. doi: 10.1038/s41598-021-83645-8. PMID: 33603041; PMCID: PMC7892880.

Statement of Authorship

I hereby declare in lieu of an oath that this dissertation has been written by me independently and without unreliable external assistance in accordance with the “Principles for the Safeguarding of Good Scientific Practice at Heinrich Heine University Düsseldorf”. This work is original and has not been submitted, in whole or in part, to any other institution. Furthermore, I have not made any prior unsuccessful attempts at obtaining a doctorate.

Melissa Kim Nowak
Düsseldorf, October 2025